Interplay between complex orders in functional materials

PhD program

Nanoscience

Academic year

2019/2020

Scuola Normale Superiore,
Istituto Italiano di Tecnologia

Candidate
Louis Ponet

Thesis Advisor
Dr. Sergey Artyukhin
Internal Supervisor
Prof. Giuseppe La Rocca

Except where acknowledged in the customary manner, the material presented in this thesis is, to the best of my knowledge, original and has not been submitted in whole or part for a degree in any university.

Louis Ponet

Acknowledgements

First and foremost I would like to thank my supervisor Dr. Sergey Artyukhin for the wonderful opportunities I was offered during my Ph.D. The freedom and encouragement that he gave me to pursue my many interests have allowed me to develop my knowledge and skills in many areas of Condensed Matter Physics, while providing me with all the answers to the many questions I had, with most illuminating, engaging, and fruitful discussions, and with overall incredible guidance and support. I would, furthermore, like to thank Prof. David Vanderbilt and Prof. Stefan Blügel for allowing me to visit their group, which broadened my scientific horizon and led to many engaging experiences. In light of the latter, I also want to thank Dr. Manuel dos Santos Dias for his friendship and the insightful discussions I had with him during my short stay. I also wish to thank Prof. Maxim Mostovoy, Prof. Sang-Wook Cheong, Prof. Andrei Pimenov, Prof. Andrei Singer, and Prof. Gustavo Catalán for their insights and wonderful collaborations. I would also like to thank Prof. Giuseppe La Rocca for his swift and helpful comments during the process of writing this Thesis. Reflecting on the academic steps that ultimately brought me to this point, I can not help but feel a deep gratitude towards Meneer Koen Geeraert for providing the initial matchstick that ignited my passion for physics.

I wish to thank the many friends I got to know along this journey for providing me with an ever kind and pleasant environment. I will never forget the many discussions on numerical codes and techniques I had with Peng, some more heated than others, all of them rewarding. Giulia and Francesco were never faltering presences of kindness and joy in our office, either through music, or origami dinosaurs. In the later years, I got to share in the wisdom of Gabriele and the humor of Michele, dark and cynical, or otherwise. The first year I spent at Scuola Normale, I'll never forget. The true close-knit group of friends I found there led me to experience truly spectacularly fun moments. I will always cherish the never-ending battle fought with Paolo, Gianmichele, and Pietro on the billiardino, the calm composure of Bibek, and deep conversations with Marcello and Donato, all topped off by a bit of benzina during our nightly endeavors. I would also like to take this moment to truly thank my friends back home for remaining an ever-reliable source of fun, happiness, and support. Florian in particular has seen all the ups and downs I went through on this, sometimes tumultuous, journey, providing me with never-ending camaraderie, deep conversations, cat videos of every variety, beverages of every color, and consolation in more trying times.

I thank my sister Marie for always being a listening ear, and my brother Philippe for sharing with me his passion for all things computers and games, and both of them for always believing in me.

This brings me, finally, to my Mother and Father, whom I can not thank enough for the many opportunities, endless support, unconditional love, perpetual encouragement, and cautious patience they have given me. I truly could not have wished for more fantastic parents.

List of publications

- **Louis Ponet**, S. Artyukhin
  First-principles theory of giant Rashba-like spin splitting in bulk GeTe
  Phys. Rev. B. **98**, 174102 (2018)

- P. Chen, **Louis Ponet**, K. Lai, R. Cingolani, S. Artyukhin
  Domain wall-localized phonons in $BiFeO_3$: spectrum and selection rules
  npj Comput. Mater. **6**, 48 (2020)

- Y. Huang, L. Zheng, P. Chen, X. Cheng, S. Hsu, T. Yang, X. Wu, **Louis Ponet**, R. Ramesh, L. Chen, S. Artyukhin, Y. Chu, K. Lai
  Unexpected giant microwave conductivity in a nominally silent $BiFeO_3$ domain wall
  Adv. Mater. **32**, 1905132 (2020)

- C. Stefani, **Louis Ponet**, K. Shapovalov, P. Chen, E. Langenberg, D. G. Schlom, S. Artyukhin, M. Stengel, N. Domingo, G. Catalan
  Mechanical softness of ferroelectric 180° domain walls
  Phys. Rev. X **10**, 041001 (2020)

- O. Yu. Gorobtsov, **Louis Ponet**, S. K. K. Patel, N. Hua, A. G. Shabalin, S. Hrkac, J. Wingert, D. Cela, J. M. Glownia, D. Zhu, R. Medapalli, M. Chollet, E. E. Fullerton, S. Artyukhin, O. G. Shpyrko, A. Singer
  Femtosecond control of phonon dynamics near a magnetic order critical point
  Nature communications *under review*

- F. Fan, Z. Gao, **Louis Ponet**, J. Wang, H. Huang, S. Artyukhin, J. Hong, S. Cheong, X. Wang
  Visualization of large-scale charged domain wall in hexagonal manganites
  Appl. Phys. Lett. **118**, 072901 (2021)

- **Louis Ponet**, S. Artyukhin, Th. Kain, Anna Pimenov, A. Shuvaev, X. Wang, S. Cheong, M. Mostovoy, Andrei Pimenov
  Magnetoelectric Crankshaft
  Nature *under review*

- B. Dhanabalan, G. Biffi, A. Moliterni, V. Olieric, C. Giannini, G. Saleh, **Louis Ponet**, M. Prato, M. Imran, L. Manna, R. Krahne, S. Artyukhin, M. P. Arciniegas

Engineering the optical emission and robustness of metal-halide layered perovskites through ligand accommodation
Adv. Mater. (2021), 2008004

Contents

1 Introduction

Theoretical condensed matter research is plagued by a fundamental issue of complexity. The sheer amount of degrees of freedom in a material of any technologically relevant scale is overwhelming (e.g. $\sim 10^{23}$ electrons per cm^3), and make it impossible to describe the quantum mechanical wavefunction exactly. The way to make progress with this undertaking has always been to try and isolate the parts of the system that play the biggest role in the effects under investigation while neglecting those that only contribute to the complexity of the problem.

As is well-known, every quantum mechanical system is governed fundamentally by its Hamiltonian. One could be so bold as to claim that if all eigenvalues and eigenstates of the Hamiltonian describing any system were found, the field of condensed matter would be completed. This is, of course, impossible for reasons stated previously.

In order to work towards this ultimate goal, the full Hamiltonian can be decomposed into its constituent parts and the interactions between them. If the latter are negligible, the subsystems can be fully decoupled and solved separately. In doing so, the notion of a hierarchy of energy scales can be introduced, allowing one's efforts to be focused on the subsystems that are most involved with the physics at the energy scales, or, through $|\psi(t)\rangle = e^{-i\frac{\mathcal{H}t}{\hbar}} |\psi(0)\rangle$, timescales of interest.

To make these considerations more concrete in the context of this Thesis, two examples can be considered. First, the charge and magnetic sectors of the Hamiltonian are often widely separated in many materials. The former, exemplified by the electronic structure of crystals, usually involves energy scales on the order of eV, whereas the latter tends to lead to contributions of a few meV. One of the interactions that couples the two is the relativistic spin-orbit interaction, which can often be ignored completely in the description of charge carriers in materials due to their low velocities.

Second is the interaction between electrons and the ions of the crystal, whose displacements are described by phonons. While the potential that is associated with the ions is of great influence on the behavior of the electrons, their dynamics are so much

slower that the electronic degrees of freedom can be assumed to be at the instantaneous ground state w.r.t. their centers. To put it differently: the mass of the ions is so high and the elastic potential that governs their movement so small, that they appear as a constant background potential for the nimble electrons. This is, of course, the core idea behind the well-known Born-Oppenheimer approximation [1]. Likewise, the influence of the electrons on the ions appears as a smeared out average, which leads to so-called mean-field approximations. In most cases, these considerations allow for a separated description of both systems. However, there are exceptions when these approximations fail spectacularly with the prime example being superconductivity, where the coupling between electrons and phonons is not only non-negligible, it downright forms the linchpin for the exotic physics that is observed in these materials.

This brings us to the subject matter of this Thesis, in which the focus will lie on similar effects that depend crucially on these often negligible interactions between two relatively well-understood subsystems. The three main interactions we investigate are: relativistic spin-orbit coupling (SOC), coupling the charge and spin sectors of the Hamiltonian; Heisenberg magnetic exchange striction, which couples spins to atomic displacements (phonons); and electrostriction, the interaction between ferroelectric polarization and strain. We will use a variety of analytical and numerical tools and techniques to unravel how these effects manifest themselves in real materials, often motivated by experimental observations.

Aside from the fundamental interest, technological development has always been a strong driving force in condensed matter research. Here too does the focus on interactions between subsystems offer promising prospects, since it allows, in principle, for an influence over one subsystem by applying a perturbation to the other. More efficient or granular manipulation of magnetic order via spin currents, or even electric fields, is one example of the many benefits that can be enabled by strongly interacting orders. Breakthroughs in the understanding of condensed matter have historically led to leaps in technology, e.g. the dramatic increase in density and efficiency of hard disks after the discovery of the giant magnetoresistance effect. However, it is often not trivial to find materials where such cross-order interactions are large enough to be effectively exploited for technological applications. It is, therefore, crucial to gain an intimate insight into the governing physics of these interactions to eventually engineer materials and devices to maximally utilize them. In this Thesis, we aim to accomplish just that by investigating a selection of real materials where the previously mentioned interactions lead to large, or unexpected, effects.

As mentioned before, spin-orbit coupling is a relativistic interaction that can often be ignored in the study of the electronic structure in crystals. In materials with heavier constituent ions, it often becomes a requirement to treat this effect perturbatively, or even on an equal footing with the other contributions to the Hamiltonian. If, moreover, the inversion symmetry is broken, this can lead to spin-polarized Bloch functions as the eigenstates of the electrons in the crystal, and a linear k-dependent spin-splitting can develop in the band structure away from time-reversal symmetric points in the Brillouin Zone (BZ). This spin-splitting is usually attributed to the Rashba-Bychkov effect, which is a purely relativistic effect that can be derived through a $\boldsymbol{k}\cdot\boldsymbol{p}$ expansion of

the effective electronic Dirac equation[1]. However, as will be demonstrated in Chapter 2, another effect must lie at the origin in order to fully explain all the properties associated with the observed spin-splitting. We will show there that the effect is rather caused by a combination of the atomic spin-orbit coupling and the electrostatic interaction of the electron's orbital angular momentum with the ferroelectric polarization. From a technological standpoint, this large polarization-dependent spin-splitting can be used to generate spin-polarized currents, where the carriers' spin orientation can be reversed by a sufficiently large external electric field that reverses the ferroelectric polarization. This could be exploited, for example, in a device first dreamt up by Datta and Das [2], a spin-based field-effect transistor.

Chapter 3 continues with a study of $GdMn_2O_5$, a hallmark multiferroic material, where an inversion symmetry breaking magnetic configuration leads to a nonzero ferroelectric polarization through the Heisenberg exchange striction and geometric frustration. Since the magnetic and ferroelectric orders originate from the same underlying mechanism, they are coupled rather strongly in this multiferroic. We will describe a very peculiar dependence of the magnetoelectric switching on the angle between the applied magnetic field and the crystalline a axis, which leads to three distinct switching regimes for the ferroelectric polarization. One of these is particularly interesting since it demonstrates a never before observed four state double hysteresis loop. Moreover, we show that the novel four state loop is topologically different from, and protected by, the two "neighboring" switching regimes that appear when the field is applied at lower or higher angles. $GdMn_2O_5$ is, therefore, another prime example where one coupled order can be influenced through the manipulation of the other. As will be shown, the behavior can be described by a relatively simple semi-classical spin model, with the four-state regime appearing for a surprisingly broad range of model parameters. Furthermore, we demonstrate that, in the four-state switching regime, half the spins perform a full 360° rotation as a result of two up–and–down sweeps of the external magnetic field. This is a microscopic analog of the "crankshaft" in a car, converting the linear up–and–down motion of the magnetic field (the "piston") into a unidirectional motion of the spins (the "driveshaft"). We will show that it is the evolution of the energy landscape that lies at the heart of this behavior is very similar to the one of a Thouless charge pump, more specifically to the one demonstrated in cold atom systems [3]. The wealth of effects that emerge because of the combination of relatively well-understood model ingredients is a clear demonstration of an often reoccurring theme in condensed matter: more is different.

In Chapter 4 the focus will be shifted towards the aspect of dynamical control with increased granularity as a result of the indirect perturbation of coupled orders. We use the control over a lattice vibration through the excitation of a coupled spin-density wave (SDW) in a thin film of elemental chromium as a case study. In this material, a nesting of the Fermi surface results in the stabilization of the SDW, which in turn will optimize bond lengths between antiferromagnetically coupled ions to maximize the gained magnetic exchange energy. In essence, this leads to a shortening of bonds between ions with large spins, and a lengthening of those between small spins near the

[1] Integrating out positrons by performing the Fouldy-Wouthuysen transformation

nodes of the SDW, causing a periodic lattice displacement (PLD) that can be probed using X-ray diffraction spectroscopy. By using optical pulses that excite the electronic subsystem forming SDW, we show that the resulting decrease in its magnitude causes an oscillation of the phonon associated with the coupled PLD. The electronic subsystem then subsequently cools back down, partly restoring the SDW, while the phonon oscillation persists due to its slow dynamics and low damping. Even in the case of a single pulse does such an indirect excitation lead to an increased oscillation amplitude of the PLD phonon compared with the one achieved through the more usual displacive mechanism. More interestingly, we show that by applying a carefully designed sequence of pulses, an indirect, but incredibly granular, control can be achieved over the amplitude of the PLD phonon mode. We also show that using multiple pulses empowers much greater phonon excitation amplitudes than can be achieved with a single pulse. The very fast (essentially instantaneous) dynamics of the SDW and relatively strong coupling to the phonon mode with much slower dynamics, lies at the core of this behavior. While the technological relevance of this process is not immediately obvious, it does highlight the capabilities that the coupling between two orders with different dynamics can offer in terms of control, to the point where a pulse train can be designed using our model, such that the PLD oscillation follows a given envelope signal almost perfectly.

We conclude this Thesis in Chapter 5 by a systematic study of the implications on the mechanical properties of 180° ferroelectric domain walls in $BaTiO_3$, due to the interaction between strain and polarization. Surprisingly, these walls appear mechanically softer to an applied tip, even though they are not ferroelastic and thus do not separate domains with different strain textures. Indeed, in ferroelastic domain walls one domain would be favored over the other by the force applied through the tip, meaning that when the tip is applied to the wall, it would excite a soft sliding domain wall mode. This mode is not present in either of the ferroelastic domains and thus the ferroelastic domain wall would appear softer. In our case, however, we uncover that a similar spirited but fundamentally different mechanism lies at the heart of the mechanical softness in these purely ferroelectric 180° domain walls. Even though they are not ferroelastic, we find that a relatively long-ranged strain texture still appears around them, which interacts mechanically with the applied tip. This in turn leads to bending or sliding of the domain wall towards the tip, leading to a large deformation and thus an apparent softening.

Since certain ferroelectric domain walls are conductive, this could open the door to the efficient manipulation of conducting channels through the application of strain, which could be used in electronic devices. Moreover, heat transport is mediated largely by phonons, whose behavior is intimately linked with the stiffness of the material. This means that the softer domain walls lead to lower phonon speeds and effects such as diffraction and even total internal reflection may occur, which in turn would lead to "phonon waveguides".

2

Spin-momentum locking in ferroelectrics with strong spin-orbit coupling

2.1 Introduction

The research field of spintronics aims to understand the behavior of spins inside materials and translate this understanding into the ability to actively control these degrees of freedom for possible technological applications [4]. Many devices have been theorized, for example, spin-field-effect transistor (FET)[2], and storage devices which utilize spin-current and associated spin-transfer torque to efficiently manipulate magnetic domains [5], both in ferromagnets [6], and antiferromagnets [7–9]. Despite fundamental interest and potential for applications, the actual realization of spin-FET devices has remained rather elusive. One of the main culprits for this limited success is that the envisioned devices require very granular, ideally electric, control of the spin of the current carriers.

This is not straightforward, since the only direct coupling between the spins and the electric field is through relativistic effects. When an electron moves through an electric field, an associated magnetic field is perceived in the electron's co-moving frame. This magnetic field can be written as:

$$\boldsymbol{B} = -\frac{\boldsymbol{v} \times \boldsymbol{E}}{c^2}, \tag{2.1}$$

where $\boldsymbol{v}$ denotes the velocity of the electron, $\boldsymbol{E}$ the electric field, and c the speed of light. The spin of the electron, $\boldsymbol{\sigma}$, will interact with this magnetic field through the Zeeman energy $H_Z = -\frac{g_s \mu_B}{\hbar}\boldsymbol{\sigma}$, where $g_s \approx 2$, and μ_B is the Bohr magneton. This will cause it to precess around $\boldsymbol{B}$ created by the applied $\boldsymbol{E}$, and eventually align with it. However, in nearly all real materials, the speed $\boldsymbol{v}$ of the current carriers is so low, and the applied electric fields so small, that the c^2 in the denominator completely overpowers the numerator, ultimately leading to a tiny effect.

There exists one class of materials for which the carrier speeds can be relatively high: the topological insulators [10–15]. In these materials, a peculiar band structure effect leads to Dirac cones and Dirac points. They get their name from the necessity of using the Dirac equation to accurately describe the relativistic behavior of electrons (and holes) at these points. It turns out that due to the band structure peculiarities, electrons (and holes) appear to have zero effective mass leading to a large Fermi velocity, on the order of $10^6\,\mathrm{m/s^2}$ in the case of graphene [11]. However, even then does the influence on the carriers' spins by external electric fields remains extremely limited. Indeed, for a field strength of 1 V/nm, the size of the magnetic field $\boldsymbol{B}$ that results from Eq. (2.1) is only on the order of $10^{-2}\,\mathrm{T}$, leading to a Zeeman energy of the spins of only $10^{-3}\,\mathrm{meV}$. This is all to say that such direct electric control of the spins through Eq. (2.1) is quite infeasible.

Leveraging the properties of particular materials, on the other hand, does allow for the sought after electric control, albeit indirectly. One group of such materials are the ferroelectric semiconductors with large atomic SOC [16–19], which is essentially identical to the previously discussed effect, with the "atomic" denotation refers to the manifestation of this effect as a result of the potential (and electric fields) around the atomic cores. These potentials are much greater than those that can be achieved with external fields, and the electrons, moreover, have a large momentum close to the ionic cores. Consequently, the SOC in atoms can lead to significant contributions and is one of the main drivers of the effect discussed in this Chapter. How exactly will be the topic of the theory Section 2.2.

Because of the ferroelectricity due to inversion symmetry breaking, an internal electric field is generated through the dipoles that are associated with the polarization. Combined with the high atomic SOC, a sizable linear energy splitting between spin-polarized states can appear in these materials [17], contrary to the tiny effect described above. This $\boldsymbol{k}$-dependent splitting manifests itself in the band structure as conical intersections surrounding time-reversal (T) invariant points of the BZ (see Fig. 2.1). These points are special in the sense that the Kramers degeneracy [20] is enforced through the translational symmetry of the lattice, rather than by the usual inversion symmetry. If we take a spin-up Bloch state at such a T-invariant point and apply the time-reversal operator ($\boldsymbol{k} \to -\boldsymbol{k}$, $\boldsymbol{\sigma} \to -\boldsymbol{\sigma}$), it is brought to a point on the opposite side of the BZ, and can be translated back to the starting point through a reciprocal lattice translation ($-\boldsymbol{k} + \boldsymbol{G} = \boldsymbol{k}$). This translation does not change the spin, however, and the resulting spin-down state thus has to have the same energy as the original up spin state, since the system obeys both T symmetry and translational symmetry. So, even though the broken inversion symmetry destroys the Kramers degeneracy at general k points, which is what allows for the spin splitting in the first place, it is still present at these T-invariant points, ultimately resulting in the intersecting cones depicted in Fig. 2.1. Due to the definite spin polarization of the non-degenerate bands, current carriers [1] traveling through the material will tend to align their spins to this spin polarization. Since the sign of the inversion symmetry breaking field creating the spin splitting is a result of the orientation of the ferroelectric polarization, it can be

[1] holes in the case of Fig. 2.1

reversed through the application of a sufficiently strong external electric field, which allows for the electrical manipulation of the carriers' spins.

The spin-polarized states have been observed both experimentally [18, 21, 22], and in *ab-initio* density functional theory (DFT) simulations [16, 17, 19]. It is, however, often not well understood what the underlying microscopic mechanisms are that lead to the observed large splitting.

We will investigate the microscopics underlying multiple contributions to the $\boldsymbol{k}$ dependent spin splitting, and comment on their respective magnitudes and symmetry requirements. These energy terms have the form:

$$H_R(\boldsymbol{k}) = \alpha_R \hat{\boldsymbol{n}} \cdot (\boldsymbol{k} \times \boldsymbol{\sigma}), \tag{2.2}$$

where α_R is a prefactor denoting the strength, and $\hat{\boldsymbol{n}}$ denotes a unit vector along the inversion symmetry breaking field. Some of these underlying effects are well-known, while others are more obscure. We will find that the more obscure ones actually dominate in most cases and that the largest contributions stem from a combination of electrostatic and relativistic effects.

As a hallmark example of ferroelectrics that demonstrate a large spin splitting, we focus in the numerical portion of this Chapter on simulations performed for GeTe. Its dispersion is exactly the one we used to demonstrate the conical shape of the band structure, displayed Fig. 2.1(a). To investigate how the microscopic effects, identified in the theory Section 2.2, manifest themselves in GeTe, we use DFT followed by a Wannierization in Sec. 2.5 to gain access to the local, real space, properties of the Bloch functions .

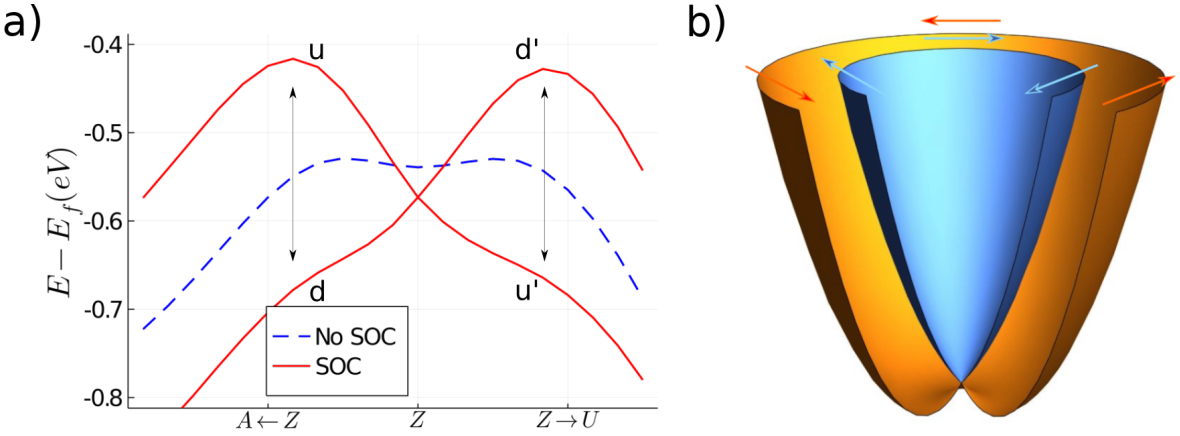

Figure 2.1: **Large Rashba splitting** a) The band dispersion of the first valence band in GeTe around the Z point of the Brillouin zone (see Fig. 2.6 for details). The blue and red graphs show the NSOC and SOC band structure, respectively. The $u - d$ and $u' - d'$ labels designate the up and down spin-polarized bands, where the prime signifies that the orientation of the spin-up–down axis depends on $\boldsymbol{k}$. b) Generic example of intersecting conical energy surfaces due to the linear spin splitting. The spin texture is indicated by the arrows. This chiral spin texture is what leads to the changing orientation of the up-down spin axis.

We finish with a conclusion that summarizes the observations and where we make

the claim that the linear spin splitting often attributed to the relativistic Rashba effect is almost exclusively a result of the other effects we shall uncover.

2.2 Theory

In this Section we handle the theoretical underpinning of the observed large spin splitting, building up the arguments in favor of the orbital angular momentum (OAM) as the enabler of the main underlying mechanism. We start with an overview of the original derivation that leads to the purely relativistic Rashba effect in order to argue why it might not be able to explain the observed spin-splitting behavior. We then continue with a close study on the proposed alternative OAM based mechanism, and investigate the two main contributions: one that arises through electrostatics, and another that is the result of atomic SOC. We will see that these latter two mechanisms manage to explain the characteristics of the large linear spin-dependent dispersion of the Bloch functions around the T-invariant k points of the BZ. During the discussion, we will utilize a 2D tight-binding Model as a concrete example.

2.2.1 Rashba-Bychkov effect

Before turning to the less well-known effects, we summarize the main points of the original Rashba-Bychkov effect, first derived in their seminal 1959 paper [23]. It is a purely relativistic effect that can be derived starting from a second-order expansion of the Dirac equation in small parameter $1/c$:

$$\hat{H}(\boldsymbol{r})\,|\psi\rangle = \left[\frac{\hat{\boldsymbol{p}}^2}{2m} - eV(\boldsymbol{r}) - \frac{e\hbar}{4m^2c^2}(\hat{\boldsymbol{\sigma}}\cdot[\boldsymbol{\nabla}V(\boldsymbol{r})\times\hat{\boldsymbol{p}}]) + \frac{\hat{\boldsymbol{p}}^2}{8m^2c^2}V(\boldsymbol{r}) - \frac{\hat{\boldsymbol{p}}^4}{8m^3c^2}\right]|\psi\rangle = E\,|\psi\rangle \tag{2.3}$$

where $|\psi\rangle$ is a two component spinor, $V(\boldsymbol{r})$ denotes the electric potential, $\hat{\boldsymbol{\sigma}}$ a vector of Pauli matrices $(\hat{\sigma}_x, \hat{\sigma}_y, \hat{\sigma}_z)$, and m and e the electron mass and charge, respectively. $\boldsymbol{\nabla} = (\frac{\partial}{\partial x}, \frac{\partial}{\partial y}, \frac{\partial}{\partial z})$ denotes spatial derivatives, and $\hat{\boldsymbol{p}} = -i\hbar\hat{\boldsymbol{\nabla}}$ the canonical momentum. The first two terms in Eq. (2.3) are the non-relativistic part of the Hamiltonian, the third one represents the SOC, the fourth is known as the Darwin effect and the fifth is the relativistic correction to the effective electron mass. As is common in the literature, we introduce the SOC constant $\lambda = \frac{e\hbar}{4m^2c^2}$. The potential $V(\boldsymbol{r})$ is periodic in a crystal, leading to eigenstates given by the Bloch wavefunctions $\left|\psi_n^{\boldsymbol{k}}(\boldsymbol{r})\right\rangle = e^{i\boldsymbol{k}\cdot\boldsymbol{r}}\left|u_n^{\boldsymbol{k}}(\boldsymbol{r})\right\rangle$, where $\left|u_n^{\boldsymbol{k}}(\boldsymbol{r})\right\rangle$ denotes the cell-periodic part, $e^{i\boldsymbol{k}\cdot\boldsymbol{r}}$ the envelope function, and n the band index. In the following we drop $\boldsymbol{r}$ in the wavefunctions, and inner products correspond to an integration over all space:

$$\left\langle \phi_n^{\boldsymbol{k}}|\psi_m^{\boldsymbol{k}'}\right\rangle = \int d\boldsymbol{r}\, e^{-i(\boldsymbol{k}-\boldsymbol{k}')\cdot\boldsymbol{r}} u_n^{\boldsymbol{k}}(\boldsymbol{r})^* u_m^{\boldsymbol{k}'}(\boldsymbol{r}). \tag{2.4}$$

To obtain the eigenvalue equation for $\left|u_n^{\boldsymbol{k}}\right\rangle$, we insert $\left|\psi_n^{\boldsymbol{k}}\right\rangle$ in Eq. (2.3), carry out the differentiation

$$\hat{\boldsymbol{p}}\, e^{i\boldsymbol{k}\cdot\boldsymbol{r}}\left|u_n^{\boldsymbol{k}}\right\rangle = -i\hbar\hat{\boldsymbol{\nabla}} e^{i\boldsymbol{k}\cdot\boldsymbol{r}}\left|u_n^{\boldsymbol{k}}\right\rangle = e^{i\boldsymbol{k}\cdot\boldsymbol{r}}(\hat{\boldsymbol{p}} + \hbar\boldsymbol{k})\left|u_n^{\boldsymbol{k}}\right\rangle, \tag{2.5}$$

and similarly substitute $\hat{\boldsymbol{p}}^2 \to (\hat{\boldsymbol{p}}+\hbar\boldsymbol{k})^2$. This leads to the following equations for $\left|u_n^{\boldsymbol{k}}\right\rangle$:

$$E_n \left|u_n^{\boldsymbol{k}}\right\rangle = \left[\hat{V}_0^{\boldsymbol{k}}(\boldsymbol{r}) + \hat{V}_1^{\boldsymbol{k}}(\boldsymbol{r}) + \hat{V}_2^{\boldsymbol{k}}(\boldsymbol{r}) + \hat{V}_3(\boldsymbol{r})\right] \left|u_n^{\boldsymbol{k}}\right\rangle \tag{2.6}$$

$$\hat{V}_0^{\boldsymbol{k}}(\boldsymbol{r}) = \frac{\hat{\boldsymbol{p}}^2}{2m} - eV(\boldsymbol{r}) + \frac{\hbar^2 k^2}{2m} \tag{2.7}$$

$$\hat{V}_1^{\boldsymbol{k}}(\boldsymbol{r}) = \hbar\frac{\boldsymbol{k}\cdot\hat{\boldsymbol{p}}}{m} \tag{2.8}$$

$$\hat{V}_2^{\boldsymbol{k}}(\boldsymbol{r}) = -\lambda\hat{\boldsymbol{\sigma}}\cdot[\boldsymbol{\nabla}V(\boldsymbol{r})\times\boldsymbol{k}] \tag{2.9}$$

$$\hat{V}_3(\boldsymbol{r}) = -\lambda\hat{\boldsymbol{\sigma}}\cdot[\boldsymbol{\nabla}V(\boldsymbol{r})\times\hat{\boldsymbol{p}}]\,. \tag{2.10}$$

We neglected the last two terms of Eq. (2.3) since they are usually small for valence electrons and do not contribute to the linear k-dependent energy of the Rashba form in Eq. (2.2).

Before turning to a $\boldsymbol{k}\cdot\hat{\boldsymbol{p}}$ expansion of the above equations, we take a moment to discuss heuristically how $\hat{V}_2^{\boldsymbol{k}}$ and $\hat{V}_3$ act on the Bloch functions, more specifically, which contribution to the local electric field $\boldsymbol{\nabla}V$ is important. Both terms originated from the application of Eq. (2.5) to the third term on the right-hand side of Eq. (2.3). We study the case of a 2D square lattice, for a Bloch function with $\boldsymbol{k} = (k_x, 0)$, and with the polarization oriented along the y-direction. A pictorial representation of this situation is shown in Fig. 2.2, where we separated the electric field into two contributions:

$$\boldsymbol{\nabla}V(\boldsymbol{r}) = -\boldsymbol{E}(\boldsymbol{r}) = -(\boldsymbol{E}_{\mathrm{a}}(\boldsymbol{r}) + \boldsymbol{E}_{\mathrm{P}}(\boldsymbol{r})), \tag{2.11}$$

with $\boldsymbol{E}_{\mathrm{a}}$ resulting from the atomic potentials and $\boldsymbol{E}_{\mathrm{P}}$ the electric field that groups the contributions that originate from the inversion symmetry breaking. One such contribution originates from the charge imbalance that results from the inversion symmetry breaking, while another could be an externally applied field. While the exact real-space distribution of $\boldsymbol{E}_{\mathrm{P}}$ depends on microscopic details, the important point for our heuristic discussion is that it is approximately constant in the region of space where the Bloch function peaks, i.e. close to the ionic cores. The purple plane in Fig. 2.2 pictorially shows the potential V_{P} associated with this field.

Focusing first on $\hat{V}_2^{\boldsymbol{k}}$:

$$\hat{V}_2^{\boldsymbol{k}}(\boldsymbol{r}) = \lambda\hat{\boldsymbol{\sigma}}\cdot[(\boldsymbol{E}_{\mathrm{a}}(\boldsymbol{r}) + \boldsymbol{E}_{\mathrm{P}}(\boldsymbol{r}))\times\boldsymbol{k}]\,, \tag{2.12}$$

we can observe in the figure that the atomic contribution with $\boldsymbol{E}_{\mathrm{a}}$ is zero since $\boldsymbol{E}_{\mathrm{a}}$ is odd throughout the unit cell, whereas $\boldsymbol{k}$ is a constant. On the contrary, $\boldsymbol{E}_{\mathrm{P}}$ is even throughout the unit cell, leading to a nonzero contribution. However, both $\boldsymbol{E}_{\mathrm{P}}$ and $\boldsymbol{k}$ are generally small, meaning that the energy contribution of $V_2^{\boldsymbol{k}}$ is also exceedingly small due to the tiny SOC constant λ, leading usually to an order of magnitude for $E_2^{\boldsymbol{k}} = \left\langle u_n^{\boldsymbol{k}}\right| \hat{V}_2^{\boldsymbol{k}}(\boldsymbol{r}) \left|u_n^{\boldsymbol{k}}\right\rangle$ of $10^{-6}\,\mathrm{eV}$.

Following a similar train of thought for $\hat{V}_3^{\boldsymbol{k}}$:

$$\hat{V}_3^{\boldsymbol{k}}(\boldsymbol{r}) = \lambda\hat{\boldsymbol{\sigma}}\cdot[(\boldsymbol{E}_{\mathrm{a}}(\boldsymbol{r}) + \boldsymbol{E}_{\mathrm{P}}(\boldsymbol{r}))\times\hat{\boldsymbol{p}}]\,, \tag{2.13}$$

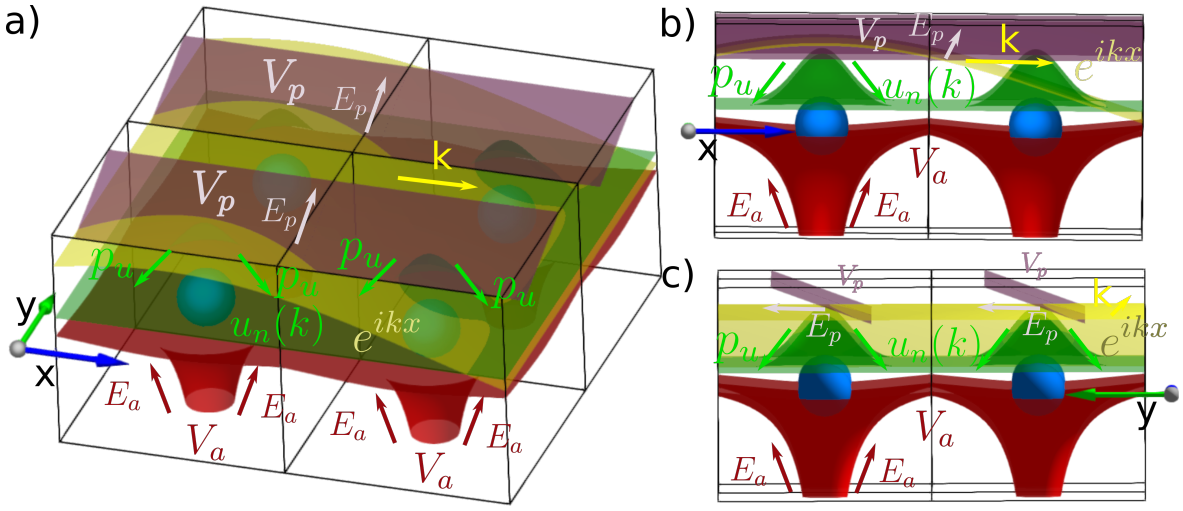

Figure 2.2: **Potentials and wavefunctions inside the unit cell.** Pictorial representation of the different electric potentials (V, surfaces) and fields ($E = \boldsymbol{\nabla} V$, arrows) in a 2D square lattice. The blue spheres represent the atoms, which produce the spherically symmetric red potential V_a and field $\boldsymbol{E}_a$. The purple plane denotes the potential V_p associated with the polarization, and the resulting field $\boldsymbol{E}_p$. The green and yellow surfaces depict the cell periodic and envelope part of the Bloch function: $\left|u_n^{\boldsymbol{k}}\right\rangle$ and $e^{ik_x r_x}$, respectively. The vectors $\boldsymbol{k}$ and $\boldsymbol{p}_u$ denote the crystalline and canonical momentum of the Bloch function, respectively. The former results from the envelope function, and the latter from the periodic part, see Eq. (2.5).

we find that $\hat{\boldsymbol{p}}$ applied to the periodic $\left|u_n^{\boldsymbol{k}}\right\rangle$ part of the Bloch function is odd throughout the unit cell (see the green arrows in Fig. 2.2), and the contribution from the even $\boldsymbol{E}_\mathrm{P}$ is zero. The shape of the atomic potential is such that $\boldsymbol{E}_\mathrm{a}$ is also odd throughout the unit cell so that its contribution to $\hat{V}_3^{\boldsymbol{k}}$ does not vanish. Moreover, because of the size and shape of the atomic potential, $\boldsymbol{E}_\mathrm{a} \gg \boldsymbol{E}_\mathrm{P}$, and similarly $\hat{\boldsymbol{p}}\left|u_n^{\boldsymbol{k}}\right\rangle \gg \boldsymbol{k}$, meaning that $\hat{V}_3^{\boldsymbol{k}}$ tends to contribute much more to the total energy than $\hat{V}_2^{\boldsymbol{k}}$.

As it turns out, $\hat{V}_3^{\boldsymbol{k}}$ is exactly the energy term that describes the atomic SOC, which is known to not be negligible for heavier ions. This term by itself does not lead to any linear k-dependent spin splitting, however. Conversely, $\hat{V}_2^{\boldsymbol{k}}$ does have the correct form of Eq. (2.2), and we thus identify it as the first contribution to the purely relativistic Rashba spin splitting.

In order to obtain the second contribution, we perform a $\boldsymbol{k}\cdot\hat{\boldsymbol{p}}$ expansion of Eq. (2.6) around a T-invariant point of the BZ, $\boldsymbol{k}_0$ [23–25]. We denote the *relative* vector between the T-invariant point $\boldsymbol{k}_0$ and $\boldsymbol{k}$ as $\boldsymbol{K}$, i.e. $\boldsymbol{K} = \boldsymbol{k} - \boldsymbol{k}_0$. The basis states are chosen to be eigenstates of $\hat{V}_0^{\boldsymbol{k}_0}$, with the perturbation resulting from $\hat{V}_1^{\boldsymbol{K}} + \hat{V}_2^{\boldsymbol{K}} + \hat{V}_3$. We will derive the energy dispersion for the nth band, with the spin-up and spin-down states of this band necessarily degenerate at the T-invariant point. Furthermore, we assume that this is the only degeneracy of this band, and we choose the spin-up and spin-down basis states at $\boldsymbol{k}_0$ so that no off-diagonal elements of $\hat{V}_1^{\boldsymbol{k}_0} + \hat{V}_2^{\boldsymbol{k}_0} + \hat{V}_3$ exist between them.

Expanding then Eq. (2.6) in small $\boldsymbol{K}$, keeping terms linear in $\boldsymbol{K}$ and up to second

order in $1/c$ (or equivalently, up to λ^2), we find:

$$\tilde{E}^{\boldsymbol{k}}_{n,\sigma} - E^{\boldsymbol{k}_0}_{n,\boldsymbol{\sigma}} = \left\langle u^{\boldsymbol{k}_0}_{n,\boldsymbol{\sigma}} \right| \hat{V}^{\boldsymbol{K}}_1 + \hat{V}^{\boldsymbol{K}}_2 + \hat{V}_3 \left| u^{\boldsymbol{k}_0}_{n,\boldsymbol{\sigma}} \right\rangle + \tag{2.14}$$

$$\sum_{m,\boldsymbol{\sigma}' \neq n,\boldsymbol{\sigma}} \frac{\left\langle u^{\boldsymbol{k}_0}_{m,\boldsymbol{\sigma}'} \right| \hat{V}^{\boldsymbol{K}}_1 + \hat{V}^{\boldsymbol{K}}_2 + \hat{V}_3 \left| u^{\boldsymbol{k}_0}_{n,\boldsymbol{\sigma}} \right\rangle \left\langle u^{\boldsymbol{k}_0}_{n,\boldsymbol{\sigma}} \right| \hat{V}^{\boldsymbol{K}}_1 + \hat{V}^{\boldsymbol{K}}_2 + \hat{V}_3 \left| u^{\boldsymbol{k}_0}_{m,\boldsymbol{\sigma}'} \right\rangle + \text{H.c.}}{E^{\boldsymbol{k}_0}_{n,\boldsymbol{\sigma}} - E^{\boldsymbol{k}_0}_{m,\boldsymbol{\sigma}'}}, \tag{2.15}$$

where the sum is performed over all states that are not identical to $\left| u^{\boldsymbol{k}_0}_{n,\boldsymbol{\sigma}} \right\rangle$, and the singularity that would result from the spin up-down degeneracy is avoided by the definition of the basis that is used. The tilde indicates that the energy dispersion is approximate. Grouping then the terms that lead to linear-in-$\boldsymbol{K}$ spin splittings, we arrive at:

$$\tilde{E}^{\boldsymbol{k}}_{n,\sigma} - E^{\boldsymbol{k}_0}_{n,\boldsymbol{\sigma}} = -\lambda \left\langle u^{\boldsymbol{k}_0}_{n,\boldsymbol{\sigma}} \right| \hat{\boldsymbol{\sigma}} \cdot (\boldsymbol{\nabla} V(\boldsymbol{r}) \times \boldsymbol{K}) \left| u^{\boldsymbol{k}_0}_{n,\boldsymbol{\sigma}} \right\rangle + \tag{2.16}$$

$$\sum_{m,\boldsymbol{\sigma} \neq n,\boldsymbol{\sigma}} \frac{\hbar}{m} \frac{\left\langle u^{\boldsymbol{k}_0}_{m,\boldsymbol{\sigma}} \right| \boldsymbol{K} \cdot \hat{\boldsymbol{p}} \left| u^{\boldsymbol{k}_0}_{n,\boldsymbol{\sigma}} \right\rangle \left\langle u^{\boldsymbol{k}_0}_{n,\boldsymbol{\sigma}} \right| - \lambda \hat{\boldsymbol{\sigma}} \cdot (\boldsymbol{\nabla} V(\boldsymbol{r}) \times \hat{\boldsymbol{p}}) \left| u^{\boldsymbol{k}_0}_{m,\boldsymbol{\sigma}} \right\rangle + \text{H.c.}}{E^{\boldsymbol{k}_0}_{n,\boldsymbol{\sigma}} - E^{\boldsymbol{k}_0}_{m,\boldsymbol{\sigma}}}.$$

The first term at the right-hand side was discussed previously in Eq. (2.12). The second term has the atomic SOC ($\hat{V}^{\boldsymbol{k}}_3$, discussed in Eq. (2.13)) which is much larger than $\hat{V}^{\boldsymbol{k}}_2$, leading usually to the same order of magnitude for both terms on the right-hand side of Eq. (2.16), even though the second is of a higher order in the perturbation theory. Notice how no spin off-diagonal terms appear in the second term due to the spin-diagonal form of $\boldsymbol{K} \cdot \hat{\boldsymbol{p}}$.

A requirement for the second term to be nonzero is that u_n and u_m have different parity along the spatial direction defined by $\boldsymbol{k}$, since otherwise $\langle u_n | \, k_x \partial_x + k_y \partial_y + k_z \partial_z \, | u_m \rangle = 0$. One example could be a p_y orbital and a s-p_z hybridized one, which would be created by a ferroelectric polarization along the z-axis. How exactly this hybridization arises will be discussed in further detail below in Section 2.2.2, in the context of a tight-binding model. The combination of the two linear-in-$\boldsymbol{k}$ terms in Eq. (2.16) can be regarded as the purely relativistic Rashba effect [25].

In summary, we have given the derivation of the relativistic Rashba effect starting from the Dirac equation applied to the Bloch functions, followed by a $\boldsymbol{k} \cdot \hat{\boldsymbol{p}}$ expansion. By carefully considering the microscopics we have found that both contributions have a similar order of magnitude of typically 10^{-6} eV. This leads us to the conclusion that the purely relativistic effect can not explain the observed spin splitting which is around 0.3 eV in GeTe, especially since this splitting appears in the bulk band structure where no large interface contributions to the electric field play a role.

In the remainder of this Chapter, we will thus focus on a different origin to the effect, one that lies in the combination of electrostatic effects with the strong atomic SOC. These electrostatics are a result of the creation of dipoles by Bloch functions with nonzero OAM, which we describe in the following Section.

2.2.2 Orbital Rashba effect

Until relatively recently, the exact role that the OAM plays in the Rashba-like linear spin splitting was not well understood. Even now, there seems to be some confusion on how the many different mechanisms arise and compare with one another. In an attempt to alleviate this confusion we will try to disentangle them and give a pedagogical description, taking inspiration from the works in Refs. [19, 26–30].

One of the reasons why OAM is often overlooked in crystals is that ignoring atomic SOC, it is usually completely quenched. This is because OAM is associated with a particular charge distribution which interacts with the charge of the surrounding ions, the so-called *crystal field*. In most cases the most favorable charge distribution in this regard leads to orbitals with zero OAM, like the p_x, p_y and p_z orbitals in the case of $L = 1$, where $\hat{L} = \hat{\boldsymbol{r}} \times \hat{\boldsymbol{p}}$ denotes the OAM operator [31]. The reason why this process is referred to as the "quenching" of OAM, is that in isolated atoms, instead, the atomic SOC favors orbitals with maximum OAM to maximize the energy gain through $\hat{H}_{\mathrm{SOC}} = \lambda \hat{\boldsymbol{\sigma}} \cdot \hat{\boldsymbol{L}}$, which leads to one of the Hund's rules.

We will show that there are two mechanisms that lead to the unquenching of OAM in crystals: the previously mentioned atomic SOC, and the electrostatic interaction due to the associated dipoles. The former leads to a small OAM even at T-invariant points, while the latter results in a linearly varying chiral OAM as $\boldsymbol{k}$ is varied away from the T-invariant point. This chirality of the OAM texture turns out to be very similar to the chirality of the spin texture that results from the purely relativistic Rashba terms (see Fig. 2.1 and Eq. (2.16)). Both unquenching mechanisms ultimately result in a contribution to the linear part of the energy dispersion. Furthermore, the sign of the linear slope of the dispersion will be found to depend on the orientation of the electron's spin relative to its OAM[2], resulting finally in the observed spin splitting.

We now proceed with a pedagogical derivation of the electrostatic contribution, based on a tight-binding model [19, 26, 30, 32, 33]. This is an extension to our earlier work in Ref. [34].

OAM due to electric dipoles

We define the tight-binding model on a 2D square lattice with lattice parameter a, one atom per unit cell, and four orbitals centered on that atom. They resemble the angular character of an s orbital and the three p orbitals: $|s^{\boldsymbol{n}}\rangle$, $|x^{\boldsymbol{n}}\rangle$, $|y^{\boldsymbol{n}}\rangle$, $|z^{\boldsymbol{n}}\rangle$, where $\boldsymbol{n}$ denotes the unit cell indices (n_x,n_y) to which the orbital belongs to. To simplify notation, we omit $\boldsymbol{n} = (0,0)$ when writing the orbitals of the central unit cell. Furthermore, we assume that these orbitals have a Gaussian radial shape:

$$\langle \boldsymbol{r}|s_{\boldsymbol{n}}\rangle = \left(\frac{2}{\pi a_0^2}\right)^{3/4} e^{-\left(\frac{|\boldsymbol{r}-\boldsymbol{n}a|}{a_0}\right)^2}, \tag{2.17}$$

$$\langle \boldsymbol{r}|\alpha_{\boldsymbol{n}}\rangle = (\alpha - a\boldsymbol{n}) \left(\frac{2}{\pi a_0^2}\right)^{3/4} \left(\frac{8}{2a_0^2}\right) e^{-\left(\frac{|\boldsymbol{r}-\boldsymbol{n}a|}{a_0}\right)^2}, \tag{2.18}$$

[2]Positive for parallel orientation of the spin and OAM and negative for antiparallel orientation.

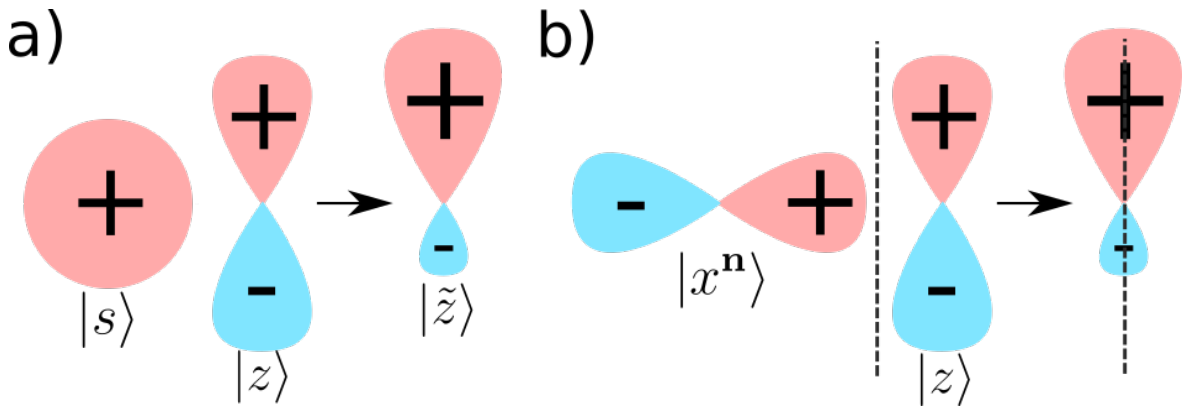

Figure 2.3: **Overlap dipoles.** a) Hybridization between $|s\rangle$ and $|z\rangle$ orbitals leading to the $|\tilde{z}\rangle$ orbital. b) Overlap between shifted $|x^{\boldsymbol{n}}\rangle$ orbital and central $|z\rangle$ orbital, the dashed line indicates a unit cell boundary. The charge imbalance in both panels reflects the nonzero dipole.

with $\alpha = x, y, z$. The reason for choosing Gaussians is to make solving the overlap integrals easier when we calculate the hopping parameters in this basis. Using any other radial shape does not lead to qualitative differences. The bare tight-binding Hamiltonian is denoted as $\hat{H}_0$ and includes the usual hopping parameters due to overlap $t_{\alpha\beta}^{\boldsymbol{n}_1\boldsymbol{n}_2} = \langle \alpha^{\boldsymbol{n}_1} | \frac{\hat{\boldsymbol{p}}^2}{2m} + \hat{V} | \beta^{\boldsymbol{n}_2} \rangle$. To mimic the inversion symmetry breaking in ferroelectric materials, i.e. with a polar space group, an electric field is applied perpendicular to the layer, the z-direction in this case. This allows for additional hopping terms, associated with $\hat{H}_{\text{isb}} = e(\hat{\boldsymbol{d}} \cdot \boldsymbol{E})$, where $\hat{\boldsymbol{d}}$ is the electric dipole moment:

$$\langle s | \hat{H}_{\text{isb}} | z \rangle = eE_z \frac{a_0}{2}, \tag{2.19}$$

$$\langle z | \hat{H}_{\text{isb}} | x^{\boldsymbol{n}} \rangle = eE_z \theta_z^n n_x, \tag{2.20}$$

$$\langle z | \hat{H}_{\text{isb}} | y^{\boldsymbol{n}} \rangle = eE_z \theta_z^n n_y, \tag{2.21}$$

with $\theta_z^n = -\frac{1}{2} a e^{-\frac{1}{2}\left(\frac{a|\boldsymbol{n}|}{a_0}\right)^2}$. The other terms of $\hat{H}_{\text{isb}}$ are zero. Fig. 2.3 shows pictorially how the electric dipoles appear as a result of the overlap between the orbitals.

The internal field E_z caused by the ferroelectric polarization is usually small, warranting a perturbative approach where $\hat{H}_{\text{isb}}$ is the perturbation on top of $\hat{H}_0$. This leads to the first type of hybridization, i.e. between the $|s\rangle$ and $|z\rangle$ orbitals in the central unit cell:

$$|\tilde{z}\rangle = |z\rangle + \frac{a_0}{2} \frac{eE_z}{\varepsilon_z - \varepsilon_s} |s\rangle , \tag{2.22}$$

$$|\tilde{s}\rangle = |s\rangle + \frac{a_0}{2} \frac{eE_z}{\varepsilon_s - \varepsilon_z} |z\rangle , \tag{2.23}$$

where $\varepsilon_s = \langle s | \hat{H}_0 | s \rangle$ and $\varepsilon_z = \langle z | \hat{H}_0 | z \rangle$. A pictorial representation of this hybridization is shown in Fig. 2.3(a).

Before continuing with a $\boldsymbol{k}\cdot\boldsymbol{p}$ expansion, we write the elements of $\hat{H}_0$ between the hybrid $|\tilde{z}\rangle$ orbital and the shifted $|x^{\boldsymbol{n}}\rangle$, $|y^{\boldsymbol{y}}\rangle$ orbitals:

$$\langle\tilde{z}|\,\hat{H}_0\,|x^{\boldsymbol{n}}\rangle = \frac{a_0}{2}\frac{eE_z}{\varepsilon_z-\varepsilon_s}\,\langle s|\,\frac{\hat{\boldsymbol{p}}^2}{2m}\,|x^{\boldsymbol{n}}\rangle \tag{2.24}$$

$$= \frac{\hbar^2}{ma_0^2}\frac{eE_z\theta_z^n}{(\varepsilon_z-\varepsilon_s)}\left[5-\left(\frac{a|\boldsymbol{n}|}{a_0}\right)^2\right]n_x, \tag{2.25}$$

$$\langle\tilde{z}|\,\hat{H}_0\,|y^{\boldsymbol{n}}\rangle = \frac{\hbar^2}{ma_0^2}\frac{eE_z\theta_z^n}{(\varepsilon_z-\varepsilon_s)}\left[5-\left(\frac{a|\boldsymbol{n}|}{a_0}\right)^2\right]n_y. \tag{2.26}$$

The contribution from the cell periodic $\hat{V}$ is zero.

In order to construct $\hat{H}_0^{\boldsymbol{k}}$ and $\hat{H}_{\text{isb}}^{\boldsymbol{k}}$, we perform a discrete Fourier transform of the orbitals similar to Eq. (B.15):

$$\left|w^{\boldsymbol{k}}\right\rangle = \frac{1}{\sqrt{N}}\sum_{\boldsymbol{n}} e^{i\boldsymbol{k}\cdot\boldsymbol{n}}\,|w^{\boldsymbol{n}}\rangle\,, \tag{2.27}$$

with $|w\rangle$ one of the four orbitals, $\boldsymbol{k}$ written in terms of crystalline coordinates ($\frac{2\pi}{a}$), and N denoting the total number of unit cells. We used $\left|w^{\boldsymbol{k}}\right\rangle$ to distinguish from the non pure $\left|\alpha^{\boldsymbol{k}}\right\rangle$ Bloch functions described below.

Filling these functions into the expression for the total Hamiltonian, similar to what was done in Eq. (B.17), results in:

$$\hat{H}_0^{\boldsymbol{k}} + \hat{H}_{\text{isb}}^{\boldsymbol{k}} = \sum_{\boldsymbol{n}} e^{i\boldsymbol{k}\cdot\boldsymbol{n}}\left(\hat{H}_0^{\boldsymbol{n}} + \hat{H}_{\text{isb}}^{\boldsymbol{n}}\right), \tag{2.28}$$

where the $\boldsymbol{n}$ denote that these are the elements of $\hat{H}_0$ and $\hat{H}_{\text{isb}}$ between orbitals shifted relative to each other by $\boldsymbol{n}$ lattice constants, i.e. $\langle\alpha|\,\hat{H}_0+\hat{H}_{\text{isb}}\,|\beta^{\boldsymbol{n}}\rangle$

Using these ingredients, and assuming that the eigenstates at $\boldsymbol{k}=\boldsymbol{0}$ are formed from the Bloch functions of $|x\rangle$, $|y\rangle$, $|\tilde{z}\rangle$ and $|\tilde{s}\rangle$ orbitals as in Eq. (2.27), we can formulate the $\boldsymbol{k}\cdot\boldsymbol{p}$ expansion:

$$\left|\alpha^{\boldsymbol{k}}\right\rangle = \left|\alpha^{\boldsymbol{0}}\right\rangle + \sum_{\beta\neq\alpha}\frac{\langle\beta^{\boldsymbol{0}}|\,\hat{H}_0^{\boldsymbol{k}}+\hat{H}_{\text{isb}}^{\boldsymbol{k}}\,|\alpha^{\boldsymbol{0}}\rangle}{\varepsilon_\alpha-\varepsilon_\beta}\left|\beta^{\boldsymbol{0}}\right\rangle = \sum_{\boldsymbol{n}}|\alpha^{\boldsymbol{n}}\rangle + e^{i\boldsymbol{k}\cdot\boldsymbol{n}}\sum_{\beta\neq\alpha}\frac{\langle\beta|\,\hat{H}_0+\hat{H}_{\text{isb}}\,|\alpha^{\boldsymbol{n}}\rangle}{\varepsilon_\alpha-\varepsilon_\beta}\,|\beta^{\boldsymbol{n}}\rangle\,. \tag{2.29}$$

In the following equations we omit the $\boldsymbol{k}=\boldsymbol{0}$ superscripts. Gathering the linear-in-$\boldsymbol{k}$ terms from the expansion of $e^{i\boldsymbol{k}\cdot\boldsymbol{n}}$ in Eq. (2.28), and writing $\varepsilon_p = \langle x|\,\hat{H}_0\,|x\rangle = \langle y|\,\hat{H}_0\,|y\rangle$, we find:

$$\left|x^{\boldsymbol{k}}\right\rangle = |x\rangle + i\Theta\frac{k_x}{\varepsilon_p-\varepsilon_{\tilde{z}}}\,|\tilde{z}\rangle\,, \tag{2.30}$$

$$\left|y^{\boldsymbol{k}}\right\rangle = |y\rangle + i\Theta\frac{k_y}{\varepsilon_p-\varepsilon_{\tilde{z}}}\,|\tilde{z}\rangle\,, \tag{2.31}$$

$$\left|\tilde{z}^{\boldsymbol{k}}\right\rangle = |\tilde{z}\rangle + i\Theta\frac{1}{\varepsilon_{\tilde{z}}-\varepsilon_p}\left(k_x\,|x\rangle + k_y\,|y\rangle\right), \tag{2.32}$$

with $\Theta = -\frac{a_0^2\pi}{a^3}\left(a_0^2 + \frac{\hbar^2}{m(\varepsilon_z - \varepsilon_s)}\right) eE_z$. Then, using the definition of the OAM operators for p orbitals:

$$\hat{L}_x = -i\hbar \begin{pmatrix} 0 & 0 & 0 \\ 0 & 0 & 1 \\ 0 & -1 & 0 \end{pmatrix}, \hat{L}_y = -i\hbar \begin{pmatrix} 0 & 0 & -1 \\ 0 & 0 & 0 \\ 1 & 0 & 0 \end{pmatrix}, \hat{L}_z = -i\hbar \begin{pmatrix} 0 & 1 & 0 \\ -1 & 0 & 0 \\ 0 & 0 & 0 \end{pmatrix}, \tag{2.33}$$

we find that,

$$\left\langle x^{\boldsymbol{k}} \right| \hat{L}_y \left| x^{\boldsymbol{k}} \right\rangle = -2\Theta \frac{k_x}{\varepsilon_p - \varepsilon_{\tilde{z}}}, \tag{2.34}$$

$$\left\langle y^{\boldsymbol{k}} \right| \hat{L}_x \left| y^{\boldsymbol{k}} \right\rangle = 2\Theta \frac{k_y}{\varepsilon_p - \varepsilon_{\tilde{z}}}, \tag{2.35}$$

$$\left\langle \tilde{z}^{\boldsymbol{k}} \right| \hat{L}_x \left| \tilde{z}^{\boldsymbol{k}} \right\rangle = -2\Theta \frac{k_y}{\varepsilon_{\tilde{z}} - \varepsilon_p}, \tag{2.36}$$

$$\left\langle \tilde{z}^{\boldsymbol{k}} \right| \hat{L}_y \left| \tilde{z}^{\boldsymbol{k}} \right\rangle = 2\Theta \frac{k_x}{\varepsilon_{\tilde{z}} - \varepsilon_p}. \tag{2.37}$$

These expressions for $\hat{\boldsymbol{L}}$ can be filled into the atomic SOC energy $\hat{H}_{soc} = \lambda \hat{\boldsymbol{L}} \cdot \hat{\boldsymbol{\sigma}}$ to arrive at the final expression for the energy of $\left|\tilde{z}^{\boldsymbol{k}}\right\rangle$:

$$\varepsilon^{\boldsymbol{k}} = \frac{2\lambda\Theta}{\varepsilon_{\tilde{z}} - \varepsilon_p} (\boldsymbol{k} \times \boldsymbol{\sigma}). \tag{2.38}$$

which has the same chiral form of the Rashba term in Eq. (2.2).

In summary, this qualitative derivation using a toy tight-binding model has led us to the first two contributions to the orbital Rashba effect, reflected in the two terms in the expression for Θ:

$$\Theta = -\frac{a_0^2\pi}{a^3}\left(a_0^2 + \frac{\hbar^2}{m(\varepsilon_z - \varepsilon_s)}\right) eE_z. \tag{2.39}$$

We want to emphasize here again that the only influence of the Gaussian radial shape is through the prefactor in front of eE_z in the definition of Θ. Other choices do not lead to different qualitative results.

Both terms in Eq. (2.39) originate from the inversion symmetry breaking electric field that enables additional hopping terms H_{isb}, favoring hybridized orbitals with nonzero OAM due to their nonzero dipoles. The first contribution came from the direct overlap dipoles between shifted $|x^{\boldsymbol{n}}\rangle$ and $|y^{\boldsymbol{n}}\rangle$ orbitals with the $|z\rangle$ orbital (panel (b) in Fig. 2.3)[26]. A second-order effect was found to originate from the hybridization of the $|s^{\boldsymbol{0}}\rangle$ and $|z^{\boldsymbol{0}}\rangle$ orbitals due to $\hat{H}_{\text{isb}}$ (panel (a) in Fig. 2.3), and the kinetic energy term between the resulting $|\tilde{z}\rangle$ orbital and neighboring $|x^{\boldsymbol{n}}\rangle$ and $|y^{\boldsymbol{n}}\rangle$ orbitals in Eqs. (2.24)-(2.26) [30]. It was found that both terms lead to a chiral texture of the OAM that varies linearly with $\boldsymbol{k}$. Through the atomic SOC, this linear-in-$\boldsymbol{k}$ OAM then couples to the spin which results in the final splitting with the Rashba-like form of Eq. (2.38).

There is one other term that contributes to the linear variation of OAM with $\boldsymbol{k}$ that originates from the atomic SOC.

Electric dipoles due to OAM

As mentioned previously, the atomic SOC leads to a degree of unquenching of the OAM, even at a T-invariant k point, e.g. $|k| = 0$ [27–29]. This means that the Bloch function of a given band is now a linear combination of p orbitals, rather than the pure one used as the starting point in the $\boldsymbol{k}\cdot\boldsymbol{p}$ expansion of Eq. (2.29):

$$|\psi\rangle = \sum_{\boldsymbol{n},\alpha} c_\alpha |\alpha^{\boldsymbol{n}}\rangle , \tag{2.40}$$

in terms of which the general formula for the OAM becomes:

$$\langle\psi| \hat{L}_\gamma |\psi\rangle = i\epsilon_{\alpha\beta\gamma} c^*_\alpha c_\beta, \tag{2.41}$$

where α, β, γ designate x, y, z.

Thus, to gain energy through $\hat{H}_{\text{soc}} = \lambda\hat{\boldsymbol{L}}\cdot\hat{\boldsymbol{\sigma}}$, the eigenstates at the high-symmetry point will be a linear combination of the p orbitals that leads to Bloch functions with some nonzero OAM. Through Hund's rule, we know that for isolated atoms this results in orbitals with maximum OAM. However, as discussed before, the associated charge distribution is unfavorable for the electrostatic repulsion due to the charge around neighboring ions, i.e. the crystal field [31]. Nonetheless, the balance between the quenching due to the crystal field and the unquenching due to atomic SOC results in orbitals with nonzero OAM at the T-invariant k point.

Performing then another expansion in terms of small $\boldsymbol{k}$ we find:

$$\left|\psi^{\boldsymbol{k}}\right\rangle = \sum_{\boldsymbol{n},\alpha} c^{\boldsymbol{k}}_\alpha e^{i\boldsymbol{k}\cdot\boldsymbol{n}} |\alpha^{\boldsymbol{n}}\rangle \tag{2.42}$$

$$= \sum_{\boldsymbol{n},\alpha} \left(c^{\boldsymbol{0}}_\alpha + \boldsymbol{k}\left.\frac{\partial c^{\boldsymbol{k}}_\alpha}{\partial \boldsymbol{k}}\right|_{\boldsymbol{k}=0} \right) (1 + i\boldsymbol{k}\cdot\boldsymbol{n}) |\alpha^{\boldsymbol{n}}\rangle . \tag{2.43}$$

Again we will omit $\boldsymbol{k} = \boldsymbol{0}$ superscripts. Focusing on the terms that vary linearly with k, we can identify the $\boldsymbol{k}\frac{\partial c^{\boldsymbol{k}}_\alpha}{\partial \boldsymbol{k}}$ term as exactly the contribution that was discussed in the toy model derivation of the previous Section. The new term originates from $ic_\alpha\boldsymbol{k}\cdot\boldsymbol{n}$ in Eq. (2.43), leading to the linear contribution

$$\varepsilon^{\boldsymbol{k}}_{\text{linear}} = \left[\left\langle\psi^{\boldsymbol{k}}\right| \hat{H}_{\text{isb}} \left|\psi^{\boldsymbol{k}}\right\rangle\right]_{\text{linear}} = i \sum_{\boldsymbol{n},\alpha,\beta} c^*_\alpha c_\beta \boldsymbol{k}\cdot\boldsymbol{n} \langle\alpha| \hat{H}_{\text{isb}} |\beta^{\boldsymbol{n}}\rangle \tag{2.44}$$

$$= -\frac{a_0^4\pi}{a^3} i(c^*_x c_z k_x + c^*_y c_z k_y) eE_z \tag{2.45}$$

$$= \frac{a_0^4\pi}{a^3}(L_y k_x - L_x k_y) eE_z, \tag{2.46}$$

where we used the definitions of $\hat{H}_{\text{isb}}$ in Eq. (2.19), and we remind the reader that L_x and L_y are the values of $\hat{L}_x$ and $\hat{L}_y$ of the Bloch function at $\boldsymbol{k} = \boldsymbol{0}$. These expressions show us that again, due to $\hat{H}_{soc} = \lambda\hat{\boldsymbol{L}}\cdot\hat{\boldsymbol{\sigma}}$ and $\hat{H}_{\text{isb}} = eE_z\hat{d}_z$, an additional term with the Rashba form in Eq. (2.2) appears in the energy dispersion, this time due to the

creation of orbitals with nonzero L_y and L_x at the high-symmetry point. A visualization of how these orbitals with nonzero OAM lead to dipoles is shown in Fig. 2.4, where a demonstration is given using a $p_x + ip_z$ orbital, with OAM L_y. As we can see, when k_x is varied away from 0, dipoles appear due to the interference between the rotated orbitals in the neighboring unit cells when the Bloch sum is performed.

Combining the linear–in–$\boldsymbol{k}$ terms found in the previous Sections, we arrive at the following effective Rashba Hamiltonian:

$$H_R^{\boldsymbol{k}} = e\boldsymbol{E}_P \cdot \left[c_1(\boldsymbol{k} \times \boldsymbol{\sigma}) + c_2(\boldsymbol{k} \times \boldsymbol{L^0})\right], \tag{2.47}$$

where $\boldsymbol{E}_P$ denotes the internal electric field from the polarization. c_1 is a result of the combined effect of the relativistic term in Eq. (2.12) and the overlap dipoles leading to Eq. (2.38), and the atomic SOC driven unquenching at $\boldsymbol{k} = \boldsymbol{0}$ results in the term with c_2 (see Eq. (2.44)).

To reiterate, the first mechanism is an electrostatically driven linear unquenching of the OAM which in turn couples to the spin through the atomic SOC, leading to the linear spin splitting. The second effect is a linear $\boldsymbol{k}$ variation of the dipoles of the Bloch functions with unquenched OAM at T-invariant points of the BZ, due to atomic SOC. Both together then result in the two terms on the right-hand side of Eq. (2.47).

With this qualitative understanding, we now turn to a concrete example of a material demonstrating a large Rashba-like spin splitting: GeTe.

2.3 Germanium telluride

At high temperatures GeTe has the standard rocksalt structure. When temperatures are lowered below $T_c \approx 720$ K [17], a displacive phonon instability occurs, freezing in a $\boldsymbol{q} = 0$ phonon that shifts the central Te ion along the [111] direction inside the Ge cage [35]. The space group after this inversion symmetry breaking phase transition becomes R3m (#160 in International Tables). Since this space group is polar, a nonzero ferroelectric polarization along the z-direction develops, as indicated by the yellow arrow in Fig. 2.5(a). The first BZ for this low-temperature structure is shown in panel (b), with the high-symmetry path we will focus on indicated by the blue line.

In the calculations reported below, we used a unit cell with lattice parameter a =4.28 Å, leading to a volume of 53.4 Å^3[36]. The Te ion is shifted by 0.25 Å away from the center of the unit cell.

The valence (conduction) bands around the Fermi level are mainly formed by s and p orbitals from the Te (Ge) ion. Since Te is significantly heavier than Ge, its atomic SOC is much larger. This will become important since we saw from the toy model that the size of the atomic SOC directly influences the size of the contribution to the spin splitting from the OAM based mechanism. The spin splitting is mostly observed around the T-invariant Z point of the BZ, along the plane perpendicular to the [111] direction (see Fig. 2.5(b)). The $Z - \Gamma$ path does not display any splitting because the electric field is along the z-direction, causing only k_x and k_y to contribute to the linear splitting as discussed in the previous Section.

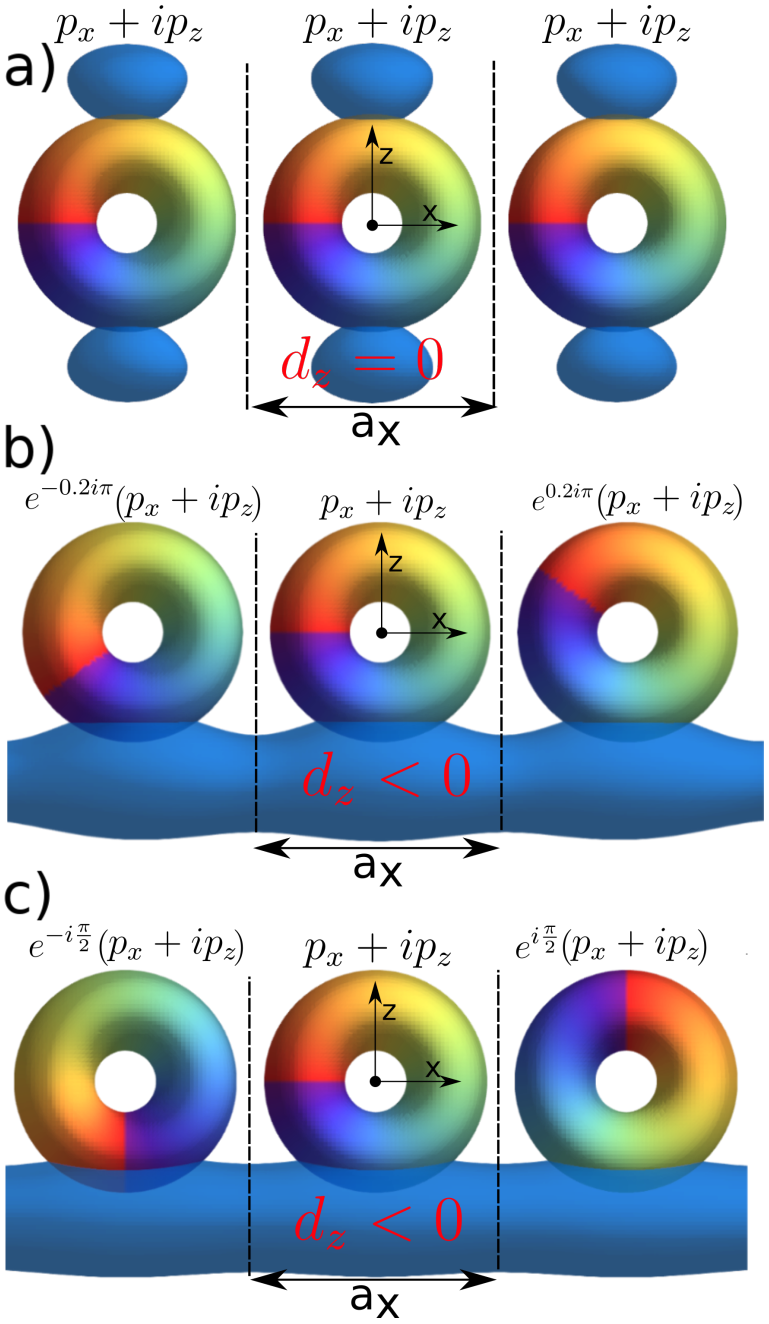

Figure 2.4: **Interference dipoles (d_z) for Bloch functions with nonzero OAM.** Three neighboring unit cells along the x direction are displayed, each with the same $p_x + ip_z$ orbital with nonzero L_y. The donut shaped isosurfaces denote the density of the orbitals, and the coloration of the surface indicates their phase. The dashed lines signify the unit cell boundary and a_x the lattice constant. The blue isosurfaces show the density of the corresponding Bloch function $\sum_{n_x} e^{ik_x n_x}(p_x^{n_x} + ip_z^{n_x})$ for different k_x values. a) $k_x = 0$: the contribution of the charge density from the top of the unit cell compensate the one from the bottom, leading to $d_z = 0$. b) $k_x = 0.1$: the phases of the shifted orbitals constituting the total Bloch function neighboring are rotated by -0.2π and +0.2π for the left and right unit cell, respectively. This is reflected in the rotated coloring of their surfaces. We see that the orbitals interfere constructively in the bottom half and destructively in the top half of the unit cells, leading to $d_z < 0$. c) $k_x = \frac{\pi}{4}$: the phases are now rotated by $\pm\frac{\pi}{2}$, and total dipole is even more substantial than for panel (b).

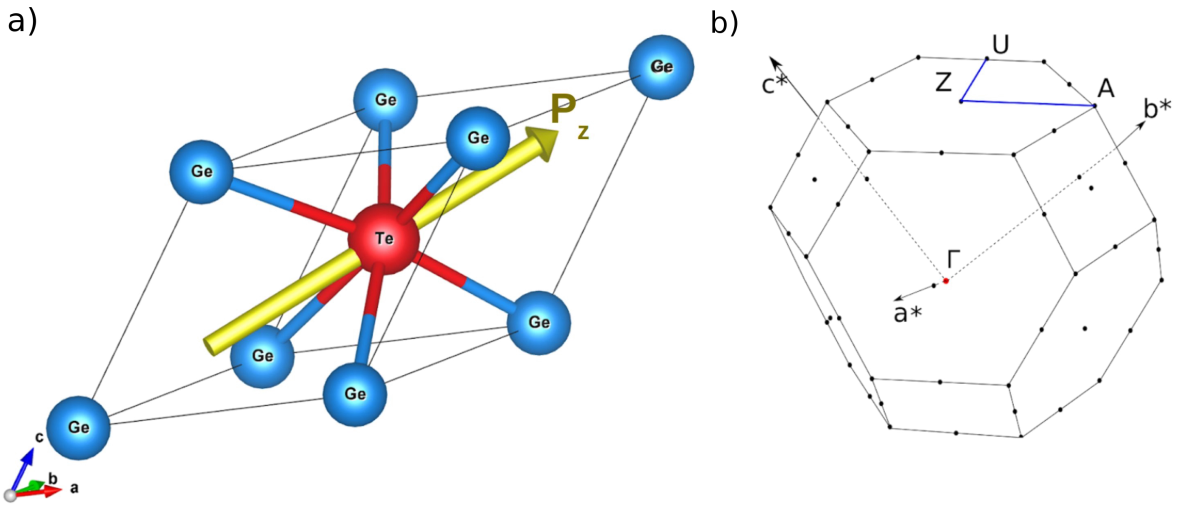

Figure 2.5: **Crystal structure of GeTe.** a) Rhombohedral unit cell, with the polarization along the [111] direction in yellow. b) First Brillouin zone with the high-symmetry k-path that is under focus indicated by the blue lines.

The situation in GeTe thus closely mimics the toy model we discussed in the electrostatics part of Section 2.2.2, and should also harbor the unquenching effect due to atomic SOC on the heavy Te leading to the second OAM based contribution. Moreover, since the splitting is observed for the bulk band structure, we can rule out the contribution due to the relativistic Rashba effect described in Section 2.2.1 because of the small internal electric field that is associated with the polarization.

2.4 Methods

We utilize ab-initio DFT calculations (see appendix A) as implemented in the Quantum ESPRESSO software package [37], in order to study the band structure in GeTe. We performed both NSOC and SOC calculations. Both calculations used the optimized norm-conserving Vanderbilt pseudo potentials [38], and a generalized-gradient approximation [39] with Perdew-Burke-Enzerhof parametrization for the exchange-correlation functional [40]. Plane waves with an energy of up to 30 Ry were included, with a 120 Ry cutoff for the density.

The reciprocal space was sampled using a 6x6x6 Monkhorst-Pack grid [41] for the self-consistent calculations, with the convergence determined by a total energy variation of below 10^{-7} Ry between successive self-consistency iterations.

Afterwards we used the Wannier90 package [42] to perform the Wannierization as described in appendix B. As the initial guess, we used projections onto hydrogenic s and p orbitals for both Ge and Te ions, since they are the main constituents of the bands around the Fermi level, as mentioned previously. A 10x10x10 k grid was used for the sampling of the BZ during the Wannierization.

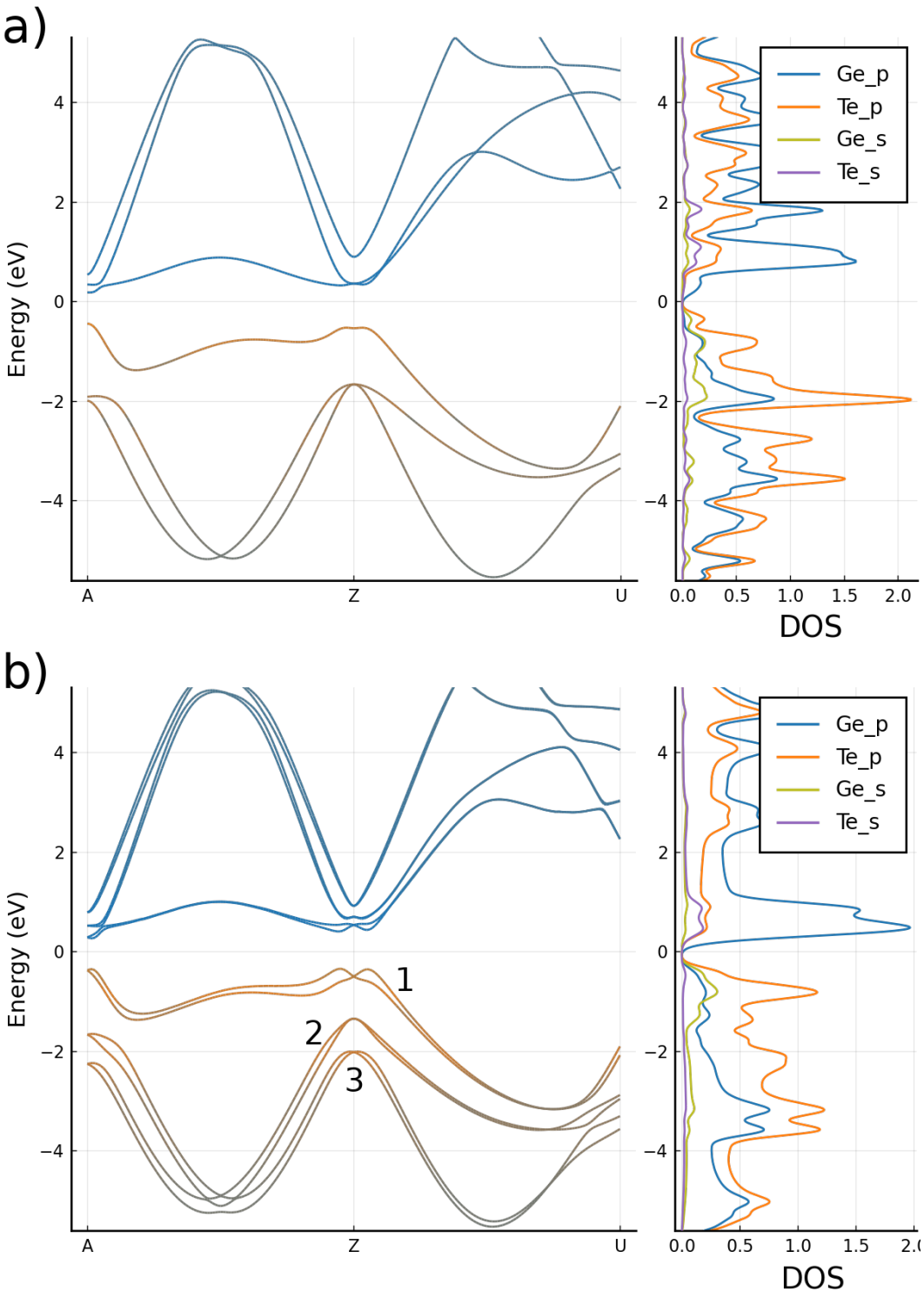

Figure 2.6: **Bandstructure of GeTe.** a) NSOC calculation. b) SOC calculation. In both panels the band structure was colored according to the contribution of the constituent orbitals, as indicated in the flanking density of state plots. The bands that have larger *s* character are located 5 eV below the shown window.

2.5 Results and discussion

The bands we will focus on are the three topmost valence bands which consist mostly of Te p orbitals, as can be seen from density of states (DOS) panels in Fig. 2.6. The only Rashba term that plays a role along the $A-Z-U$ path is of the form:

$$H_R^{\boldsymbol{k}} = \alpha_R(k_x\sigma_y - k_y\sigma_x), \tag{2.48}$$

since $\boldsymbol{E} = (0, 0, E)$, and the size of the field is included in α_R if we use the form of Eq. (2.2).

The proposed mechanism is a result of the real space properties of the Bloch functions, making a description in terms of localized Wannier functions the ideal tool for our investigation. The Wannierization, as described in Section B, provides us with a set of localized s- and p-like orbitals situated on Te and Ge, and a tight-binding model from which we can interpolate the band structure. The densities of the Wannier functions for the spin-up Te orbital are displayed in Fig. 2.7(a), with the spin-down orbitals having similar charge distributions. The combined spread of the 16 spinor Wannier functions[3] is 53.4 Å^2 (see Eq. (B.7) for details). The Wannier interpolation of the ab-initio band structure is shown in Fig. 2.8, which demonstrates a close agreement between the interpolated and ab-initio bands in the chosen window, and the valence bands in particular.

We then use the set of localized orbitals $|\alpha\rangle$, to calculate the real space operators that are of importance for the mechanism we are trying to confirm, namely the dipole matrix elements and OAM. We will use the center of mass $\langle\alpha|\,\hat{\boldsymbol{r}}\,|\beta\rangle$ as an indication of the local dipoles of the Bloch functions[4]. The OAM can be calculated as:

$$\langle\alpha|\,\hat{\boldsymbol{L}}\,|\beta\rangle = -i\hbar\,\langle\alpha|\,\hat{\boldsymbol{r}}\times\hat{\boldsymbol{p}}\,|\beta\rangle\,, \tag{2.49}$$

where we take $\hbar = 1$ in our calculations. We will focus on the OAM around the Te ion, since it has the largest atomic SOC, and is most prevalent in the valence bands. This means that in Eq. (2.49) we take $\hat{\boldsymbol{r}}$ to be the relative distance to the center of Te. This is only the local contribution to the OAM, while it is known that in certain solids there may also exist an itinerant contribution, which we neglect in our investigation here. For further information on this latter, we refer the inclined reader to the works on the *Modern Theory of Orbital Magnetization* in Refs. [47–50]. The spin operator $\hat{\boldsymbol{\sigma}}$ in terms of the orbitals is also accessible.

In order to calculate these orbitals for the Bloch functions, we first write them as a linear combination of the Fourier transforms of the Wannier functions:

$$\left|\psi_n^{\boldsymbol{k}}\right\rangle = \sum_\alpha c_{\alpha,n}^{\boldsymbol{k}} \sum_{\boldsymbol{R}} e^{i\boldsymbol{k}\cdot\boldsymbol{R}}\left|\alpha^{\boldsymbol{R}}\right\rangle, \tag{2.50}$$

[3] 4x2 for the Te ion and 4x2 for the Ge ion.

[4] We do this because we are mainly interested in the variation of the dipoles of the Bloch functions away from the Z point, rather than their absolute values. Indeed it has been shown that the definition of the electric dipoles in a crystalline environment requires some care. For further details we refer to the works on the *Modern Theory of Polarization* [43–47].

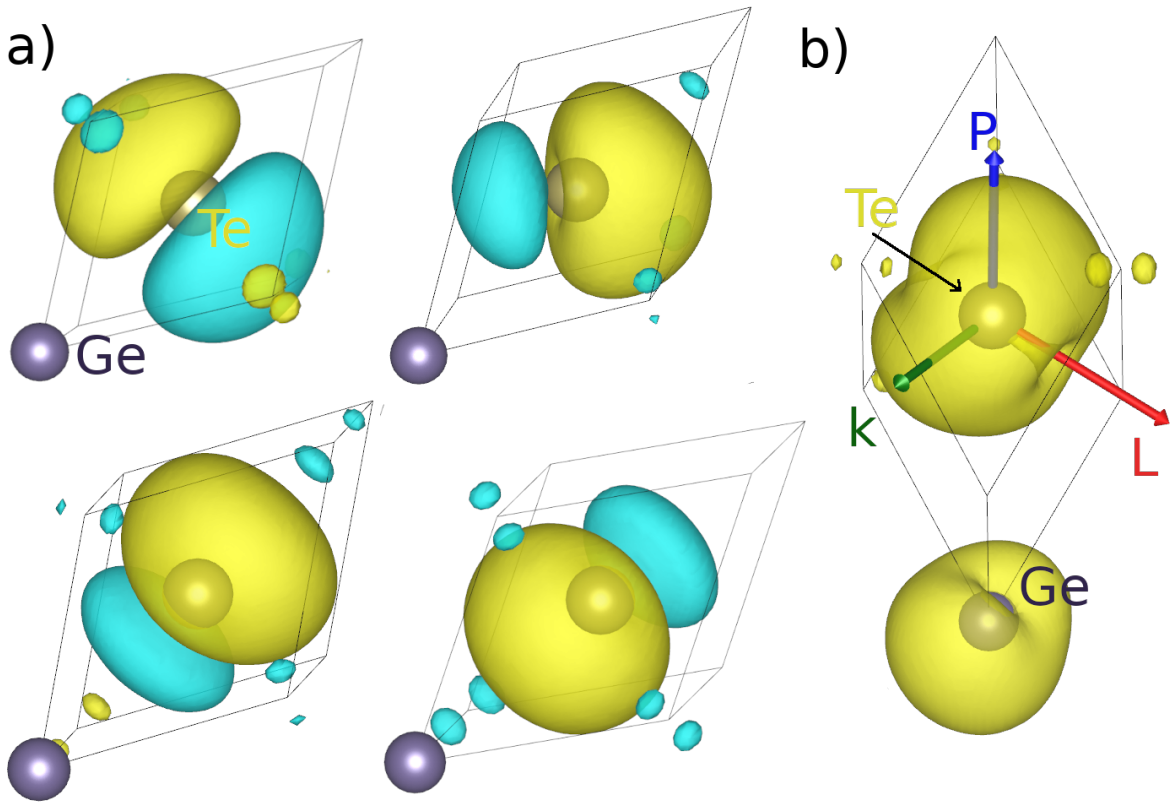

Figure 2.7: **Wannier functions** a) The spin-up Wannier functions of the orbitals around the Tellurium ion. The isosurface is constructed from the norm of the wavefunctions, with the coloration denoting the sign of the real part. b) The charge density in the central unit cell of the Bloch function of the top valence band, at $k = (0,\ 0.1,\ 0.9)$ Å^{-1}. The OAM ($\boldsymbol{L}$), polarization ($\boldsymbol{P}$), and $\boldsymbol{k}$ vector are shown by the red, blue, and green arrows, respectively. In each panel, the unit cell is denoted by the wireframe, and the Te and Ge ions are yellow and grey, respectively.

where the $c^{\boldsymbol{k}}_{\alpha,n}$ can be found by diagonalizing $H^{\boldsymbol{k}}$, and $\boldsymbol{R}$ denotes the lattice vector that identifies the unit cell wherein the Wannier function $\left|\alpha^{\boldsymbol{R}}\right\rangle$ lies. As an example of such a Bloch function, we have depicted the density inside the central unit cell of the top valence band at $\boldsymbol{k} = (0, 0.1, 0.9)$ Å^{-1} in Fig. 2.7(b).

Using Eq. (2.50) then allows us to calculate the OAM of the Bloch functions as:

$$\boldsymbol{L}^{\boldsymbol{k}} = \left\langle \psi^{\boldsymbol{k}}_n \right| \hat{\boldsymbol{L}} \left| \psi^{\boldsymbol{k}}_n \right\rangle = \sum_{\alpha,\beta} \left(c^{\boldsymbol{k}}_{\alpha,n}\right)^* c^{\boldsymbol{k}}_{\beta,n} \sum_{\boldsymbol{R},\boldsymbol{R}'} e^{i\boldsymbol{k}\cdot(\boldsymbol{R}'-\boldsymbol{R})} \left\langle \alpha^{\boldsymbol{R}} \right| \hat{\boldsymbol{L}} \left| \beta^{\boldsymbol{R}'} \right\rangle . \tag{2.51}$$

Since we are only interested in the OAM around the Te atom, and the Wannier functions are well localized within the unit cell, we neglect the intercell contributions. The sum over $\boldsymbol{R}$ and $\boldsymbol{R}'$ then reduces to a sum over $\boldsymbol{R}$ identical terms

$$\boldsymbol{L}^{\boldsymbol{k}} = \left\langle \psi^{\boldsymbol{k}}_n \right| \hat{\boldsymbol{L}} \left| \psi^{\boldsymbol{k}}_n \right\rangle = \sum_{\boldsymbol{R}} \sum_{\alpha,\beta} \left(c^{\boldsymbol{k}}_{\alpha,n}\right)^* c^{\boldsymbol{k}}_{\beta,n} \left\langle \alpha^{\boldsymbol{0}} \right| \hat{\boldsymbol{L}} \left| \beta^{\boldsymbol{0}} \right\rangle , \tag{2.52}$$

with similar expressions for the spin and center of mass of the Bloch functions. The term inside the sum $\sum_{\boldsymbol{R}}$ is an example of what we refer to as a "local" property of the

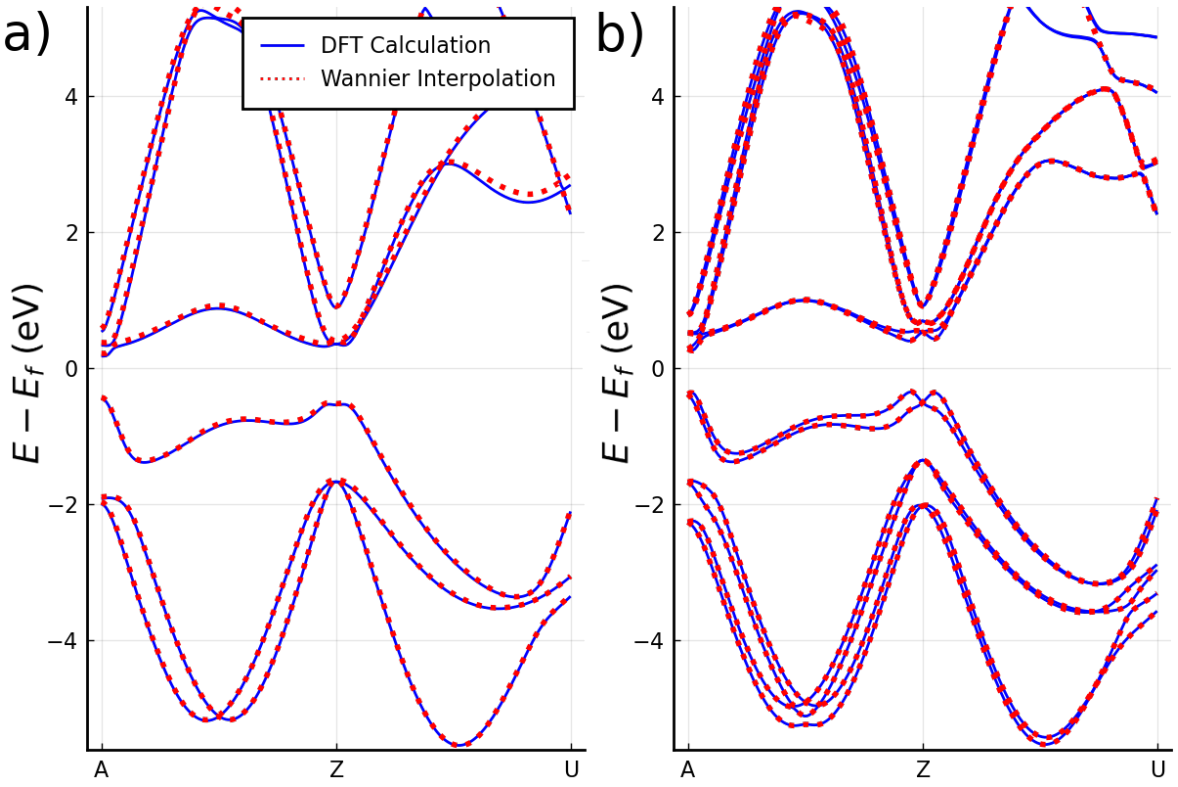

Figure 2.8: **Wannier interpolation.** Bandstructure interpolation by the tight-binding Hamiltonian in terms of the Wannier functions for NSOC (a) and SOC (b) calculations.

Bloch function, i.e. inside one unit cell. Reaching back to the Bloch function displayed Fig. 2.7(b), we have represented its OAM by the red vector. Note the donut-like shape of the charge density, a recurrent theme among orbitals with nonzero OAM (see Fig. 2.4 for another example). Compared with the densities of the Wannier functions shown in panel (a), this donut shape has a higher electrostatic energy due to the interaction with the charges on the neighboring Ge ions. Still, the atomic SOC and the dipole mechanism favor this shape for its nonzero OAM.

The calculated local properties of the Bloch functions are shown in Fig. 2.9 and Fig. 2.10 for the first and third valence band, respectively, demonstrating many interesting features which we now discuss in further detail.

The main confirmation of our claim that OAM is at the root of the large splitting can found in the panels that depict L_x and L_y, namely the green graphs. These green-colored graphs are the result of calculations without relativistic effects included, which can be verified from the panels that depict the eigenvalues, colored in the same way. There is a clear linear variation of the OAM as $\boldsymbol{k}$ varies away from the Z point, even though no atomic SOC is included. The only possible explanation for this unquenching can be found in expressions (2.34)–(2.37). Moreover, k_x remains zero along the A–Z path, and we can observe that only L_x develops due to the nonzero k_y. Only when k_x is nonzero, along the Z–U path, does L_y show up. This dependence on k_x and k_y is fully consistent with the expressions for L_x and L_y in Eqs. (2.34)–(2.37).

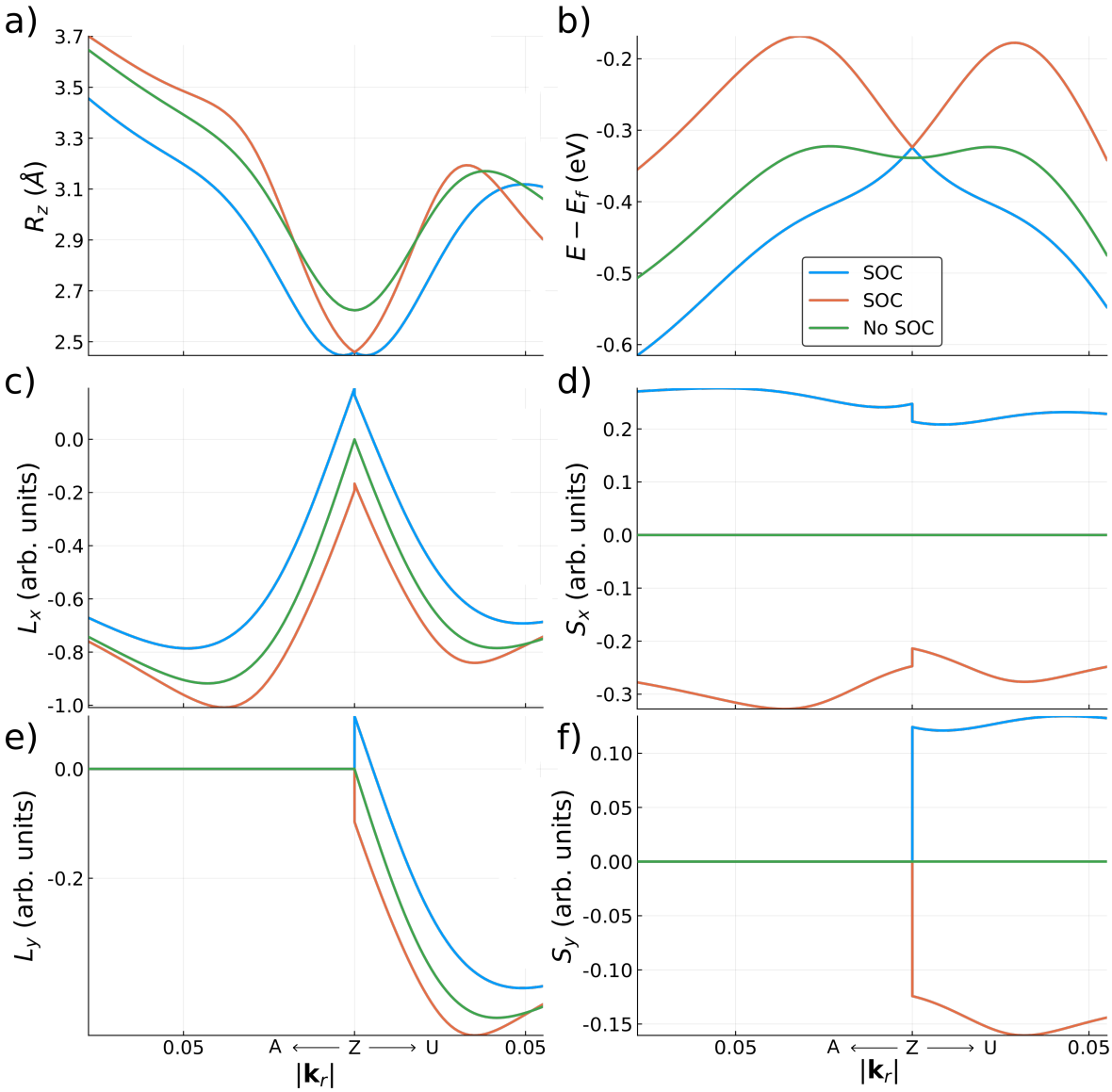

Figure 2.9: **Properties of the Bloch functions in the first valence band.** a) Center of mass in the unit cell. b) Eigenvalues. (c-f) L_x, S_x, L_y and S_y around the Te ion, respectively. The values are plotted in function of the relative distance to the Z point, $|\boldsymbol{k}_r| = |\boldsymbol{k} - \boldsymbol{k}_Z|$, along the $A \to Z \to U$ path shown in Fig. 2.5(b). The green graphs denote the values of NSOC calculations, whereas the orange and blue graphs denote those of the two spin-split bands resulting from the SOC calculations. See Fig. 2.6(b) for the location of this first valence band in the band structure.

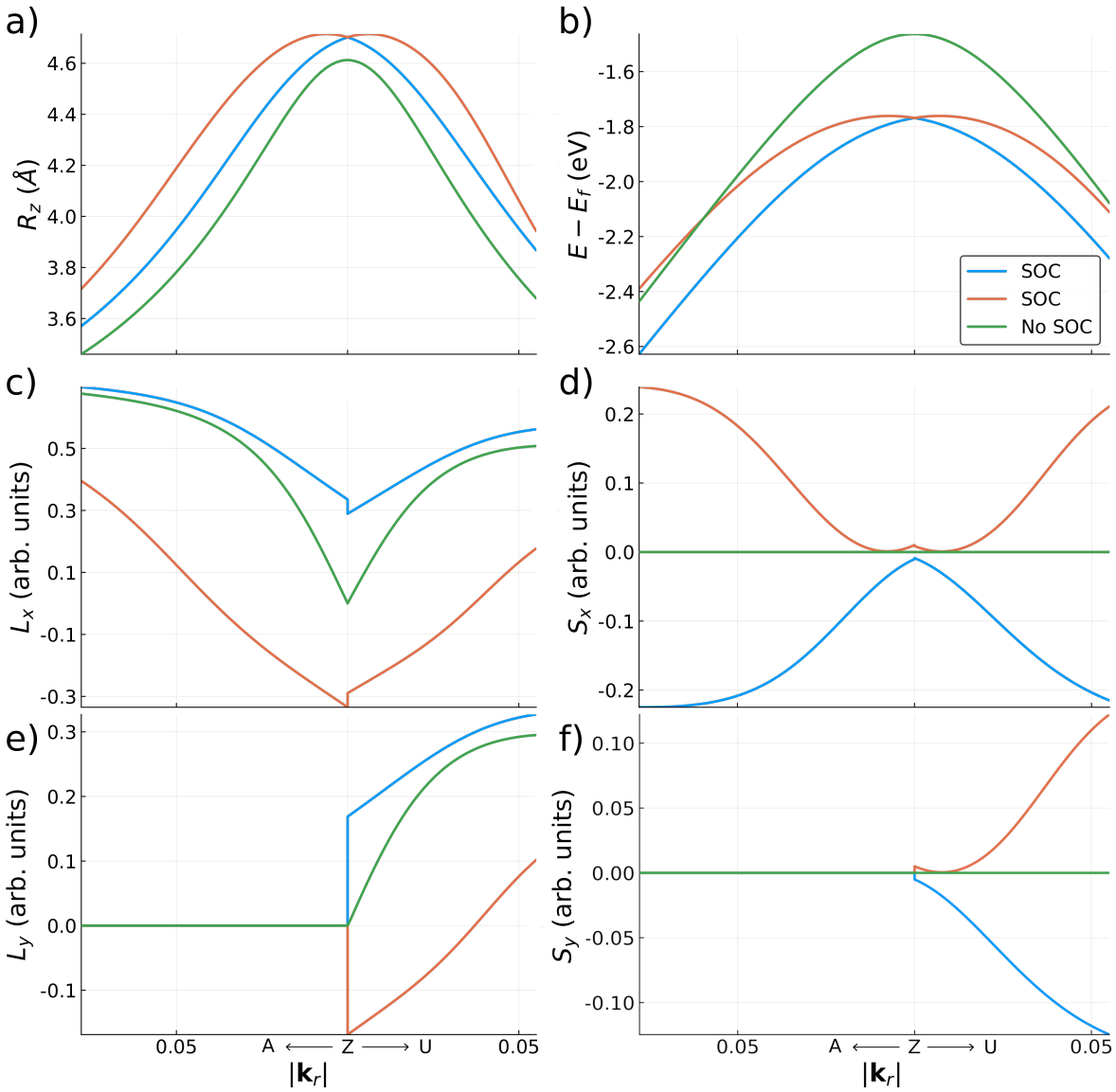

Figure 2.10: **Properties of the Bloch functions in the third valence band.** The panels depict the same properties as Fig. 2.9, but for the third valence band (see number 3 in Fig. 2.6(b)).

If we then include the atomic SOC, we can see that an additional unquenching of the OAM shows up. This leads to a nearly constant shift of the OAM with opposite signs for the two sub bands and is the sole contributor to the unquenching at the T-invariant Z point. How this unquenching leads to the second contribution of the linearly varying OAM was discussed in Eq. (2.44), where we found that it results from the combination of the linear $\boldsymbol{k}$ due to the first-order expansion of $e^{i\boldsymbol{k}\cdot\boldsymbol{R}}$, and a nonzero OAM at the T-invariant point. We can find the signature of this contribution in the change of the linear slope of the OAM for the SOC calculations compared with the one resulting from the NSOC calculations. This is especially clear for the third valence band shown in Fig. 2.10.

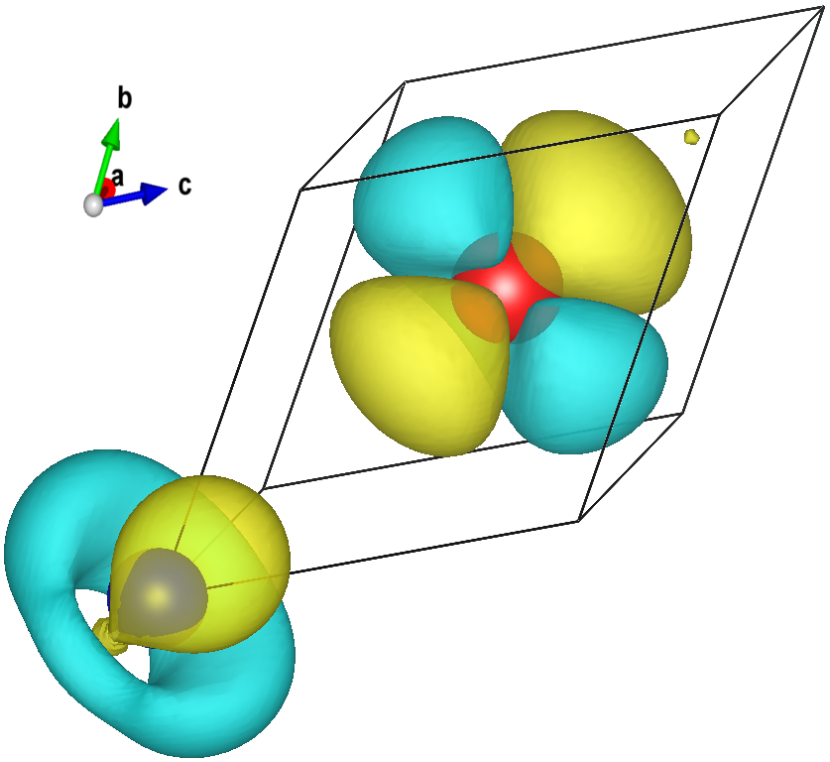

Figure 2.11: **Bloch function dipole.** The variation of the charge density of the Bloch function of the first valence band $\frac{\partial|\psi(k)|^2}{\partial k}\Big|_{k=Z}$ away from Z towards A. Te and Ge ions are in red and grey, respectively. The charge asymmetry around Ge showcases the nonzero dipole moment along z, which couples to the local electric field near Ge ion.

The most convincing argument, perhaps, can be extracted from the top-left panels of Figs. 2.9 and 2.10 that depict the variation of the center of mass of the Bloch functions. Indeed, not only does it change when $\boldsymbol{k}$ is moved away from the Z point, it changes differently for the two spin-split bands, as their OAM is shifted opposite to one another. As an example, we have depicted the charge variation of the Bloch functions in the first valence band in Fig. 2.11, demonstrating clearly how the dipole develops.

To conclude, we would like to comment on the OAM and spin textures of the first and third valence band. From their values at the Z point (see Fig. 2.9(c-f) and Fig. 2.10(c-f)), we can clearly see that these bands have a different total angular momentum j. In the first valence band, the spin and OAM are aligned at Z, allowing us to conclude that it is the $j_{3/2}$ band. The opposite orientation in the third valence band then gives away that this is one of the two $j_{1/2}$ bands, with the second valence band being the other (number 2 in Fig. 2.6). These observations have also been confirmed experimentally [22, 51]. The much smaller splitting and the opposite orientation of the OAM and spin in the third valence band compared with the first band seems to indicate that the two OAM based mechanisms, described throughout this Chapter and resulting in the two terms in Eq. (2.47), are working against each other in this band.

The OAM and spin texture for the first and third valence band are shown for the whole BZ in Fig. 2.12. The zoom onto the Z point in Fig. 2.13 reveals one last

very peculiar feature of the Bloch functions: the relative orientations of the OAM and spin reverse in a very narrow region around the Z point. This draws attention to the inclusion of H_R in Eq. (2.47), which breaks threefold symmetry and results in j not being a good quantum number anymore. This causes a highly non-trivial spin and OAM texture to be present in these two sub bands, with both textures varying considerably throughout the BZ.

2.6 Conclusions

To conclude this Chapter, we take a step back and summarize the original problem, proposed resolution, and numerical investigation of the large Rashba-like spin splitting in bulk ferroelectric materials.

The impetus of this research was the observation that the linear spin splitting that occurs in these bulk materials can be orders of magnitude larger than what is explainable by the purely relativistic Rashba effect. Moreover, a closer inspection led to the conclusion that the splitting is heavily influenced by the character of the bands, resulting in a different orientation and size of the splitting in each band. To substantiate these claims, we investigated the original derivation that leads to the purely relativistic Rashba effect, and discussed why it fails to explain these observations.

We then continued with a study of the proposed alternative mechanism, based on the combination of orbital angular momentum, electrostatics, and atomic SOC. Through the use of a toy tight-binding model and $\boldsymbol{k} \cdot \boldsymbol{p}$ expansions, we identified two contributing factors to this mechanism, both originating from the unquenching of OAM. The first arose due to an electrostatically driven linear unquenching which in turn coupled to the spin through the atomic SOC. The second originated from a linear $\boldsymbol{k}$ variation of the dipoles of the Bloch functions with, at T-invariant points of the BZ, unquenched OAM as a result of the atomic SOC. Combining these terms led us to the newly proposed Rashba-like effective Hamiltonian in Eq. (2.47).

After identifying the possible underlying mechanism we proceeded with a numerical investigation into the effect, with GeTe as the chosen test case. This choice was made because the bands that show a very large spin splitting are formed by s and p orbitals which were the basis of the tight-binding model we used in our derivations.

By studying the local properties of the Bloch functions that constitute the spin-split bands, we were able to substantiate our claim that the origin of the splitting is the OAM based mechanism, rather than the purely relativistic one. The generality of our derivation and remarkable consistency with the behavior in GeTe, leads us to believe that similar linear spin splittings in ferroelectric solids are almost exclusively the result of the OAM based mechanism.

Finally, we make some suggestions as to what might be the design rules to maximize the Rashba-like spin splitting. Since the internal electric field directly determines the size of the linear OAM unquenching, and the contribution due to dipoles resulting from the atomic SOC unquenching, the first goal is to maximize the ferroelectric polarization. Furthermore, a material constituted by heavy ions with large atomic SOC is desirable due to its role in converting the linear unquenched OAM into a spin splitting, and

the unquenching of the OAM at T-invariant k points. And finally: to maximize the unquenching of the OAM, a highly isotropic crystalline environment that minimizes the electrostatic penalty of having nonzero OAM is beneficial. Finding a material that achieves these three goals could enable more performant spintronic devices with the much needed electric control of spin polarization.

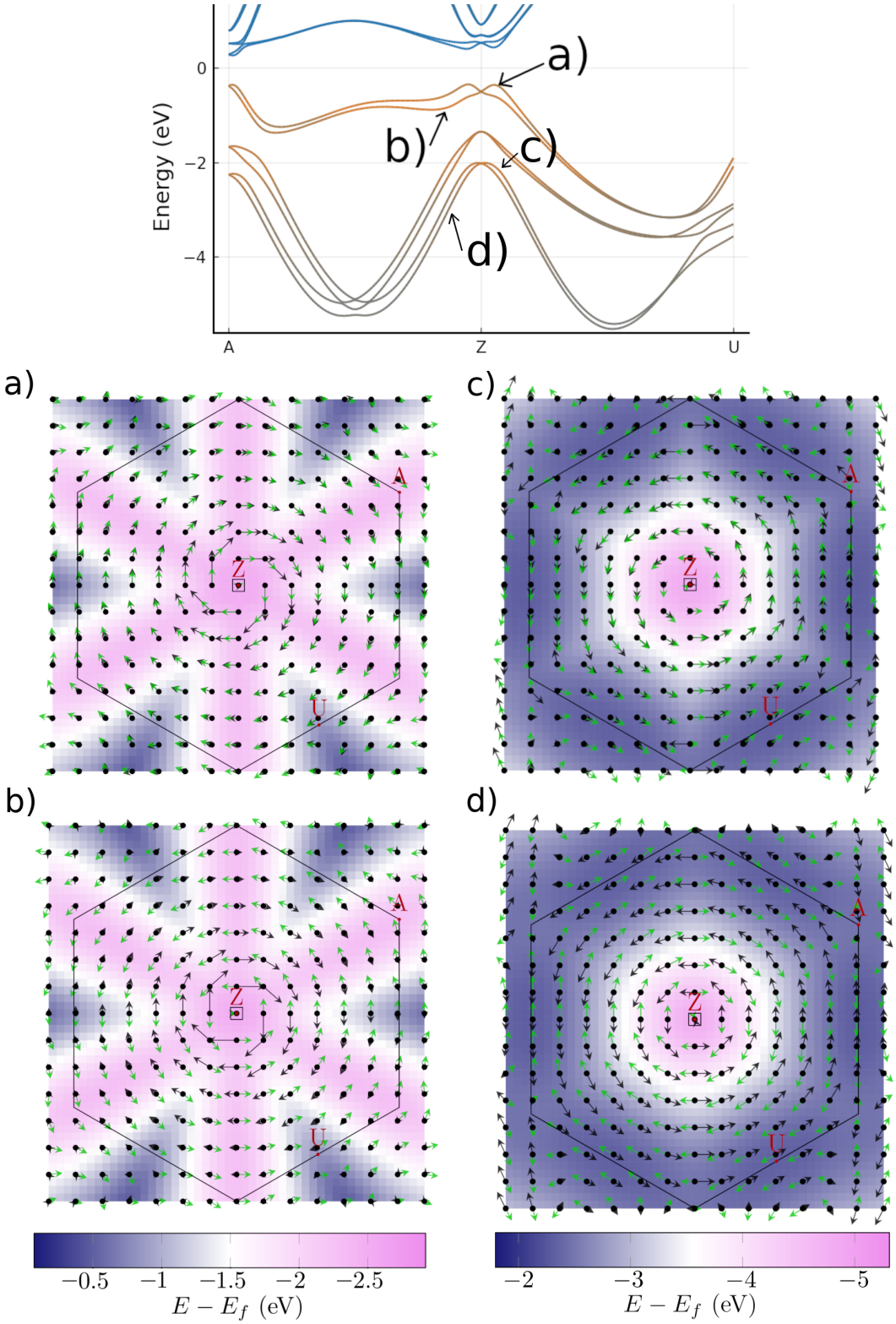

Figure 2.12: **OAM and spin in the BZ.** Panels (a-d) show the OAM (black arrows) and spin (green arrows) textures of the bands indicated by the same labels in the top panel. In each panel, a scaling factor for the length of the arrows was chosen for clarity. The color maps indicate the energy of the bands relative to the Fermi level. The small box around the Z point indicates the area magnified in Fig. 2.13.

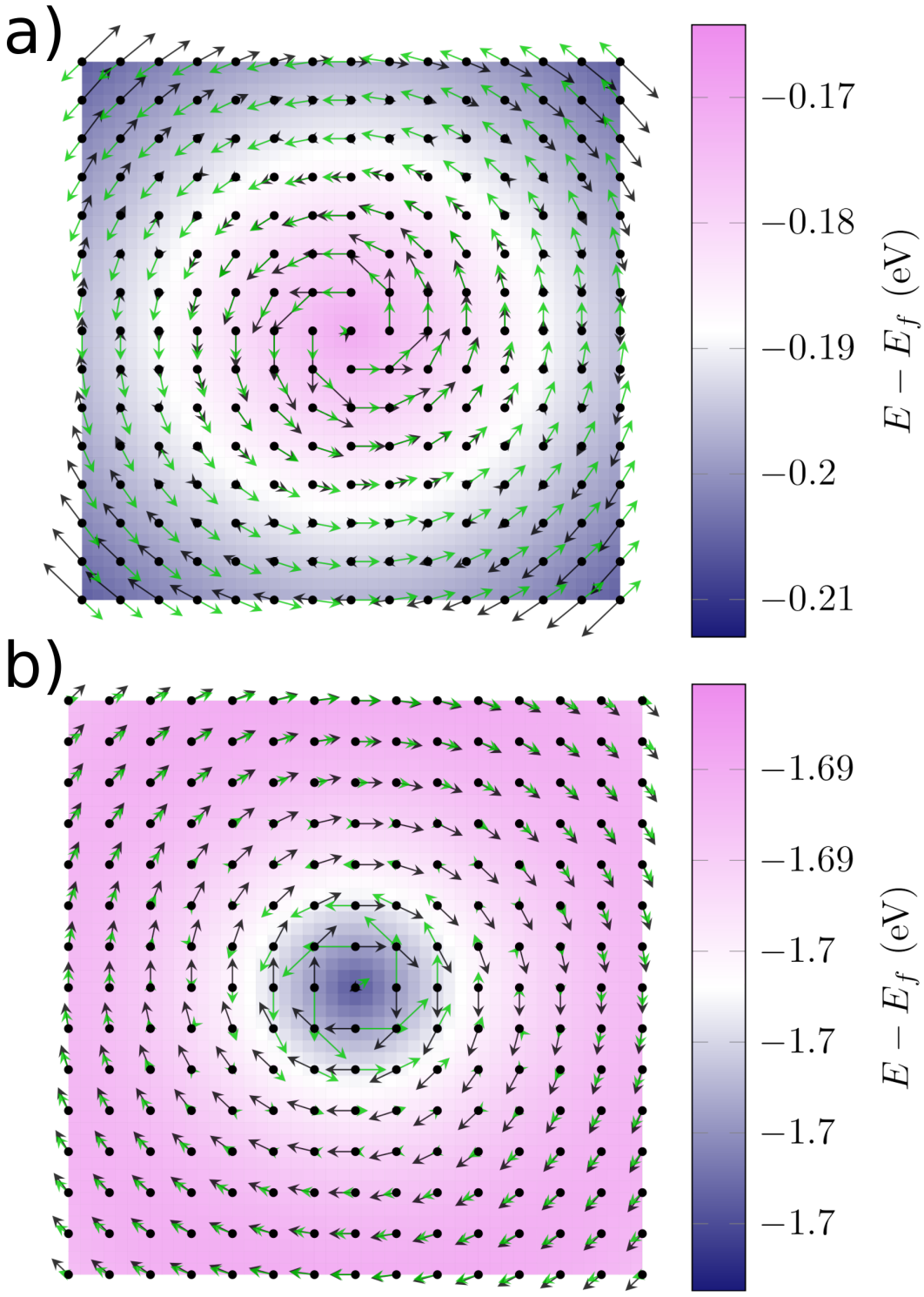

Figure 2.13: **Zoom of OAM and spin around Z.** a) Zoom of panel (b) in Fig. 2.12. b) Zoom of panel (c) in Fig. 2.12. These two zooms were chosen because they highlight the changing character most clearly, which is reflected in the change of the relative orientations of the OAM and spin, i.e. the black and green arrows.

3

Magnetoelectric crankshaft: topologically protected switching in multiferroic $GdMn_2O_5$

3.1 Introduction

Efficient control and probing of robust order has historically been one of the main technological drivers for research in condensed matter. The hallmark example is the impact that the discovery of giant magnetoresistance has had on the efficiency of the read head in hard disks, by using direct electrical readout rather than a solenoid [8, 52–55]. This is achieved by constructing the read head as a multilayer sandwich composed of a pinned magnet, a non-magnetic metal, and a soft magnet. The latter will align itself to the information storing magnetic domains on the platter of the hard disk. The resistivity of the stack then depends strongly on the mutual alignment of the pinned and soft magnets, as a result of the giant magnetoresistance. By applying a constant bias voltage to the read head, the magnetically stored information can then be probed electrically through the measurement of the resulting current. Underlying this mechanism is the Stoner effect, causing the conducting states around the Fermi level of metallic magnets to have a well-defined spin polarization depending on the internal magnetization. If current flows through these metallic magnets, the carriers with spins aligned to the pinned magnet will be scattered strongly by the soft magnet if the latter's magnetization is antiparallel to the former, leading to low conductivity. Conversely, when the magnetizations of the two magnets are aligned, the carriers will scatter weakly, which results in high conductivity. This development has led to a significant increase in the efficiency of hard drives.

There remains, however, the issue of writing the information in the first place. In

modern state-of-the-art high-density storage technologies, this is still done by applying an external magnetic field with an electromagnet to reorient the ferromagnetic domains. One can imagine this to be quite an inefficient process, both from the point of view of granularity (stray fields and non-locality of magnetic fields limit the minimum size of the domains), as from that of energy loss through heat dissipation. Improving these figures of merit drives much of the current research in the field of spintronics, with promising applications like spin-transfer torque devices [5–9]. These use an inverse effect to the one described above. First, a current is created with carriers that have a well-defined orientation of the spin by using e.g. a pinned ferromagnet, as in the read head. Subsequently, this current is forced through (or close to) a magnetic domain by the bias electric field. If the spin of the carriers and the magnetization of the domain are misaligned, strong scattering occurs which rotates the spin moments of the carriers. However, this will cause an opposite torque on the magnetization of the domain, due to the conservation of angular momentum. This transfer of torque is where the classification of *spin-transfer torque* devices originates from. If enough such spin-polarized current flows through the domain, its magnetization will eventually be reoriented along the spins of the incident carriers. This method circumvents the need for electromagnets to create a magnetic field by using circular currents, greatly increasing the efficiency and allowing for greater domain density.

It is clear that the longevity associated with magnetic order, combined with the ease and efficiency of manipulation through electrical means is highly desirable. This brings us to the topic of this Chapter, namely the magnetoelectric effect in multiferroic insulators. As the name implies, the magnetoelectric effect allows for the electric control of magnetic order or the magnetic control of ferroelectric polarization [56–60], the former being the most attractive from a technological point of view. In practice, however, the effectiveness of this cross-order control is often limited, and multiferroic materials are rare, to begin with. The reasons why are summarized briefly below, following the discussion of Khomskii in Ref. [57].

Two main classes of multiferroic materials can be identified: type-I and type-II multiferroics. In the former, the ferroelectric polarization and magnetic order stem from different origins and are thus largely decoupled. The latter, instead, develops ferroelectricity as a result of an inversion symmetry breaking magnetic configuration. In this case, the two orders are coupled strongly, but the size of the ferroelectric polarization is often limited, and generally much lower than for type-I multiferroics.

We use the ABO_3 perovskites with a magnetic transition metal B ion as an example in order to understand why multiferroics are so rare. Magnetic order is almost exclusively caused by partially filled valence shells, partially-filled d shells in this case. Ferroelectricity, on the other hand, can find its origin in various microscopic effects. In many of them, the ferroelectricity is caused by an off-center shift of the B ion in the surrounding oxygen octahedron (see Chapter 5 for a detailed discussion on ferroelectricity in $BaTiO_3$). This is due to the formation of strong covalent bonds between one (or three) oxygens and the B ion, using the latter's empty d states. While it is not fully understood why, the presence of any electrons in the d shell of the B ion severely hampers this process which is one of the root causes for the rarity of multiferroicity in these materials, since magnetism requires at least some filling. A more detailed study

on the rarity of multiferroics was performed in Ref. [61].

One of the ways both orders can appear simultaneously is with A ions that have lone pairs (filled outer s shell), e.g. $BiFeO_3$, where the Bi^{3+} ion harbors such a lone pair, which is highly polarizable. When the temperature is lowered, this leads to an instability that favors the alignment of such pairs, causing the polarization in the ferroelectric phase of this material. The ordering temperatures for the ferroelectric and magnetic order are 1100 K and 643 K, respectively, with a polarization $P \sim 90\mu C/cm^2$. $BiFeO_3$ is thus a clear example of a multiferroic material, however, the two orders have completely different origins and the cross-order coupling is thus extremely low. Nonetheless, some more recent developments have shown promising ways to overcome the limited magnetoelectric coupling in $BiFeO_3$, allowing for a degree of control over weak ferromagnetic moments by an external electric field [62]. For further details on the mechanisms of the ferroelectricity in the other type-I cases, either through charge ordering or tilting of the oxygen octahedra, we refer the reader back to Ref. [57].

On the phenomenological side, the simplest Landau free energy one can write down for a homogeneous type-I multiferroic, by expanding the free energy F in terms of ferroelectric polarization P and magnetization M (both scalars), is:

$$F(P,H) = F_0 + \frac{a}{2}(T-T_P)P^2 + \frac{b}{4}P^4 - PE \tag{3.1}$$

$$+ \frac{\alpha}{2}(T-T_M)M^2 + \frac{\beta}{4}M^4 - MH - \frac{g}{2}P^2M^2, \tag{3.2}$$

with T denoting the temperature, E the electric field, and H the magnetic field. All coefficients are taken to be positive, such that below the ferroelectric (ferromagnetic) transition temperature T_P (T_M) nonzero P (M) develops. The lowest order symmetry-allowed term that couples P and M is $-gP^2M^2$, obeying both the time-reversal and inversion symmetries of the parent structure above the transition temperatures T_P and T_M. Minimizing the energy with respect to both orders for $T < T_M, T_P$ and no applied external fields, leads to,

$$\frac{\partial F}{\partial P} = 0 \Leftrightarrow P^2 = -a(T-T_P)/b + gM^2 \tag{3.3}$$

$$\frac{\partial F}{\partial M} = 0 \Leftrightarrow M^2 = -\alpha(T-T_M)/\beta + gP^2. \tag{3.4}$$

Both order parameters thus depend on the value of the other through the magnetoelectric coupling g. This leads to a change in one when an external field is applied to the other. As mentioned before, however, the different microscopic origins of both orders usually result in a tiny value of g. Indeed, the effective dielectric constant ε of $BiMnO_3$ only displays a weak anomaly at the ferromagnetic transition temperature (T_M) and is only weakly affected by an external magnetic field, leading to a change of ε at an external magnetic field of 9 T of only 0.6% compared with its value at zero-field. This means that the electrical behavior of this material is almost impervious to an external magnetic field, a clear demonstration of the problems with cross-order control in type-I multiferroics.

In an effort to improve this sought-after control, we turn to the type-II multiferroics. As mentioned before, the ferroelectricity in these materials is a result of the inversion breaking magnetic order that sets in below T_N. Due to the shared microscopic origin, the coupling between the magnetic and ferroelectric orders in these materials is generally much higher than for type-I multiferroics, leading to an increased magnetoelectric effect [63, 64]. However, one caveat is that in this case, the ferroelectric polarization is much lower since the associated distortions are a result of the force due to the weak magnetoelectric coupling[1]. This leads to reduced effectiveness of external electric fields as a method of effective control of the magnetic order.

Here, we focus specifically on $GdMn_2O_5$ (see Fig. 3.1(a)) that demonstrates an exceptional tunability of the ferroelectric polarization through an applied magnetic field [57, 65]. The orthorhombic RMn_2O_5 manganites have a very complex crystalline structure, which leads to a wealth of different phases depending on the temperature, rare-earth ion R, external magnetic field, and even electric-field poling history [66–71].

In the next Section, we first give a summary of the transitions and phases that are important for this Chapter, followed by a discussion on the experiments that were performed by our collaborators in Sec. 3.3. Afterward, we continue in Sec. 3.4 with a description of the system in terms of an effective spin Hamiltonian involving the Gd spins, and the antiferromagnetic (AFM) order parameters $\boldsymbol{L}$ describing the two Mn chains. We demonstrate that our model reproduces the overall behavior observed by the experiments remarkably well, and discuss its energetic properties, in Sec. 3.6.1. After uncovering the source of the peculiar magnetoelectric switching, we shift our focus in Sec. 3.6.2 to the magnetic configuration, and how it changes because of the applied magnetic fields. Finally, we comment on the topological nature in Sec. 3.6.3 of the switching behavior and the generality of the model, and conclude with an intuitive argument in Sec. 3.6.4, and resulting simplified model in Sec. 3.7 in an attempt to further rationalize our observations.

3.2 Gadolinium manganite

All RMn_2O_5 have crystallographic group $Pbam$ [72] in the paramagnetic phase at high temperature, which is eventually lowered to P_ab2_1a (P_aca2_1 in conventional International Tables of Crystallography settings, which has $Pca2_1$ as the corresponding space group) when the commensurate magnetic order condenses below $T_N \approx 33$ K [65, 73]. This order is characterized by the propagation vector $\boldsymbol{q} = (1/2, 0, 0)$, i.e. there is a unit cell doubling along the crystalline a-direction, as shown in Fig. 3.1(a). The magnetic configuration repeats along the crystalline c-direction. The magnetic phase transition goes hand in hand with a sharp anomaly in the dielectric constant ε_b, signaling the onset of the improper ferroelectric polarization along the b-direction (P_b) [65, 73, 74]. When the temperature is lowered further, P_b saturates to a maximum value of around 3600 $\mu C/m^2$, the largest found for any rare-earth manganite. However, it is still tiny

[1] The order parameter describing the ferroelectric polarization is a pure slave order parameter, that would not develop on its own in these materials. It is only nonzero because of the appearance of the primary order parameter that describes the magnetic order below T_N (i.e. there is no T_P).

compared to proper ferroelectrics like $BaTiO_3$ with $P \approx 3 \times 10^5 \mu C/m^2$ at room temperature [75, 76]. The magnetic unit cell is traversed by two antiferromagnetic (AFM) Mn chains, which are formed by pyramidally coordinated Mn^{3+} and octahedrally coordinated Mn^{4+} ions, as indicated by the cyan lines and purple polygons in Fig. 3.1(a). The Mn spins inside the chains lie mostly along the fourfold symmetry axis of the Mn^{3+} pyramids, making angles of $\pm 23.4°$ with the a-axis.

The improper ferroelectricity is generated through the symmetric Heisenberg exchange striction due to the strong AFM exchanges combined with the geometric frustration of the Mn chains [77]. This frustration appears due to the odd number of AFM bonds in the Mn pentagons surrounding each Gd ion, similar to an AFM triangular lattice, which does not allow for all the AFM exchanges to be satisfied simultaneously (i.e. by having completely antiparallel spins on each AFM bond). Fig. 3.1 panel (a) and the more detailed panel (c) demonstrate how this geometric frustration manifests itself in $GdMn_2O_5$. When the magnetic order sets in, magnetic exchange energy is simultaneously optimized with the elastic energy on each bond. This results in the contraction of bonds with a mostly antiparallel alignment of spins, and the extension of bonds with more parallel spins, indicated by the orange and blue arrows in Fig. 3.1(b,c), respectively.

The simplest form of this behavior can be understood by considering Heisenberg exchange between two spins i, j, on a dimer. The exchange coefficient can be written in terms of the hopping t_{ij} and Coulomb repulsion U as: $J(r_i, r_j) \approx \frac{t_{ij}^2}{U}$. It depends through t_{ij} only on the length of the bond, such that $J(r_i, r_j) = J(r_i - r_j) = J(r)$[2]. The energy W for each bond can then be written, following Ref. [78], as:

$$W_{ij} = J(r)\boldsymbol{S}_i \cdot \boldsymbol{S}_j + \frac{\kappa \delta r^2}{2r_0}, \tag{3.5}$$

with spins $\boldsymbol{S}_i$ and $\boldsymbol{S}_j$, κ the elastic stiffness of the bond, r_0 the mean separation between neighboring Mn^{3+} and Mn^{4+} ions in the paramagnetic state, and $\delta r = r - r_0$. Minimizing the energy of the bond through $\frac{\partial W}{\partial r} = 0$ then leads to the change in bond length δr given by:

$$\delta r = -\frac{\partial J}{\partial r}\frac{r_0}{\kappa}\boldsymbol{S}_i \cdot \boldsymbol{S}_j, \tag{3.6}$$

when the magnetic order sets in below T_N. Thus, AFM bonds ($J > 0$) with antiparallel spins contract ($\delta r < 0$), and bonds with parallel spins extend ($\delta r > 0$). In the case of RMn_2O_5, this causes the octahedrally coordinated Mn^{4+} ion to shift towards one of the two neighboring Mn^{3+} pyramids in the Mn^{3+} – Mn^{4+} – Mn^{3+} sequences, as demonstrated in Fig. 3.1(b). As mentioned before, this causes a lowering of the symmetry from $Pbam$ to $P_a b 2_1 a$, and, as the Born effective charges of the Mn^{3+} and Mn^{4+} ions differ, to a nonzero polarization along the b-axis [57]. It was shown, however, that this ionic displacement is largely compensated when electronic correlation effects are taken into account. These lead to an additional increase of the electronic charge between the ions, which almost fully cancels the positive contribution to the polarization due to the

[2] In real materials this process is more complex due to the presence of multiple orbitals, and multiple neighboring ions.

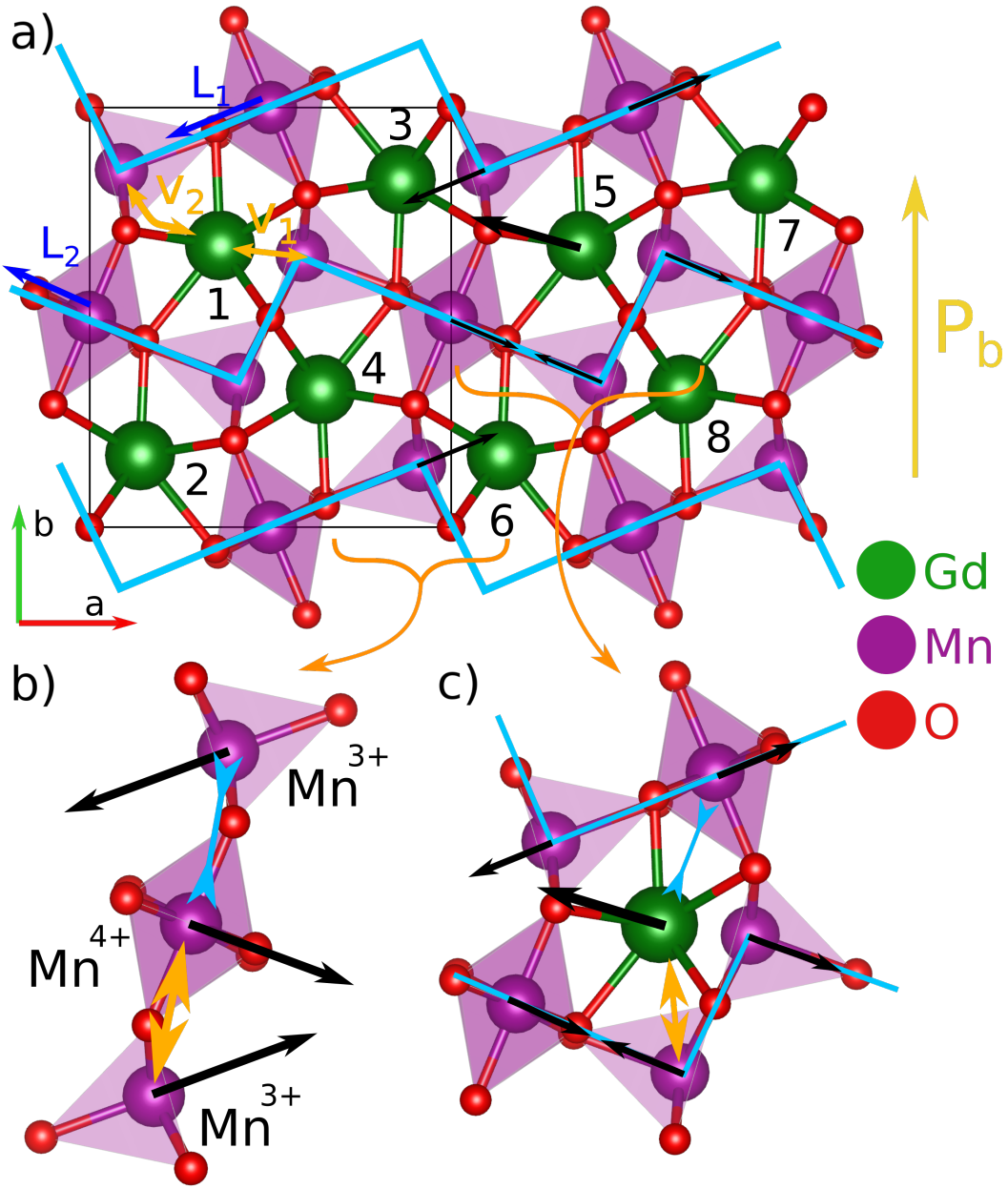

Figure 3.1: **Unit cell and magnetic configuration of $GdMn_2O_5$.** a) The magnetic unit cell with the AFM zig-zag chains along the a-direction (cyan lines) denoting which Mn ions are linked by large AFM exchange, leading to the blue $\boldsymbol{L}_1$ and $\boldsymbol{L}_2$ Néel vectors used in the theoretical model (see Sec. 3.4). The boundary of the structural unit cell is marked by the black rectangle. The orange arrows denote the exchange paths between Gd and neighboring Mn ions in both chains, corresponding to v_1 and v_2 in the model. The two sources of the symmetric Heisenberg exchange striction are shown in (b) and (c). The black arrows indicate the zero-field orientation of the spins, and are correspondingly marked on the full structure in (a). The yellow and blue arrows in (b) and (c) denote the expanding and contracting bonds, respectively. The resulting polarization P_b is shown by the large yellow arrow in panel (a).

ionic displacement, resulting ultimately in the relatively small values of the polarization ($P_b \sim 10^3 \mu\text{C/m}^2$ without correlations, rather than $\sim 10^4 \mu\text{C/m}^2$ with correlations) [79].

There is a second source of polarization in $GdMn_2O_5$, also due to the symmetric Heisenberg exchange striction, but this time between the spins of Gd and Mn [65]. All the exchanges between Gd and the surrounding Mn ions are again AFM. A similar train of thought can then be followed as before, causing the bonds with parallel spins to extend and those with antiparallel spins to contract (see Fig. 3.1(c)).

Gd^{3+} is special compared with the other magnetic rare-earth ions in the RMn_2O_5 family because it has a very isotropic electronic configuration ($4f^7$), i.e. there is no unquenched orbital angular momentum and associated anisotropic charge distribution (as discussed profusely in the Rashba Chapter 2). This means that the large spin (nominally $S = 7/2$) can orient itself freely to optimize the magnetic interactions with its neighboring Mn atoms, without incurring any penalties through the atomic SOC combined with nonzero OAM. This leads to a high magnetic susceptibility and associated magnetoelectric effect, surpassing the other RMn_2O_5 compounds both in size and tunability of P_b, with a measured variation of up to $5000\,\mu$ C/m^2 when a magnetic field is applied [65].

Now that the stage is set, we continue with a description of the puzzling experimental observations that motivated the study in this Chapter.

3.3 Experimental methods and results

The measurements we present in this Section were performed in the group of A. Pimenov, on single crystal $GdMn_2O_5$ samples grown by S.-W. Cheong's group. Magnetic fields were applied under varying angles ϕ_H to the crystalline a-axis, and swept up and down while tracking the evolution of P_b. The results for such measurements at 2 K are displayed in Fig. 3.2. Only positive fields were applied, but the behavior is identical for fields with opposite signs, as we will show later in Section 3.6.2. In previous experimental measurements, the magnetic field was only applied along the crystalline a-axis, i.e. $\phi_H = 0$ [65].

In the following we will refer to three distinct switching regimes: the low angle, "magic" angle, and high angle regime. They correspond to the values of ϕ_H shown in panels (a), (b), and (c) of Fig. 3.2, respectively. Before delving into a detailed analysis of the experiments, we would like to point out that the low angle behavior shown in the left side of panel (a) does not coincide with the behavior found in previous experiments in Ref. [65] on the same sample, shown on the right. There it was found that when the field is applied along the a-axis, a two-state switching with a reversal of the polarization is observed, similar to the 1–4 branch in panel (b) of Fig. 3.2. We are not quite sure what leads to this discrepancy between the measurements. It could be related to the poling history of the sample or some domain related behavior. This discrepancy is not that important in light of the current discussion, but it is nonetheless at odds with our theoretical findings which demonstrate behavior similar to the previous measurements in Ref. [65].

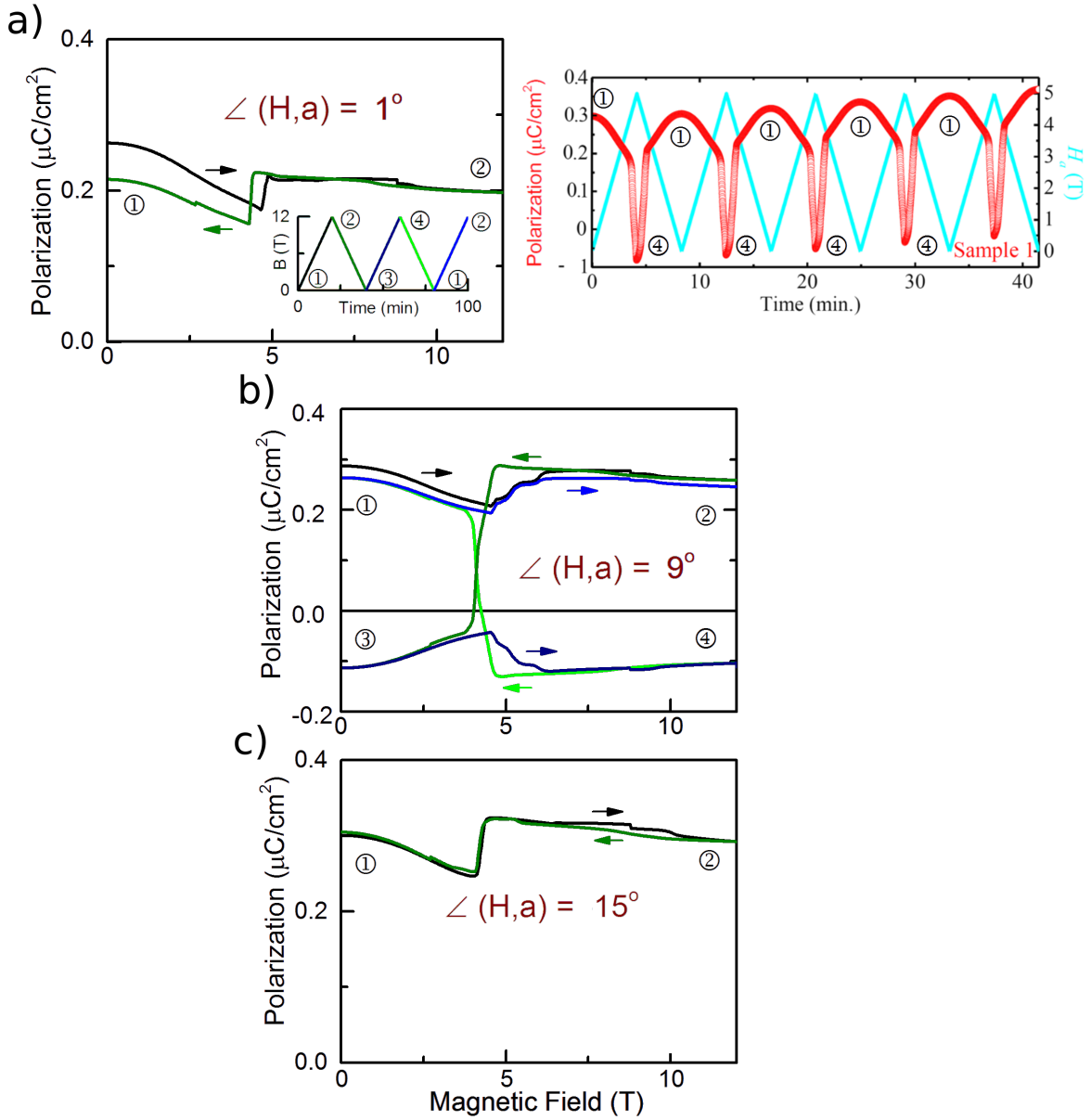

Figure 3.2: **Experimental measurements of the ferroelectric polarization at 2.3 K.** a) Magnetic field applied at 1° which leads to a two-state hysteresis loop. The left panel shows the result of our measurements, whereas the right one shows the previous measurements of Ref. [65]. This behavior on the right panel is identical to our theoretical results (see Sec. 3.6). b) Magnetic field applied at 9°, where the four-state hysteresis loop appears. c) Field applied at 15°, again leading to a two-state hysteresis loop. In these plots, we have denoted the four discussed states by the labels 1-4. The arrows and graph color denote the direction of magnetic field change during the sweep, as indicated by the inset of the left graph of panel (a).

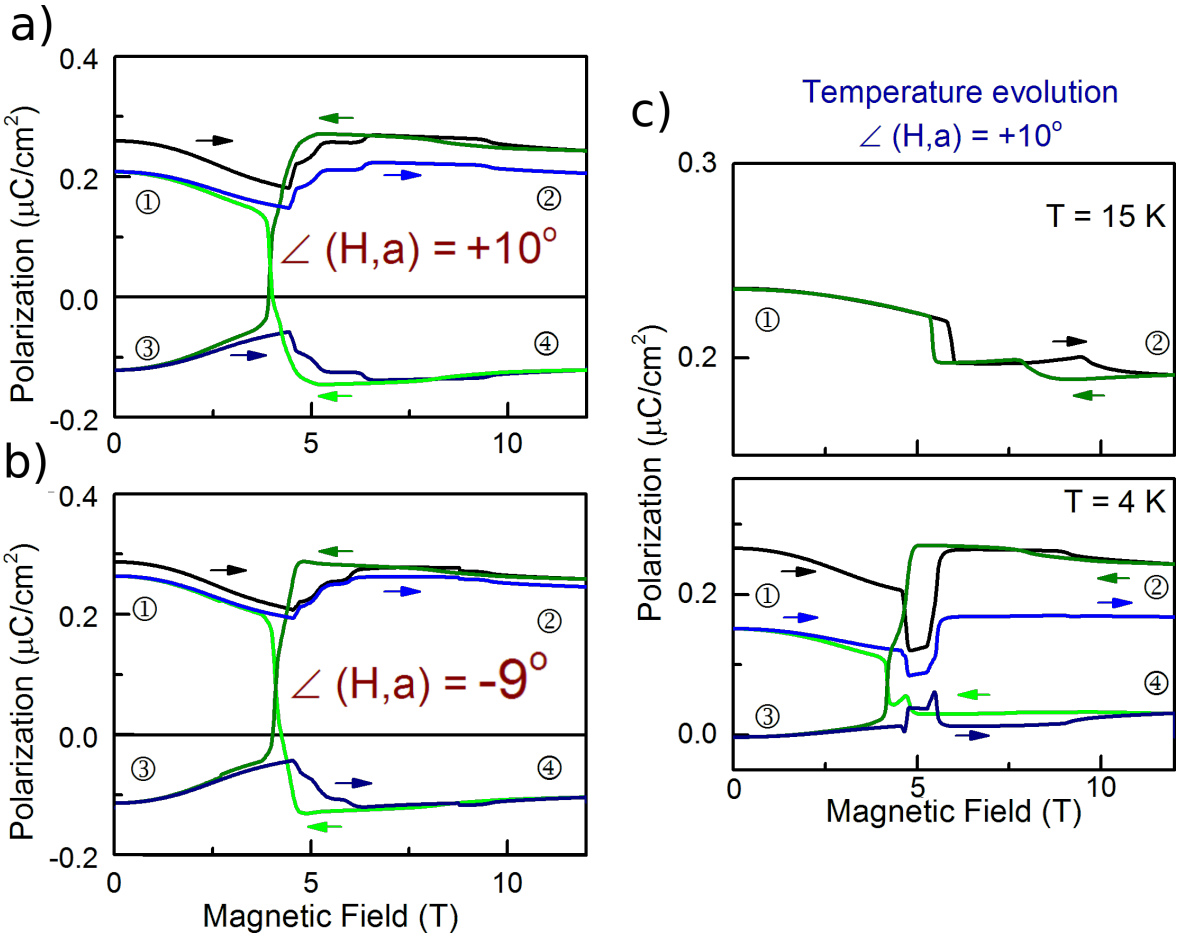

Figure 3.3: **Angle and temperature dependence of the four-state switching.** By comparing panels (a) and (b) we can see that changing the sign of the field angle ϕ_H does not influence the four-state switching. c) Temperature dependence of the hysteresis loop at the magic angle. Above 4 K (upper panel) the more usual two-state hysteresis loop is observed, whereas below 4 K (lower panel) the four-state behavior starts to arise. The states, colors, and arrows are indicated in the same way as in Fig. 3.2.

Turning back to the results shown in Fig. 3.2, we can observe that the switching behavior changes significantly with ϕ_H. In the high angle case, showcased in panel (c), we can observe a two-state switching loop, in which P_b does not vary much but a clear jump appears around a field magnitude of 5 T. This signals a sudden change in the magnetic configuration of the system since P_b is a direct result of it. The most peculiar, and completely novel, behavior can be found around the magic angle $\phi_H \sim 9°$ in panel (b) of Fig. 3.2. During the up-down-up-down field sweeps, we find that four different states are visited sequentially in this switching regime, with four different values of P_b.

At this stage, we would like to draw the attention of the reader to two facts.

First, compared to the usual magnetoelectric switching with one low field state and one high field state, here a single up–down cycle of the field reverses the polarization, and correspondingly leads to a different final state. In order to return the system to its original configuration another up–down cycle is required.

Second, this four-state loop is fully deterministic, meaning that when multiple such double cycles are applied, the system tracks close to the same P_b loop every time.

If we ignore for a brief moment the low-angle behavior displayed in the left panel of Fig. 3.2(a), and replace it with the behavior on the right [65], i.e. following the 1–4 branch in panel (b), we can imagine the four-state switching as an interpolation between the high and low angle switching regimes. This is a very important observation and will lead to one of the main results of this work: the topological nature of the magnetoelectric switching in this material.

Turning now to the measurements displayed in Fig. 3.3, we find that the four-state loop is not affected by a sign change of ϕ_H (compare panels (a,b)). From the two panels in (c), displaying measurements at 15 K and 4 K with ϕ_H along the magic angle, we can observe that the four-state hysteresis loop only appears at low temperatures. For higher temperatures, a more usual two-state loop is found, similar to the high angle loop in panel (c) of Fig. 3.2.

To conclude this Section, we would like to point out that we focus on the overall switching behavior, i.e. we ignore the details that can be found by careful study of the P_b graphs. For example, in Fig. 3.2(b) one can observe three distinct steps that appear around 5 T during the 1→2 and 3→4 switching. These steps are, however, absent at the same field magnitude, when the system is on the 2→3 and 4→1 branch. Their origin might be related to the spins in the Mn chains rotating individually, rather than in unison as we will assume in our model. Further research is required to solidify this statement, here we rather choose to focus on unraveling the main behavior of the four-state loop flanked in ϕ_H parameter space by two more usual two-state switching loops.

3.4 Theory

In order to describe the puzzling experimental observations, we construct a semi-classical model with eight Gd spins denoting the eight sublattice magnetizations and two AFM order parameters that describe the Mn chains. The Gd spins are described by unit vectors $\boldsymbol{S}_i, i = 1..8$, and we denote the two AFM order parameters as $\boldsymbol{L}_\alpha, \alpha = 1, 2$ (also unit vectors). See Fig 3.1(a) for further details. Furthermore, the ferroelectric polarization is represented by the slave order parameter P_b. Using a single $\boldsymbol{L}_\alpha$ to describe the orientation of all the Mn ions in a chain assumes that their spins are perfectly AFM ordered, i.e. $\boldsymbol{S}_i = \boldsymbol{L}, \boldsymbol{S}_{i+1} = -\boldsymbol{L}$. This simplification is justified by the large intrachain AFM exchanges, compared with the relatively small exchanges between the two chains [80].

A further simplification we adopt here is to confine all spins to the *ab*-plane. Indeed, it was shown experimentally that the *c*-direction acts as the magnetic hard-axis, and that the magnetic order is repeated along the crystalline *c*-direction [65]. This lowers the dimensionality of the problem from 3D to 2D, with a single angle for every Gd spin and Mn chain as the remaining degrees of freedom, thus greatly simplifying the numerical complexity. Since all spins and AFM order parameters are taken as unit vectors, their sizes are implicitly included in the model parameters.

The first step in order to derive the effective Hamiltonian in terms of the above order parameters is to convert the microscopic interactions of the individual Mn spins into the effective interactions of the $\boldsymbol{L}_\alpha$. More specifically, we include two energy contributions due to small spin cantings away from the perfect collinear intrachain spin configuration, as showcased in Fig. 3.4.

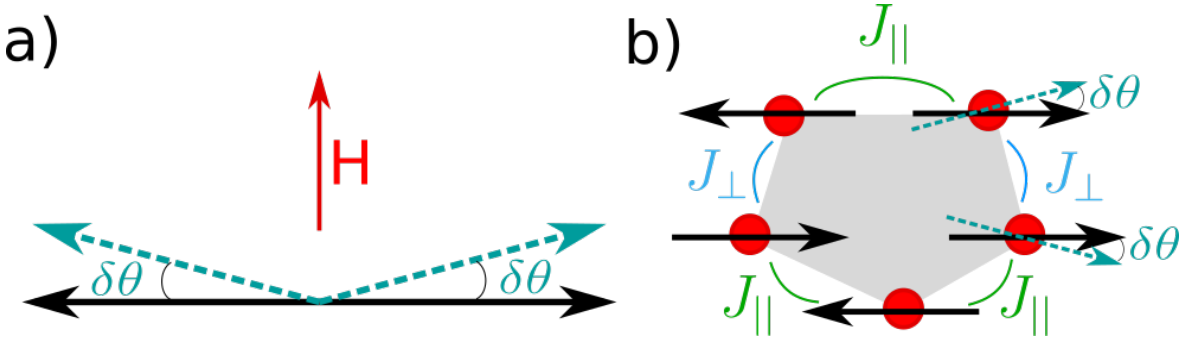

Figure 3.4: **Energy contributions due to spin canting.** a) The Zeeman contribution due to the weak ferromagnetic moment along the field (H, red arrow), as a result of the spin canting. b) The contribution due to Heisenberg exchange when previously parallel Mn spins are canted towards a more AFM alignment. This is a direct result of the geometric frustration. The collinear configuration is denoted by the black arrows, with the dashed teal arrows showing the orientation due to the slight canting by the angle $\delta\theta$.

Starting with the contribution due to the Zeeman energy when a magnetic field $\boldsymbol{H}$ is applied, we can write:

$$E_Z = -g\mu_B \boldsymbol{H} \cdot (\boldsymbol{\sigma}_i + \boldsymbol{\sigma}_{i+1}), \tag{3.7}$$

where $g \approx 2$, μ_B denotes the Bohr magneton, and $\boldsymbol{\sigma}_i$ and $\boldsymbol{\sigma}_{i+1}$ two neighboring Mn spins inside a chain. Obviously, no energy gain is possible for perfectly antiparallel spins since then $(\boldsymbol{\sigma}_i + \boldsymbol{\sigma}_{i+1}) = 0$.

However, if the chain is oriented perpendicular to the applied field, and both spins cant slightly towards the applied field, a weak ferromagnetic moment is created that will couple to this field (see Fig. 3.4(a)). To include this contribution, we perform an expansion in the small canting angle $\delta\theta$ away from the collinear configuration:

$$\begin{aligned} E &= J_{||}\boldsymbol{\sigma}_i \cdot \boldsymbol{\sigma}_{i+1} - g\mu_B \boldsymbol{H} \cdot (\boldsymbol{\sigma}_i + \boldsymbol{\sigma}_{i+1}) \\ &\approx J_{||}\cos(2\delta\theta) - g\mu_B H\left[\cos(\theta_L - \theta_H + \delta\theta) + \cos(\theta_L + \pi - \theta_H - \delta\theta)\right] \\ &= J_{||}\left(1 + 2\delta\theta^2\right) - 2g\mu_B H \sin(\theta_L - \theta_H)\delta\theta, \end{aligned} \tag{3.8}$$

where $J_{||}$ denotes the intrachain magnetic exchange coefficient, and θ_L (θ_H) the angle between L (H) and the a-axis. Minimizing with respect to $\delta\theta$ then leads to

$$\frac{\partial E}{\partial \delta\theta} = 0 = 4J_{||}\delta\theta - 2g\mu_B H \sin(\theta_L - \theta_H) \tag{3.9}$$

$$\Leftrightarrow$$

$$\delta\theta = \frac{g\mu_B H \sin(\theta_L - \theta_H)}{2J_{||}}. \tag{3.10}$$

Inserting this expression for $\delta\theta$ back into Eq. (3.8), and keeping only the first-order terms, we obtain the following expression for the Zeeman contribution through spin canting:

$$E_Z = -\frac{g^2\mu_B^2 H^2 \sin(\theta_L - \theta_H)^2}{J_{||}} = -\frac{g^2\mu_B^2 H^2 \left(1 - \cos(\theta_L - \theta_H)^2\right)}{J_{||}}$$
$$= \frac{g^2\mu_B^2}{J_{||}} \left((\boldsymbol{H} \cdot \boldsymbol{L})^2 - H^2\right). \tag{3.11}$$

This energy gain is maximized when $\boldsymbol{L}$ is oriented perpendicular to $\boldsymbol{H}$ leading to $\boldsymbol{L} \cdot \boldsymbol{H} = 0$, which is exactly what happens in the well-known spin-flop transition. If a strong enough magnetic field is applied along the easy-axis of a system with a single AFM order parameter, a sudden flip of the spins perpendicular to the easy-axis will occur as soon as the possible gain from the Zeeman energy (3.11) in the flopped state overcomes the lost easy-axis anisotropy energy. This spin-flopped state, with the AFM order perpendicular to $\boldsymbol{H}$, is exactly the one displayed in Fig. 3.4(a).

An additional energy contribution results from the geometric frustration which forces certain spins in the two chains to be parallel to each other, as shown by the two rightmost arrows in Fig. 3.4(b). This is very unfavorable for the interchain AFM exchange with coefficient $J_\perp$, again leading to some gained energy if these spins cant slightly towards a more AFM alignment.

Adopting a similar strategy as above, this contribution can be derived starting from

$$E_{ic} = J_{||}(\boldsymbol{\sigma}_{1,i} \cdot \boldsymbol{\sigma}_{1,i+1} + \boldsymbol{\sigma}_{2,i} \cdot \boldsymbol{\sigma}_{2,i+1}) + J_\perp(\boldsymbol{\sigma}_{1,i+1} \cdot \boldsymbol{\sigma}_{2,i+1}) \tag{3.12}$$
$$\approx 2J_{||}\cos(\delta\theta) + J_\perp\left(\cos(\theta_1 + \delta\theta - \theta_2) - \cos(\theta_1 - \theta_2 - \delta\theta)\right), \tag{3.13}$$

where $\boldsymbol{\sigma}_{\alpha,i}$ denotes the ith spin of chain $\boldsymbol{L}_\alpha$, and θ_1 (θ_2) signifies the angle w.r.t. the a-axis of $\boldsymbol{L}_1$ ($\boldsymbol{L}_2$). Expanding again to second order leads to:

$$E_{ic} = 2J_{||}(1 + \delta\theta^2) - 2J_\perp \sin(\theta_1 - \theta_2)\delta\theta. \tag{3.14}$$

Minimizing this contribution with respect to $\delta\theta$, leads to:

$$\delta\theta = \frac{J_\perp}{2J_{||}} \sin(\theta_1 - \theta_2). \tag{3.15}$$

Substituting this expression for $\delta\theta$ into Eq. (3.14), and keeping only terms up to first order in $\frac{J_\perp^2}{J_{||}}$ since it is assumed that $J_\perp << J_{||}$, nets us the final expression for this energy contribution:

$$E_{ic} = -\frac{J_\perp^2}{J_{||}} \sin(\theta_1 - \theta_2)^2 = \frac{J_\perp^2}{J_{||}}(\cos(\theta_1 - \theta_2) - 1) = \frac{J_\perp^2}{J_{||}}(\boldsymbol{L}_1 \cdot \boldsymbol{L}_2)^2 - \frac{J_\perp^2}{J_{||}}, \tag{3.16}$$

where the last contribution is a constant, merely causing a shift in the energy, and can thus be omitted in our numerical simulations. The maximum gain in energy ($\frac{J_\perp^2}{J_{||}}$) is achieved when the chains are oriented perpendicular to each other ($\boldsymbol{L}_1 \cdot \boldsymbol{L}_2 = 0$).

These two contributions (Zeeman and Heisenberg exchange) compete with each other, and with the easy-axis anisotropy energy

$$E_{ea} = -K_L \sum_{\alpha} (\boldsymbol{L}_\alpha \cdot \boldsymbol{n}_\alpha)^2, \tag{3.17}$$

where K_L denotes the strength of the easy-axis anisotropy, and $\boldsymbol{n}_\alpha$ denote the orientation of the easy axes: $\boldsymbol{n}_1 = (\cos\theta_n, \sin\theta_n)$ and $\boldsymbol{n}_2 = (\cos\theta_n, -\sin\theta_n)$ with $\theta_n = 23.4°$. These are the fourfold axes of the pyramidally coordinated Mn ions, aligned with the long edges of the cyan chains in Fig. 3.1(a).

Bringing everything together leads us to the total contribution of the chains to the effective Hamiltonian:

$$H_L = \gamma(\boldsymbol{L}_1 \cdot \boldsymbol{L}_2)^2 + \sum_{\alpha} \chi((\boldsymbol{H} \cdot \boldsymbol{L}_\alpha)^2 - H^2) - K_L \sum_{\alpha} (\boldsymbol{L}_\alpha \cdot \boldsymbol{n}_\alpha)^2, \tag{3.18}$$

with $\gamma = \frac{J_\perp^2}{J_{||}}$, and $\chi = \frac{g^2\mu_B^2}{J_{||}}$.

The next step is to find the combination of cross-order coupling terms between the Gd spins ($\boldsymbol{S}_i$) and the chains ($\boldsymbol{L}_\alpha$) that transform as the unit representation of the symmetry group of the system. This combination will then lead to the required invariance of the energy under the applications of all the symmetry operations of the system. In order to achieve this, we first list the generators of the paramagnetic parent P*bam* phase:

$$I : (x, y, z) \to (-x, -y, -z) \tag{3.19}$$

$$2_z : (x, y, z) \to (-x, -y, z) \tag{3.20}$$

$$2_y : (x, y, z) \to (\frac{1}{2} - x, \frac{1}{2} + y, z) \tag{3.21}$$

I and 2_z are the same symmetry operations in the 2D case we are solving. Next, a doubling of the unit cell is necessary to fit the overall AFM state, leading to an additional symmetry operation for the translation along the a-axis $a : (x, y, z) \to (x + a, y, z)$ (not taking spins into account), and a halving of the x-component of the fractional translation $2_y : (x, y, z) \to (\frac{1}{4} - x, \frac{1}{2} + y, z)$. In effect, applying these symmetry operations to the degrees of freedom of our model, and bearing in mind the spin flip when transforming the chains between the two halves of the magnetic unit cell, leads to the following transformation table: We start with the Heisenberg exchange

	S_1	S_2	S_3	S_4	S_5	S_6	S_7	S_8	L_1	L_2	P_b
I	S_8	S_7	S_6	S_5	S_4	S_3	S_2	S_1	-L_1	L_2	-P_b
2_y	S_4	S_3	S_2	S_1	S_8	S_7	S_6	S_5	L_1	L_2	P_b
a	S_5	S_6	S_7	S_8	S_1	S_2	S_3	S_4	-L_1	-L_2	P_b
T	$-S_5$	$-S_6$	$-S_7$	$-S_8$	$-S_1$	$-S_2$	$-S_3$	$-S_4$	-L_1	-L_2	P_b

Table 3.1: **Symmetry operations in $GdMn_2O_5$.** Transformations of Gd spins (S_i), AFM vectors ($\boldsymbol{L}_\alpha$) and polarization (P_b) under the symmetry operations of $GdMn_2O_5$.

terms between the Gd spins ($\boldsymbol{S}_i$) and the Mn chains ($\boldsymbol{L}_1$ and $\boldsymbol{L}_2$), with the effective exchange constants v_1 and v_2. The former (latter) couples each Gd spin with the chain that harbors the closest (furthest) Mn ion. See the orange arrows in Fig. 3.1(a) for a schematic depiction of these exchange paths. Starting from terms with $\boldsymbol{S}_1$ and $\boldsymbol{S}_2$, and taking the above table of transformations into account, we can identify the following sets of terms:

$$\begin{aligned}
&\boldsymbol{S}_1 \cdot (v_1\boldsymbol{L}_2 + v_2\boldsymbol{L}_1) \xrightarrow{I} \boldsymbol{S_8} \cdot (v_1\boldsymbol{L}_2 - v_2\boldsymbol{L}_1) \xrightarrow{a} \boldsymbol{S_4} \cdot (-v_1\boldsymbol{L}_2 + v_2\boldsymbol{L}_1) \xrightarrow{I} \boldsymbol{S_5} \cdot (-v_1\boldsymbol{L}_2 - v_2\boldsymbol{L}_1),\\
&\boldsymbol{S}_2 \cdot (v_1\boldsymbol{L}_1 + v_2\boldsymbol{L}_2) \xrightarrow{I} \boldsymbol{S_7} \cdot (-v_1\boldsymbol{L}_1 + v_2\boldsymbol{L}_2) \xrightarrow{a} \boldsymbol{S_3} \cdot (v_1\boldsymbol{L}_1 - v_2\boldsymbol{L}_2) \xrightarrow{I} \boldsymbol{S_6} \cdot (-v_1\boldsymbol{L}_1 - v_2\boldsymbol{L}_2).
\end{aligned} \tag{3.22}$$

The combined sum of them transforms according to the identity representation, leading to the following contribution to the total Hamiltonian:

$$\begin{aligned}
H_{LS} =&(\boldsymbol{S}_1 - \boldsymbol{S}_5) \cdot (v_1\boldsymbol{L}_2 + v_2\boldsymbol{L}_1) + (\boldsymbol{S}_2 - \boldsymbol{S}_6) \cdot (v_1\boldsymbol{L}_1 + v_2\boldsymbol{L}_2) +\\
&(\boldsymbol{S}_3 - \boldsymbol{S}_7) \cdot (v_1\boldsymbol{L}_1 - v_2\boldsymbol{L}_2) + (\boldsymbol{S}_4 - \boldsymbol{S}_8) \cdot (-v_1\boldsymbol{L}_2 + v_2\boldsymbol{L}_1).
\end{aligned} \tag{3.23}$$

A similar process can be applied starting from $P_b\,\boldsymbol{S_1} \cdot (\beta_2\boldsymbol{L}_1 + \beta_3\boldsymbol{L}_2)$ and $P_b\,\boldsymbol{S_2} \cdot (\beta_2\boldsymbol{L}_1 + \beta_3\boldsymbol{L}_2)$, which signify the symmetric Heisenberg exchange striction contributions to the Hamiltonian. This leads to:

$$\begin{aligned}
H_{P_b} =& - P_b[E_b + \beta_1(\boldsymbol{L}_1 \cdot \boldsymbol{L}_2) + (\boldsymbol{S}_1 - \boldsymbol{S}_5)(\beta_2\boldsymbol{L}_2 + \beta_3\boldsymbol{L}_1) + (\boldsymbol{S}_2 - \boldsymbol{S}_6)(\beta_2\boldsymbol{L}_1 + \beta_3\boldsymbol{L}_2)\\
&+ (\boldsymbol{S}_3 - \boldsymbol{S}_7)(\beta_2\boldsymbol{L}_2 - \beta_3\boldsymbol{L}_1) + (\boldsymbol{S}_4 - \boldsymbol{S}_8)(\beta_2\boldsymbol{L}_1 - \beta_3\boldsymbol{L}_2)],
\end{aligned} \tag{3.24}$$

where the facultative interaction of P_b with an external electric field E_b was also included. We can identify three final terms that originate purely from the Gd spins:

$$H_S = \frac{1}{2}(g\mu_B)^2 \sum_{i \neq j} \left(\frac{\boldsymbol{S}_i \cdot \boldsymbol{S}_j}{r_{ij}^3} - 3\frac{(\boldsymbol{S}_i \cdot \boldsymbol{r}_{ij})(\boldsymbol{S}_j \cdot \boldsymbol{r}_{ij})}{r_{ij}^5} \right) - \sum_i \left(K_S(\boldsymbol{N}_i \cdot \boldsymbol{S}_i)^2 + g\mu_{\mathrm{B}}\boldsymbol{H} \cdot \boldsymbol{S}_i \right). \tag{3.25}$$

The first describes the magneto-dipolar interaction between Gd spins, which could be relatively large due to the size of the Gd spins (nominally S=7/2) and relative proximity of the neighbors. In the numerical simulations, these interactions were restricted to their five nearest neighbors, including periodic images. Adding further neighbors did not lead to qualitative differences in the results. The term with K_S denotes the easy-axis anisotropy for the Gd ions, this time with anisotropy axes $\boldsymbol{N}_i$ which are unit vectors having alternating angles $\pm 12°$ to the a-axis. K_S is significantly smaller than K_L due to the isotropic environment and valence configuration of the Gd ions. The final term denotes the Zeeman energy of the Gd ions in the external magnetic field $\boldsymbol{H}$.

To conclude this Section, we gather all the terms in our effective Hamiltonian:

$$\begin{aligned} H = \gamma(\boldsymbol{L}_1 \cdot \boldsymbol{L}_2)^2 + \sum_\alpha \chi((\boldsymbol{H} \cdot \boldsymbol{L}_\alpha)^2 - H^2) \\ - K_L \sum_\alpha (\boldsymbol{L}_\alpha \cdot \boldsymbol{n}_\alpha)^2 - \sum_i \left(K_S (\boldsymbol{N}_i \cdot \boldsymbol{S}_i)^2 + g\mu_{\mathrm{B}} \boldsymbol{H} \cdot \boldsymbol{S}_i \right) \\ + \frac{1}{2}(g\mu_B)^2 \sum_{i \neq j} \left(\frac{\boldsymbol{S}_i \cdot \boldsymbol{S}_j}{r_{ij}^3} - 3\frac{(\boldsymbol{S}_i \cdot \boldsymbol{r}_{ij})(\boldsymbol{S}_j \cdot \boldsymbol{r}_{ij})}{r_{ij}^5} \right) \\ + \sum_{i,\alpha} V_{i\alpha} \boldsymbol{S}_i \cdot \boldsymbol{L}_\alpha \\ - P_b[8\beta_1(\boldsymbol{L}_1 \cdot \boldsymbol{L}_2) + (\boldsymbol{S}_1 - \boldsymbol{S}_5)(\beta_2 \boldsymbol{L}_2 + \beta_3 \boldsymbol{L}_1) \\ + (\boldsymbol{S}_2 - \boldsymbol{S}_6)(\beta_2 \boldsymbol{L}_1 + \beta_3 \boldsymbol{L}_2) + (\boldsymbol{S}_3 - \boldsymbol{S}_7)(\beta_2 \boldsymbol{L}_2 - \beta_3 \boldsymbol{L}_1) \\ + (\boldsymbol{S}_4 - \boldsymbol{S}_8)(\beta_2 \boldsymbol{L}_1 - \beta_3 \boldsymbol{L}_2)] + P_b^2/2. \end{aligned} \tag{3.26}$$

3.5 Methods

Before continuing with the results and a discussion of the physics, we comment briefly on the numerical aspects of our simulations used throughout the rest of this Chapter. The first question to address is what model parameters to use in conjunction with the Hamiltonian in Eq. (3.26). This is not particularly straightforward, since our model is phenomenological, and the order parameters and interactions arise from a combination of the microscopic ones. One could, instead, formulate a model in terms of all the microscopic degrees of freedom, i.e. all the spins of both Gd and Mn ions, which would not only lead to a more computationally demanding model, the increased complexity also makes developing an intuitive understanding much harder. That means that calculating the coefficients separately from first principles is very hard, if not impossible. Even in the case of a fully microscopic spin model, it is not well-known in general how to acquire a correct set of exchange parameters from DFT. We thus opted to rather make physically inspired initial guesses for the model parameters, after which we further refined these in order to best reproduce the experimental behavior.

We know, for example, that the Gd – Mn magnetic exchange parameter towards the closest chain is larger than towards the other ($v_1 > v_2$), and that the order of magnitude for this energy contribution is a few meV. Furthermore, as we mentioned a few times already, the single-ion anisotropy energy for Gd is expected to be small due to the isotropic environment and valence configuration with completely quenched orbital angular momentum. Instead, the single-ion anisotropy of the Mn ions and, by proxy, the chains, is again on the order of a few meV. Lastly, due to the large intrachain $J_{||}$ and small interchain $J_\perp$ magnetic exchanges, we know that $\gamma = \frac{J_\perp^2}{J_{||}}$ and $\chi = \frac{J_{||}}{g^2\mu_B^2}$ are very small.

Taking all these considerations into account, we found that the following model parameters reproduce the observations of the experiments well: $v_1 = 7.9$ meV, $v_2 = 0.15$ meV, $K_L = 1.1$ meV, $K_S = 0.09$ meV, $\gamma = 0.05$ meV, $\chi = 0.01$ meV^{-1}.

The parameters for the exchange striction were then also chosen to fit the experimental hysteresis loop as well as possible: $\beta_1 = 0.06\,\mu\mathrm{C/cm^2}$, $\beta_2 = 0.06\,\mu\mathrm{C/cm^2}$, $\beta_3 = 0.04\,\mu\mathrm{C/cm^2}$.

However, these parameters are by no means a requirement for the overarching behavior to appear in our model. As we will show in greater detail in the Section discussing the topological nature of the switching behavior 3.6.3, a great deal of freedom exists in choosing these parameters, if the only requirement is to reproduce the three switching regimes. This lies at the heart of our claim that this effect might exist in other materials since neither the model itself nor its parameters depend greatly on the microscopic details of $GdMn_2O_5$.

The next question is how to simulate the experimental set-up, which is, in contrast to the question about the model parameters, much easier to answer. Since the behavior only shows up at temperatures below ~ 4 K, is remarkably deterministic, and is a result of quasi-statically applied magnetic fields, we simulated it as a series of simple minimization problems. This entails taking one of the degenerate starting configurations, increasing the field by a small amount, minimizing the energy, applying a further increased field, and so on, thus tracking the local minimum at all steps. It is quite remarkable that performing this relatively simple process, purely based on optimizing the energetics of the system, leads to a faithful reproduction of the observed behavior, which is another indication of the topological nature of the switching behavior. As we will show more explicitly below, it is sort of an extreme variant of the behavior of Thouless charge pumps, and especially of their recent realization in ultra-cold gases [3, 81–85]. It is extreme in the sense that it requires no tunneling whatsoever, which forms the core reason behind the fully deterministic behavior.

We now turn to a discussion of the results obtained from these simulations of the effective spin Hamiltonian Eq. (3.26).

3.6 Results and discussion

The magnetoelectric switching regimes of P_b obtained from the simulations, are showcased in Fig. 3.5, displaying the same three regimes as the experimental results in Figure 3.2. Comparing the two figures demonstrates the close agreement between the two.[3]. The insets in each panel of Fig. 3.5 depict schematically the sequence of states that are visited by the system during the field sweeps.

As mentioned before, it appears that the magic angle regime (Fig. 3.5(b)) is an interpolation between the low and high angle regimes. At the start, it follows the high angle behavior moving 1→2, mimicking the low angle behavior then results in a reversal of the polarization on the 2→3 branch, followed by an inversion symmetry partner of the high angle regime moving 3→4 and finally another low angle-like reversal of the polarization, bringing the system from state 4 back to the initial state 1.

To gain a deeper understanding of this peculiar behavior, we focus first on the energetics of the model, as calculated by the simulations. The intricacies of the energetics are ultimately what results in the deterministic, unidirectional, switching of the

[3] We compare the low angle regime with the right-hand side of Fig. 3.2(a).

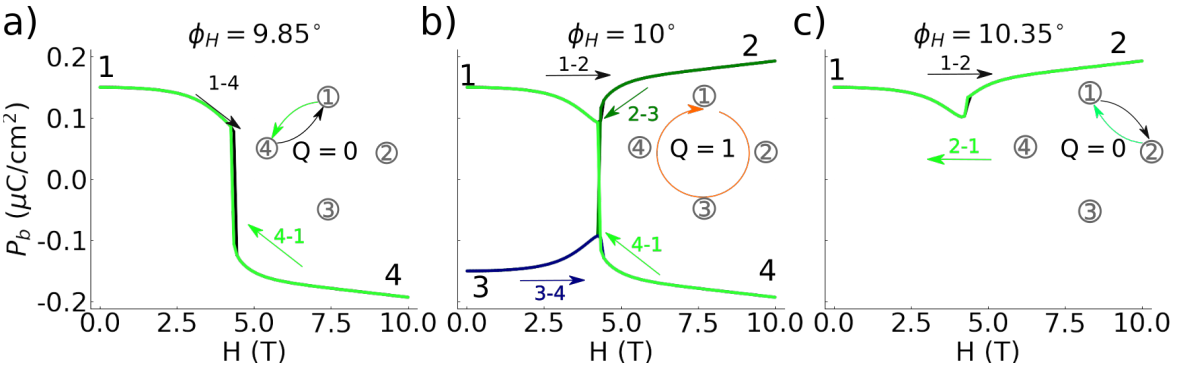

Figure 3.5: **Simulation of the angle dependent magnetoelectric switching.** The evolution of ferroelectric polarization P_b during the magnetic field sweep cycle is depicted for the low (a), magic (b), and high (c) angle regimes. In each panel, the four-states and field cycle progression are marked in the same way as in Fig 3.2. The four-states hysteresis loop is observed for the field at the magic orientation in panel (b). The insets indicate the sequence of states visited during the cycle for each regime and winding numbers (see Section 3.6.3 for further details on the latter).

system.

3.6.1 Energetics

Before continuing, let us take a moment to recall some of the symmetries of the system, whose transformation properties were listed in Tab. 3.1 during the construction of the Hamiltonian. We focus on how the transformations due to inversion (I) and time-reversal (T) symmetry relate the angles of $\boldsymbol{L}_1$ and $\boldsymbol{L}_2$ ($\phi_{\boldsymbol{L}_1}$ and $\phi_{\boldsymbol{L}_2}$). The energy surfaces in terms of the angles are depicted in Fig. 3.6, for a varying field with strength $|H|$ and angle $\phi_H = +10°$. We observe that there are four degenerate energy minima, a result of the breaking of both T and I symmetries in the low-temperature phase. The angles ϕ_{L_1} and ϕ_{L_2}, that describe in part the state of the system, can be transformed into each other through the relations:

$$I: \quad (\phi_{L_1}, \phi_{L_2}) \to (\phi_{L_1} + \pi, \phi_{L_2}), \tag{3.27}$$

$$T: \quad (\phi_{L_1}, \phi_{L_2}) \to (\phi_{L_1} + \pi, \phi_{L_2} + \pi). \tag{3.28}$$

These symmetry operations are indicated by the black arrows in the top-left and bottom right panels of Fig. 3.6.

When the strength of the magnetic field increases, we see that two long vertical "valleys" appear along the ϕ_{L_1}-direction of the energy surface, separated by π along ϕ_{L_2}. We focus on the case where the initial state of the system corresponds to the top-left minimum, indicated by the bright white dot in the top-left panel, and a single up–down field sweep is applied. Following its trajectory, indicated by the shaded white lines, we find that the system first flows from the original minimum to the one that is related by inversion symmetry. This has rotated ϕ_{L_1} by π, while leaving ϕ_{L_2} unchanged. Through the $\boldsymbol{L}_1 \cdot \boldsymbol{L}_2$ part of the exchange striction, this causes the reversal of P_b, which

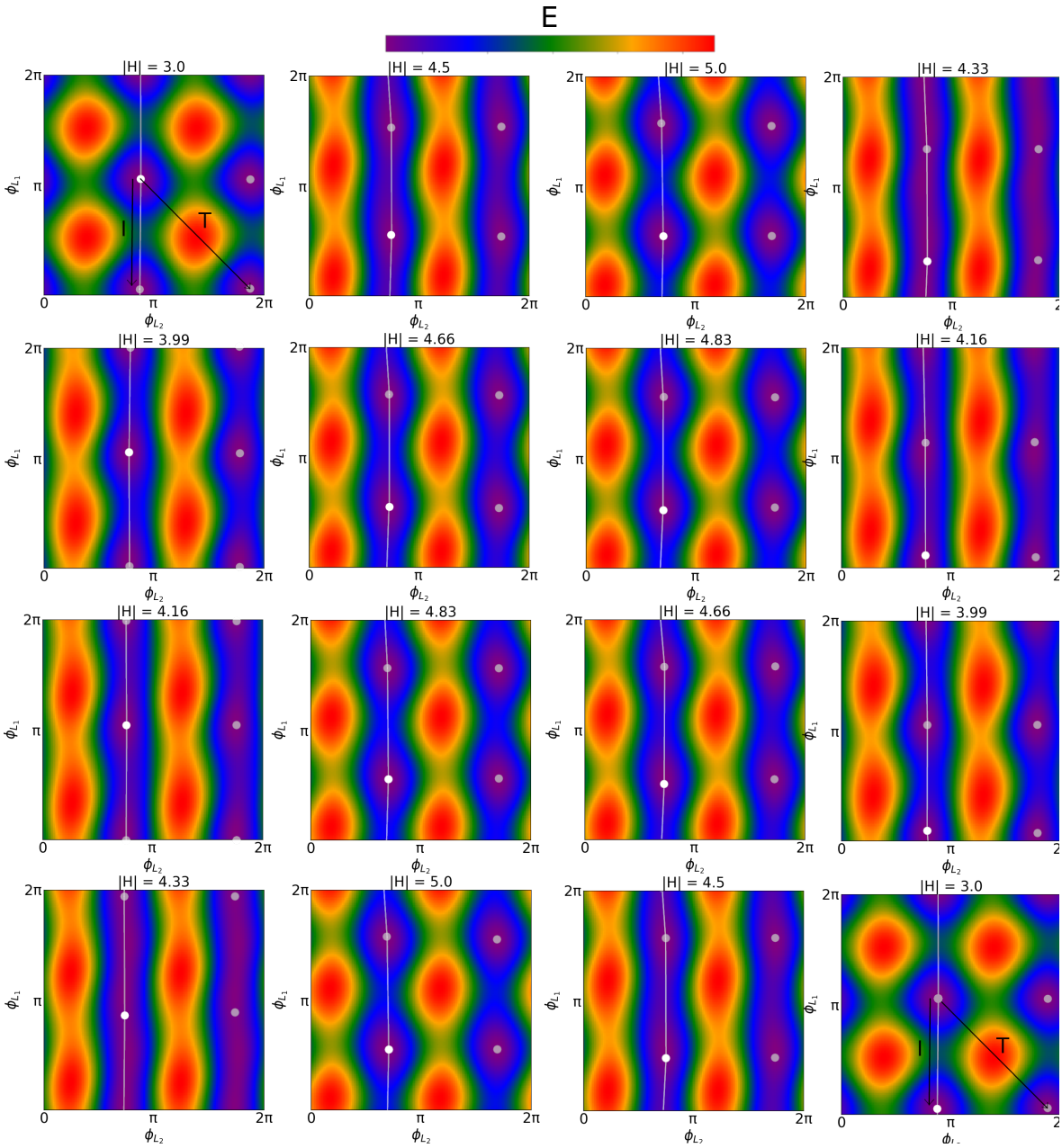

Figure 3.6: **Energy surfaces in terms of (ϕ_{L_1}, ϕ_{L_2}) for $\phi_H = +10°$.** The shaded dots denote the four degenerate minima, related by time-reversal (T) and inversion (I) symmetry operations indicated by the black arrows. The full white dot corresponds to the example situation discussed in the main text. An indication of its trajectory during a double up–down field sweep is given by the shaded lines.

is consistent with the inversion symmetry operation. The process we have described here corresponds to the first up–down cycle of the P_b plot of Fig. 3.5(b), i.e. the one that leads to the 1→2→3 branch.

As it turns out when the field is swept up and down a second time, the state progresses through the valley in the same direction, i.e. downwards through the edge

at the bottom of the window, reappearing at the top, and finally landing in the original top-left minimum (see Fig. 3.6). This corresponds to the 3→4→1 branch of Fig. 3.5(b).

The sequence of states visited during this double up–down cycle of the field at $\phi_H = 10°$, constitutes half of the possible configurations of the system (two low field and two high field states). The other half is related to the first by time-reversal symmetry as indicated by the diagonal black arrow in the top-left and bottom right panels of Fig. 3.6. A similar trajectory through this valley on the right-hand side of the energy surface would be followed if the initial state was in one of the two zero-field minima it harbors. We can thus conclude that the up–down cycling of the magnetic field at $\phi_H = 10°$ does not allow for a transition between the two valleys, and ϕ_{L_2} changes very little during the cycling process.

From these considerations, it seems that no such unidirectional trajectory is followed in the two-state regimes (Fig.3.5(a, c)) at low or high field angle ϕ_H. This is rather puzzling since one would imagine that the minima behave in a similar way as in Fig. 3.6 since they are required to obey the same symmetries.

In fact, they do.

However, and this is the crux of the matter, the barriers between the minima do not. As it turns out, there are no symmetries that relate the barriers that flank a minimum from either side, allowing them to change asymmetrically. From our observations, it is the field angle ϕ_H that influences these asymmetric barriers, ultimately resulting in the three different switching regimes.

We thus turn to a more careful investigation of the barriers, first by studying the results of Nudged Elastic Band simulations, displayed in Fig. 3.7, followed by a simple theoretical argument.

The Nudged Elastic Band calculations are a way to track how the low points of the valley in Fig. 3.6 change for different field strengths. This is done by taking two extremal states, then constructing a set of images that interpolate in configuraion space between these two states. The total energy of the entire chain is then optimized using a small elastic-like energy term that binds the images together, so that they find the lowest energy barrier between the two states. Similar to the previous discussion, we track the evolution of the system starting in state 1, indicated at the far left of Fig. 3.7(a). In the following we use ij to denote the energy barrier between states i and j.

As the field increases (color change and vertical shift) the local minimum around state 1 becomes metastable when barrier 12 between state 1 and 2 vanishes, moving the system towards state 2. Notice that the barrier between 14 is still present at that point. When the field is subsequently lowered, barrier 23 lowers faster than 12, causing the system to progress to state 3. A similar process then brings state 3→4→1 during the next up–down field sweep, since barriers 34 and 12 (14 and 23) are related by the inversion transformation and $E_{34} = E_{12}$ ($E_{41} = E_{23}$) (see the effect of I in Fig. 3.6 for a visual confirmation of this statement). From this analysis, it is clear that indeed the barriers evolve asymmetrically when the field changes. This is not surprising seen as the states at the top of the barriers[4] that flank a given minimum are in no way related

[4]They are an interpolation between the states on either side of the barrier.

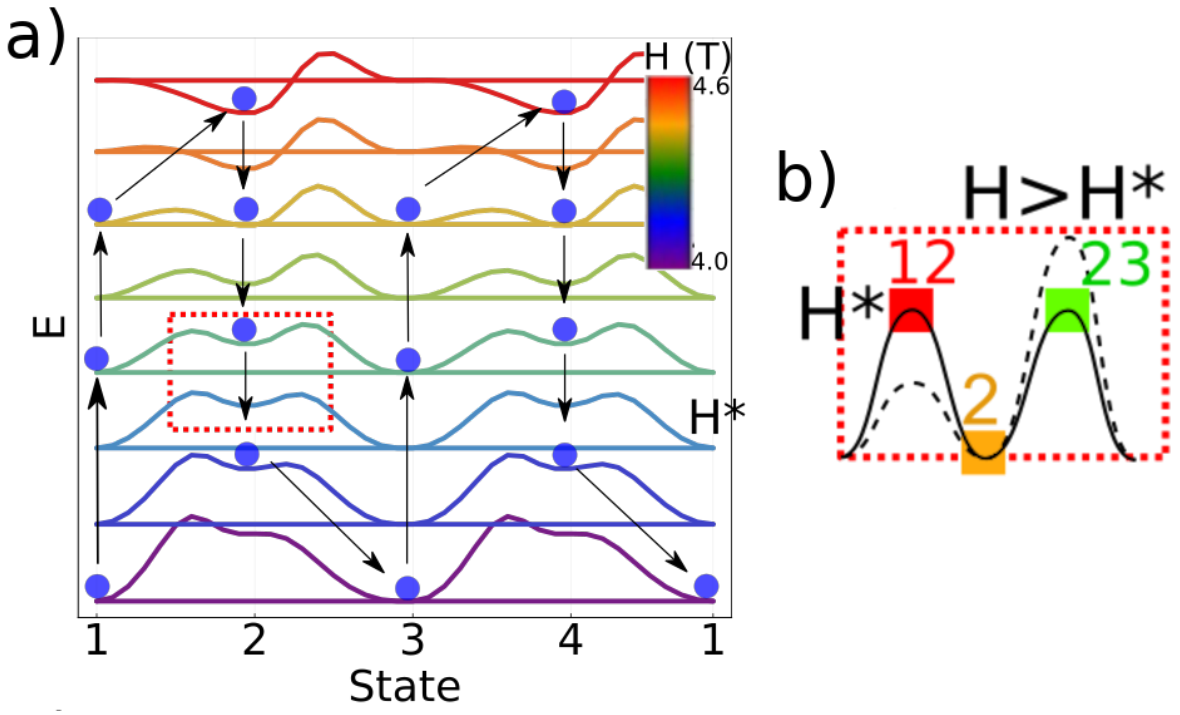

Figure 3.7: **Nudged Elastic Bands calculation.** a) Evolution of transition barriers between states 1, 2, 3, 4 as the magnetic field is swept through the hysteresis region at $\phi_H = 10°$. The plots are shifted vertically, and the model parameters were slightly altered for clarity which increases the width of the hysteresis region. The curve colors encode the corresponding magnetic field strength. The blue circles and arrows show the trajectory of the energy minimum during the field sweeps. b) Zoom of the corresponding dashed red box in panel (a), showing the asymmetric evolution of barrier 12 between states 2 and 1, and 23 between states 2 and 3, around the critical field H^* where the barriers are of equal height. The dashed black curve shows an example of the asymmetric barrier evolution discussed in the main text.

by symmetry.

Interestingly, this evolution of the potential energy surface is equivalent to that of a Thouless charge pump, in particular, the one induced by circular motion in the two-dimensional parameter space of the Rice-Mele model [81] recently realized in ultra-cold gases [3, 84, 85].

Combining the demonstration of the asymmetric evolution of the barriers in Fig. 3.7, with the earlier discussion on the energy surfaces shown in Fig. 3.6, leads us to the following conclusion, visualized in Fig. 3.8. For a system starting at state 1, if the field is applied at a low angle, the barrier between states 1 and 4 is always lower than the one between states 1 and 2, leading to a 1→4→1 sequence as in Fig. 3.5(a) and 3.8(a). Conversely, when the field is applied at a high angle, the barrier towards state 2 is always lower than the one towards state 4, leading to the 1→2→1 toggling shown in Fig. 3.5(c) and 3.8(c). There then has to exist a crossover angle where a combination of the two appears, leading in this case to the unidirectional cycling between 1→2→3→4 as depicted in Figs. 3.5(b), 3.8(b), and more detailed in Figs. 3.6, and 3.7(a).

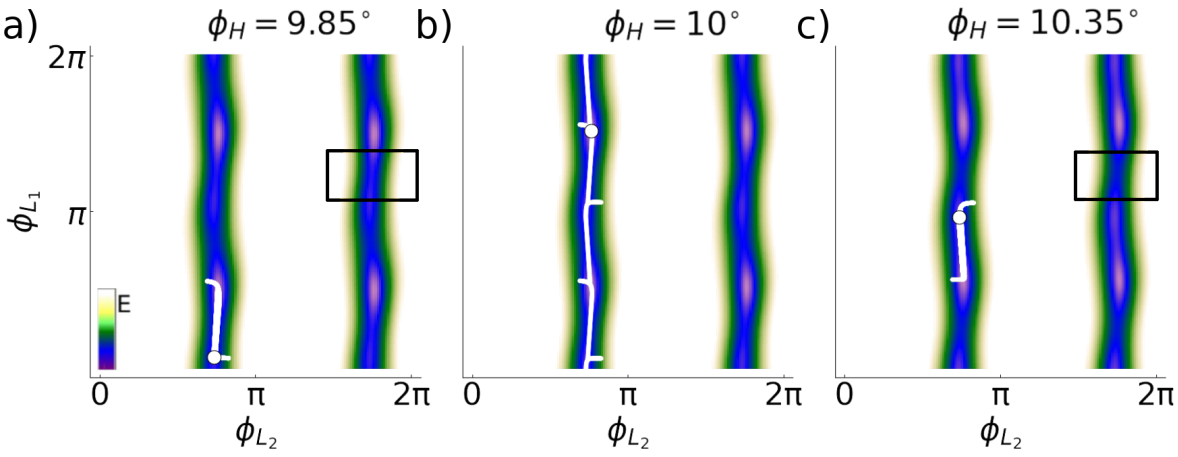

Figure 3.8: **Angle dependence of the trajectory through (ϕ_{L_1}, ϕ_{L_2}) space.** The trajectories of the system through (ϕ_{L_1}, ϕ_{L_2}) space during the field sweep cycle are displayed in white for the low, magic and high angle regimes in panels (a),(b) and (c), respectively. The background color maps display the energy landscape at a field strength chosen to highlight the differences between the three regimes (see the black box for a demonstration of the different barrier heights).

To hint at the origin of the asymmetric barrier evolution from a theoretical point of view, we can perform a simple Taylor expansion for the barrier energies 12, 23 at a field strength H^* when $E_{12} = E_{23}$, as depicted in Fig. 3.7(b). This can be written as,

$$E(H) = E(H^*) + \left.\frac{\partial E}{\partial H}\right|_{H=H^*} (H - H^*). \tag{3.29}$$

Filling in $\frac{\partial E}{\partial H} = -M$, and subtracting the expressions for both barriers, we find:

$$E_{12}(H) - E_{23}(H) = (M_{23} - M_{12})(H - H^*), \tag{3.30}$$

where M_{ij} denotes the value of the total magnetization for the state at barrier ij. This suggests that in the case of $\phi_H = 10^\circ$ we have been discussing so far, $M_{23} < M_{12}$, which is confirmed by our simulations. Indeed, starting at state 2, when $H < H^*$ as the field decreases, this leads to $E_{23} < E_{12}$ causing the system to move from state 2 to state 3.

3.6.2 Magnetic configuration

Now that we have a firm grasp on the energetics of the problem, we turn to an investigation of the behavior of the spins that results from it. Again, we focus first on the most interesting situation of the magic angle regime at $\phi_H = 10^\circ$. The magnetic configurations for the four-states that are sequentially visited are shown in Fig. 3.9. In the low field states 1 and 3, Mn spins align closely with the anisotropy axes of the two chains. The Gd spins (green) align in largely antiferromagnetically with the closest Mn ion (purple) of the chain that they are most strongly coupled to (v_1 in Fig. 3.1(a)). This causes a roughly left–left–right–right sequence of the Gd spins along the a-axis at low field.

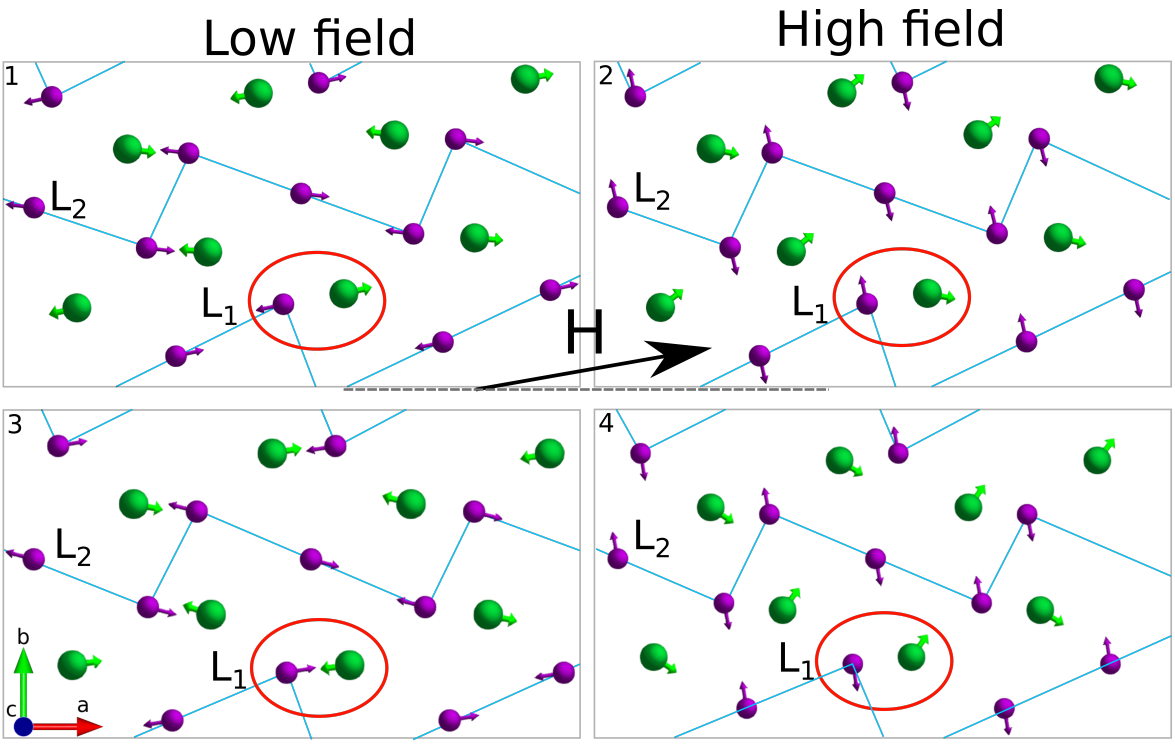

Figure 3.9: **Magnetic configurations at $\phi_H = 10°$.** The configurations corresponding to the four-states are labeled by the numbers in the top-left corner of each panel. Gd ions are displayed in green, Mn in purple. The cyan lines highlight the orientation of the chains. An Mn ion of chain L_1 and neighboring Gd ion are highlighted by the red ellipse to demonstrate the 360° rotation in 90° increments.

In the high field states 2 and 4, Mn spins are nearly orthogonal to the magnetic field, in order to maximize the gain on Zeeman energy (see Eq. (3.11)). The Gd spins, in this case, are again influenced mostly by the antiferromagnetic exchange with the nearest Mn ion, but they are tilted towards the field due to the Zeeman interaction. The higher the strength of the applied field, the more will the Gd spins align with it.

As could already be deduced from our earlier discussion on the trajectory through the (ϕ_{L_1}, ϕ_{L_2}) space (Fig. 3.6), we can observe that the spins associated with $\boldsymbol{L}_1$ perform a unidirectional rotation during the up–down field sweeps. The Gd spins that are coupled strongest to this chain perform a similar rotational motion, but with less well-defined increments. Indeed, focusing on the highlighted spins in Fig. 3.9, we see that the chains rotate with increments of around 90° between the states, performing a full 360° rotation by the time they arrive back at the original configuration. This peculiar "crankshaft"-like behavior is a direct result of the evolution of the energy minima and barriers as discussed in the previous Section. We use this crankshaft analogy because the material seemingly converts the linear up–down motion of the magnetic field (the "piston") into the circular motion performed by the spins (the "driveshaft").

This brings us to the final remark we wish to make on the motion of the spins. By applying the field at a negative magic angle $\phi_H = -10°$, we find that $\boldsymbol{L}_2$ now

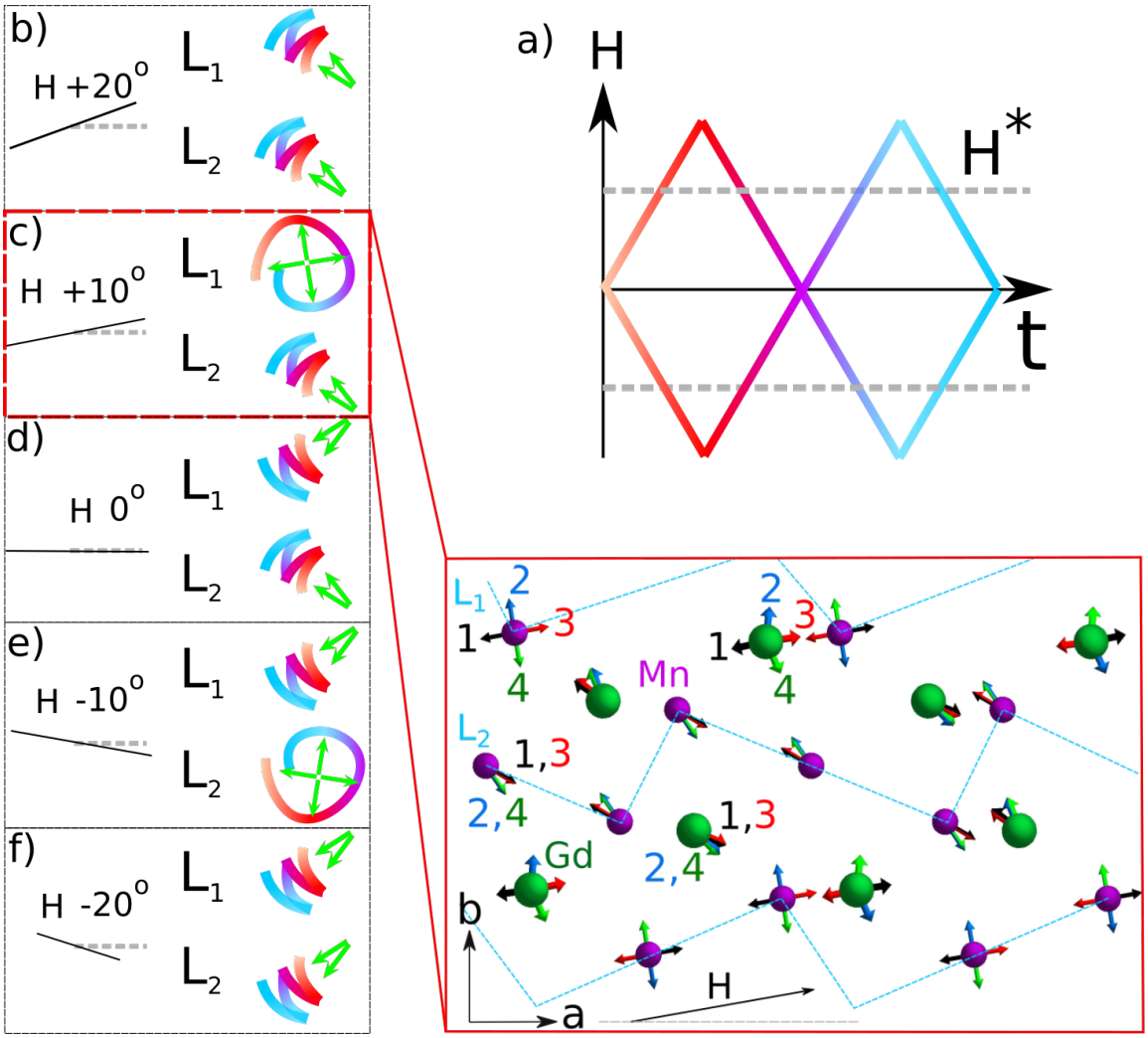

Figure 3.10: **Magnetic switching behavior for different magnetic field angles.** a) The time evolution of the magnetic field strength, where the color gradient encodes the time, corresponding to the color gradients found in the other panels. Two graphs are shown to indicate that the behaviors displayed in panels (b-f) does not depend on which of the branches is followed. The grey dotted line denotes the switching field. (b-f) The switching behavior of $\boldsymbol{L}_1$ and $\boldsymbol{L}_2$ for various angles of the applied magnetic field, ranging between +20° in (b) and -20° in (f). The green arrows denote the AFM order parameter orientations during the field sweep in (a), where the color gradients (red to blue) correspond to the same timing as shown in panel (a). The microscopic spin configuration of the magic angle regime in panel (c) is detailed in the right panel surrounded by the red square. Spin configurations (1, 2, 3, 4) are labeled as in Fig. 3.5(b). The full rotation is performed by the chain that is most parallel to the direction of the applied field.

performs the full cycle rotation, along with the Gd spins that it couples strongest with, leading to the same magnetoelectric hysteresis loop as for $\phi_H = 10°$ (compare panels (a,b) in Fig. 3.3). This behavior follows from another symmetry operation that is present in the system: the $\tilde{2}_x$ crystal symmetry combined with a translation by a, S_a,

under which $(L_1^x, L_1^y) \to (L_2^x, -L_2^y)$. In this case, horizontal valleys would appear in the potential energy landscape instead of the vertical ones in Figs. 3.8 and 3.6. Accordingly, $\boldsymbol{L}_2$ at this negative magic angle rotates in the opposite direction compared to $\boldsymbol{L}_1$ at $\phi_{\mathrm{H}} = +10°$. The rotation direction is unchanged under the magnetic field reversal ($\boldsymbol{L}_{1,2}$ is invariant under T combined with S_a, whereas $\boldsymbol{H}$ changes sign), and under the combined reversal of $\boldsymbol{L}_1$ and $\boldsymbol{L}_2$. These considerations are brought together in the left panels of Figure 3.10, summarizing all the switching regimes found in $GdMn_2O_5$. Notice how all field cycling procedures depicted in panel (a) lead to the same spin behavior.

Since the ferroelectric polarization P_b is a direct result of the magnetic configuration, we briefly comment on how these different switching behaviors for the spin are translated into the plots of the polarization in Fig. 3.5 and Fig. 3.2. Most of the evolution of P_b can be understood from the $\boldsymbol{L}_1 \cdot \boldsymbol{L}_2$ part. The contribution arising from the Gd–Mn exchange striction behaves similarly due to strong coupling between them (v_1), with an additional superposed contribution due to the slight rotations that the Gd spins perform away from the switching field strength $|H| \sim 5$ T. At $\phi_{\mathrm{H}} = \pm 20°$, both Néel vectors $\boldsymbol{L}_\alpha$ toggle between two directions in such a way that the angle between them and, hence, the ferroelectric polarization changes very little (Figs. 3.10(b,f), 3.2(c), and 3.5(c)). On the other hand, at $\phi_H = 0°$, $\boldsymbol{L}_1$ and $\boldsymbol{L}_2$ tilt in opposite directions. The resulting large variation of the angle between these two vectors gives rise to the two-state switching with the polarization reversal (Figs. 3.10(d), 3.2(a), and 3.5(a)). This suggests that the small-amplitude relative rotation of $\boldsymbol{L}_1$ and $\boldsymbol{L}_2$ is an electromagnon mode that could be excited by oscillating H_a or E_b. On the boundary between the two extremes one of the $\boldsymbol{L}_\alpha$ toggles while the other performs the full 360° rotation, leading to the four-state polarization loops.

3.6.3 Topology

We have hinted multiple times throughout the previous Chapters at the topological nature of the switching behavior. We will sharpen our previous statements in this Section and comment on the generality and robustness of the observed behavior.

Comparing the trajectories (white lines in Fig. 3.8 and Fig. 3.6) that describe the field evolution of the state of the system, we see that it is confined to one of the vertical valleys, as discussed previously. This is the case for all possible switching regimes. When $\phi_H = +10°$, ϕ_{L_1} varies strongest, whereas for $\phi_H = -10°$, ϕ_{L_2} varies the most, while in both cases the system as a whole remains inside the valley that hosts the original state.

In the two-state regimes (Fig. 3.8(a, c)), the system remains in the neighborhood of the starting point, with the trajectory contractible to a single point, whereas in the four-state regime in Fig. 3.8(b), the system progresses through the entire valley in a unidirectional sense, connecting the top and bottom edges while $\boldsymbol{L}_1$ rotates a full 360°. In the latter case, the path can not be fully contracted to a single point, which highlights its *topologically distinct* nature compared to the two-state switching regimes. Indeed, in the $(\phi_{\mathrm{L1}}, \phi_{\mathrm{L2}})$-space with a torus topology, we can assign a winding number

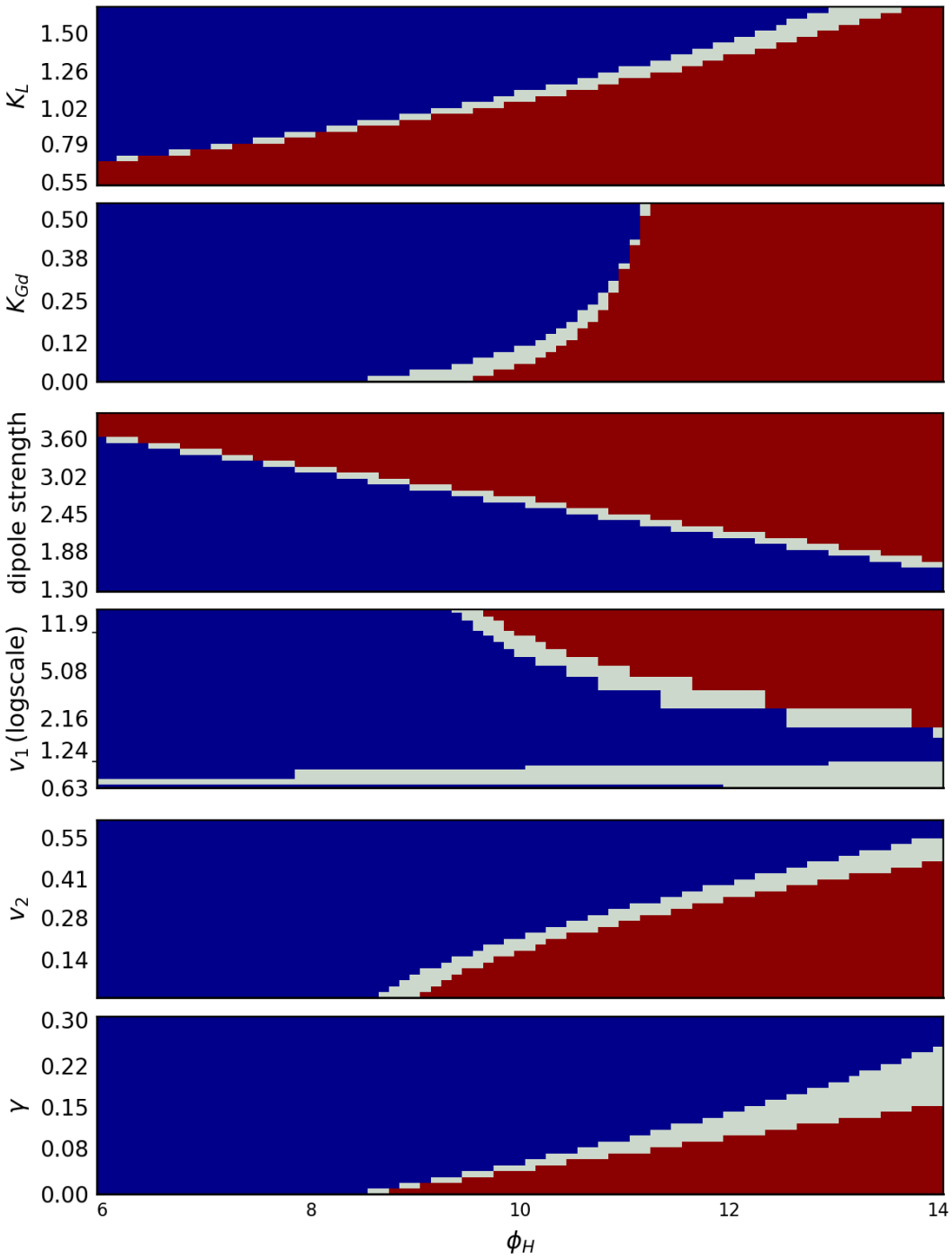

Figure 3.11: **Magic Angle region.** The panels demonstrate the influence of selected model parameters on the magic angle region. In each panel, only the parameter labeled on the vertical axis is varied, whereas the others are kept at the values reported in the methods Section 3.5. All parameters are reported in units of meV. The blue and red regions denote the angles ϕ_H for which the low angle and high angle two-state switching regimes appear, respectively. The grey boundary region is where the magic angle four-state switching occurs, characterized by a winding number of 1, and is topologically protected by the neighboring regimes.

Q to such trajectories, defined as:

$$Q = \frac{1}{2\pi}\int_0^{t_0} dt(L_1^x\partial_t L_1^y - L_1^y\partial_t L_1^x) - (L_2^x\partial_t L_2^y - L_2^y\partial_t L_2^x), \tag{3.31}$$

where the integral is taken over the time interval, t_0, during which the magnetic field is ramped up and down twice and the system is returned to its initial state. In the two-state switching regimes, $Q = 0$, whereas for the four-state switching we find $Q = 1$. This means that as long as the low and high angle regimes are present in a material (Fig 3.8 (a,c)), there will always exist a boundary region near the magic angle that interpolates between the two (Fig 3.8(b)), leading to the circular four-state magnetoelectric switching loop.

We finish this Section by demonstrating the generality of this behavior that results from its topological nature. The size and position of the ϕ_H interval for which the four-state regime appears depend on the details of the model parameters, but similarly to other topological boundaries (e.g. magnetic domain walls, topologically protected edge states in topological insulators), it can not be destroyed when the neighboring "domains" are present (high and low angle switching regimes in this case). The influence of varying a single model parameter is demonstrated in Fig. 3.11, where the blue and red regions correspond to the angles ϕ_H where the low and high angle regimes appear, respectively. Indeed, we see that for many parameters the four-state region (displayed in grey) exists as the boundary between the regions of the two-state regimes. One can also observe that the influence of some parameters is greater than others. For instance, taking $v_1 = 0.7$ meV dramatically increases the width of the four-state switching region to the interval $[5.2°, 17.6°]$ for ϕ_H. However, even for very high values of v_1 does the four-state switching appear. A small variation to K_L, the strength of the Mn single-ion anisotropy, on the other hand, leads to a significant change to the characteristics of the topologically protected region. This is not surprising, since the behavior of the Mn chains is very similar to that of the usual spin-flop transition, which crucially depends on the easy-axis anisotropy. This latter point will be expanded upon in the next Section.

We have so far given a detailed description of the observed behavior, experimentally and from the simulations of our effective model. While the model reproduces the experiments remarkably well, and we have found that a combination of symmetries and energetics lies at the core of the peculiar switching behavior, one may wonder if this can be rationalized further. In an attempt to do just this, we proceed in the following Section with some intuitive considerations.

3.6.4 Intuition

First of all, we would like to point out the similarity of the behavior of $\boldsymbol{L}_1$ and $\boldsymbol{L}_2$ with the well-known spin-flop transition in antiferromagnets. As mentioned before around Eq. (3.11), when a magnetic field is applied along the easy-axis of an antiferromagnetic material, the antiferromagnetic order will flip perpendicular to it when the field grows. This occurs when the Zeeman energy that can be gained through canting outweighs the penalty incurred from the misalignment with the easy axis.

The sudden spin-flop is a result of a similar flattening of the energy potential as what happens in our case at the switching field. A visual representation of this flattening can be found in the energy surface displayed in the panel for a field magnitude $|H| = 4.33$ in Fig. 3.6, where the valley has an almost uniform purple color. In such flat potentials, a small imbalance to one direction leads to a big movement of the order parameter, which is exactly what leads to the sudden reorientation of the spins in spin-flop transitions. In our case, a clear signature of these sudden variations is found in the jumps of P_b in Fig. 3.5 around the aforementioned field of ~ 4 T. The remarkable difference of the behavior described here, compared to the vanilla spin-flop transition, is that a well-defined flop direction is preferred. In spin-flops it makes no difference whether the system flops by $+90°$ or $-90°$. Here it does, and the "flop direction" of $\boldsymbol{L}_1$ or $\boldsymbol{L}_2$ at the switching field strength is always the same.

While further microscopic studies are needed to completely unravel the reason behind this, we suggest that this coaxing of the $\boldsymbol{L}$ is due to the exchange interaction with the Gd spins. We attempt to describe the idea by following the evolution of the two highlighted spins in Fig. 3.9.

When the field is ramped up, the long Gd spin (S=7/2) orients itself to it, while the chain $\boldsymbol{L}_1$ remains relatively strongly pinned because of its high anisotropy. Since the field is applied at an angle smaller than the 23.4° angle of the $\boldsymbol{L}_1$ easy axis, the force applied by the Gd spin to the chain pushes it towards one of the two flop directions.

When the chain then eventually flops with a 90° increment, the Gd spin reorients to optimize the exchange with the chain. This leads to an alignment of the Gd spin that was originally at a positive relative angle w.r.t. the field ($\phi_{Gd} > 10°$), to now be at a negative relative angle ($\phi_{Gd} < 10°$). When the field subsequently decreases, the Gd rotates further in the same direction, towards negative angles, thus pulling the Mn chains towards one of the flop directions, leading to another 90° rotation (this time the flop happens to align again with the easy axis anisotropy due to a diminished Zeeman energy gain through canting).

We hope that this intuitive picture shines some light on what might be happening microscopically to cause the behavior, although we concede the claim that this is a complete microscopic explanation. We will give an additional demonstration of this intuitive argument in the context of a simplified model, derived in the next Section.

3.7 Simplified model

Having modeled the topologically protected switching in $GdMn_2O_5$ with all its complexity, one may wonder what the minimal requirements are to have similar behavior where the spins rotate 360° while the applied field only oscillates along a single axis. It is clear from the spin configurations in Fig. 3.9, and previous considerations, that the chain with Mn moments most parallel to the applied field does the full rotation, while the other chain merely toggles around its starting orientation. As mentioned before, the Gd spins mostly follow the behavior of the chain they are most strongly coupled to. This warrants an attempt to reproduce the behavior of the rotating spins using only a single Mn chain with the Gd spins that are coupled to it via v_1. In the particular case

where the magic angle is along $\phi_H = +10°$, we therefore keep L_1, S_2, S_3, S_6 and S_7 as the remaining variables in the model (see Fig. 3.12). Furthermore, we neglect the easy axis anisotropy of Gd spins because of its small contribution due to the isotropic environment of the Gd spins. This leaves us with the following Hamiltonian, combining two parts, one with the dipolar terms H_{dip} and another with all the other terms, H':

$$\begin{aligned} H &= H' + H_{dip} \\ H' &= v_1(\boldsymbol{S}_2 + \boldsymbol{S}_3 - (\boldsymbol{S}_6 + \boldsymbol{S}_7)) \cdot \boldsymbol{L}_1 \\ &\quad - g\mu_B(\boldsymbol{S}_2 + \boldsymbol{S}_3 + \boldsymbol{S}_6 + \boldsymbol{S}_7) \cdot \boldsymbol{H} \\ &\quad + K_L(\boldsymbol{L}_1 \cdot \boldsymbol{n})^2 \\ H_{dip} &= \frac{1}{2}(g\mu_B)^2 \sum_{i \neq j} \left(\frac{\boldsymbol{S}_i \cdot \boldsymbol{S}_j}{r_{ij}^3} - 3\frac{(\boldsymbol{S}_i \cdot \boldsymbol{r}_{ij})(\boldsymbol{S}_j \cdot \boldsymbol{r}_{ij})}{r_{ij}^5} \right). \end{aligned} \tag{3.32}$$

Due to the symmetries of this simplified model and the geometry of the material we find that $S_2 = S_3$ and $S_6 = S_7$, reducing the model to two copies of a single Gd spin in the first half of the magnetic unit cell (S_3), one in the second half of the unit cell (S_6), and the chain inbetween (L_1) (see the red box in Fig. 3.12). This leads us to the equations:

$$\begin{aligned} H' &= 2v_1(\boldsymbol{S}_3 - \boldsymbol{S}_6) \cdot \boldsymbol{L}_1 - 2g\mu_B(\boldsymbol{S}_3 + \boldsymbol{S}_6) \cdot \boldsymbol{H} \\ &\quad + K_L(\boldsymbol{L}_1 \cdot \boldsymbol{n})^2 \\ H_{dip} &= (g\mu_B)^2 \left(\frac{\boldsymbol{S}_3 \cdot \boldsymbol{S}_6}{r_{36}^3} - 3\frac{(\boldsymbol{S}_3 \cdot \boldsymbol{r}_{36})(\boldsymbol{S}_6 \cdot \boldsymbol{r}_{36})}{r_{36}^5} \right), \end{aligned} \tag{3.33}$$

as a minimal model that still demonstrates the crankshaft-like behavior.

This minimal model embodies the intuitive explanation that we laid out in the previous Section, relying on the interaction between the two Gd spins and the magnetic field to push the AFM order into the positive direction at the switching field. When the chain flips, the exchange field from the Mn ions then pushes the Gd spins further in the same positive direction, thus completing the first part of the cycle. During the second cycle, the same considerations lead to the continued positive rotation of the spins.

3.8 Conclusions

We have examined the very peculiar and novel magnetoelectric switching behavior in $GdMn_2O_5$, a hallmark multiferroic system. Based on the incredible experimental observations performed by our collaborators in A. Pimenov's group, we have constructed a semi-classical spin model in an attempt to reproduce the behavior. Not only was this attempt very successful in mimicking the experimental observations, but it also allowed us to gain a deeper insight into what causes the effect.

We identified three separate polarization switching regimes that occur for different values of the angle ϕ_H that the applied magnetic field makes with the a-axis of the crystal. Accordingly, we termed these the low angle, high angle, and magic angle

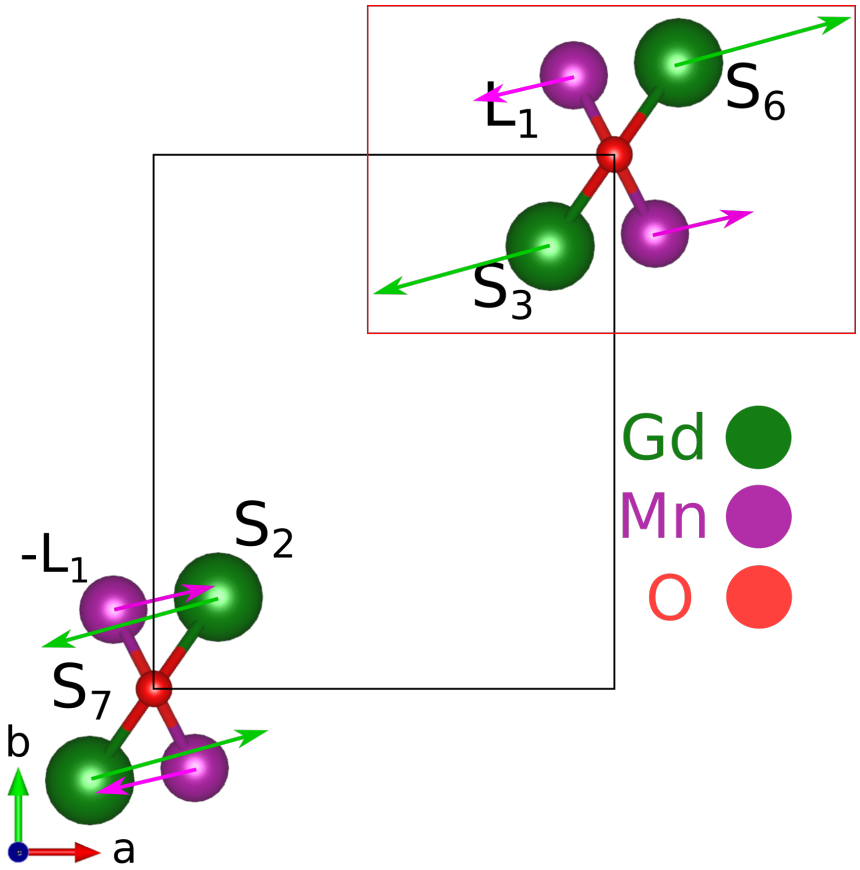

Figure 3.12: **Spins in the simplified model.** The zero-field configuration of the spins that perform the full rotation (360°), used in the simplified model (3.32), and indicated by the arrows. Spins S_6 and S_7 are translated for clarity by b and $2a$, respectively, from their original position in the second half of the cell. Due to the symmetry of the model and the geometry, the two clusters are copies of each other, allowing us to focus on the top right cluster, encased in the red box.

switching regimes, the latter fully deserving its designation due to the novel four-state double hysteresis loop that it leads to. The magnetoelectric switching is fully deterministic in each regime, hinting at the energetics as the source for this behavior. Using a semi-classical effective spin Hamiltonian in terms of the Gd spins, and the AFM order parameters $\boldsymbol{L}_\alpha$ that describe the Mn chains, we were able to unravel the characteristics of the system. This physics is a prime example of the often recurring theme in condensed matter, where a combination of relatively simple terms in the Hamiltonian can lead to very interesting and unexpected emergent phenomena.

Since the four-state switching regime at the magic angle is the most novel, we focused much of our effort on understanding its underlying mechanism. Extrapolating the gained knowledge we were then able to rationalize the behavior of the low and high angle regimes as well.

Focusing first on the evolution of the energy landscape of the model in Fig. 3.6, we understood that the trajectory of the system through the four-states is not only

described by the variation of their energy minima but that a crucial role is played by the energy barriers between them. We verified this by performing Nudged Elastic Band calculations that describe how the barriers between the four states evolve as a function of the applied field strength (see Fig. 3.7), fully uncovering the mechanism behind the unidirectional trajectory through the energy landscape. The main observation is that the barriers between neighboring states are not related by symmetry and are thus allowed to evolve asymmetrically, a fact confirmed by the different magnetizations of the barrier states.

We then turned our attention to the behavior of the spins associated with the effective model. Incredibly, we found that the undirectional cycling of the four-state regime is reflected in the full 360° rotation of half the spins by increments close to 90° (see Fig. 3.10 for a summary of all switching regimes). This is a microscopic analog to the crankshaft in a car, transforming the linear back–and–forth motion of the applied magnetic field (the piston) into circular motion of the spins (crankshaft). Since the polarization in these materials is a direct result of the magnetic configuration, we managed to link the uncovered spin behavior directly to the observations of the magnetoelectric switching in the experimental measurements.

Moreover, by realizing how the magic angle switching regime appears as a boundary between the low and high angle regimes, and by studying the difference in their trajectories through the energy landscape, we identified the topological nature of the switching behavior. We then defined a topological winding number, associated with the spin rotations, which is 0 for the two-state switching regimes (low and high angle), and 1 for the four-state switching regime. In order to verify the generality and robustness of this topological behavior, we performed further simulations with varied model parameters, demonstrating the existence of the four-state regime in a wide range of cases (see Fig. 3.11).

Combining all our observations, we concluded by attempting an intuitive explanation of the switching from a microscopic point of view, comparing the behavior of the spins in $GdMn_2O_5$ to the well-known spin-flop transition. While our investigation explained the lion's share of the observed magnetoelectric switching behavior in $GdMn_2O_5$, there remain some unanswered questions, mainly concerning the influence of domains, and what leads to the smaller jumps of the polarization curves in Fig. 3.2.

We would like to conclude with some speculations on the technological applicability of this interesting behavior. First, the clearest similarity is with a binary counter, where $GdMn_2O_5$ could be a single crystal analog where the two polarization states denote either a 0 or 1 bit. It could then be trivially used as a binary counter for magnetic field pulses. Second, the flatness of the energy surface close to the switching field could open the door to a degree of electric control over the magnetic configuration [64, 86]. This may then be utilized in storage devices that store data magnetically, but read and write it electrically. The main limiting factor is the exceedingly low temperature that is required to observe these effects in $GdMn_2O_5$ (see Fig. 3.3(c)).

4

Coupling between spin and lattice in chromium

4.1 Introduction

In all previous Chapters, we discussed situations for which the order parameters were static, or at least at instantaneous equilibrium. For GeTe, the polarization and resulting spin splitting were fixed. Even though the thermal excitation of polar phonons can lead to a non-trivial dynamical splitting in the band structure, on the slower phonon timescale electrons can still be assumed to be at the instantaneous equilibrium with the ionic potential [87]. This is because, as alluded to before, the electronic dynamics is generally many orders of magnitude faster than the atomic ones, meaning that the Born-Oppenheimer approximation remains valid. In the study on $GdMn_2O_5$, the changing magnetic structure and corresponding ferroelectric polarization were orders of magnitude faster than the slowly varying applied magnetic field, again allowing for an equilibrium description. This allows for further research into the dynamics of these effects since they are certainly accessible by using faster varying magnetic fields.

New physics arises, however, when two orders with different timescales for their dynamics are coupled. Especially when a slave order parameter has slower dynamics than the primary one can interesting effects arise. This is the case in the material we study here, chromium, an itinerant antiferromagnetic metal [88, 89]. It is the hallmark example of a material that exhibits a SDW as a result of local repulsive interactions of the electron gas, combined with a nesting of the Fermi surface. Due to exchange striction, this SDW creates an associated periodic lattice distortion (PLD), i.e. a decrease in the bond lengths between nearest neighbors with large spin magnitudes, while a tensile strain is present near the SDW nodes where the neighboring spins are small. The magnitude of the SDW can be diminished through excitation with optical

pulses which heat up the electron gas of which it is constituted. The dynamics of the order parameter that describes the SDW is extremely fast (with a fs characteristic timescale), meaning that it responds very quickly to the pulses. The dynamics of the PLD is instead related to the motion of massive ions and is therefore much slower, with generally a ps characteristic timescale. By using ultrafast pump-probe experiments that have a sub-picosecond resolution, these PLD dynamics can be studied and, more importantly, controlled very precisely through excitation of the much faster responding SDW.

In this Chapter we explore and investigate the additional possibilities opened up by applying a sequence of optical excitations spaced at various points in time. We start by demonstrating the experimental observations made by applying not one, but two optical pulses to the SDW, and how their spacing changes drastically the response of the probed PLD. This showcases the additional complexity and control achieved over the standard single pump-probe experiments that were performed previously [90, 90]. Among various possibilities, this additional control allows for the suppression of the intermediate nonequilibrium state thus reproducing adiabatic transitions on much faster timescales than would be possible without this control, which is termed "shortcuts to adiabaticity" in quantum technology [91–93]. After developing a phenomenological model in Sec. 4.3, and fitting its parameters to reproduce the two pump-probe experiments, we utilize it to design a train of pulses such that the PLD oscillation follows a particular envelope function in Sec. 4.5. We also comment on the characteristics of the model in order to gain a deeper understanding of what lies at the heart of this extended control.

4.2 Experimental methods and results

Before focusing on the theoretical modeling of the interacting SDW and PLD, we summarize the experimental techniques employed by A. Singer's group and the resulting measurements that we are seeking to explain. A thin film (28 nm) of Cr was used, supporting around seven periods of the SDW with a Néel temperature T_N of 290 K, slightly lower than the bulk value of 308 K. The experimental procedure is depicted schematically in Fig. 4.1(a). The film was illuminated by two sequential 40 fs optical pulses at times τ_1 and τ_2, heating up the electronic subsystem and, consequently, the SDW. The film thickness was chosen to be smaller than the optical skin depth of Cr, meaning that the pulses excite the entire volume of the sample homogeneously.

The PLD is pinned by the boundary conditions of the thin film, enforcing a half-integer number of periods along the depth of the sample (seven in our case)[90, 94, 95]. Using an x-ray XFEL, the magnitude of the PLD, i.e. Cr ion displacements, can be probed directly by measuring the intensity the Laue fringe that corresponds with the well-defined wavevector of the PLD [90, 96], as shown in Fig. 4.1(b-c), where the PLD Laue fringe is highlighted by the red box. The high peak selectivity that is achievable by XFELs allows us to resolve very narrow Bragg peaks or Laue fringes. This in turn makes accurate measurements on thin films accessible, even if they are deposited on thick substrates whose Bragg peaks would normally overpower the thin film signatures.

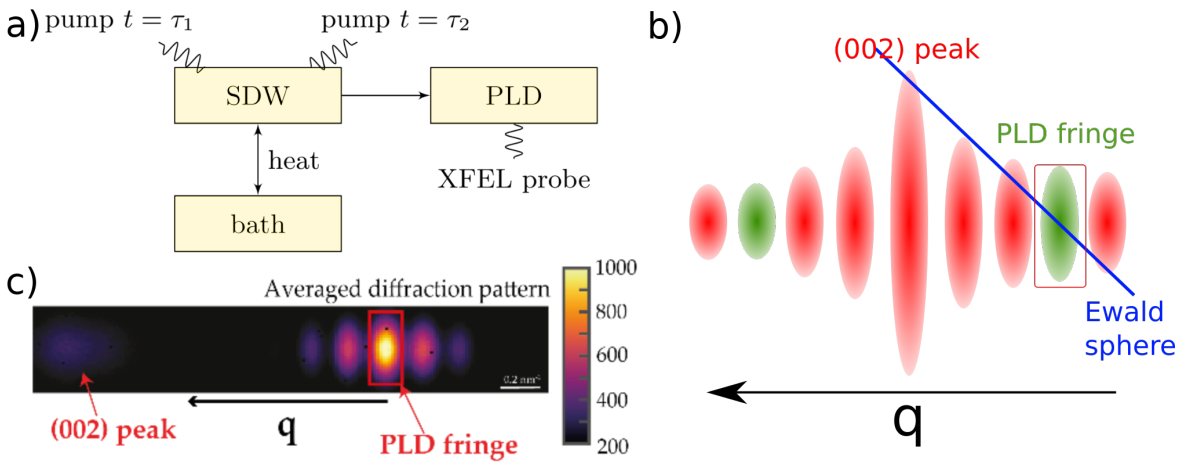

Figure 4.1: **Experimental methods** a) Schematic of the experimental setup where two optical pump pulses are applied to the SDW at $t = \tau_1, \tau_2$, leading to an oscillation of the PLD which is probed through the XFEL. The heat from the pulses is subsequently transferred from the SDW to the heat bath, cooling down the SDW. b) Schematic representation of X-ray diffraction measurements in panel (c). The (002) peak is the central Bragg peak with the ellipses representing the Laue fringes due to the thin film geometry. Here $\boldsymbol{q} = \frac{4\pi}{\lambda}\sin(\theta)$ is the scattering vector with λ being the x-ray wavelength. The central peak is weaker than the fringes due to the position of the Ewald sphere, as depicted by the blue line in (b).

To further increase the contrast of the PLD peak, the Ewald sphere is tilted along a particular direction, as indicated by the blue line in Fig. 4.1(b). Furthermore, again due to the pinning of the PLD to the boundaries of the thin film, its phase can be obtained from the interference between its corresponding fringe peaks and those that originate from the thin film geometry [90]. This allows us to track the time evolution of the amplitude and phase of the PLD, giving us access to its dynamics that appear as a result of the applied pulses to the SDW.

The sets of measurements that form the starting point for our further investigation are displayed in Figs. 4.2 and 4.3 [97]. It is important to realize that the SDW order is not directly accessible through these measurements. In effect, this means that we are studying the excitation caused to the PLD because of its coupling with the externally perturbed SDW.

We can observe that the PLD has an oscillation time period of approximately 450 fs, and a damping time of around 3 ps. We first focus on Fig. 4.2(a), where the PLD amplitude is represented as a heatmap with the time evolution of the x-ray probe intensity on the horizontal axis, and the delay between the two consecutive pumps on the vertical axis. Each horizontal slice corresponds to an experiment such as those in panel (b) and (c) of the same figure. Consequently, the blue and purple line demonstrate the horizontal slice corresponding to the measurement highlighted by the box with the same color. Still in Fig. 4.2(a), the very dark vertical band of troughs around probe delay $t = 0$ followed by a less dark band of throughs in the next period indicates the fast restoration of the oscillation equilibrium. This means that the heat transfer rate between the electrons that constitute the SDW and the bath is relatively

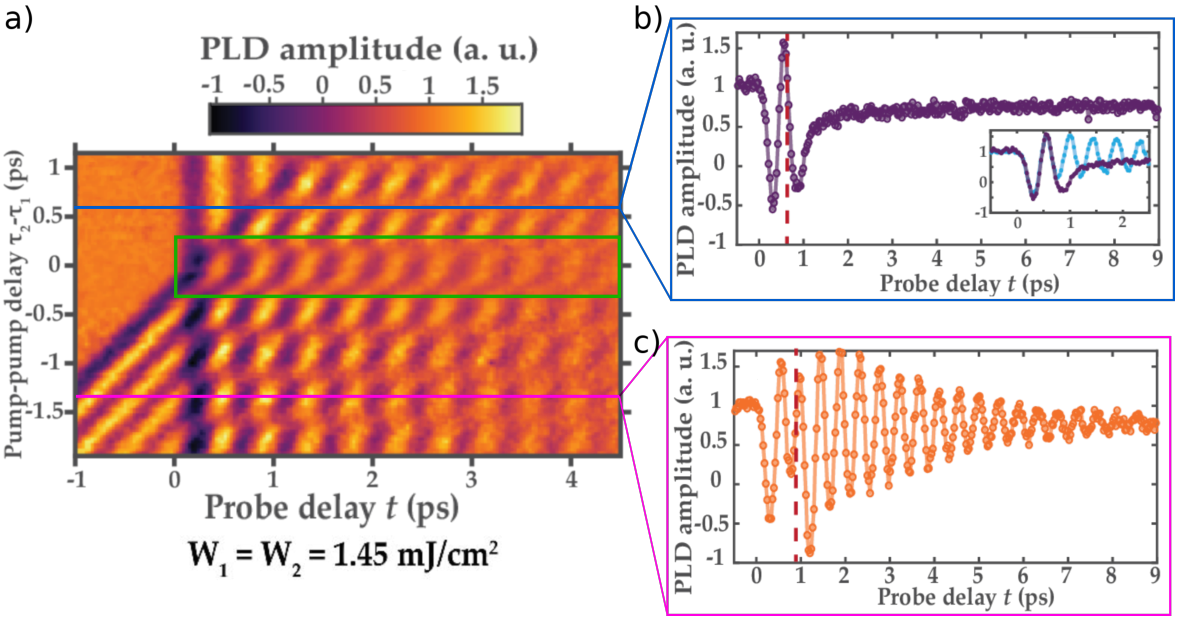

Figure 4.2: **Pump-pump delay-dependent interference.** a) Heat map of the measured PLD amplitude upon excitation by two pulses at different τ_1 and τ_2, with a fluence of 1.45 mJ/cm^2 each. The green box highlights the area of lower oscillation amplitude of the PLD when the temperature of the SDW exceeds T_N due to concurrent pulses. b) Destructive interference when $\tau_2 - \tau_1 = 620$ fs, corresponding to the horizontal slice of panel (a) marked by the blue line. The blue graph in the inset demonstrates how the evolution would be without the second pulse. c) Constructive interference when $\tau_2 - \tau_1 = 845$ fs, corresponding to the purple slice in panel (a). In both panels (b) and (c), the dashed red line marks the arrival time of the second pulse. The dots denote the experimentally measured values, and the graphs – the theoretical simulations (see Fig. 4.4 for more details).[97]

high, leading to a thermalization between the two within a picosecond after heating. This partially restores the SDW which in turn leads to the partial restoration of the oscillation equilibrium. Further thermalization between the Cr lattice and the substrate occurs on a nanosecond timescale, beyond the scope of these experiments. Furthermore, we find that the system as a whole (bath and electrons) heats by approximately 45 K as a result of the pulses, which is reflected in the diminished final amplitude of the PLD. However, since this amplitude is nonzero, we can deduce that the final temperature of the system is below the Néel temperature of the SDW.

The most interesting observation is that, by changing the timing of the second pulse τ_2, the dynamics of the PLD can be controlled to a high degree, as demonstrated in Fig. 4.2(a). It is possible to fully quench the oscillation of the PLD, or its amplitude can instead be increased by the second pulse. The horizontal bands display periodically alternating regions of these two behaviors, termed as "destructive" and "constructive" interference. Two representative horizontal slices are taken and displayed in Fig. 4.2(b,c), demonstrating destructive and constructive interference, respectively.

The maximum PLD amplitude that is reached after the second pulse is 150% of the original value. This is significantly higher than the excitation amplitudes associated

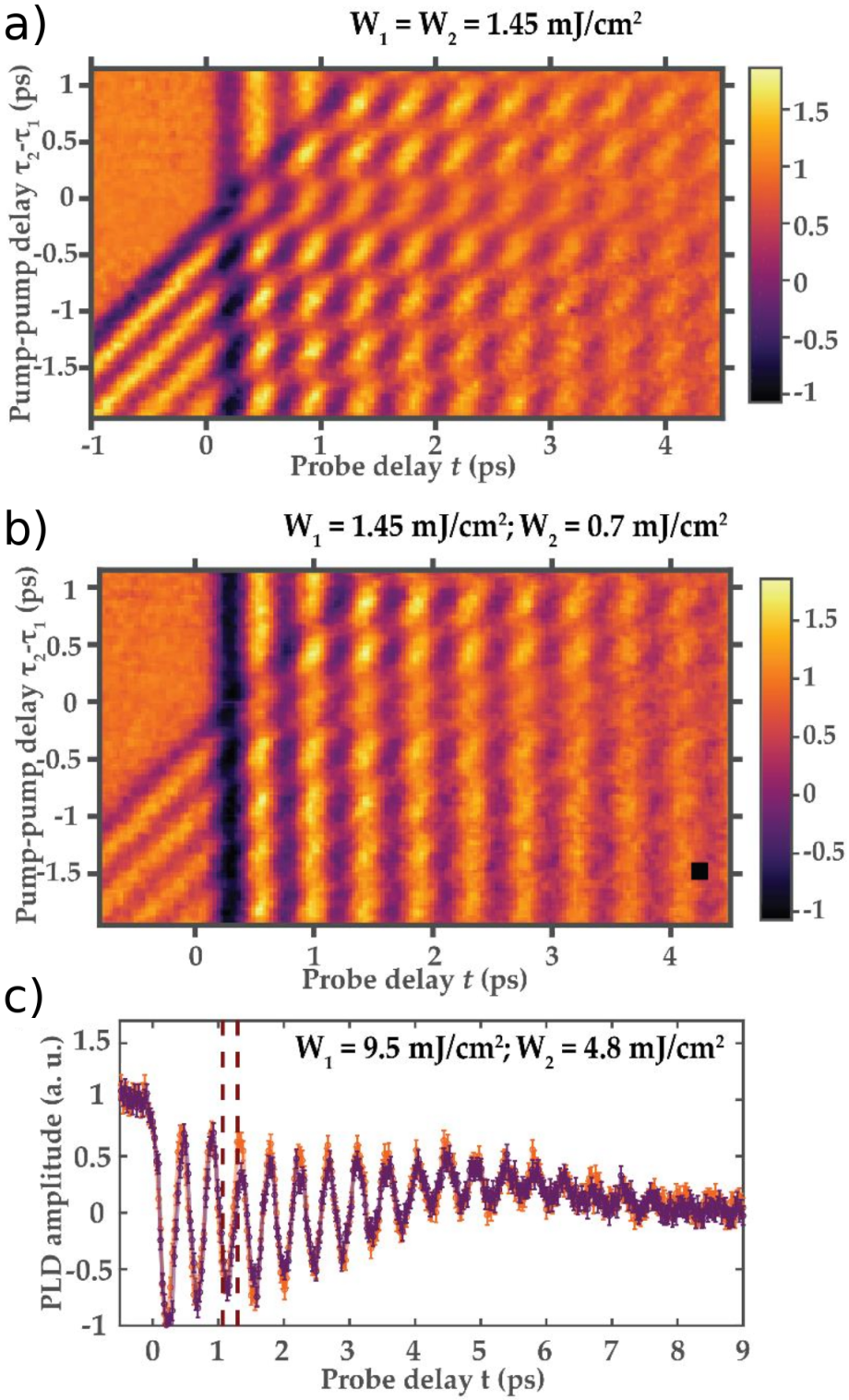

Figure 4.3: **Interference dependence on pulse fluence.** a) Map of the PLD amplitude before and after excitation by two pulses with fluences $W_1 = W_2 = 1.45\text{mJ/cm}^2$. b) Similar to (a) but with fluences $W_1 = 1.45\text{mJ/cm}^2$ and $W_2 = 0.7\text{mJ/cm}^2$, demonstrating the diminished influence of the second pulse. c) Amplitude of the PLD in the constructive and destructive pump-pump delay conditions, with pump spacing similar to panels (b, c) of Fig. 4.2, but for fluences $W_1 = 9.5$ mJ/cm^2 and $W_2 = 4.8$ mJ/cm^2. The vertical dashed lines mark the arrival time of the second pulse in each experiment. In these measurements the SDW is fully melted by the first pulse, and the timing of the second pulse has no influence on the behavior.

with the conventional displacive excitation mechanism, which leads to a ratio of around one [96, 98]. Furthermore, if the second pulse arrives before the SDW had time to cool down, a smaller maximum oscillation amplitude is achieved, as can be seen from the horizontal band around $\tau_2 - \tau_1 = 0$ ps, and highlighted by the green box, in Fig. 4.2(a). As will be further discussed below, this indicates that the combined fluence of the two pulses was high enough to raise the temperature of the SDW above T_N.

The influence of the pulse's fluence is detailed in Fig. 4.3. Experiments performed with a high fluence initial pulse, cause the SDW to heat up and remain above T_N for the entirety of the experiment, demonstrating that the impact of the second pulse, in this case, is completely lost. Indeed, varying its timing changes nothing to the oscillation of the PLD, as can be seen from Fig. 4.3(c). If control is the goal, it is thus important that the SDW is allowed to cool down below T_N before exciting it again. The SDW order parameter, furthermore, depends strongest on temperature when it is close to the critical point where it varies as the square root, thus increasing the pulse efficiency in that temperature region. These considerations will be discussed in greater detail in Section 4.5, after the theoretical description is given.

Finally, it was experimentally verified that no timescales related to the behavior of topological defects such as domain walls are present. This would be reflected in a changing width and intensity of the diffraction peaks associated with the PLD (Fig. 4.1(b)), which is not observed. This can be explained by the small thickness of the film, allowing only a single SDW wavevector direction, such that no domains are formed in the "depth" of the film. Furthermore, the XFEL pulses had a diameter of 0.2 mm, which envelopes multiple SDW domains in the plane of the film[99], making the measurements statistical over domains. These considerations also support our previous claim that the optical pulses can be assumed to excite the thin film homogeneously.

4.3 Theory

In order to model the effect that the two photon pulses have on the material, we split it up into multiple thermodynamic subsystems. The first consists of the electronic degrees of freedom, including the SDW, which thermalize very quickly among themselves due to the strong electron-electron interactions. The timescale for this thermalization was measured by high-resolution angle-resolved photoemission spectroscopy to be below 100 fs [99], allowing us to assign a temperature T_L to it, where L is used to denote the SDW order parameter, as will be discussed further below.

The second subsystem is that of the lattice phonons which act as a heat bath. In this case, we exclude the mode that describes the PLD oscillation, since it is not thermal on the timescales we are interested in. As was mentioned before, its characteristic timescale is on the order of picoseconds rather than the femtosecond timescales of the electronic SDW.

Similar to the electrons, the phonon bath harbors strong interactions within itself allowing us to assign a second temperature T_b to it. The interaction between the electrons at T_L and the bath at T_b is what leads to the heat transfer between them, resulting in equilibration between the two subsystems within 1 ps. We thus assume that

the PLD mode is completely detached from the other phonons, instead only interacting strongly with the SDW order parameter L (see below).

The evolution of the temperatures can be described by the so-called two temperature model:

$$\begin{aligned} C_L\dot{T}_L &= -k(T_L(t) - T_b(t)) + Q_{ph}(t) \\ C_b\dot{T}_b &= -k(T_b(t) - T_L(t)), \end{aligned} \tag{4.1}$$

with k the heat transfer rate, and C_L, C_b the heat capacities of the electronic degrees of freedom and of the bath, respectively. The dots signify time derivatives. As one could expect, we find that the heat capacity of the bath is larger than that of the electronic system by an order of magnitude, as will be confirmed when we detail the model parameters in the methods Section 4.4. Finally, the heat injected by the pulses is modeled by a Gaussian $Q_{ph}(t) = Ae^{\frac{-(t-\tau)^2}{\xi^2}}$, with A the strength, ξ the duration and τ the time delay.

The changes to T_L through heating and subsequent cooling affects the SDW amplitude L and indirectly the PLD one y, as described by a Landau-type theory [100]. These order parameters are related to the Fourier component of the SDW with wavevector q, i.e. $L = S_q$, and to the acoustic phonon amplitude $y = u_{2q}$. The phonon mode is the second harmonic ($2q$) of the SDW because the exchange striction only acts on the magnitude of the spins, not on the phase so that during one period of the SDW oscillation two periods of the PLD occur. This leads to the following expression for the free energy:

$$f(L, y, T_L) = \frac{\alpha}{2}(T_L - T_N)L^2 + \frac{\beta}{4}L^4 - gL^2y + \frac{\rho y_0^2\omega_0^2}{2}y^2 + \frac{b}{4}y^4, \tag{4.2}$$

where L, y and T_L are the time dependent variables, and all coefficients are taken positive. The double-well potential that causes the SDW phase transition is characterized by the coefficients α and β, and critical temperature T_N below which the SDW order sets in. The coupling between L and y due to exchange striction is described by the term with g. Only even orders of L appear in the free energy since the energy is time-reversal even, but L is time-reversal odd. The PLD order parameter y with density ρ is described by the harmonic oscillator potential with frequency ω_0 and displacement amplitude y_0, and has a vanishing equilibrium value in the absence of L since it is not the primary order parameter. The fourth-order term $\frac{b}{4}y^4$ is only included to provide a better fit to some of the anharmonic features observed by the experiment. It is not needed in order to bound the energy potential in terms of y, as would be required if y was the primary order parameter with a negative second-order coefficient a, like in the case of $\alpha(T - T_N)$ for L. It is the interaction with the primary order parameter L that provides the "force" $F = -df/dy = gL^2$ to move y up in its own harmonic potential, leading ultimately to the nonzero equilibrium value. While this sounds trivial, this concept is key in order to understand the observed behavior.

As mentioned before, the dynamics of L are much faster than those of y. In writing down the Lagrangian of the system we, therefore, choose to take L to be always at its

instantaneous minimum in the potential of Eq. (4.2), characterized at each time by the values of y and T_L. This can be achieved by solving $\frac{\partial f}{\partial L} = 0$, leading to:

$$L(t) = \begin{cases} \pm\sqrt{\frac{-\alpha(T_L - T_N)+2gy}{\beta}} & T_L <= T_N \\ 0 & T_L > T_N \end{cases}. \tag{4.3}$$

The time evolution of the system can then described using the Lagrangian:

$$\mathcal{L}(L, y, \dot{y}, t) = \frac{m_y \dot{y}(t)^2}{2} - f(L, y, t), \tag{4.4}$$

with associated Euler-Lagrange equation for y:

$$\frac{\partial \mathcal{L}}{\partial y} - \frac{d}{dt}\frac{\partial \mathcal{L}}{\partial \dot{y}} = \gamma_y \dot{y}, \tag{4.5}$$

where γ_y denotes the damping parameter for y. Substituting Eq. (4.2) for f leads to

$$\rho y_0^2 \ddot{y} = -\rho y_0^2 \omega_0^2 y - b y^3 - \gamma_y \dot{y} + g L^2. \tag{4.6}$$

This equation, together with Eqs. (4.1) describing the temperature evolution of the SDW (T_L) under influence of the optical pulses, fully describes the dynamics of the coupled system. One obvious remark can be made here: to be completely exact, the energy dissipated through the damping term γ_y in Eq. (4.6) should be absorbed into the phonon bath and thus influence T_b. However, the case can be made that since this is only a single mode, its contribution to the heating of the bath will be negligible compared with the one as a result of the thermalization with the electronic degrees of freedom.

4.4 Methods

To solve the time evolution of L and y through the differential equations in Eqs. 4.6, we used the numerical integration methods implemented in the DifferentialEquations.jl package [101]. More specifically, the Tsit5 algorithm was used, which has adaptive time stepping to capture the sharp optical pulses. Originally, the dynamics were fully solved both for L and y, but it was confirmed during the fitting process that the dynamics of L are indeed significantly faster than those of y. Solving dynamics with significantly different timescales is in general hard from the numerical point of view, meaning that taking L to be always at the minimum of the potential makes solving the equations numerically much easier. The starting temperature of the bath was fixed at 115 K in all simulations, and the thin film value of T_N was taken, i.e. 290 K which is slightly lower than the bulk Cr Neél temperature of $\sim$ 308 K.

Most parameters of the model were not perfectly known a priori and thus had to be fitted to the experimental measurements. To aid with the fitting, judicious choices for the starting values of some parameters were be made. For example, it was known that the optical pulse width τ was around 40 fs, and that the oscillation frequency of the

PLD $\omega_0 \approx 14$ THz or equivalently had a period of around 450 fs. Furthermore, from previous experiments, the ratio between the heat capacities for the bath and electronic degrees of freedom, $\frac{c_b}{c_L}$, was determined to be around 7 [99], and the heat transfer rate around 42×10^{16} W/m^3 K [102].

The time evolution of the system was then solved for each set of trial parameters on an interval from -2 ps to 8 ps, where the lower bound is chosen so that the numerical integration starts from a complete equilibrium initial condition. This is necessary because when the sharp pulse arrives at 0 ps, some energy already enters the system slightly before 0 ps due to the Gaussian shape. The error of the solution $\tilde{x}$ w.r.t. the experimental measurements x is then estimated as the mean square sum $err = \sum_{i=1}^{n} \frac{(x_i - \tilde{x}_i)^2}{n}$, where i denote the indices of the measurement points. The numerical optimization was done through the Optim.jl package [103], where we found that the Nelder-Mead simplex algorithm [104] works best for this very non-linear problem.

4.5 Results and discussion

The experimental measurements we use as a basis to fit our model were discussed in Section 4.2, and shown in Fig. 4.2. We took eleven representative experiments, which can be thought of as horizontal slices of Fig. 4.2(a), in order to fit the model parameters to get the best total fit across all datasets, allowing only the pulse fluence to fluctuate between sets.

The parameters that were thus found are

$$\alpha = 1.6 \times 10^7 \frac{\mathrm{J}}{\mathrm{K\,m^3}},\ \beta = 1.55 \times 10^{11} \frac{\mathrm{J}}{\mathrm{m^3}},\ g = 1.1 \times 10^3 \frac{\mathrm{J}}{\mathrm{m^3}}, \tag{4.7}$$

$$\frac{\omega_0}{2\pi} = 2.24\,\mathrm{THz},\ b = 1.1 \times 10^{12} \frac{\mathrm{J}}{\mathrm{m^3}},\ \rho = 7150 \frac{\mathrm{kg}}{\mathrm{m^3}},\ y_0 = 0.5 \times 10^{-12}\,\mathrm{m}, \tag{4.8}$$

$$\gamma_y = 1.4 \times 10^{-9} \frac{\mathrm{J}}{\mathrm{m^3}},\ C_L = 1.4 \times 10^4 \frac{\mathrm{J}}{\mathrm{m^3\,K}},\ C_b = 7.57\,C_L, \tag{4.9}$$

$$k = 3.74 \times 10^{17} \frac{\mathrm{W}}{\mathrm{m^3 \cdot K}},\ \xi = 40\,\mathrm{fs},\ A = 2.86 \times 10^6 \frac{\mathrm{J}}{\mathrm{m^3}} \tag{4.10}$$

The results of this fitting procedure is shown in Fig. 4.4, demonstrating an excellent agreement between the theory and experiment across the board.

To get a deeper understanding of the underlying effect, we look at the evolution of the free energy surfaces for both order parameters, shown in Fig. 4.5. The characteristic double-well potential for $L \neq 0$ is clearly visible throughout the simulation. As expected, we can observe that, when the pulses hit and T_L rapidly increases, the potential for L varies as rapidly, leading in turn to a quick shift of the minimum of the single well potential for y, which ultimately results in an oscillation of y due to its relatively slow dynamics. While the temperature T_L decreases again, L, and consequently the minimum of the potential for y, shift back towards their original equilibrium position. However, the oscillation of y remains for quite a long time during this shift, since the damping is not particularly large (of the order of 4 ps) compared with the cooling rate of the SDW (T_L).

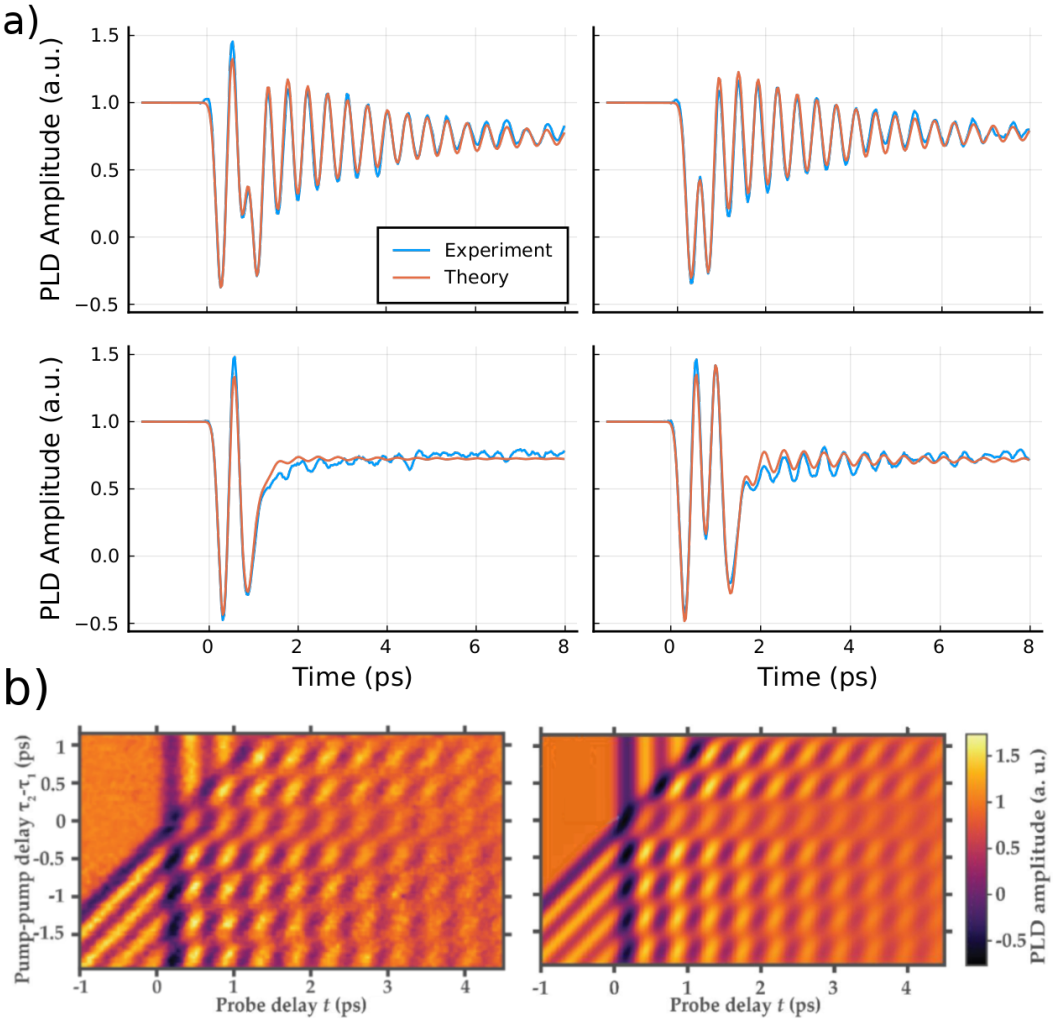

Figure 4.4: **Demonstration of the quality of the theoretical fit.** a) The smoothed experimental measurements and theoretical fits are indicated in each panel by the blue and orange graphs, respectively. b) Demonstration of the equivalence between the experimental (left) and simulated (right) PLD amplitude map.

This already presents us with the first hint at the benefit of indirectly exciting the PLD through the SDW, which we clarify through the use of a thought experiment of a hypothetical system for which the PLD is the primary order parameter with associated double-well potential, and with no other coupled order parameters. The only possibility to excite an oscillation, in this case, is by heating up the system above the critical temperature. This would change the shape of the hypothetical energy potential, shifting its minimum to 0, and again, due to the slow dynamics, an oscillation would occur. However, as with any normal oscillator, the value of the PLD would never exceed the starting value during the oscillation, as the thermalization, and restoration of the potential will occur on much longer timescales.

Here, however, due to the relatively fast thermalization of the SDW with the bath, the potential surface for y recovers on a faster timescale than it would on its own,

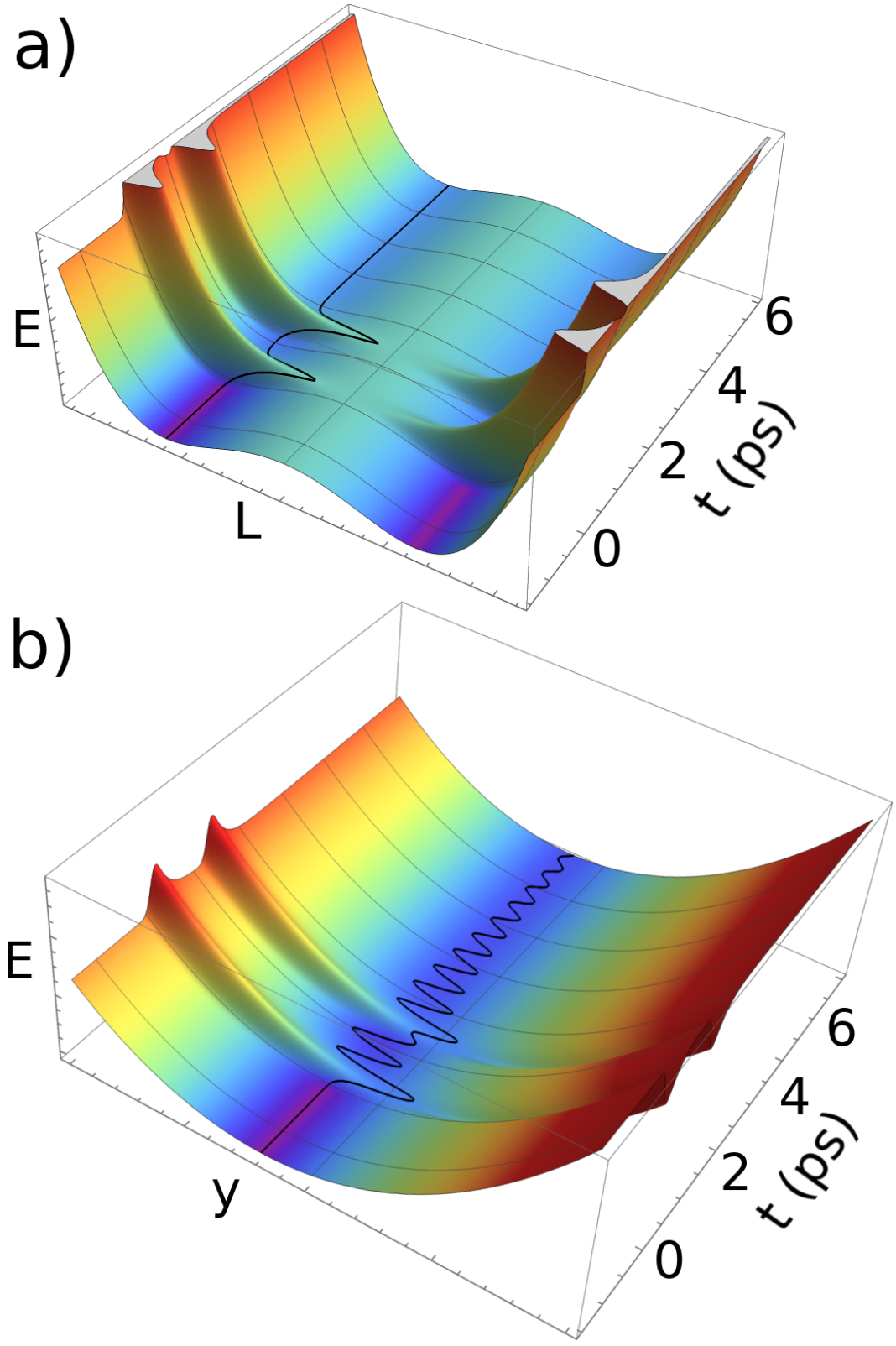

Figure 4.5: **Time evolution of the energy surfaces of L and y.** The trajectory of each order parameter is indicated by the black graph. The energy surface in panel a (b) is calculated by varying L (y) at each time step, while keeping y (L) at the value corresponding to the trajectory in panel b (a). The fast dynamics of L is reflected by the trajectory tracking its minimum at all times.

leading to a relative movement of the potential opposite to the movement of y itself. This relative movement transfers additional momentum to y as the SDW is cooling down, and the potential is being restored, leading ultimately to a higher oscillation amplitude, even when only a single pulse is applied. This was observed experimentally in previous measurements by A. Singer's group and reported in Ref. [96].

We want to reiterate that, since it is the magnitude of L which is the driver of the energy surface of y, the effect is most pronounced when L is close to T_N because a small change in temperature causes a large variation of the equilibrium position of L as shown by the square root temperature dependence in Eq. (4.3).

Having multiple such pulses that can rapidly change the potential surface for y opens up many additional possibilities, allowing for constructive interference (Fig. 4.4(a-b)) or, by shifting the potential surface in the same direction as the movement of y, for a complete destructive interference (see Fig. 4.4(c-d)).

This behavior can be leveraged further by applying a train of pulses, for which we now investigate exactly what can be achieved. Two goals will be investigated: maximizing the oscillation amplitude, and designing the pulse train so that the envelope of the oscillation perfectly tracks a given signal function.

The maximal change in the value of L, and thus the potential surface for y, can be achieved by heating it all the way to T_N. It is then important to keep this initial shift of the potential for y in place until y crosses the minimum, converting as much potential energy into kinetic energy. This can be done by heating L slightly above T_N, where the additional temperature and finite cooling rate will keep the potential shift present for long enough. Fig. 4.6(a) demonstrates this part of the strategy, with the peaks of T_L in red indicating that T_L exceeds T_N. Exactly at this point, L should start to re-condense causing the potential surface of y to start moving in the opposite direction to y's movement, which in the end supplies it with additional momentum, as was described above. Since the sign of L does not matter for the position of the minimum for y, it can only cause a shift in one direction, meaning that, similar to someone pushing a swing, the ideal intervals for the subsequent pulses are close to multiples of the period of y. The optimal number of periods between pulses depends on the cooling rate of L, and damping rate of y. The former influences how much T_L can cool back down within one period of y, and thus the size of the maximum kinetic energy gain of y through subsequent heating of T_L, while the latter is the main source of kinetic energy loss. From our simulations, unless the damping is really negligible, it is always most beneficial to supply a pulse at each oscillation period of y. The results in Fig. 4.6(a,b) demonstrate this. In panel (a) a pulse was applied at each period, whereas in (b) every other period. We artificially increased the heat capacity of the bath to infinity to mimic a possible strongly cooled regime, which would be ideal for maximizing the oscillation amplitude. With the damping rate of y taken as the one fitted to the experiment, the maximal amplitude thus achieved is about 450% the original value, quite a remarkable increase.

We can go one step further, however, and design a pulse train such that the oscillation amplitude follows a particular "signal" envelope function, demonstrating the incredibly high degree of control over the PLD that this coupled system could allow for. To limit the dimensionality of the manifold of possible solutions, we formulated

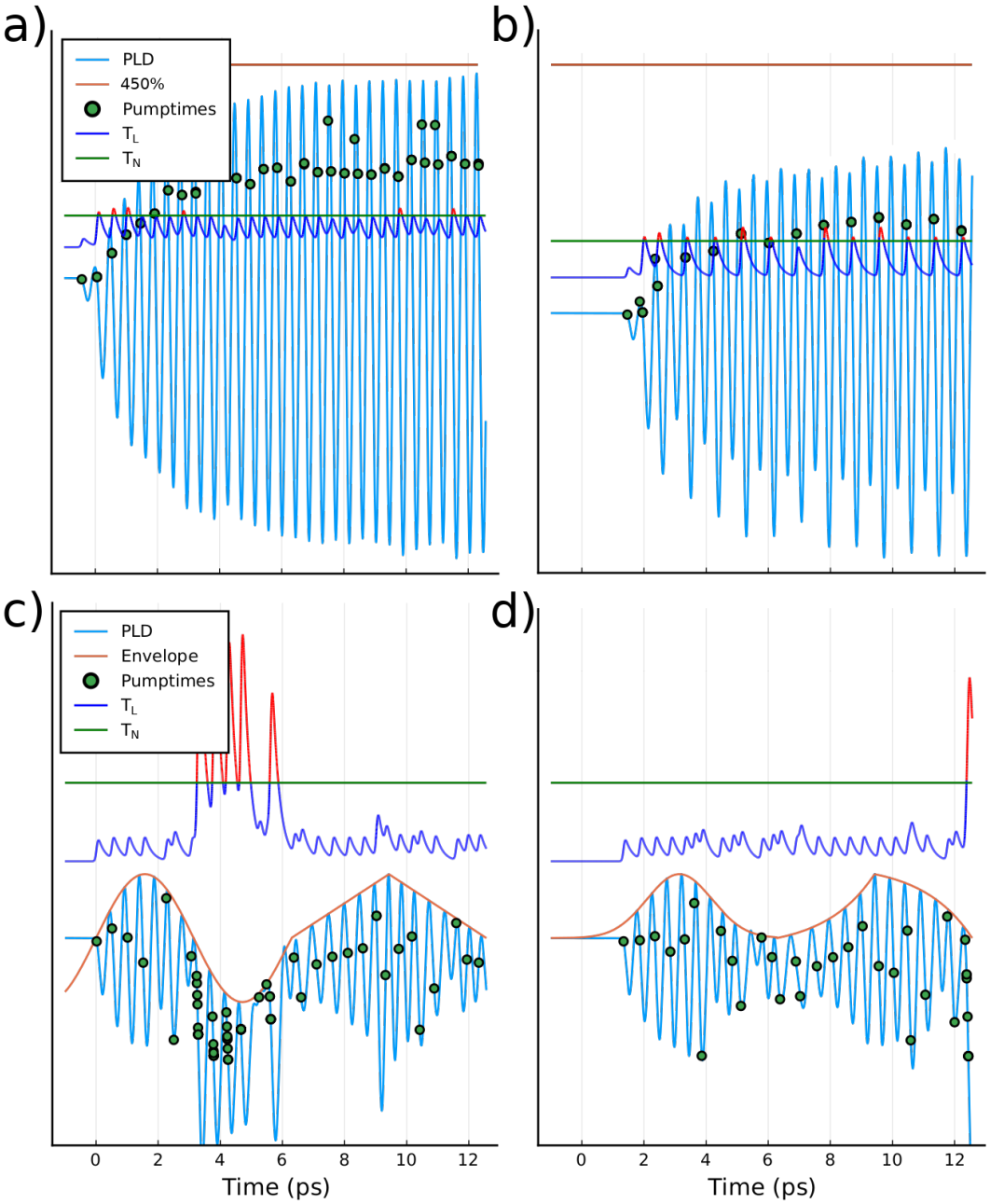

Figure 4.6: **Pulse train design.** a), b) Two possible schemes to maximize the oscillation amplitude. In (a) pulses were applied each period, whereas in (b) only every other period. c), d) Two examples of perfect control. In (c) the envelope was taken as one period of a sinusoid followed by a sawtooth with the same width and height. In (d) the envelope consists of a Gaussian followed by an exponential and inverse exponential.

the following rules:

- Each pulse has a fixed fluence.
- Pulses are grouped in sets per period of PLD oscillation.
- The first pulse group only has a single pulse, which fixes the required fluence.
- The maximum allowed pulses per group is fixed.

We then tested this procedure on different envelope functions, showcased in Fig. 4.6(c,d). The groups of pulses can be fitted sequentially since the later pulses do not influence the oscillation caused by the earlier ones. As in the maximum amplitude simulations, the assumption of an infinite C_b was made here. This is done so the oscillation equilibrium of y does not change because of the heating due to the pulses. The results demonstrate how a carefully chosen pulse train enables indirect, but close to optimal control of the PLD order parameter.

To comment on the experimental viability of such a pulse train, we can make the following remarks. The time resolution that can be achieved with the optical pulses used in our experiments is on the order of the pulse width, i.e. 40 fs. There exist other optical lasers that have widths down to a few fs, which could allow for the required accurate time positioning of the pulses. Moreover, through the use of prisms, a high fluence pulse can be split into many smaller pulses, which can in turn be controlled by the opening or closing of apertures.

This is all to say that technically speaking such pulse trains can be generated, and we are hopeful that such experiments can be performed in the future.

4.6 Conclusions

In this Chapter, we discussed the effects of cross-order coupling beyond quasi-static phenomena. The results show that the coupling between the SDW and PLD through exchange striction in chromium is another prime example of cross-order control, where, in this case, the perturbation applied by optical pulses to the SDW leads to an excitation of the PLD mode. Moreover, the slower dynamics of the PLD compared to the SDW opens up new behavior and additional dynamical control that would not be possible without the coupling. If the PLD would have dynamics on the same timescale as the SDW, changing its potential through exciting the latter would not be very impactful since it would follow the minimum of the potential as fast as the excited SDW would change it.

Through the use of a relatively simple model, we were able to reproduce the experimental observations to an incredible degree, as demonstrated by the quality of the fits in Fig. 4.4. Together with the remarkable indirect control through the SDW, this model allowed us to design a train of pulses in order to either maximize the PLD oscillation amplitude (up to 450%), or even make it follow a give envelope function (see Fig. 4.6). The control also allows for the destruction of the PLD oscillation at a

moment's notice, leading to a possible shortcut to adiabaticity where the final state is at a higher temperature than the original one.

Such control would not have been possible through the direct excitation of the PLD mode and is thus another clear demonstration of the many benefits that coupled orders might present. Whether this can be directly exploited for technological means remains a question, seen as XFELs are rather large. However, this behavior through coupled order parameters may be a promising route to robust coherent control. We hope that our understanding and the demonstration of perfect control in Cr could open the road to finding other similar situations with more technologically viable properties.

5

Mechanical softening in ferroelectric domain walls

5.1 Introduction

We have so far studied the behavior of ordered materials under the assumption of perfect homogeneity. This forms the base for understanding the more complex inhomogeneous scenarios that appear in reality because of the spontaneous symmetry breaking that occurs at the phase transition temperature T_c.

As usual, we can associate an order parameter (OP) with the order that develops as a result of this symmetry breaking. It is thus zero above T_c and nonzero below. The energy potential for the OP obeys the same symmetries as the parent structure, and will thus have as many degenerate minima as the dimensions of the transformation operator that describes the broken symmetry. Each of these minima are associated with a different direction of the OP which can be transformed into each other by applying this operator. During a phase transition in a large system, regions that are separated in space will each individually acquire one of these equivalent values of the OP. Such regions are referred to as domains, with the narrow boundaries between them called domain walls inside of which the OP is interpolated.

We already encountered examples of such OPs: in GeTe the ferroelectric polarization describes the order of the electric dipoles inside the crystal; in $GdMn_2O_5$ we found two primary OPs, $\boldsymbol{L}_1$ and $\boldsymbol{L}_2$, describing the antiferromagnetic order inside each Mn chain, and one slave order parameter P_b that denotes the resulting polarization; in chromium we discussed a similar antiferromagnetic OP with, in that case, an associated periodic lattice displacement.

In the case of $GdMn_2O_5$ we have shown that there are four combinations of the primary OPs that have the same energy, and how they can be transformed into each other

by the time-reversal and inversion symmetry operators (see Fig. 3.6). In chromium the antiferromagnetic OP has two energy equivalent values, again related by time-reversal symmetry and visualized in Fig. 4.5(a).

We now turn back, to the discussion on inhomogeneity, domains, and the domain wall (DW). There are, actually, some ways to achieve a completely homogeneous situation, even in relatively large systems. One example is through poling, where an external field is applied during the phase transition to coax the system towards one of the orientations of the OP. Another is through expelling the DWs in the sample by keeping it close to the phase transition. This happens because at the DWs the OP is forced away from the minimum, making them energetically less favorable than a uniform domain. Consequently, by keeping the system close to the phase transition for an extended period, it is sometimes possible to expel them from the material.

In the case of ferromagnetic or ferroelectric materials, the homogeneity is usually limited by the depolarizing fields that develop at the domain surface (see Fig. 5.1). These favor an antiparallel orientation of the OP in neighboring domains, making it energetically highly unfavorable, and ultimately impossible, to have a large single uniform domain when the sample size increases.

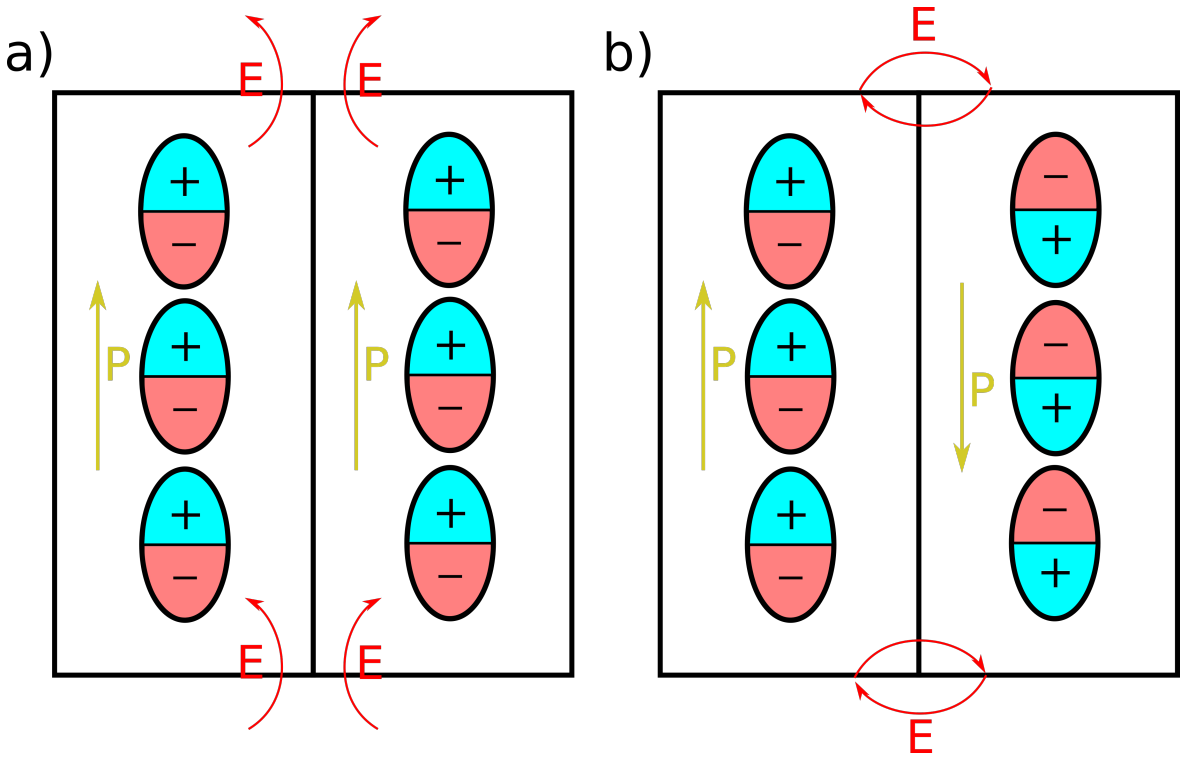

Figure 5.1: **Depolarizing fields.** a) A single domain. b) At a domain wall between two domains with opposite polarization. In both panels, the dipoles are shown by the ovals leading to the polarization denoted by the yellow arrows. The associated depolarizing electric fields are shown by the red arrows. The orientation of these fields is such that for the single domain in panel (a) the depolarizing energy is large compared with that of the two domains in panel (b).

It is thus clear that DWs will be present more often than not, with their density influenced by factors such as poling, cooling rate, and sample quality [105–107]. We focus here on the DWs that are present in ferroelectric materials.

Another interesting observation is that, even though DWs occupy only a fraction of the entire volume, they can lead to the biggest contributions to macroscopic effects [108]. Indeed, most of the research into DWs was originally focused on their dynamics, since switching in ferroelectric materials is mainly a result of domain nucleation and associated DW movement [109, 110]. This is termed as *extrinsic* switching since it depends on the morphology of the sample, i.e. domain and DW distribution, rather than the microscopics and properties of individual unit cells [111]. The reason why extrinsic switching is usually favored can be understood from the following energetic argument. When an external electric field is applied to the sample, it is energetically more favorable for the DWs to move in order to grow the favored domains[1], rather than to uniformly rotate the polarization in the domain as a whole. The latter requires overcoming the prohibitively large energy barrier that separates different orientations of the polarization [112]. This uniform rotation is called *intrinsic* switching, since it can be described by the microscopics of a single unit cell, i.e. only depends on the properties of the material, and does not depend on the sample's domain and DW pattern [111]. This relatively low energy cost associated with the DW movement will also turn out to be one of the main contributors to the subject of this Chapter: the mechanical softening at purely ferroelectric, non-ferroelastic DWs.

Because of the scaling down of technological devices into the nanoscale realm, the focus has more and more shifted towards the DWs themselves as the subject of study, rather than just as being the boundaries between domains. The physics that govern the region of the DW is usually richer than that of the domains. One of the reasons is that, as we mentioned before, the OP is locally forced away from the energetic minimum. In the case of a double-well potential (or so-called Mexican hat potential), associated with many second-order phase transitions, the OP at the center of the wall is at the top of the barrier. The curvature of the energy potential is inverted at this top, which has been argued to make perturbing the OP easier at the DW [113]. The electronic band structure is also different due to the local structural differences in the wall compared with the domains, which can lead to enhanced conductivity, photovoltages, and current rectification [114–117].

In the extreme case, certain ferroelectric DWs can even become conductive, opening the door to very promising technological applications [118]. One example is in information storage devices, where the small size of the DWs is beneficial for the information density. It was shown by Seidel et al.[118] that the conducting DWs can be created or destroyed at will by applying electric fields between opposing electrodes. This is used to write the "data" by changing the conductivity of the device in well-defined increments. Probing the conductivity is then equivalent to reading the "data".

While this kind of technological promise has historically driven most of the research of DWs towards their electronic properties, interest in their mechanical characteristics has increased in more recent years. This field is much less developed and has many

[1] Domains with the polarization along the electric field.

outstanding questions.

Before continuing, it is useful to first define the elastic strain tensor ε_{ij} as the symmetrized gradient of the deformation u:

$$\varepsilon_{ij} = \frac{1}{2}(\partial_i u_j + \partial_j u_i), \tag{5.1}$$

where the indices i, j iterate through x, y, z. The vector $\boldsymbol{u}(\boldsymbol{r})$ relates points $\boldsymbol{r}$ in the reference structure to $\boldsymbol{r}+\boldsymbol{u}(\boldsymbol{r})$ in the deformed structure. The strain arises in ferroelectric materials as a secondary OP due to the electrostrictive coupling to the polarization P. Its contribution to the free energy density can be written as:

$$f_q = -q_{ijkl}\varepsilon_{ij}P_k P_l, \tag{5.2}$$

where q_{ijkl} denotes the strength of the coupling, the indices i, j, k, l again iterate through x, y, z, and Einstein summation over repeated indices is implied. The longitudinal part, $q_{iiii}\varepsilon_{ii}(P_i)^2$, usually leads to the largest contribution to the strain [119], causing a tensile strain ($\varepsilon_{ii} > 0$) and a stretching of the material along P_i [120].

Due to the high degree of symmetry in crystals, many equivalent orientations of P are possible, each with an associated strain. The DWs separating these are equally numerous and have a distinct strain texture due to the variation of P across the DW.

For example, a 180° degree DW separates domains with completely anti-parallel P vectors. Due to the square dependence on P of the energy in Eq. (5.2), ε will be identical in both domains. Still, the different values of P inside the wall versus in the domains will cause a local variation of ε. More precisely, the strain is diminished at the wall since $P = 0$, leading to an indentation at the surface of the material. As we will thoroughly discuss below, this local strain variation lies at the heart of the mechanical softening of the 180° DW.

Other types of DW such as 90° DWs instead separate domains with different strain textures, which are referred to as twin domains, and are consequently separated by twin or ferroelastic DWs. See Refs. [120–122] for a more in-depth study of the possible domains and domain walls in ferroelectrics.

The mechanical properties of ferroelectric DWs are not only of fundamental but also of technological interest. It has been shown that ferroelectric-ferroelastic DWs can be moved by applying stress [123]. This may not be so surprising, since the different strain textures of the domains interact differently with the mechanical perturbation, causing a force imbalance on the DW and an associated movement. More interesting, perhaps, is the fact that the polarization can be directly influenced by mechanical means, for example through the flexoelectric effect, whose contribution to the energy density can be written as:

$$f_{fl} = \frac{1}{2}\Gamma_{ijkl}(\varepsilon_{ij}\partial_k P_l - P_l\partial_k\varepsilon_{ij}), \tag{5.3}$$

where Γ_{ijkl} is the flexoelectric tensor. An applied strain gradient $\partial_j\varepsilon_{kl}$ will thus appear as an effective internal electric field $E_i = -\frac{\partial f}{\partial P_i} = \Gamma_{ijkl}\partial_j\varepsilon_{kl}$, coupling directly to P_i. While this effect is generally small (i.e. the Γ_{ijkl} are small), the size of strain gradients scales inversely with the size of the sample, meaning that it becomes increasingly

more important at the nanoscale of current state-of-the-art electronic devices. Thus, using a tip in contact with the material to apply such a strain gradient allows one to mechanically write domain patterns and DWs at will [124–127].

In this Chapter we discuss the mechanical softening of 180°, purely ferroelectric DWs. They are non ferroelastic in the sense that they separate domains that have identical strain textures. A similar softening has been previously observed and studied for ferroelastic DWs [113, 128], but purely ferroelectric DWs have largely flown under the radar of such mechanical studies. One reason is that the width of 180° DWs is on the order of a couple of unit cells (5 - 20 Å[129]), and since they do not separate domains with different strains, they were perceived too small to be detected by mechanical means. This is because these studies usually involve the application of a tip to the surface of the sample, and the contact radius of such a tip is at least 100 unit cells. As mentioned before, however, even 180° DWs have a distinct strain texture associated with them, which extends much further than the narrow region in which the polarization reverses. This texture can be picked up mechanically by the applied tip and ultimately allows one to make the experimental observations that will be discussed in the next Section, which were the impetus of the research presented in this Chapter.

From the practical point of view, this mechanical detection of ferroelectric DWs means that they can be probed without applying a bias voltage, which may prove useful for conducting ferroelectrics. Moreover, since phonon spectra are determined by the stiffness of the material, the softer DWs will harbor phonon modes with lower speeds. In turn, this may result in effects such as phonon refraction or even total internal reflection inside the walls, turning the DWs into "phonon waveguides". Because heat is transported by phonons, this would allow for heat propagation through the DWs with little dissipation. From the ability to create and destroy 180° DWs by voltage, regular patterns with internal elastic contrast could be created, effectively leading to a phononic crystal. This is interesting, since periodically poled ferroelectric crystals are already used in photonic applications [130].

We start in Sec. 5.2 by introducing the experimental techniques and observations that lie at the base of this Chapter. Afterwards, we continue with a short overview of the crystalline properties of $BaTiO_3$ in Sec. 5.3, an archetypal example of a ferroelectric perovskite. This is followed by a detailed theoretical study in Sec. 5.4, a description of our numerical simulations in Sec. 5.5, and a discussion of the obtained results in Sec. 5.6. Finally, we conclude by summarizing the results in Sec. 5.7.

5.2 Experimental methods and results

In this Section, we summarize the experiments performed by the group of Prof. Catalan that were the impetus of this research [131]. In order to determine the generality of the DW softening, three single crystal samples were studied: $LiNbO_3$, $BaTiO_3$, and $PbTiO_3$. It was found that all three show the same behavior, allowing us to focus on $BaTiO_3$. The results of the experimental measurements are shown in Fig. 5.2.

Piezoresponse force microscopy (PFM) [132] was used to determine the domain structure of the sample, displayed in panels (a) and (c). In PFM, the mechanical

response of an electrically conductive tip in contact with the sample is measured when an alternating current voltage is applied to the sample. Because of the piezoelectricity that is present in any ferroelectric material, this alternating current field leads to a periodic expansion and contraction of the sample, which is detected through the deflection of a laser beam that shines on the cantilever that holds the tip. As we will discuss further below (see 5.4.3), the piezoelectric coefficients have opposite signs for the up versus down polarized domains, meaning that the phase of the oscillation can be measured as a probe for the orientation of the polarization. These phases are exactly what is shown in panels (a,c) of Fig. 5.2. The amplitude of the oscillation gives an idea of the absolute value of the polarization, which leads to the darker regions of the DWs in panel (d) of the same figure. Since the PFM measurements are performed for an out-of-plane direction, the variations in the color signature of the in–plane polarization in the bottom right domain of panels (c-f) in Fig. 5.2 is an indication of the noise of the measurements rather than an actual orientation of the polarization, since any in-plane direction should result in the same PFM phase. In order to accurately map the in–plane polarized domains, one would have to use PFM in a perpendicular configuration, however, we are mostly interested in the out-of-plane polarization domains so these latter were omitted in these experiments.

Turning back to the analysis of the domains in Fig. 5.2, we can identify multiple different kinds: in the region shown in panels (a,b) domains with out-of-plane (c-direction) polarization are found, whereas panels (c-f) display a more complex region with both out-of-plane and in–plane (a-direction) polarization. The top-left portion of these latter panels demonstrates the existence of bubble domains with out-of-plane polarization and curved 180° DWs. The bottom right portion shows an area with in-plane domains separated by straight 180° DWs. On the boundary between these two regions, we find a 90° twin DW, which is different from 180° DWs because it separates domains with different polarization as well as strain.

In order to probe the spatial variation of the stiffness of the sample, measurements based on CRFM were performed. This technique is based on scanning probe microscopy where an atomic force microscopy tip is placed on a cantilever and is brought into contact with the surface of the sample (see Fig. 5.3 for a pictorial representation). The maximal mechanical load was 20 micro Newtons, and the surface contact radius of the tip is estimated to be 7 nm. The combined system of the cantilever and the sample then acts as a series of springs, whose resonance frequency can be measured as a probe of the local stiffness of the sample [133]. In a nutshell, Hooke's law states that the resonance frequency of a linear spring is given by $\omega = \sqrt{\frac{k}{m}}$, thus when the sample has a higher stiffness k, it leads to a higher resonance frequency of the tip-sample spring. A map of the local stiffness of the sample is then created by scanning the tip across the sample while measuring this resonance frequency, as shown in Fig. 5.2(b,e). The only limiting factor of the spatial resolution is the scanning speed and total duration of the experiment. A clear contrast can be observed between soft areas (brown) close to the wall and harder areas (purple) inside the domains, with an apparent reduction of the stiffness by $\approx 19\%$ at the walls.

The experimental observations hint at the strain texture that is associated with the

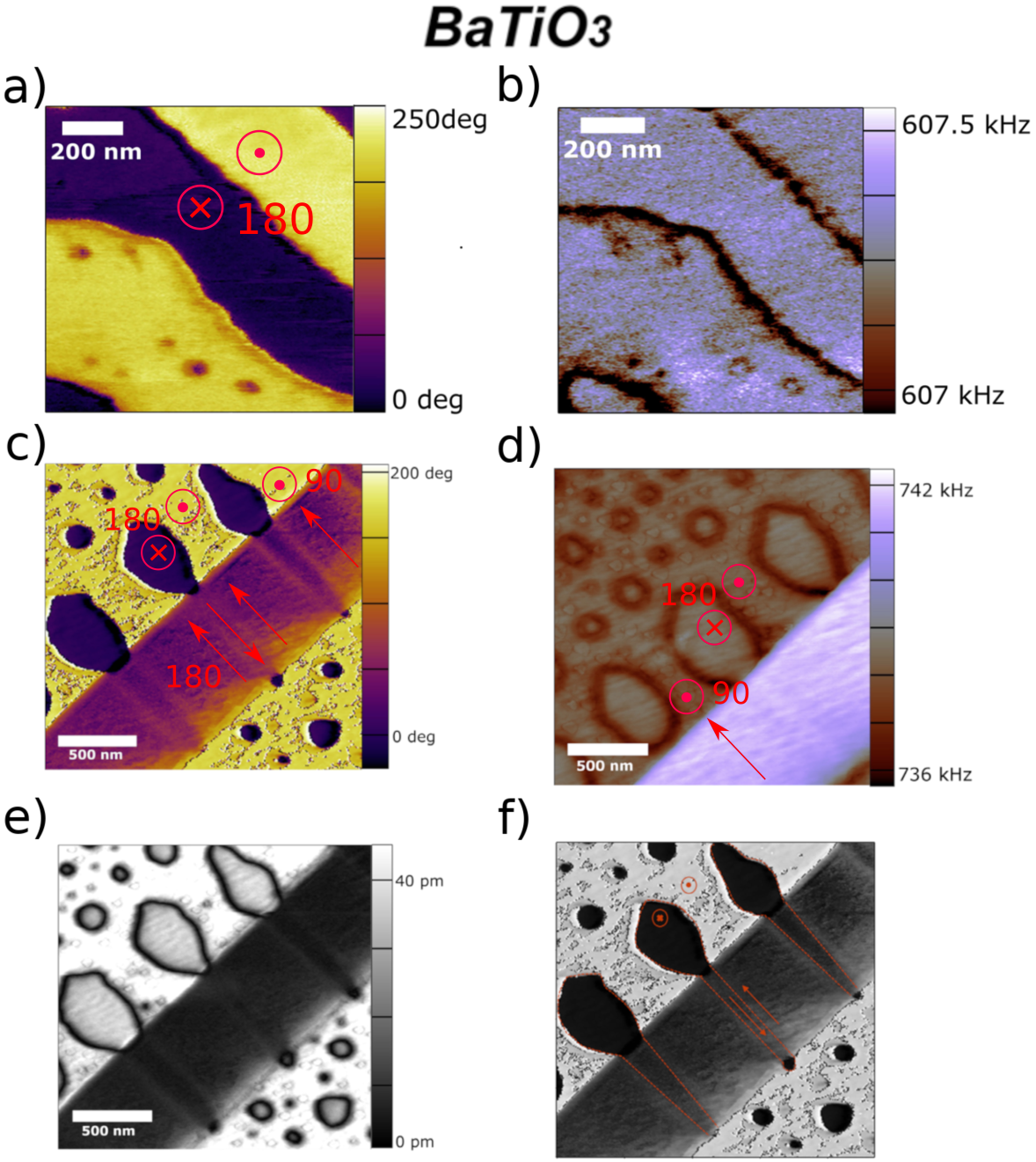

Figure 5.2: **Experimental Measurements** Two regions of the BTO sample are characterized. Panels (a,b) show a region with mostly straight DWs. Panels (c-f) show a more complex region with bubble domains, and a twin wall separating the top-left area with out-of-plane polarization from the bottom right area with in-plane polarization (along the *a*-direction). Panels (a,c) show the PFM phase, and panels (b,d) the CRFM measurements demonstrating softer DW regions (brown) and stiffer domains (purple). Panel (e) shows the out-of-plane PFM amplitude, and panel (f) displays a schematic representation of the polarization, reconstructed from these measurements. The red vectors indicate some orientations of the polarization, and the numbers at the DWs denote the angle between the polarization of the neighboring domains.

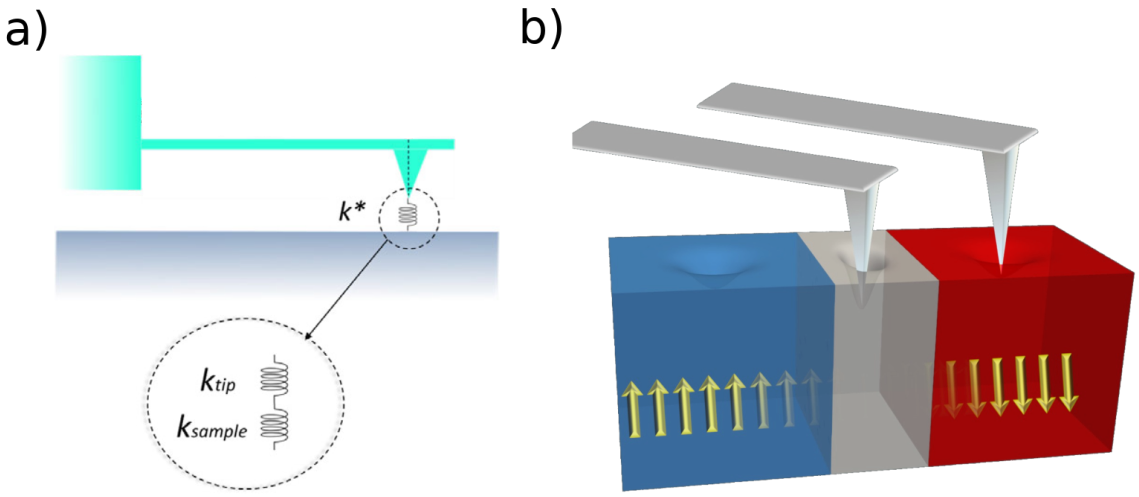

Figure 5.3: **Schematic of the CRFM setup.** a) The tip is placed on a cantilever and brought into contact with the sample surface. The combined cantilever-surface system acts as a series of two springs, with spring constants indicated by k_{tip} and k_{sample}, respectively. b) A pictorial representation of the 180° domain wall. The polarization direction is indicated by the arrows, and up and down domains are colored blue and red, respectively. The increased depth of indentation at the wall indicates the softening effect.

ferroelectric DWs as a large contributor to the softening. Indeed, the softer regions (brown in Fig. 5.2(b,e)) extend up to 70 nm away from the DWs, much farther than the width of the region wherein the polarization reverses (a couple of unit cells or 5 - 20 Å[129]). This argument is strengthened by the fact that the soft regions are even more pronounced around the bubble DWs in panel (e) than around the straight DWs in panel (b). Indeed, it is known that strain textures of round DWs decay as a power-law as compared with the exponential decay away from straight DWs [134], whereas the length scale associated with the reversal of the polarization remains the same for both types of DW.

In order to verify that the application of the tip to the surface does not change the domain morphology, up to 10 sequential measurements were performed, the results of which did not show a significant variation. As mentioned in the introduction, it is possible to switch the polarization mechanically through the flexoelectric effect (see Eq.5.3), but the tip needs to be applied with much greater force than in these experiments. Finally, the CRFM tip is conductive and grounded in a short-circuit configuration during the measurements, allowing for polarization charge screening.

This concludes the overview of the experimental measurements performed by C. Stefani et al. in Ref. [131] that lie at the base of this Chapter. We now turn to a short summary of $BaTiO_3$.

5.3 Barium titanate

As mentioned previously, $BaTiO_3$ is not special from the point of view of the DW softening, and all 180° ferroelectric DWs should demonstrate the same behavior.

It is chosen here because it is a well studied archetypal example of an ABO_3 perovskite. It has a ferroelectric polarization $P \approx 30 \times 10^5 \mu C/m^2$ at room temperature [75, 76, 135], and due to its excellent dielectric, piezoelectric and photorefractive properties, it can be found in many devices like capacitors [136], electromechanical transducers [137] and nonlinear optics [138].

The crystalline structure of $BaTiO_3$ is shown in Fig. 5.4. Starting from the cubic paraelectric $Pm3m$ phase at high temperature (panel (a)), it undergoes phase transitions at 393 K, 273 K and 183 K to the ferroelectric tetragonal $P4mm$ (panel (b)), orthorhombic $Amm2$ and rhombohedral $R3m$ phases, respectively [75, 76, 120]. The microscopic origin of the ferroelectricity in $BaTiO_3$ has previously been studied with variational DFT calculations [139], uncovering the intricate role that the hybridization between Ti and O orbitals plays. This leads to the Born effective charges of the Ti and O ions to be quite different from what would be expected from a purely ionic picture. The Born effective charge tensor $Z^*_{\kappa,\gamma\alpha}$ is defined in terms of the change in the γ component of the polarization that occurs due to an infinitesimal periodic displacement δ of atom κ in the direction α:

$$Z^*_{\kappa,\gamma\alpha} = Z_\kappa \delta_{\gamma\alpha} + \Delta Z_{\kappa,\gamma\alpha}. \tag{5.4}$$

There are thus two contributions: Z_κ is the ionic charge of the atom, and $\Delta Z_{\kappa,\gamma\alpha}$ is the electronic contribution due to the displacement. Z_κ is then equal to +2 for Ba, +4 for Ti, and -2 for O, if the electron charge is taken to be -1. From the DFT calculations, it was found that the electronic contribution $\Delta Z_{\kappa,\gamma\alpha}$ due to hybridization is quite significant. This leads to the total Born effective charges for Ti and O to be $Z^* = 7.29$, and $Z^*_{||} = -5.75$, respectively. The $||$ in the latter denotes that the value was calculated for a movement of the oxygen along the O–Ti bond. These large electronic contributions stem from the strong variation of the hybridization between O $2p$ and Ti $3d$ orbitals as the atoms are displaced. For further details, see Ref. [139].

All experiments were performed at room temperature, so we focus on the tetragonal phase shown in Fig. 5.4(b).

5.4 Theory

Three possible mechanisms to explain the softening of purely ferroelectric DWs were put forward by Tsuji et al. [140]: the accumulation of defects (oxygen vacancies) at DWs, reduced depolarization energy created by piezoelectricity at the DWs, and the existence of DW localized phonon modes [141] (e.g. breathing and sliding). We will discuss each of these contributions, with a more detailed investigation into the last one. First, we introduce the continuum Ginzburg-Landau-Devonshire (GLD) model that forms the backbone of the theoretical description. We also show how the strain texture of the wall appears, and how more naive arguments fail to explain the softening.

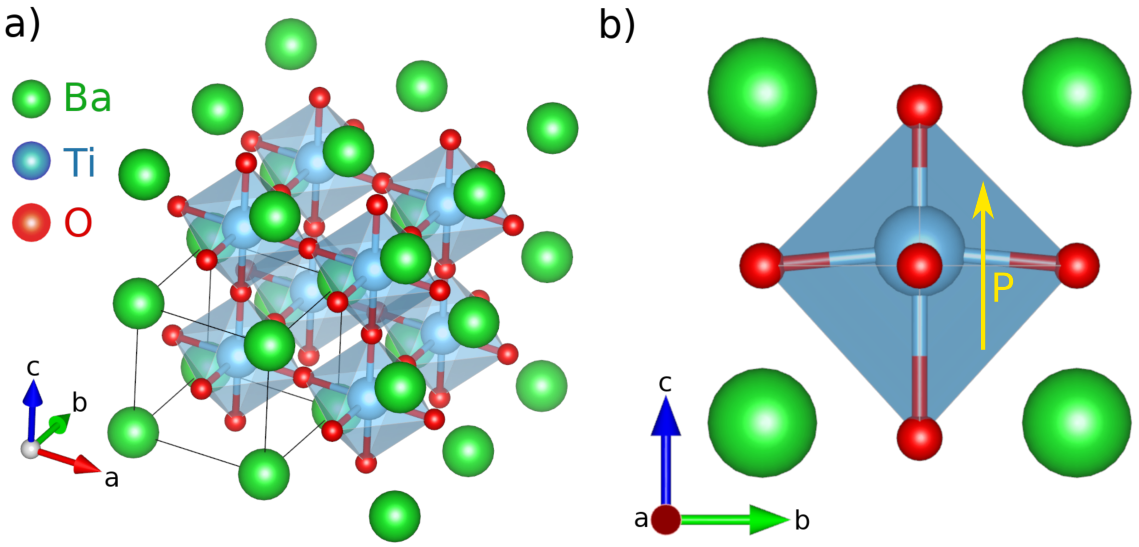

Figure 5.4: **Crystal structure of $BaTiO_3$.** a) Paraelectric $Pm3m$ phase. b) Unit cell of the tetragonal $P4mm$ phase with the associated polarization in yellow. The Oxygen octahedra around Ti are displayed as the shaded polygons.

5.4.1 Ginzburg-Landau-Devonshire model

The model that we use is based on the developments in Refs. [120, 129, 142]. We chose a continuum model because of the mesoscopic length scales that are involved with the problem. One could argue that this simplification is detrimental to the description of the very sharp DWs. Especially to describe the movement of the DW, it is necessary to take the Peierls-Nabarro barriers into account that exist due to the lattice structure. Naively, it seems that only atomistic first-principles based calculations manage to reproduce these accurately [143], since in a perfect continuum picture no such barriers exist. However, as we will touch on in further detail when the simulation technique is discussed in Section 5.5, a numerical analog to these inter-cell barriers appears [144].

A fully microscopic ab-initio simulation[2] of the strain mediated softening is infeasible from the computational point of view, requiring a dynamic calculation describing the movements of 10s of thousands of atoms during a period of many seconds.

We therefore turn our attention to the GLD model. The free energy density in terms of the primary OP for the ferroelectric polarization P and elastic strain slave

[2]Using DFT calculations, for example.

α		G	$\mathrm{Jm^3C^{-2}}$	q	$\mathrm{JmC^{-2}}$
α_1	$3.34 \cdot 10^5(T-381)$ $\mathrm{JmC^{-2}}$	G_{11}	$51 \cdot 10^{-11}$	q_{11}	$14.2 \cdot 10^9$
α_{11}	$4.68 \cdot 10^6(T-393) - 2.02 \cdot 10^8$ $\mathrm{Jm^5C^{-4}}$	G_{12}	$-2 \cdot 10^{-11}$	q_{12}	$-0.74 \cdot 10^9$
α_{12}	$3.23 \cdot 10^8$ $\mathrm{Jm^5C^{-4}}$	G_{44}	$2 \cdot 10^{-11}$	q_{44}	$1.57 \cdot 10^9$
		C	$\mathrm{Jm^{-3}}$		
α_{111}	$-5.52 \cdot 10^7(T-393) + 2.76 \cdot 10^6$ $\mathrm{Jm^9C^{-4}}$	C_{11}	$27.5 \cdot 10^{10}$		
α_{112}	$4.47 \cdot 10^9 \mathrm{Jm^9C^{-4}}$	C_{12}	$17.9 \cdot 10^{10}$		
α_{123}	$4.91 \cdot 10^9 \mathrm{Jm^9C^{-4}}$	C_{44}	$5.43 \cdot 10^{10}$		

Table 5.1: **GLD model parameters for $BaTiO_3$.** Voigt notation [145] is used to limit the amount of indices, e.g. $C_{11} = C_{zzzz}$, $C_{12} = C_{xxzz}$ and $C_{44} = C_{xzxz}$. All coefficients are taken from Ref. [120]. The temperature T is taken to be 300 K in the simulations.

OP $\varepsilon_{ij} = \frac{1}{2}(\partial_i u_j + \partial_j u_i)$ can be written as:

$$f = f_L + f_G + f_c + f_q + f_{fl}, \tag{5.5}$$
$$f_L = \alpha_{ij}(T)P_iP_j + \alpha_{ijkl}(T)P_iP_jP_kP_l + \alpha_{ijklmn}P_iP_jP_kP_lP_mP_n, \tag{5.6}$$
$$f_G = \frac{1}{2}G_{ijkl}\partial_i P_j \partial_k P_l, \tag{5.7}$$
$$f_c = \frac{1}{2}C_{ijkl}\varepsilon_{ij}\varepsilon_{kl}, \tag{5.8}$$
$$f_q = -q_{ijkl}\varepsilon_{ij}P_kP_l, \tag{5.9}$$
$$f_{fl} = \frac{1}{2}\Gamma_{ijkl}(\varepsilon_{ij}\partial_k P_l - P_k\partial_l\varepsilon_{ij}), \tag{5.10}$$

where ∂_i signify spatial derivatives, and the indices enumerate x, y, z with an implied summation over repeated ones. The first term is the Landau free energy which describes the phase transition and formation of the ferroelectic polarization P. Both the second and fourth-order coefficients α_{ij} and α_{ijkl} are temperature dependent and switch sign at the phase transition temperature. This means that a sixth-order term with α_{ijklmn} has to be included in order to bound P below the transition temperature. The second term f_G denotes the Ginzburg contribution to the energy, penalizing the spatial variation of P. This term influences the width of DWs, where a larger G leads to wider walls and vice versa. The elastic energy density is described by f_c with stiffness tensor C_{ijkl}, which has the form of the standard Hooke's law. f_q signifies the electrostriction, which is the main term that couples the polarization to the strain, and causes the domains to be stretched along the direction of the polarization. It is the balance between this term and the elastic one that leads to the strain texture associated with the wall. Lastly, to be complete, we can include the flexoelectric contribution f_{fl}, coupling gradients of strain to P and vice versa. In the results here reported, we chose to neglect it since we found from our simulations that it leads to tiny effects that do not influence the behavior we seek to explain. The coefficients of the model for $BaTiO_3$ are reported in Tab. 5.1, where due to the parent cubic symmetry, only a limited set of these is unique. For example $C_{xxxx} = C_{yyyy} = C_{zzzz}$, and $C_{xyxy} = C_{yxyx} = C_{yzyz} = C_{zyzy} = C_{xzxz} = C_{zxzx}$, and similar relations exist for G, q, and f.

To find the static equilibrium state in the most general sense, the integrated free

energy $F[P,\varepsilon] = \int d^3x\, f[P(x),\varepsilon(x)])$ needs to be minimized, for which the variational method can be used. This leads to the well-known Euler-Lagrange equations [120, 121]:

$$\frac{\partial}{\partial x_j}\left(\frac{\partial f}{\partial P_{i,j}}\right) - \frac{\partial f}{\partial P_i} = 0, \tag{5.11}$$

$$\frac{\partial}{\partial x_j}\frac{\partial f}{\partial \varepsilon_{ij}} = 0, \tag{5.12}$$

where $P_{i,j} = \partial_j P_i$ and the last equation is a result of the stress-free mechanical equilibrium condition.

We start our analysis of the model with the one-dimensional case of a single domain with uniform P_z (which we write P in the following) and ε_{zz} (written as ε) and no external forces, for which Eq. 5.5 reduces to:

$$f = \alpha_1 P^2 + \alpha_{11} P^4 + \alpha_{111} P^6 - q_{11}\varepsilon P^2, \tag{5.13}$$

and Eq. (5.11) subsequently leads to:

$$\frac{\partial f}{\partial \varepsilon} = 0 \Leftrightarrow \varepsilon = \frac{qP^2}{C}, \tag{5.14}$$

$$\frac{\partial f}{\partial P^2} = 0 = \alpha_1 + (2\alpha_{11} - \frac{q^2}{C})P^2 + 3\alpha_{111}P^4 \tag{5.15}$$

$$\Leftrightarrow \tag{5.16}$$

$$P^2 = \frac{-(2\alpha_{11} - \frac{q^2}{C}) + \sqrt{(2\alpha_{11} - \frac{q^2}{C})^2 - 12\alpha_{111}\alpha_1}}{6\alpha_{111}}. \tag{5.17}$$

If the parameters of Tab. 5.1 are filled in, we find $P = \pm 0.311$ C/m^2 and $\varepsilon = 5 \cdot 10^{-3}$. The value of the polarization is higher than the one found when electrostriction is not included ($P = 0.265$ C/m^2 [120]), because the system can lower its energy through $-qP^2\varepsilon$ by increasing P and having tensile strain $\varepsilon > 0$. This is limited by the elastic energy penalty due to C. Similarly, when all terms are included in the full numerical simulation, we find for the domains that P_z is higher still, with values of ± 0.363 C/m^2 and $1.4 \cdot 10^{-2}$ for the polarization and strain, respectively.

The effective stiffness $\tilde{C}_{ijkl}$ can be found by taking the double derivative of the free energy with respect to ε:

$$\tilde{C}_{ijkl} = \frac{\partial^2 f}{\partial \varepsilon_{ij}\partial \varepsilon_{kl}}, \tag{5.18}$$

or, making the same assumptions as above (only P_z and ε_{zz}), we arrive at an effective stiffness of

$$\tilde{C} = C - \frac{q^2}{2\left(\alpha_{11}^2 - 3\alpha_{111}\left(\alpha_1 - \frac{q^2P^2}{C}\right)\right)}. \tag{5.19}$$

Again filling in all the parameters, we find an effective stiffness $\tilde{C}_d = 0.778\,C$ in the domain. At the wall P is zero, and, if there was no shear strain penalty, so is ε. This would then lead to an effective stiffness of $\tilde{C}_w = 0.642\,C = 0.82\,\tilde{C}_d$, according

to Eq. (5.19). While this looks like a triumph for the theory (since the experimental measurements found a 19% softer wall), in reality, the shear elastic constants C_{44} and compatibility relations lead to a nonzero strain ε_{zz} at the wall. From our simulations, we find that ε_{zz} at the surface of the wall has a value of around 40% of the one in the domain (see Fig. 5.5(b)). Filling this value into Eq. (5.19) leads to $\tilde{C}_w = 0.79\,C = 1.01\tilde{C}_d$, i.e. this naive derivation leads to a stiffer rather than softer wall. Our simulations confirm this result, which can thus not explain the experimentally observed softening.

We, therefore, turn to the three previously mentioned, less naive mechanisms: defects, piezoelectricity, and domain wall movement described by localized phonons.

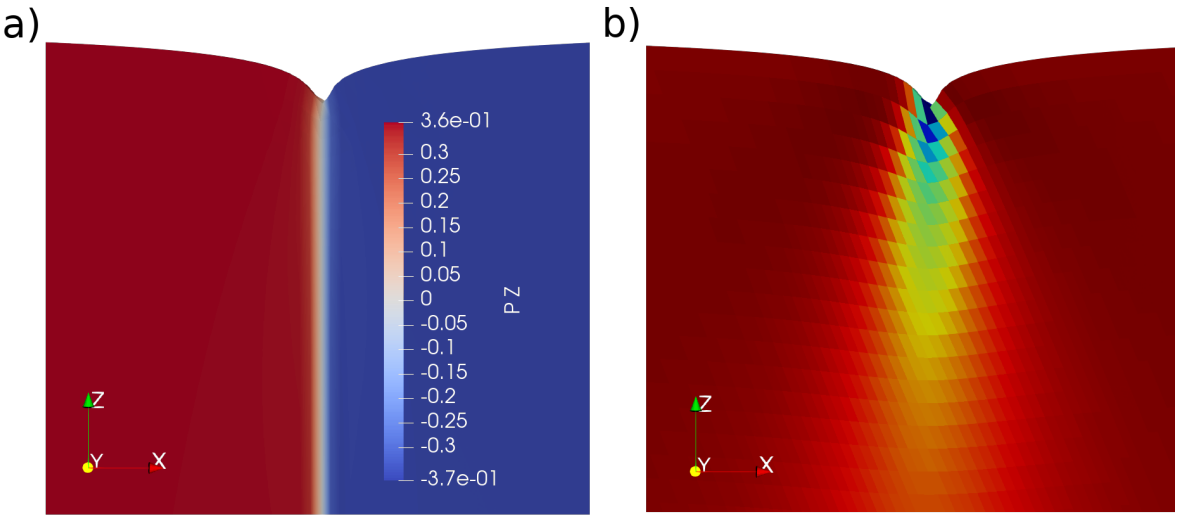

Figure 5.5: **Domain wall profile.** The surface profile an out-of-plane the 180° DW is shown. a) The polarization P_z is denoted by the red and blue coloring. b) The magnitude of ε_{zz} is encoded in the false colors. The enhanced deformation of the geometry illustrates the effect of the strain texture associated with the wall.

5.4.2 Defects

A thorough theoretical study on the behavior of defects in $BaTiO_3$ DWs was done by Xiao et al. in Ref. [146]. It was shown there that a large accumulation of defects was found to exist at 90° DWs, but not in 180° DWs. Looking again at the experimental measurements in Fig. 5.2(b,e,f) we can make an argument that supports this claim. The supposed mechanism for softening due to defects is a weakening of the interatomic bonds since the largest portion of defects are oxygen vacancies [140]. This should be fairly isotropic, or at least orthotropic, in the tetragonal phase of $BaTiO_3$ since it is close to the parent cubic structure. Defect mediated softening should thus not depend on the orientation of the polarization. However, if we compare in Fig. 5.2(e) the stiffness signatures of the 180° DWs with out-of-plane polarization, and those with in-plane polarization, we see that only the former demonstrate the softening. This region of the sample is small enough so that variations in the quality of the sample and

the defect density are small. From these two arguments, we can safely exclude defects as a contributing factor to the DW softening.

5.4.3 Piezoelectricity

The second mechanism that could lead to softening can not be neglected, however [131, 140]. When the tip is applied to the sample it causes a non-uniform pressure field at the surface. It is larger at the center of the contact region and smaller at the edges and decays into the material. This in turn leads to a non-uniform strain which causes a non-uniform polarization through the piezoelectricity $\partial_l P_i \sim e_{ijk}\partial_l \varepsilon_{jk}$, where e_{ijk} are the piezoelectric coefficients. Since the polarization is constituted by electric dipoles, their non-uniform distribution causes bound charges. The tip thus effectively creates internal depolarizing fields, similar to how bound charges at the surface of domains lead to depolarizing fields, as was discussed in the introduction (see Fig. 5.1). As we will show now, these resulting fields are larger in the domain compared with those in the DWs. For illustrative purposes, we look at an example situation, in which the tip is applied along the z-direction, and the DW lies in the yz-plane. See Fig. 5.6 for further details. It is important to bear in mind that the components of the piezoelectric tensor all switch signs across the DW, i.e. $e_{ijk}(P_z) = -e_{ijk}(-P_z)$. Two distinct contributions can then be identified, resulting from the longitudinal and shear parts of the piezoelectric tensor, shown in Fig. 5.6 (a) and (b), respectively.

The longitudinal piezoelectricity leads to a change of the polarization which is given by $P_z - P_z^0 \sim e_{zzz}\varepsilon_{zz}$, where P_z^0 denotes the value of P_z without an applied tip. Moreover, since the pressure field due to the tip leads to a high strain ε_{zz} at the surface that decays into the material, causing $\partial_z P_z \sim e_{zzz}\partial_z \varepsilon_{zz}$ to also be nonzero, which creates additional bound charges. As shown by the + and - in Fig. 5.6(b), the bound charges in the domain are all identical. The resulting depolarizing field and associated energy contribution are large.

If the tip is applied at the DW, however, positive bound charges appear on one side and negative on the other, because of the opposite signs of e_{zzz} in the two domains. The depolarizing fields compensate in this case, and the resulting energy penalty is lower. This could lead to a softening at the DW since this lower energy penalty allows for a deeper indentation and thus results in a softer appearing material. However, as discussed in the experimental Section, the tip is conductive and grounded at all times. This causes short-circuit conditions which completely screen the bound charges created through longitudinal piezoelectricity.

We, therefore, look whether the shear part of the piezoelectricity (see Fig. 5.6(a)) can lead to the softening. When a tip is applied, this part generates a small in-plane component to the polarization, $P_x \sim e_{xzz}\,\varepsilon_{zz}$. Because of the round shape of the tip, the pressure field is non-uniform and the resulting strain varies as $\partial_x \varepsilon_{zz}$ In turn, the polarization also varies as $\partial_x P_x \neq 0$, and associated bound charges are created along the x-direction. Moreover, $\partial_x \varepsilon_{zz}$ is negative on the left side of the tip and positive on the right, causing the resulting bound charges to be oriented in a head-head or tail-tail configuration. This leads to large depolarizing fields in the domain.

If the tip is applied at the DW, instead, where the piezoelectric components switch

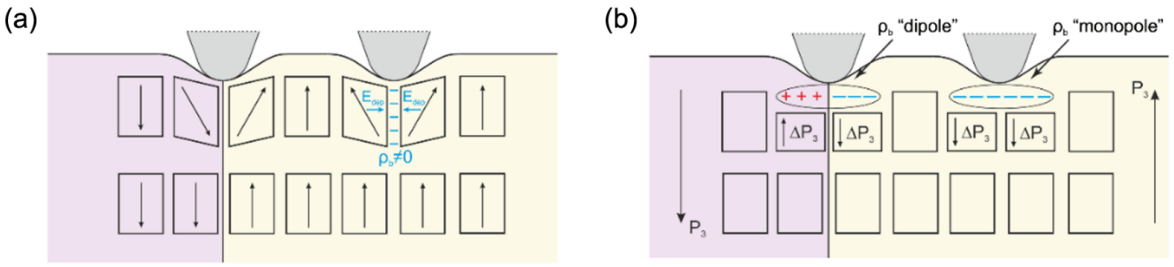

Figure 5.6: **Piezoelectric effect.** A pictorial representation of the contribution of the shear (a) and longitudinal (b) piezoelectric effect. The black arrows denote the direction of the polarization, with the wall located on the boundary between the purple and yellow shaded domains. The tip is represented by the grey bell-shapes, with the resulting change in bound charge in red and blue, and by the + and -. An example of the depolarizing field is shown by the light blue arrows in panel (a). All changes to the polarization due to the applied tip are exaggerated for clarity.

sign, the bound charges along x are created in a head to tail configuration. This leads to a significantly lower depolarizing field compared with the domain case, and the reduced energy penalty results in an apparent DW softening. In this case, the bound charges can not be screened effectively by the short-circuited tip, ultimately resulting in the first nonzero contribution to the softening of ferroelectric DWs.

Simulations similar to those that will be discussed later were performed by our collaborators for a 2D geometry, confirming this mechanism (see Ref. [131] for further details). It was found that that the shear piezoelectricity (Fig. 5.6(a)) leads to the wall appearing 5%-10% softer than the domains. However, this piezoelectric effect is a result of the reversal of the polarization at the DW, and it can thus not account for the wide region of softening observed in the experiments (70 nm). We, therefore, turn to the strain texture of the DW as the possible source of this long-range softening, since it has a much wider profile than the DW itself.

5.4.4 Domain wall localized phonons

The crux of the matter is that due to the fundamentally different structure of the DW, additional soft phonon modes appear which are not present in the domain [141]. The two most important ones are the breathing and sliding modes, shown in Fig. 5.7(a,b), respectively. These can be excited mechanically by the applied tip, ultimately making the DW appear softer. Both are a result of the previously described diminished strain at the wall, resulting in a dip at the surface of the material, as shown in Fig. 5.5. The breathing mode is associated with a change in the width of this dip (see Fig. 5.7(a)). When a tip with a wider radius than the dip is pressed into the material, it will apply a force on either side of the wall, increasing its width. This is favorable for the Ginzburg part $\partial_i P_j \partial_k P_l$ of the free energy density since wider walls have lower $\partial_i P_j$. When the tip is pressed at the domain, we saw that through the piezoelectric effect, the polarization decreases locally. This leads to a nonzero $\partial_i P_j$, in turn resulting in a nonzero contribution to the Ginzburg energy which was previously zero for the domain.

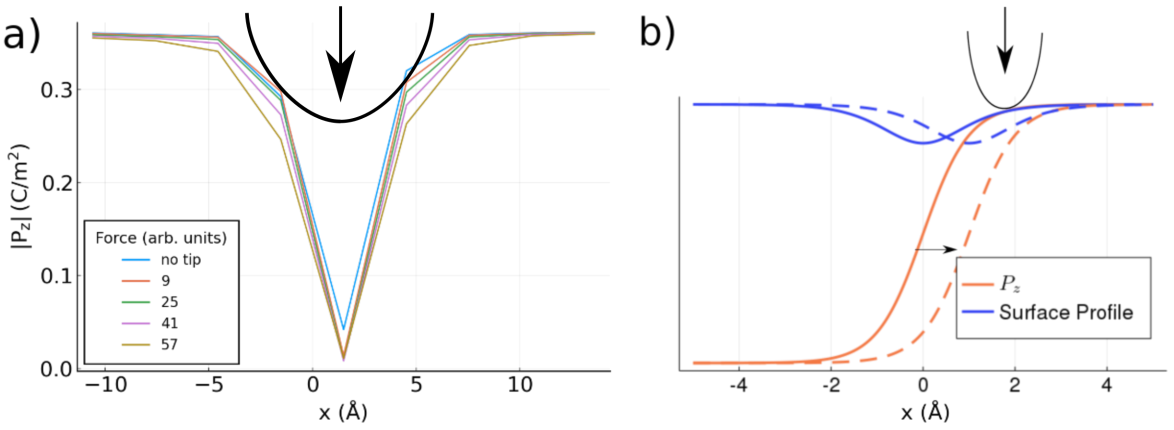

Figure 5.7: **Breathing and Sliding modes.** a) Demonstration of the widening of the DW upon application of a tip, representing a breathing mode. The higher the force of the tip, the wider the wall becomes. The wall is not centered at 0 because of the numerical Peierls-Nabarro and mesh dimensions, however, the applied force is centered exactly above the wall. b) Pictorial demonstration of the sliding mode, which gets excited by the tip, making the wall slide towards it.

The energy difference between these two cases makes the DW appear softer than the domains. However, a similar argument can be made as for the previously discussed piezoelectric contribution in that the tip needs to be in contact with both sides of the DW to maximize the excitation of the breathing mode. Since its contact radius is only around 7 nm, it is hard to believe that the excitation of the breathing mode contributes significantly to the softening observed when the tip is applied 30 nm away from the wall. Moreover, from the two localized DW modes, the breathing is significantly harder than the sliding one, because it is associated with an expensive elastic deformation of the sample. The sliding mode, shown in Fig. 5.7(b), instead describes a rigid motion of the DW perpendicular to its plane, thus not incurring such elastic penalty.

This brings us, finally, to what we claim as the main contributor to the softening effect. Indeed, closer inspection of the energy terms in Eq. (5.5) leads to the conclusion that no energy penalties are incurred by the rigid sliding DW motion in the perfect continuum case. If the tip is then applied in an area where the strain texture associated with the wall is present, it will try to move this profile underneath it in order to achieve mechanical equilibrium. This is because the tensile strain caused by the electrostriction f_q is opposite to the compressive force applied by the tip. To restore mechanical equilibrium, the material needs to balance these two forces. Since the tensile strain is already diminished at the DW, moving it underneath the tip is a relatively inexpensive way to partly achieve this balance. The movement of the preexisting dip towards the tip then leads to relatively large deformation, making the material appear soft. One can say, equivalently, that the presence and excitation of the soft sliding mode lead to a lower energy penalty when the tip is applied. In the domain, this sliding mode is not present leading to a higher energy penalty for the deformation and thus a higher observed stiffness.

While in the ideal continuum case, the sliding mode is completely free, in reality,

this is not the case. As mentioned before, in a real material there are Peierls-Nabarro barriers between the unit cells, possible pinning defects, and electrostatic effects that will increase the energy of the sliding mode. While it is extremely hard to make an analytical description of the behavior, we can still make statements about two extreme situations. If the force applied by the tip is large enough, the wall will fully slide towards it, maximizing the elastic energy gain. If instead, the force is very small, the wall remains inside the original Peierls-Nabarro potential but deviates from the equilibrium position.

A simple free energy expansion can be made to illustrate the latter case. The wall at position x_{DW} (originally zero) is pinned by a parabolic potential with strength a, and perturbed by a tip applying a force F_z at x_{tip}, leading to the energy:

$$E = E_0 - F_z u_z(x_{tip} - x_{DW}) + \frac{1}{2} a x_{DW}^2. \tag{5.20}$$

We expand this equation under the assumption of a small x_{DW}, i.e. that the wall does not move far from the $x_{DW} = 0$ equilibrium case. Minimizing the energy under this assumption, we obtain $x_{DW} = -Fu'(x_{tip})/a$, with a correction to the stiffness $\delta C = u'(x_{tip})^2/a^2$. From this, we can conclude that the effect is greatest when tip is applied where $u'(x_{tip})$ is large, i.e. within the strain variation around the wall caused by the above discussed electrostrictive coupling in Eq. (5.2).

In reality, depending on the size of the tip, where it is applied, and the size of the force, a combination of the two above mentioned extremes will occur. From the experimental observations, we can posit that the applied force is large enough to fully slide the top of the wall towards the center of the tip if it is positioned close enough to the wall. In doing so, the dip at the surface of the wall moves underneath the tip maximizing the elastic energy gain. As discussed before, this leads to a large apparent softening and is most likely to be what happens within the 70 nm region around DWs. Since it is clear from the repeated experimental measurements that the walls do not move permanently, we claim that the lower portion of the wall remains at the center of its original Peierls-Nabarro potential. This is probably due to pinning by defects or the substrate.

Due to the complexity of the model, and the interaction of the strain with the tip, we forfeit the hunt for a purely analytical description and instead proceed with numerical simulations to verify the above statements.

5.5 Methods

There are generally speaking two ways of minimizing the total free energy $F = \int_V d\boldsymbol{r} f$ of the system with volume V: either through solving the system of Euler-Lagrange equations in Eq. (5.11), or by direct minimization of F. Both are completely equivalent on a mathematical level but require different numerical implementations. In our code, we chose the latter. Moreover, since minimizing F w.r.t ε requires a careful consideration of the compatibility conditions between the different elements (so that the material does not break)[147], we chose to use the displacement u instead. This means we rewrite the equations in Eq. (5.5) by filling in $\varepsilon_{ij} = \frac{1}{2}(\partial_i u_j + \partial_j u_i)$.

To solve the model, we thus have to compute and minimize this total free energy by integrating the free density in Eq. (5.5), written in terms of the values and gradients of the two order parameters P and u, over the entire system. In the continuum formulation, these have a value at each point in space and are thus sometimes referred to as fields, with the resulting models often referred to as phase-field models. Finding the values of P and u that minimize the total free energy $F[P,u] = \int_V d\boldsymbol{r} f(\boldsymbol{P}(\boldsymbol{r}), \boldsymbol{u}(\boldsymbol{r}))$ then leads to the equilibrium configuration of the system.

We perform this integration numerically, due to the complexity of Eq. (5.5) and the highly heterogeneous situation that occurs when a tip is applied. The Finite Elements Method (FEM) provides a framework to do exactly that. Its ability to handle complex geometries and large length scales makes it one of the most well-established methods to numerically solve realistic mathematical and physical models (see appendix C for further details).

Using the parameters from previous ab-initio results [120] and reported in Tab. 5.1, we first optimized the equilibrium situation for both a uniform domain and a single domain wall. The result of the latter is shown in Fig. 5.5. A Gaussian force field, $\frac{a}{\sigma\sqrt{2\pi}} e^{-\frac{(x-x_{\text{tip}})^2}{2\sigma^2}}$ with $\sigma = 1 \cdot 10^{-9}$ representing the contact radius and $a = 1 \cdot 10^{-18} \frac{eV}{nm^3}$, was then applied at various positions x_{tip} throughout both geometries.

The single-domain simulation is used to gauge the influence of finite-size effects that are inherently present in our open boundary condition simulations, using a geometry of finite dimensions (L_x, L_y, L_z). If the tip is applied to the side of the geometry, in the case of a single domain, it deforms more than when it is applied to the center because there is less material on one of the sides of the tip to support it. We have tested the extent to which this contributes to our simulations, as demonstrated in Fig. 5.8(a) for different lengths L_x of the geometry. As one could expect, the effect is most influential in simulations with a small geometry. Since this is nonphysical, we use the domain simulation to calculate the amount of such spurious additional deformation and compensate for it in the DW simulation assuming that the finite-size effect is identical since the geometry is the same in both cases.

To conclude this Section, we would like to comment on the issue of the Peierls-Nabarro barriers [148, 149], since they influence the movement of the DW. In essence, they are a result of the non-homogeneity of the crystalline lattice on the unit-cell length scale. This causes the DW to have a preferred center inside the unit cells, usually either on the edge or in the middle. A thorough study from first principles was performed by Meyer et al. [143], where it was correctly stated that only by using this degree of granularity, one can achieve quantitative ab-initio results. The pure continuum GLD model we use does not account for the physical Peierls-Nabarro barriers, as we discussed previously, making the DW sliding completely penalty free, which is at odds with the behavior in real materials. We are thus faced with the commonly reappearing issue of requiring to simulate physics that occur at different length scales.

In this case, however, we are to some extent saved by a spurious numerical effect that mimics the naturally occurring Peierls-Nabarro barriers. This was investigated by Marton in Ref. [144] for the case of $BaTiO_3$. It boils down to the fact that it is numerically favorable to situate the center of the wall at a node rather than inside

an element, because of the approximated interpolation of the fields. In this way, the simulation avoids sampling the paraelectric state, which is at the top of the double-well potential of the Landau part f_l of the energy in Eq. (5.5). When the wall is forced to move across the grid due to the applied tip, it is forced to overcome this high energy configuration in order to transition between equilibrium positions. This in turn results in the numerical analog of the Peierls-Nabarro barrier.

5.6 Results and discussion

Since we implemented our own version of the Finite Element Method, we first performed some consistency checks with previous calculations before turning to the simulations of the DW softening.

The DW energy we obtained is 15.2 mJ/m^2, very close to the value of 16 mJ/m^2 previously found from a first-principles calculation in Ref. [150]. Furthermore, we verified that it is not influenced by the size of the numerical geometry or the density of the mesh, indicating that the numerics of our method does not influence the energetics of the static wall.

To confirm the existence and consistent behavior of the numerical Peierls-Nabarro barriers, we performed simulations where we rigidly shifted the wall from its central position inside the grid, similar to the procedure followed in Ref. [144]. The energy was then calculated at each step in order to get an indication of the numerical Peierls-Nabarro barriers of our mesh. The results for different element sizes are shown in Fig. 5.8(c,d). The barriers are very close to the harmonic shape of the real Peierls-Nabarro barriers for all element sizes, where larger sizes lead to larger barrier energies and periodicity, as expected. In the following simulations, we chose the element size to be 0.3 nm which offers a good balance between the amount of pinning and the computational cost.

We now turn to the DW-localized modes. First, we demonstrate the influence of the breathing mode, shown in Fig. 5.7(a). The absolute value of the polarization is used as an indication of the DW width, and a tip was applied to the center of the wall with varying force. We can see that the wall indeed widens slightly when higher forces are applied, but that the effect is small, and the necessary force to achieve any widening is significantly larger than the experimental one.

As discussed in the theory Section 5.4, the domain wall sliding mode is a more likely candidate to explain the long-range DW softening. To mimic the experimental conditions, we applied the tip force field at various distances away from the wall. In order to minimize the impact of the numerics, more specifically the sampling of the force field, we always centered the tip exactly at a mesh node. This means that the total force applied to the sample by the tip is identical for all simulations. The relative softening is then estimated as the ratio between the surface deformations in the domain and at the wall. Two sets of simulations were performed, one for which the bottom of the wall was pinned to the original equilibrium position in order to mimic a bending of the DW, and one where we let the wall as a whole slide freely. The former behaves very similarly to the latter, except that it acquires an additional penalty due to the

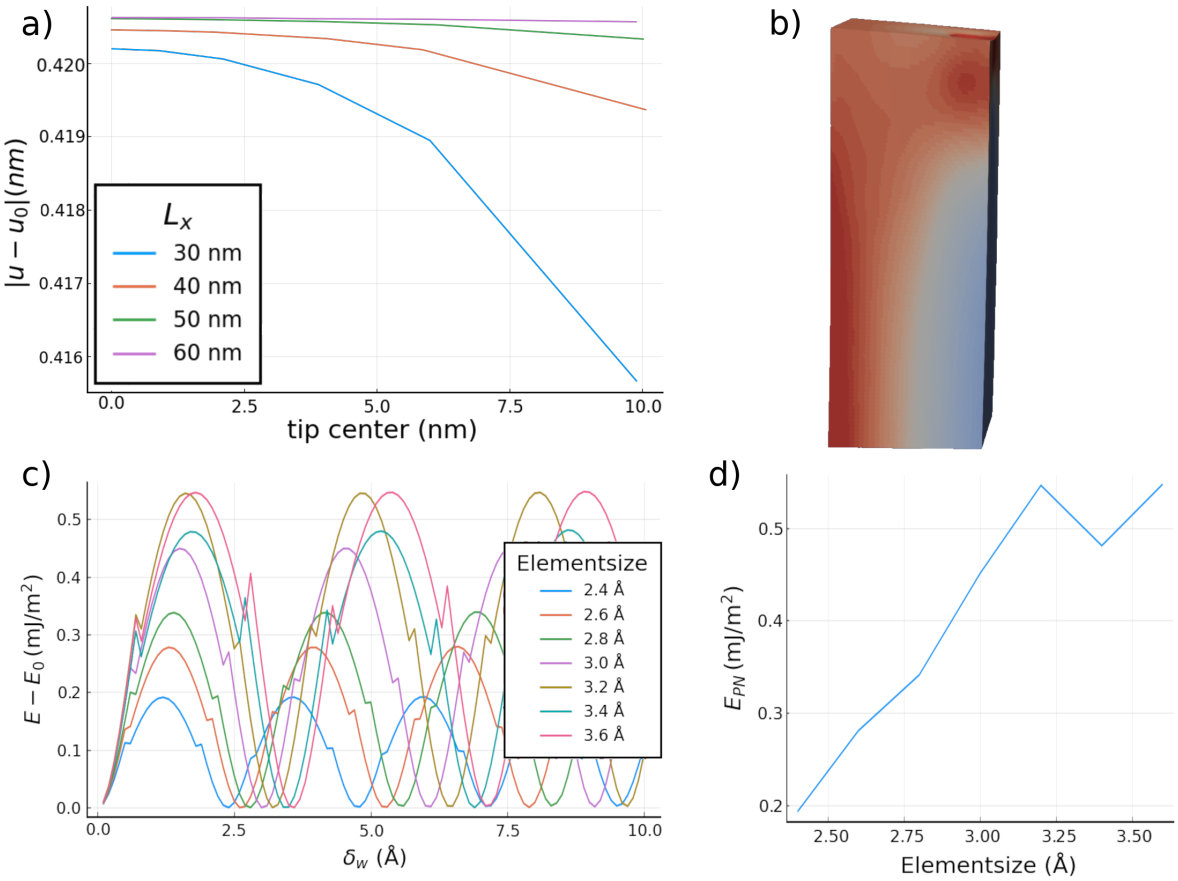

Figure 5.8: **Numerical effects.** a) Maximum indentation of the domain by the applied tip, depending on its center along the x-dimension of the geometry with length L_x. b) Visual demonstration of the asymmetric deformation and ε_{zz} due to open boundary conditions, where the tip is applied close to the edge of the sample. c) The evolution of the energy when the wall is shifted with δ_w away from the original position at 0. This mimics the Peierls-Nabarro barriers of the crystal. The periodicity of the lattice is mimicked by mesh, where the distance between barrier maxima is given by the element size. It is also clear that large element sizes lead to larger barriers. d) The dependence of the Peierls-Nabarro barrier height on the element size.

increased DW area and non-zero Peierls-Nabarro barriers that the DW is located on. The results of the former are shown in Fig. 5.9, and of the latter in Fig. 5.10. As seen in Fig. 5.9(e) and Fig. 5.10(e), and predicted by the above statements, the wall is softest not in the center, but rather at the point where u' or ε_{xz} is highest, leading to the highest force applied to the wall making it bend or slide. Comparing the two simulation protocols, we can also observe that when the wall is allowed to slide, the region where the softening takes place is much wider, and the degree of softening is higher. We find a maximum softening of about 20% in this case, which is remarkably close to the experimental measurements.

The situation in the real sample is probably a combination of these two, the argument for which is as follows. Due to the relatively small z-dimension that we used

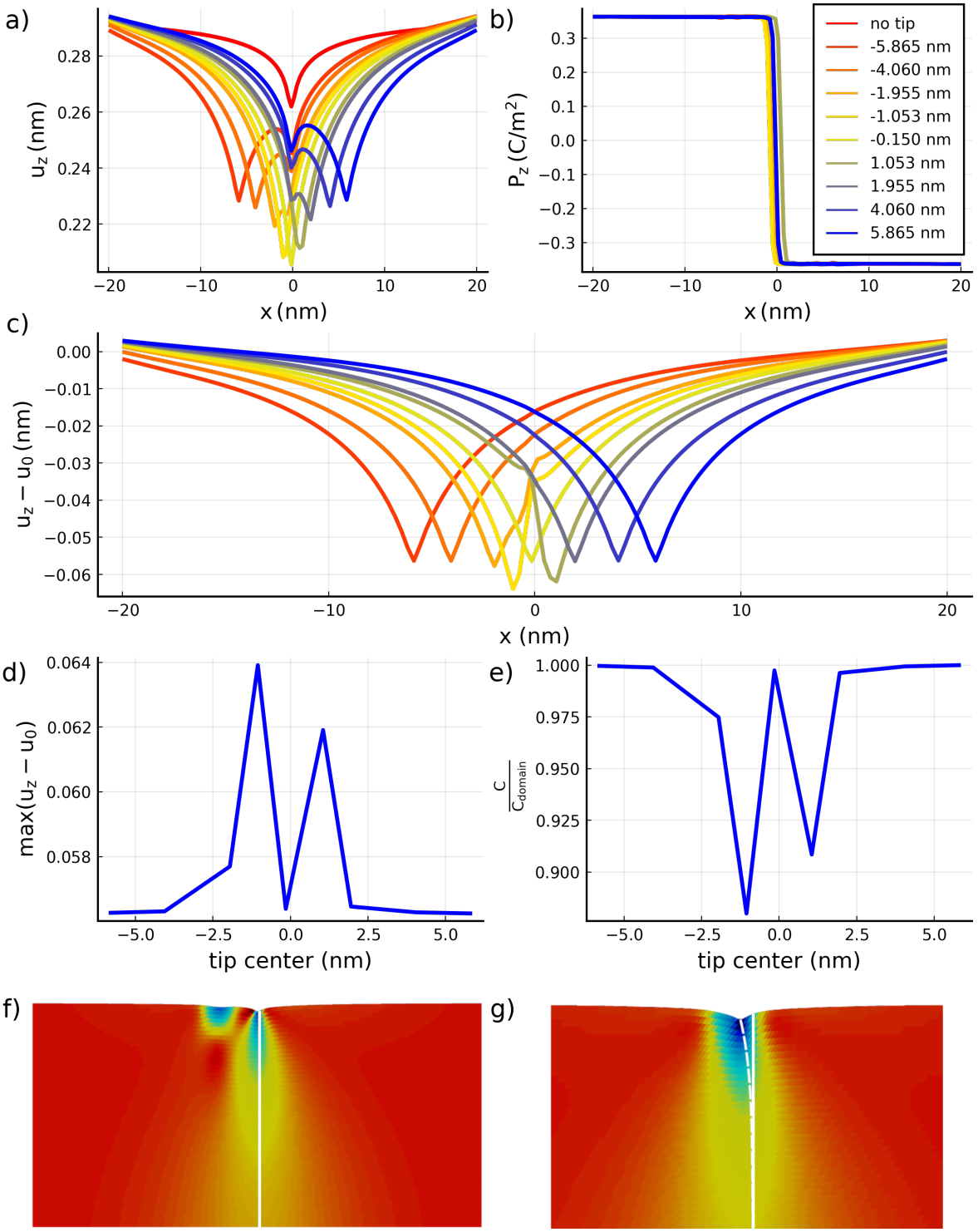

Figure 5.9: **Bending Wall** Simulations where the bottom of the wall is kept fixed to the equilibrium without a tip. In each panel, the coloring indicates the position where the tip is applied to the sample. a) Surface profile of the wall. b) Polarization distribution at the surface. Notice the movement of the wall center when the tip is applied. c) Deformation of the surface after applying the tip. d) Maximum absolute value of the deformation in (c). e) Relative stiffness depending on where the tip is applied. f) Strain profile when the tip is too far fromthe wall to make it bend. The wall is represented by the white line and does not move due to the tip. g) Bending of the wall when the tip is applied close to the wall. The full and dashed white lines denote the position of the wall before and after the tip is applied, respectively.

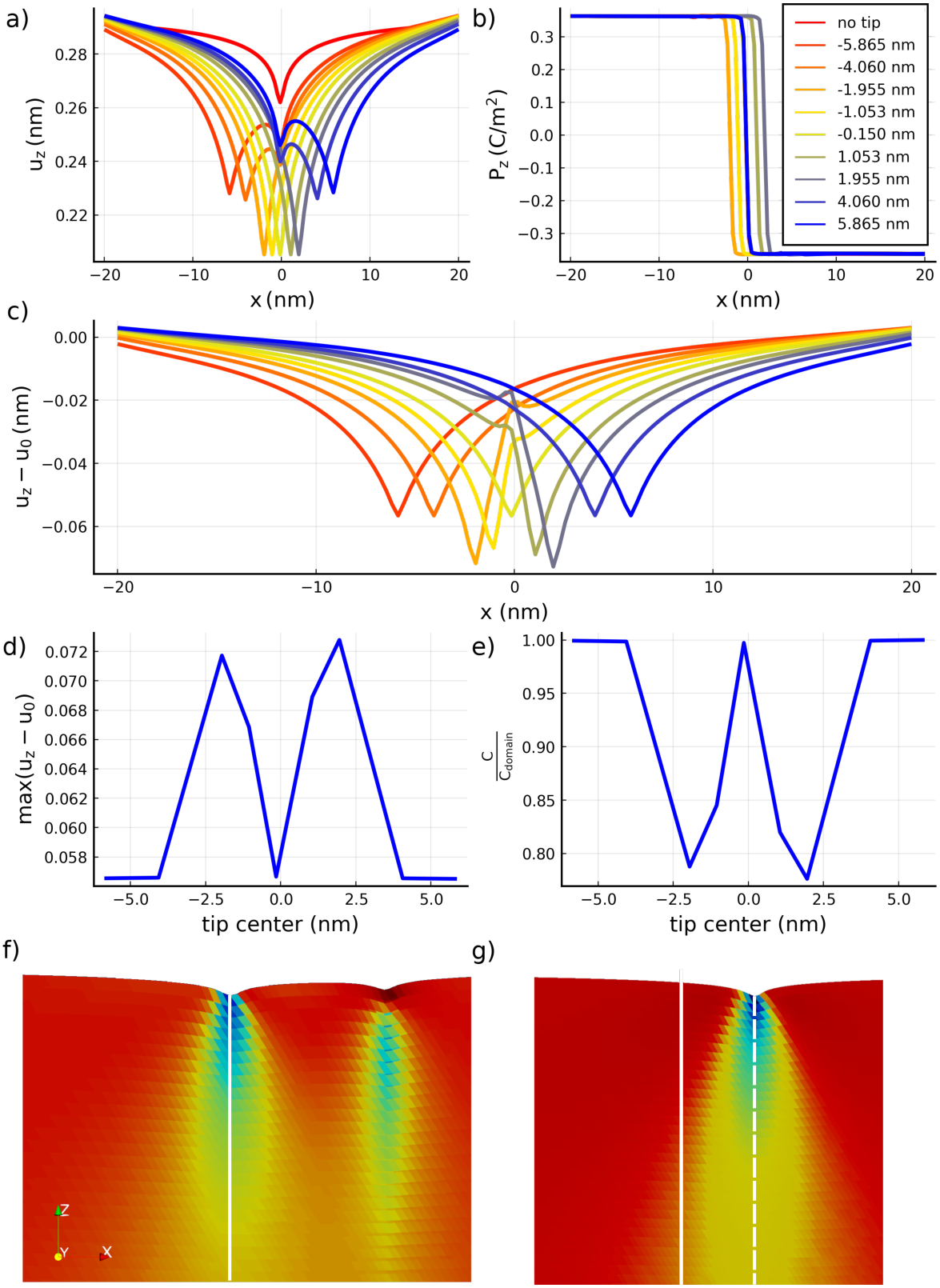

Figure 5.10: **Sliding Wall** Simulations where the bottom of the wall is allowed to change. The panels denote the same as in Fig. 5.9. Allowing the wall to fully slide leads to a bigger softening and wider softening region.

for our simulations (20 nm) compared with the sample in the experiment (0.3 cm), a bending of the wall much more difficult to achieve in our simulations in comparison with reality because the relative increase of the DW area upon bending is much larger. In the real sample the wall, therefore, most likely appears as rigidly sliding towards the tip inside the 70 nm in-plane region around the wall. On the other hand, the wall is most likely pinned inside the material by some defects or the substrate and will move back towards the equilibrium position when the tip moves too far away from it. The full result on large lengthscales is therefore analogous to the bending of the wall in our simulations.

We claim that these lead to the main source of the observed softening in purely ferroelectric DWs.

5.7 Conclusions

In this Chapter we have demonstrated how purely ferroelectric, i.e. non-ferroelastic, 180° DWs can appear mechanically softer than the domains they separate. Using experimental observations as the starting point, we investigated many possible mechanisms and deduced which were most likely to contribute the most. The main observation was that the region of the softening is relatively wide, whereas the ferroelectric DWs are known to be very narrow. This pointed us towards the strain texture as the main property of the DWs that could lead to this softening behavior. Indeed from earlier work by Chen et al. in Ref. [141] we knew that DWs host localized phonon modes. Focusing on the breathing and sliding phonon modes of the DW, we performed Finite Element Method simulations using our in-house code to confirm our suspicions. From our simulations, and further supported by intuitive arguments, we found that the sliding mode plays the biggest role in the DW softening. It is an interesting illustration of the fundamentally different behavior of DWs in comparison with the domains they separate.

On the technological side, the mechanical softening could allow for the efficient mechanical distinction between DWs and domains. If the domains represent a 0 bit and the walls a 1 bit, this would result in the efficient reading of data through the resonance frequency of the tip. Furthermore, the sliding towards the tip of the indentation at the surface of the DW could open the door to mechanically move pre-formed DWs in a thin film sample. The thin film should help reduce the DW pinning by defects and Peierls-Nabarro barriers leading to a higher DW mobility. The fact that no elastic penalty is incurred through the sliding of purely ferroelectric 180° DWs would make such mechanical manipulation of DWs and domain structures in ferroelectrics very efficient. This is in stark contrast to the previously studied twin or ferroelastic DWs, which can also be excited mechanically, but at greatly elevated energy costs since their movement is associated with large elastic deformations.

A

Density Functional Theory

Many of the physics in condensed matter originates from the behavior of electrons inside materials, i.e. the electronic structure, which can be studied quantitatively in two ways.

The first is to formulate an analytical model whose parameters are subsequently fitted to experimental observations. In this case, the Tight-Binding method is a useful tool example that is often employed in condensed matter for its flexibility and simplicity.

The starting point of any Tight-Binding model is the set of orbitals that are used as the basis. In electronic problems, one often uses the valence orbitals of the constituent ions of the crystal [32, 33]. The Hamiltonian can then be constructed as a set of hopping parameters between these orbitals, where the symmetries of the problem are used to limit the set of independent parameters. These hopping parameters are termed as such because they describe the energetics the process of annihilating an electron on the first orbital and creating it on the second. This "hops" the electron between the two. The limited set of model parameters can then be fitted to experimental measurements such as angle resolved photoemission spectroscopy [151].

The topic of this Section, however, is the second way of calculating the electronic structure, i.e. from first principles, using only the ions and crystalline structure as the input. While historically there have multiple methods of achieving this (e.g. Hartree-Fock), we here focus specifically on the DFT method. Ever since its theoretical inception in the sixties in the seminal works of P. Hohenberg, W. Kohn, and L. J. Sham [152, 153], and especially after later numerical developments that have turned it into a highly efficient and predictive method [39, 154–159], it has been one of the prime tools in a condensed matter theorist's toolbox.

We will not delve into the fine details in light of conciseness, resorting instead to a very high-level overview following the excellent introduction by R. Martin in Ref. [160]. On a rudimentary level, DFT is built on top of three main theoretical pillars.

The first pillar is the observation that any property of a system of interacting particles can be written as a functional of the ground-state density $n_0(\boldsymbol{r})$. This means that DFT is, in principle, an exact theory of many-body systems. Writing the Hamiltonian as

$$\hat{\mathcal{H}} = -\frac{\hbar}{2m_e}\sum_i \nabla_i^2 + \sum_i V_{\text{ext}}(\boldsymbol{r}_i) + \frac{1}{2}\sum_{i\neq j}\frac{e^2}{|\boldsymbol{r}_i - \boldsymbol{r}_j|}, \tag{A.1}$$

where the indices i, j iterate over the electrons[1], the statement is that $V_{\text{ext}}(\boldsymbol{r})$ is uniquely defined by $n_0(\boldsymbol{r})$, and vice versa. Thus, as soon as the ground-state density is found, the exact Hamiltonian of the system is known. This in turn allows one to, theoretically speaking, find all other eigenstates of the system, fully characterizing the system.

The second pillar is formed by the ability to define a universal functional for the total energy of the system $E[n]$ in terms of the density $n(\boldsymbol{r})$, which is valid for any external potential $V_{\text{ext}}(\boldsymbol{r})$. The density that globally minimizes this functional is then equal to the ground-state density $n_0(\boldsymbol{r})$.

In order to turn these foundational first two pillars into a practically usable framework, one has to address the question of the form of the energy functional $E[n]$, leading us straight to the third pillar: the Kohn-Sham Ansatz [153]. In essence, this ansatz makes the assumption that the original many-body problem can be replaced by an auxiliary independent-particle problem, both having exactly the same ground-state density $n_0(\boldsymbol{r})$. This means that theoretically speaking, calculations for the many-body problem can be exactly translated instead into calculations using independent-particle methods. It is found that a set of independent particle equations can thus be formulated, lumping all the cumbersome many-body exchange and correlation effects together into the so-called "exchange-correlation" functional $E_{xc}[n]$. If the exact form of $E_{xc}[n]$ was known, DFT would lead to the exact solutions of the original many-body problem. The success of the DFT method from a numerical and quantitative point of view can be wholly attributed to the ability to find local or semi local approximations to this functional that manage to reproduce the original many-body problem quite well, using a mean-field description.

Bringing everything together, we can write down the total energy functional of the auxiliary independent-particle system as:

$$E_{KS} = T_s[n] + \int d\boldsymbol{r} V_{\text{ext}}(\boldsymbol{r})n(\boldsymbol{r}) + E_{\text{Hartree}}[n] + E_{II} + E_{xc}[n], \tag{A.2}$$

where T_s denotes the independent-particle kinetic energy, V_{ext} the external potential due to the nuclei and any other external fields, E_{II} the Coulomb interactions between the nuclei, and $E_{\text{Hartree}}[n]$ the classical Coulomb contributions:

$$E_{\text{Hartree}} = \frac{1}{2}\int d\boldsymbol{r} d\boldsymbol{r}' \frac{n(\boldsymbol{r})n(\boldsymbol{r}')}{|\boldsymbol{r} - \boldsymbol{r}'|}. \tag{A.3}$$

These formulae are at the core of the method, i.e. by minimizing the total energy in Eq. (A.2), we can obtain the ground-state density which fully describes the system. To

[1] The ionic terms are easily included and are not the core difficulty and thus omitted here.

do this, most practical implementations use a self-consistent algorithm which iteratively constructs the energy contributions from the previous trial density n_i, diagonalizes the resulting Hamiltonian, and uses the eigenstate with the lowest energy to construct a new trial density n_o, after which the algorithm is repeated until n_o is sufficiently close to n_i. Equivalently, this means that $E[n_i] \approx E[n_o]$ through the Hohenberg-Kohn theorems, i.e. self-consistency between the density and resulting V_{ext} is reached. It can be shown that this process leads to, at least, a local minimum of the Kohn-Sham functional (A.2). The question of how to reach the global minimum of any function, let alone any functional, is from an entirely different caliber that we wish to avoid in this Thesis. In the vast majority of practical cases, no matter what starting density is used, the final self-consistent density will be that of the ground-state. Indeed, many practical codes initialize the density completely randomly.

There are many ways to numerically implement DFT, with the basis set used to construct the Hamiltonian being the main differentiating factor. Since we are interested in extended systems such as crystals, a plane-wave basis set comes very naturally. We know that the eigenstates for the periodic potentials found in crystalline systems are Bloch functions [161]:

$$\left|\psi_n^{\boldsymbol{k}}\right\rangle = e^{i\boldsymbol{k}\cdot\boldsymbol{r}} \left|u_n^{\boldsymbol{k}}\right\rangle, \tag{A.4}$$

where $e^{i\boldsymbol{k}\cdot\boldsymbol{r}}$ denotes the envelope function, and $\left|u_n^{\boldsymbol{k}}\right\rangle$ the cell-periodic part (see left-hand side of Fig. B.1(a)), and n the band index. Using a plane-wave basis $\left|\phi^{\boldsymbol{G}}\right\rangle$ such that $\left\langle \boldsymbol{r}|\phi^{\boldsymbol{G}}\right\rangle = e^{i\boldsymbol{G}\cdot\boldsymbol{r}}$, we can write the Bloch functions as:

$$\left|\psi_n^{\boldsymbol{k}}\right\rangle = e^{i\boldsymbol{k}\cdot\boldsymbol{r}} \sum_{\boldsymbol{G}} c_n^{\boldsymbol{G}} \left|\phi^{\boldsymbol{G}}\right\rangle. \tag{A.5}$$

By using these plane-wave basis functions, the energy contributions in Eq. (A.2) can be calculated. In practice one rather constructs the Hamiltonian of the system and diagonalizes it in order to find the coefficients $c_n^{\boldsymbol{G}}$ in Eq. (A.5) corresponding to the lowest eigenstates of the system (up to the Fermi level). A new trial density can then be constructed from these, which is used in the Hamiltonian of the next iteration, and so on until self-consistency is reached.

One problem arises when using this plane-wave basis set, namely that close to the ionic cores $\left|u_n^{\boldsymbol{k}}\right\rangle$ varies sharply in space, and fast oscillating plane-waves with high wavevector $\boldsymbol{G}$ are needed to resolve this sharp variation. This leads to a large basis set, and thus operators (such as the Hamiltonian) with large dimensions, making the calculations extremely expensive.

To overcome this issue, another approximation is often used: the so-called pseudopotentials that replace the exact ionic potentials [154–157]. Pseudopotentials are defined in such a way that the wavefunctions match identically the exact ones (i.e. as a result of the real ionic potentials) outside a chosen core region around the ion but have less sharp variations inside the core region. Smoother wavefunctions can be described by plane waves with smaller wavevectors, leading ultimately to a drastic reduction of the required size of the basis set used in the plane-wave-based DFT calculations. Using the pseudopotential approximation generally leads to good results for most properties that are of interest, since in many cases these properties do not depend on the exact shape of the wavefunctions close to the ionic cores.

While DFT offers impressive efficiency and predictive power for many materials, rationalizing the results obtained with it is often less trivial. This is mainly because of the still relatively large basis set that is used in the calculations, and the fact that a description in terms of extended plane waves is often hard to grasp on an intuitive level. At the start of this appendix, we commented on the simplicity and flexibility that is offered by the use of Tight-Binding models. There we saw that the parameters of these models can be fitted from experimental observations, which leads to an empirical method.

However, one may wonder if, instead of using angle-resolved photoemission experiments as an input for the model, the results of a DFT calculation could be employed. The DFT calculation would then act as a "numerical experiment", and the Tight-Binding model as a way to rationalize the behavior. The required bridge connecting the two can be formed by the Wannier functions and Wannierization, discussed in appendix B.

B
Wannier functions

Tight-Binding models have appeared in various forms throughout history, originally proposed by Bloch [32], and sometimes also referred to as the *linear combination of atomic orbitals* method [33]. This last description hints at how they are constructed.

First, a set of real space orbitals is defined inside the unit cell which is repeated throughout the rest of the system to construct the full basis. The elements of the Hamiltonian are then calculated from the overlap integrals between these local orbitals:

$$t_{\alpha\beta}^{\boldsymbol{ij}} = \left\langle \alpha^{\boldsymbol{i}} \right| \hat{H} \left| \beta^{\boldsymbol{j}} \right\rangle = \int_V d\boldsymbol{r}\, \alpha^*(\boldsymbol{r} - \boldsymbol{R}_i) H(\boldsymbol{r}) \beta(\boldsymbol{r} - \boldsymbol{R}_j), \tag{B.1}$$

where $\left|\alpha^{\boldsymbol{i}}\right\rangle$ is the orbital α located on ionic site i with center $\boldsymbol{R}_i$, and $t_{\alpha\beta}^{\boldsymbol{ij}}$ the *hopping parameters* between the two orbitals, because they describe the process of annihilating an electron from orbital $\left|\beta^{\boldsymbol{j}}\right\rangle$ and creating it on $\left|\alpha^{\boldsymbol{i}}\right\rangle$. This Hamiltonian is periodic in the sense that if both $\left|\beta^{\boldsymbol{j}}\right\rangle$ and $\left|\alpha^{\boldsymbol{i}}\right\rangle$ are shifted by the same lattice translation, the hopping parameter will remain unchanged. Fourier transforming and diagonalizing the Hamiltonian then leads to the Bloch functions (BFs) and electronic band structure of the crystal [161].

Another way of constructing such a model is by extracting the localized orbitals and hopping parameters from a first-principles based calculation such as DFT. In Chapter 2 that describes the Rashba spin-splitting in GeTe, we opt for this method. This circumvents the need to perform many experiments in order to investigate the details of the band structure, and how certain effects are manifested in different materials.

The main question to answer then becomes how to define such a set of localized orbitals starting from the extended BFs written in terms of the plane-wave basis set that is used in DFT. There are many ways to do this, but the most natural one, in this case, is by using a set of Wannier functions (WFs) [162] as the target localized basis.

We will here give a short recap of the excellent reviews by Marzari et. al. [163, 164], starting with the clearest case of a single isolated band n with BFs $\left|\psi_n^{\boldsymbol{k}}\right\rangle$ (see the red

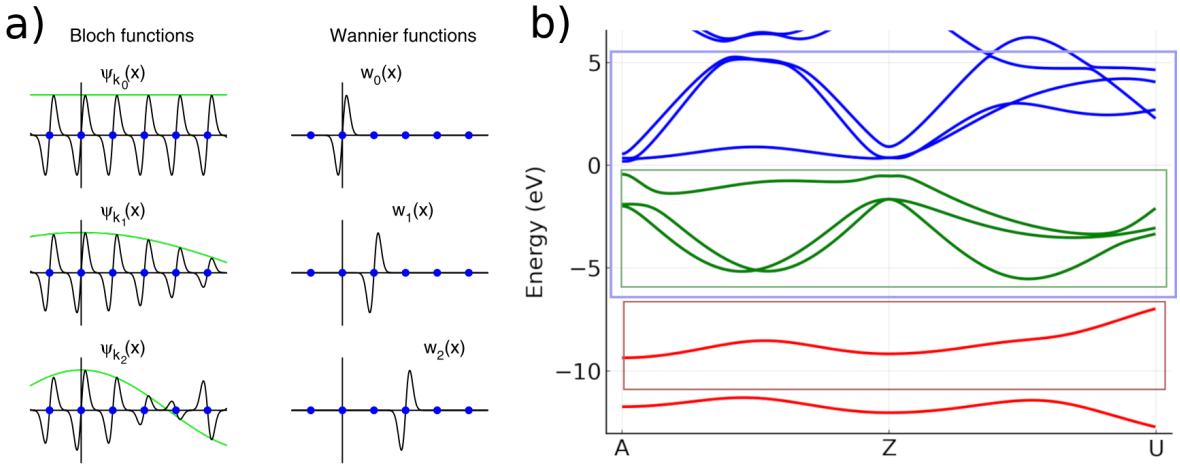

FIGURE B.1: a) A comparison between Bloch functions (left) and Wannier functions (right). The green graph in the left panel denotes the envelope function $e^{i\boldsymbol{k}\cdot\boldsymbol{r}}$, whereas the black one denotes the periodic part $\left|u_n^{\boldsymbol{k}}\right\rangle$. This image was taken from Ref. [164]. b) Bandstructure of semiconductor GeTe, demonstrating three cases for Wannierization: red is a single disconnected band, green shows a disconnected composite manifold of bands, blue shows the situation when bands need to be disentangled.

window in Fig. B.1(b)). The BF can then be written as a straightforward discrete Fourier transform of the WF:

$$\left|\psi_n^{\boldsymbol{k}}\right\rangle = e^{i\boldsymbol{k}\cdot\boldsymbol{r}}\left|u_n^{\boldsymbol{k}}\right\rangle = \sum_{\boldsymbol{R}} e^{i\boldsymbol{k}\cdot\boldsymbol{R}}\left|w_n^{\boldsymbol{R}}\right\rangle, \tag{B.2}$$

with $\left|w_n^{\boldsymbol{R}}\right\rangle$ denoting the localized WF centered in the unit cell defined by lattice vector $\boldsymbol{R}$, and n the band index. The comparison between BFs and WFs is made in Fig. B.1. When $k = 0$ we can see that $\left|u_n^{\boldsymbol{k}}\right\rangle$ is simply the sum over the WFs centered at different unit cells. In the case of $k \neq 0$, similar to how the envelope part modulates the periodic part of the BF, the contribution of each WF to the total sum needs to be modulated discretely through $e^{i\boldsymbol{k}\cdot\boldsymbol{R}}$.

The inverse Fourier transform over the BF in the first BZ can then be performed in order to generate the localized WFs,

$$\left|w_n^{\boldsymbol{R}}\right\rangle = \frac{V}{(2\pi)^3}\int_{BZ} d\boldsymbol{k} e^{-i\boldsymbol{k}\cdot\boldsymbol{R}}\left|\psi_n^{\boldsymbol{k}}\right\rangle, \tag{B.3}$$

where V denotes the real-space volume of the unit cell. In these and following equations, the normalization convention is used such that $\int_V d\boldsymbol{r}\left\langle\psi_n^{\boldsymbol{k}}(\boldsymbol{r})|\psi_n^{\boldsymbol{k}}(\boldsymbol{r})\right\rangle = 1$. As can be seen from the right panel in Fig. B.1, WFs centered in different unit cells are shifted copies of one another.

One of the most useful properties of the WFs lies in the realization that, through

the gauge freedom at each $\boldsymbol{k}$ of the BF[1], the shape of the WFs is not unique:

$$\left|\psi_n^{\boldsymbol{k}}\right\rangle \Rightarrow \left|\tilde{\psi}_n^{\boldsymbol{k}}\right\rangle = e^{i\phi_n^{\boldsymbol{k}}}\left|\psi_n^{\boldsymbol{k}}\right\rangle, \tag{B.4}$$

$$\left|w_n^{\boldsymbol{R}}\right\rangle \Rightarrow \left|\tilde{w}_n^{\boldsymbol{R}}\right\rangle = \frac{V}{(2\pi)^3}\int_{BZ} d\boldsymbol{k} e^{-i(\boldsymbol{k}\cdot\boldsymbol{R}+\phi_n^{\boldsymbol{k}})}\left|\psi_n^{\boldsymbol{k}}\right\rangle. \tag{B.5}$$

This means that by varying $\phi_n^{\boldsymbol{k}}$ we can adapt the WF basis in order for it to fulfill certain symmetries, or to localize the WFs as much as possible.

In most practical problems we are interested in groups of bands, rather than just a single band. The easiest case is when these form a composite manifold that is detached from other bands, such as the green valence bands in Fig. B.1(b). It is useful to generalize the notion of the single band phase freedom $\phi_n^{\boldsymbol{k}}$ to the many-band gauge transformation $U_{nm}^{\boldsymbol{k}}$:

$$\left|\tilde{\psi}_m^{\boldsymbol{k}}\right\rangle = \sum_m U_{nm}^{\boldsymbol{k}}\left|\psi_n^{\boldsymbol{k}}\right\rangle, \tag{B.6}$$

where n, m enumerate the bands inside the composite manifold and the tilde is used to distinguish between $\left|\tilde{\psi}_m^{\boldsymbol{k}}\right\rangle$ and the original BFs. We do this because these transformed states are no longer eigenstates of the Hamiltonian if $U_{nm}^{\boldsymbol{k}}$ has off-diagonal elements. Traces performed over such an isolated set of bands are invariant w.r.t. to these gauge transformations, leading to the invariance of observables such as the Hamiltonian which lies at the core of the ability to isolate and focus on this subproblem. Choosing a decent gauge, in this case, is a necessity to extract well-localized WFs. This is because composite band manifolds will generally harbor band crossings and degeneracies where the BFs become non analytic making $\frac{\partial u_n^{\boldsymbol{k}}(\boldsymbol{r})}{\partial \boldsymbol{k}}$ not smooth. When the inverse Fourier transform is then performed on the BFs themselves, this non smoothness will result in badly localized real-space WFs. Indeed, only for smoothly varying $u_n^{\boldsymbol{k}}(\boldsymbol{r})$ will cancellations appear when $\boldsymbol{R}$ is large, due to the fast varying exponent $e^{i\boldsymbol{k}\cdot\boldsymbol{R}}$ in Eq. (B.3). It is thus important to choose the $U_{mn}^{\boldsymbol{k}}$ in Eq. (B.6) so that the rotated wavefunctions $\left|\tilde{\psi}_n^{\boldsymbol{k}}\right\rangle$ vary as smoothly as possible, which will ultimately lead to the WFs that are as localized as possible when the inverse Fourier transform is performed.

In order to quantify this localization of the WFs, a spread functional can be written as:

$$\Omega = \sum_n \left\langle w_n^{\boldsymbol{0}}\right| r^2 \left|w_n^{\boldsymbol{0}}\right\rangle - \left|\left\langle w_n^{\boldsymbol{0}}\right| \boldsymbol{r} \left|w_n^{\boldsymbol{0}}\right\rangle\right|^2, \tag{B.7}$$

which can be trivially split into a gauge-invariant and gauge-dependent part

$$\Omega = \Omega_I + \tilde{\Omega}, \tag{B.8}$$

$$\Omega_I = \sum_n \left[\left\langle w_n^{\boldsymbol{0}}\right| r^2 \left|w_n^{\boldsymbol{0}}\right\rangle - \sum_{m,\boldsymbol{R}} \left|\left\langle w_m^{\boldsymbol{R}}\right| \boldsymbol{r} \left|w_n^{\boldsymbol{0}}\right\rangle\right|^2\right], \tag{B.9}$$

$$\tilde{\Omega} = \sum_{n,m}\sum_{\boldsymbol{R}\neq n,\boldsymbol{0}} \left|\left\langle w_m^{\boldsymbol{R}}\right| \boldsymbol{r} \left|w_n^{\boldsymbol{0}}\right\rangle\right|^2. \tag{B.10}$$

[1]The solution to Schrödinger equation does not determine uniquely its phase.

For a set of isolated bands it thus suffices to minimize the gauge-dependent part in order to find the unique set of maximally localized Wannier functions (MLFW)[2] that consitute these bands [164, 165].

We can then transform the position dependent operators into reciprocal space as [166]:

$$\left\langle w_n^{\boldsymbol{R}} \right| \boldsymbol{r} \left| w_m^{\boldsymbol{0}} \right\rangle = i\frac{V}{(2\pi)^3} \int d\boldsymbol{k} e^{i\boldsymbol{k}\cdot\boldsymbol{R}} \left\langle u_n^{\boldsymbol{k}} \right| \boldsymbol{\nabla}_{\boldsymbol{k}} \left| u_m^{\boldsymbol{k}} \right\rangle, \tag{B.11}$$

and

$$\left\langle w_n^{\boldsymbol{R}} \right| r^2 \left| w_m^{\boldsymbol{0}} \right\rangle = -\frac{V}{(2\pi)^3} \int d\boldsymbol{k} e^{i\boldsymbol{k}\cdot\boldsymbol{R}} \left\langle u_n^{\boldsymbol{k}} \right| \boldsymbol{\nabla}_{\boldsymbol{k}}^2 \left| u_m^{\boldsymbol{k}} \right\rangle, \tag{B.12}$$

which can be used to write and minimize $\tilde{\Omega}$ in terms of $\left|u_n^{\boldsymbol{k}}\right\rangle$ and $U_{nm}^{\boldsymbol{k}}$ directly. The optimal set of $U_{nm}^{\boldsymbol{k}}$ can then be used to generate the set of MLFW. If maximal localization is not the only goal, WFs with other desirable characteristics can be generated by tweaking the $U_{nm}^{\boldsymbol{k}}$. This is often done to ensure that the WFs adhere to the symmetries of atomic orbitals, which can be useful to develop a further intuitive understanding using well-known orbitals. More details on the different construction methods and can be found in Ref. [164].

Up to now, we discussed the case of an isolated set of bands. In some cases, such a set does not exist in the energy range of interest, and the bands are connected, or *entangled*, with the bands outside this range. An example of this case is shown by the blue bands in Fig. B.1(b). If we are seeking J WFs we then need to select J states $\left|\tilde{\psi}_n^{\boldsymbol{k}}\right\rangle$ at each k-point from a bigger set $J^{\boldsymbol{k}}$:

$$\left|\tilde{\psi}_n^{\boldsymbol{k}}\right\rangle = \sum_{m=1}^{J^{\boldsymbol{k}}} V_{nm}^{\boldsymbol{k}} \left|\psi_m^{\boldsymbol{k}}\right\rangle. \tag{B.13}$$

These $\left|\tilde{\psi}_n^{\boldsymbol{k}}\right\rangle$ can then be used in the previously described localization procedure. The matrices $V_{nm}^{\boldsymbol{k}}$ are in general rectangular with dimension $J \times J^{\boldsymbol{k}}$. This leads to a two-step procedure where first a subspace is selected for each k-point, followed by the final gauge selection to arrive at the localized basis of WFs:

$$\left|w_n^{\boldsymbol{R}}\right\rangle = \frac{V}{(2\pi)^3} \int_{BZ} d\boldsymbol{k} e^{-i\boldsymbol{k}\cdot\boldsymbol{R}} \sum_{m=1}^{J} U_{nm}^{\boldsymbol{k}} \sum_{l=1}^{J^{\boldsymbol{k}}} V_{ml}^{\boldsymbol{k}} \left|\psi_l^{\boldsymbol{k}}\right\rangle. \tag{B.14}$$

There are again many ways to do this subspace selection (or *disentanglement*). The most prevalent two are by projection onto atomic-like orbitals, or by again minimizing the total spread of the WFs. We utilize the latter in this work. In this case, the maximal localization aims to find at each k-point the $V_{nm}^{\boldsymbol{k}}$ that leads to the maximal overlap of the selected subspace with its neighboring k-points. As discussed before, this smoothness in reciprocal space translates into the subspace as a whole being more localized in real space. Indeed, it can be shown [164] that this intrinsic smoothness

[2] It can be proven that these WFs will be exponentially localized in the case of normal insulators.

is exactly what Ω_I measures in Eq. (B.9). In many cases, it is desirable to adapt the algorithm so that the BFs of the bands inside a "frozen" energy window are exactly interpolated by the resulting WFs and associated Tight-Binding Hamiltonian.

These considerations set the theoretical stage for the Wannierization procedure. In the following, we give some comments on the numerical aspects of this method.

The continuous integration over the BZ in previous equations is performed on a discrete k grid in numerical calculations. In order to adhere closely to the continuous case, the discrete Fourier transform pair can be defined as:

$$\left|\tilde{\psi}_n^{\boldsymbol{k}}\right\rangle = \sum_{\boldsymbol{R}} e^{i\boldsymbol{k}\cdot\boldsymbol{R}} \left|w_n^{\boldsymbol{R}}\right\rangle, \tag{B.15}$$

$$\left|w_n^{\boldsymbol{R}}\right\rangle = \frac{1}{N}\sum_{\boldsymbol{k}} e^{-i\boldsymbol{k}\cdot\boldsymbol{R}} \left|\tilde{\psi}_n^{\boldsymbol{k}}\right\rangle, \tag{B.16}$$

where N denotes the number of unit cells in the periodic supercell in real space, equal to the number of k-points in the discrete mesh over the BZ. This discretization enforces periodic boundary conditions on the BFs over this supercell, meaning that the WFs in this definition also have this supercell periodicity. The localization criterion then means that the WFs are localized inside the supercell. If the mesh spacing tends to zero, the supercell tends to infinity, restoring the earlier definitions using continuous Fourier Transforms, and the original notion of WFs.

After finding the $U_{nm}^{\boldsymbol{k}}$ and $V_{nm}^{\boldsymbol{k}}$ matrices of Eq. (B.14), any operator $\hat{f}^{\boldsymbol{k}}$ defined in terms of the BFs can be transformed into $\hat{F}^{\boldsymbol{R}}$ in the Wannier representation. It is important to realize that, depending on the coarseness of the k grid used in the first-principles calculation, $\hat{F}^{\boldsymbol{R}}$ can only be calculated for limited values of $|\boldsymbol{R}|$, spanning the supercell defined by the discretization of the BZ. Since the WFs are well localized, $\hat{F}^{\boldsymbol{R}}$ tends to decay rapidly with $|\boldsymbol{R}|$. The values of $\hat{f}^{\boldsymbol{k}}$ can then be interpolated from $\hat{F}^{\boldsymbol{R}}$ by performing the inverse procedure. This allows the efficient calculation of $\hat{f}^{\boldsymbol{k}}$ on a finer k mesh than the one used in the DFT calculations, provided that the WFs are well localized inside the supercell. This efficient interpolation is one of the great advantages of using localized WF, since the size of the WF basis, and thus dimensions of the matrices is much lower than the one used in DFT (e.g. many plane waves).

The final process that we use in this Thesis to extract a Tight-Binding Hamiltonian in a WF basis, starting from an ab-initio DFT simulation, can thus be summarized as follows:

1. Perform a self-consistent DFT calculation in order to find the ground state density and BFs on a discrete k mesh.

2. Define the J trial orbitals (e.g. atomic-like) that are most suitable for the bands or problem under investigation. This can be done e.g. by performing a density of states calculation, projecting on the atomic orbitals.

3. Select an inner "frozen" window containing the most important bands, and, if entangled, an outer window from which to disentangle a J-dimensional subspace for each k-point.

4. Use a projection on the trial orbitals defined in (2) as the initial guess, followed by minimization of Ω_I (Eq. (B.7)) to find the $V_{ml}^{\boldsymbol{k}}$ matrices.

5. Find the final gauges $U_{nm}^{\boldsymbol{k}}$ minimize the spread of each of the J WFs.

The main quantity we will use this interpolation for is the Hamiltonian:

$$\tilde{H}_{nm}^{\boldsymbol{k}} = \left\langle \tilde{\psi}_n^{\boldsymbol{k}} \right| H \left| \tilde{\psi}_m^{\boldsymbol{k}} \right\rangle = \sum_{\boldsymbol{R}} e^{i\boldsymbol{k}\cdot\boldsymbol{R}} \left\langle w_n^{\boldsymbol{0}} \right| H \left| w_n^{\boldsymbol{R}} \right\rangle . \tag{B.17}$$

This Hamiltonian can then be diagonalized by unitary transformations $W^{\boldsymbol{k}}$ in order to recover the interpolated band structure of the J bands in the chosen window:

$$H_{nm}^{\boldsymbol{k}} = [W^{\boldsymbol{k}\dagger} \tilde{H}_{nm}^{\boldsymbol{k}} W^{\boldsymbol{k}}]_{nm} = \delta_{nm} \varepsilon_n^{\boldsymbol{k}}. \tag{B.18}$$

This concludes our very condensed introduction and overview of the construction and use Wannier functions as a tool to aid in the theoretical understanding of the behavior of electrons in extended systems. Further details on the Wannierization process can be found in Ref. [164], and specific details on the implementation in the Wannier90 package used throughout this work can be found in Ref. [42].

C

Phase-Field modeling with the Finite Elements Method

We give a short introduction to the methods we used in order to simulate phase-field models such as the one defined in Chapter 5, Eq. 5.5. The Finite Element Method constitutes a big part of these simulations, thus, in light of making this Thesis relatively self contained, we give a short summary of the topic, based on Ref. [167].

A fundamental building block is the isoparametric representation. In this representation, the geometry is divided into a set of elements that obey certain connectivity requirements, the main one being that each node must be connected to the same number of neighbor nodes. As an example, we describe the often used triangular elements for 2D geometries, shown in Fig. C.1(a,b). A global-to-local coordinate transformation is then performed by using shape functions that define the morphology of the element. In the case of the triangle, they are defined in terms of the edge lengths and angle between them. Starting from the global coordinates of the nodes (x_i, y_i), any coordinate inside the element can be written as:

$$x(\zeta, \eta) = \sum_i^n N_i(\zeta, \eta) x_i, \tag{C.1}$$

$$y(\zeta, \eta) = \sum_i^n N_i(\zeta, \eta) y_i, \tag{C.2}$$

and functions f are similarly interpolated as:

$$f(\zeta, \eta) = \sum_i^n N_i(\zeta, \eta) f_i. \tag{C.3}$$

In these equations, i iterates through the n nodes of the element, and ζ and η are the axes of the local coordinate system (see Fig. C.1(a)). From these equations, it is clear

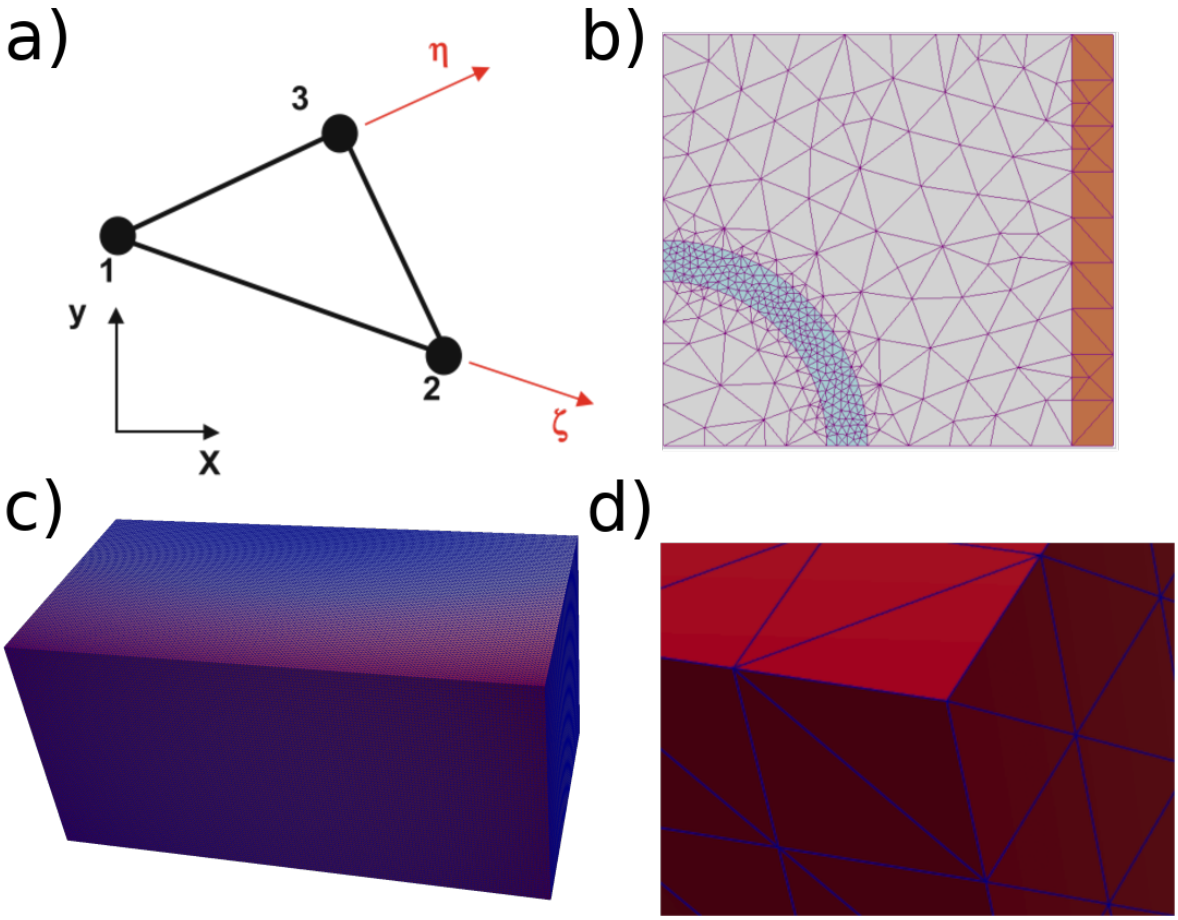

FIGURE C.1: **Finite Element Method.** a) Isoparametric local coordinate system for a triangular element. Image taken from Ref. [167]. b) 2D geometry spanned by triangular mesh demonstrating the flexibility of FEM meshes. Image taken from Ref. [168]. c) Example of the geometry that is used in our simulations. d) Zoom in on the corner of the mesh shown in (c).

that each node has a separate shape function. They have to be chosen in such a way that they adhere to certain conditions:

- Interpolation condition: N_i is 1 at node i and zero at the other nodes.
- Local support condition: N_i vanishes at each edge that does not contain i.
- Interelement compatibility condition: Satisfies continuity between neighboring elements that include node i.
- Completeness condition: Any field that is a linear polynomial in x and y is represented exactly.

Since we need the derivatives of the P and u fields in order to calculate the free

energy density, we perform the chain rule and find for any function f:

$$\frac{\partial f}{\partial \zeta} = \sum_i^n \frac{\partial N_i}{\partial \zeta} \cdot f_i, \qquad \frac{\partial f}{\partial \eta} = \sum_i^n \frac{\partial N_i}{\partial \eta} \cdot f_i. \tag{C.4}$$

In the numerical implementation, these derivatives are found for each element by first computing the Jacobian with the partial derivatives of the global coordinates x and y w.r.t the local ones ζ and η and then performing an inversion. This inversion also requires calculating the determinant of the Jacobian, which can be reused to calculate the area or volume of the element to be used during the integration.

Certain points, called quadrature points, are then selected inside each element. The function values of the P and u fields are interpolated at these points using their values at the nodes of the element and the shape functions. Filling them into the free energy density, such as the one in Eq. (5.5), results in an approximation of the contribution of each element to the total free energy, which is then found by summation. The nodal values of the fields are therefore the variables of our model. A big bonus of the isoparametric representation, applied in this way, is that gradients of the fields can be evaluated purely locally, inside each element (see Eq. (C.4)). It also allows for great flexibility through the density of the chosen grid, the morphology of the elements, and the order of the interpolating shape functions N_i that are used in Eq. (C.3).

We developed our own code in order to run the FEM simulations, based on the building blocks supplied by the JuAFEM.jl package. We use a rectangular geometry uniformly spanned by tetrahedron elements, as shown in Fig. C.1(c,d). This choice is made since the uniform mesh mimics numerically the Peierls-Nabarro barriers that are present in any crystal due to the lattice.

The last ingredient of the simulation is a way to optimize the fields in order to reach the equilibrium condition at minimum energy. To achieve this we use the Conjugate Gradient Method [169, 170] as implemented in the package Optim.jl [103]. It is an iterative scheme that uses the gradient and previous step to choose the next step direction. This requires us to determine the partial derivatives of the total energy in terms of all the degrees of freedom, i.e. the value of each component of P and u at the node points of the mesh. We chose to use a forward automatic differentiation scheme as implemented in ForwardDiff.jl [171], again for its remarkable simplicity and speed (as an idea, on a 24 core E5-2680 v3 server, the $\approx$ 3.5 million partial derivatives are computed in around 2 seconds). The core concept of this method lies in the realization that any computer program can be decomposed into elemental operations. By defining the derivatives of these, and by utilizing the chain rule, it is then possible to generate the "symbolically" differentiated program numerically. The forward mode method in ForwardDiff.jl uses dual numbers that carry the information of both the value, as well as the residual value. These residuals accumulate the derivative values as the number flows through the operations of the program, which can be collected at the end to construct the partial derivatives. For further information see Ref. [172].

D
List of developed codes

In this appendix a list of the codes that were developed during, and in support of, this Thesis. All were developed using the Julia programming language.

- DFControl.jl – Job control for `Quantum ESPRESSO` [37] and `Wannier90` [42].
- DFWannier.jl – Post-processing for `Wannier90` calculations.
- Landau.jl – Real-space Finite-Element-Method based solver for Landau models (see appendix C for further details).
- Glimpse.jl – OpenGL-based 3D rendering toolkit.
- Overseer.jl – Classic entity-component-system.

Acronyms

SOC spin-orbit coupling. 2, 6, 7, 8, 9, 10, 11, 12, 15, 16, 17, 19, 20, 21, 23, 24, 25, 27, 37

BZ Brillouin Zone. 2, 6, 8, 10, 17, 19, 26, 27, 29, 104, 107

SDW spin-density wave. 3, 4, 61, 62, 63, 64, 65, 66, 67, 68, 69, 70, 72, 74

PLD periodic lattice displacement. 4, 62, 63, 64, 65, 66, 67, 69, 70, 72, 74, 75

FET field-effect transistor. 5

T time-reversal. 6, 8, 10, 12, 16, 17, 25, 27, 28

DFT density functional theory. 7, 19, 45, 84, 85, 99, 100, 101, 102, 103, 107

NSOC non-spin-orbit coupling. 7, 19, 20, 23, 24, 25

OAM orbital angular momentum. 8, 11, 12, 15, 16, 17, 18, 19, 21, 22, 23, 25, 26, 27, 28, 29, 30, 37

DOS density of states. 21

AFM antiferromagnetic. 34, 35, 36, 37, 40, 41, 42, 43, 53, 58, 59

XFEL x-ray free-electron laser. 62, 63, 66, 75

OP order parameter. 76, 77, 78, 79, 85, 86

DW domain wall. 77, 78, 79, 80, 81, 82, 83, 84, 85, 86, 88, 89, 90, 91, 92, 93, 94, 95, 98

PFM piezoresponse force microscopy. 80, 81, 82

CRFM contact resonance force microscopy. 81, 82, 83

GLD Ginzburg-Landau-Devonshire. 84, 85, 86, 93

FEM Finite Elements Method. 93, 110, 111

BF Bloch function. 103, 104, 105, 107

WF Wannier function. 103, 104, 105, 106, 107, 108

MLFW maximally localized Wannier functions. 106

References

[1] M. Born and R. Oppenheimer, *Zur Quantentheorie der Molekeln*, Annalen der Physik **389**(20), 457 (1927), URL http://doi.wiley.com/10.1002/andp.19273892002. 2

[2] S. Datta and B. Das, *Electronic analog of the electro-optic modulator*, Applied Physics Letters **56**(7), 665 (1990), URL http://dx.doi.org/10.1063/1.102730. 3, 5

[3] M. Lohse, C. Schweizer, O. Zilberberg, M. Aidelsburger, and I. Bloch, *A thouless quantum pump with ultracold bosonic atoms in an optical superlattice*, Nature Physics **12**(4), 350 (2016), URL https://doi.org/10.1038/nphys3584. 3, 46, 50

[4] V. K. Joshi, *Spintronics: A contemporary review of emerging electronics devices*, Engineering Science and Technology, an International Journal **19**(3), 1503 (2016), URL http://dx.doi.org/10.1016/j.jestch.2016.05.002. 5

[5] A. D. Kent and D. C. Worledge, *A new spin on magnetic memories*, Nature Nanotechnology **10**(3), 187 (2015), URL http://www.nature.com/doifinder/10.1038/nnano.2015.24. 5, 32

[6] A. S. Nunez, R. A. Duine, and A. H. MacDonald, *Antiferromagnetic Metal Spintronics* pp. 3098–3114 (2011), URL http://dx.doi.org/10.1098/rsta.2011.0014. 5

[7] A. S. Núñez and A. H. MacDonald, *Theory of spin transfer phenomena in magnetic metals and semiconductors*, Solid State Communications **139**(1), 31 (2006), URL http://dx.doi.org/10.1016/j.ssc.2006.05.004. 5

[8] A. S. Núñez, R. A. Duine, P. Haney, and A. H. MacDonald, *Theory of spin torques and giant magnetoresistance in antiferromagnetic metals*, Physical Review B - Condensed Matter and Materials Physics **73**(21), 1 (2006), URL http://dx.doi.org/10.1103/PhysRevB.73.214426. 31

[9] T. Jungwirth, X. Marti, P. Wadley, and J. Wunderlich, *Antiferromagnetic spintronics*, Nature Nanotechnology **11**(3), 231 (2016), URL http://www.nature.com/doifinder/10.1038/nnano.2016.18. 5, 32

[10] C. L. Kane and E. J. Mele, *Z2 topological order and the quantum spin hall effect*, Physical Review Letters **95**(14), 3 (2005), URL http://dx.doi.org/10.1103/PhysRevLett.95.146802. 6

[11] K. S. Novoselov, A. K. Geim, S. V. Morozov, D. Jiang, M. I. Katsnelson, I. V. Grigorieva, S. V. Dubonos, and A. A. Firsov, *Two-dimensional gas of massless Dirac fermions in graphene*, Nature **438**(7065), 197 (2005), URL http://www.nature.com/doifinder/10.1038/nature04233. 6

[12] A. H. Castro Neto, F. Guinea, N. M. R. Peres, K. S. Novoselov, and A. K. Geim, *The electronic properties of graphene*, Reviews of Modern Physics **81**(1), 109 (2009), URL http://dx.doi.org/10.1103/RevModPhys.81.109.

[13] L. Fu and C. L. Kane, *Topological insulators with inversion symmetry*, Physical Review B - Condensed Matter and Materials Physics **76**(4), 1 (2007), URL http://dx.doi.org/10.1103/PhysRevB.76.045302.

[14] L. Fu and C. L. Kane, *Time reversal polarization and a Z2 adiabatic spin pump*, Physical Review B - Condensed Matter and Materials Physics **74**(19), 1 (2006), URL http://dx.doi.org/10.1103/PhysRevB.74.195312.

[15] D. Pesin and A. H. MacDonald, *Spintronics and pseudospintronics in graphene and topological insulators.*, Nature materials **11**(5), 409 (2012), URL http://www.ncbi.nlm.nih.gov/pubmed/22522641. 6

[16] S. Picozzi, *Ferroelectric Rashba semiconductors as a novel class of multifunctional materials*, Frontiers in Physics **2**, 10 (2014), URL http://dx.doi.org/10.3389/fphy.2014.00010. 6, 7

[17] D. Di Sante, P. Barone, R. Bertacco, and S. Picozzi, *Electric control of the giant rashba effect in bulk gete*, Advanced Materials **25**(4), 509 (2013), URL http://dx.doi.org/10.1002/adma.201203199. 6, 7, 17

[18] K. Ishizaka, *Giant Rashba-type spin splitting in bulk BiTeI*, Nature materials **10**(7), 521 (2011), URL http://dx.doi.org/10.1038/nmat3051. 7

[19] M. Kim, J. Im, A. J. Freeman, J. Ihm, and H. Jin, *Switchable S = 1/2 and J = 1/2 Rashba bands in ferroelectric halide perovskites.*, Proceedings of the National Academy of Sciences of the United States of America **111**(19), 6900 (2014), URL http://dx.doi.org/10.1073/pnas.1405780111. 6, 7, 12

[20] H. A. Kramers, *Kramers theorem*, URL https://www.oxfordreference.com/view/10.1093/oi/authority.20110803100043434. 6

[21] M. Liebmann, C. Rinaldi, D. Di Sante, J. Kellner, C. Pauly, R. N. Wang, J. E. Boschker, A. Giussani, S. Bertoli, M. Cantoni, L. Baldrati, M. Asa, I. Vobornik, G. Panaccione, D. Marchenko, J. Sanchez-Barriga, O. Rader, R. Calarco, S. Picozzi, R. Bertacco, and M. Morgenstern, *Giant Rashba-Type Spin Splitting*

in Ferroelectric GeTe(111), Advanced Materials **28**(3), 560 (2016), URL http://dx.doi.org/10.1002/adma.201503459. 7

[22] J. Krempaský, H. Volfová, S. Muff, N. Pilet, G. Landolt, M. Radović, M. Shi, D. Kriegner, V. Holý, J. Braun, H. Ebert, F. Bisti, V. A. Rogalev, V. N. Strocov, G. Springholz, J. Minár, and J. H. Dil, *Surface versus bulk contributions to the giant Rashba splitting in the ferroelectric α-GeTe(111) semiconductor*, Physical Review B **94**(20), 205111 (2015), URL http://dx.doi.org/10.1103/PhysRevB.94.205111. 7, 26

[23] E. Rashba and V. Sheka, *Symmetry of Energy Bands in Crystals of Wurtzite Type II . Symmetry of Bands with Spin-Orbit Interaction*, Fiz. Tverd. Tela: Collected Papers (2), 162 (1959), URL http://nrs.harvard.edu/urn-3:HUL.InstRepos:29426010. 8, 10

[24] P. O. Löwdin, *A note on the quantum-mechanical perturbation theory*, J. Chem. Phys. **19**(11), 1396 (1951), URL https://dx.doi.org/10.1063/1.1748067.

[25] M. S. Bahramy, R. Arita, and N. Nagaosa, *Origin of giant bulk Rashba splitting: Application to BiTeI*, Physical Review B - Condensed Matter and Materials Physics **84**(4), 2 (2011), URL http://dx.doi.org/10.1103/PhysRevB.84.041202. 10, 11

[26] L. Petersen and P. Hedegård, *Simple tight-binding model of spin-orbit splitting of sp-derived surface states*, Surface Science **459**(1), 49 (2000), URL http://dx.doi.org/10.1016/S0039-6028(00)00441-6. 12, 15

[27] S. R. Park, C. H. Kim, J. Yu, J. H. Han, and C. Kim, *Orbital-angular-momentum based origin of rashba-type surface band splitting*, Physical Review Letters **107**(15), 1 (2011), URL http://dx.doi.org/10.1103/PhysRevLett.107.156803. 16

[28] J. H. Park, C. H. Kim, J. W. Rhim, and J. H. Han, *Orbital Rashba effect and its detection by circular dichroism angle-resolved photoemission spectroscopy*, Physical Review B - Condensed Matter and Materials Physics **85**(19), 1 (2012), URL http://dx.doi.org/10.1103/PhysRevB.85.195401.

[29] S. R. Park and C. Kim, *Microscopic mechanism for the Rashba spin-band splitting: Perspective from formation of local orbital angular momentum*, Journal of Electron Spectroscopy and Related Phenomena **201**, 6 (2015), URL http://dx.doi.org/10.1016/j.elspec.2014.12.009. 16

[30] D. Go, J.-P. Hanke, P. M. Buhl, F. Freimuth, G. Bihlmayer, H.-W. Lee, Y. Mokrousov, and S. Blügel, *Surface orbitronics: new twists from orbital Rashba physics*, Scientific Reports **7**(1), 46742 (2016), URL http://dx.doi.org/10.1038/srep46742. 12, 15

[31] C. J. Ballhausen, *Crystal and ligand field theory*, International Journal of Quantum Chemistry **5**(S5), 373 (2009), URL http://doi.wiley.com/10.1002/qua.560050844. 12, 16

[32] F. Bloch, *Über die quantenmechanik der elektronen in kristallgittern*, Zeitschrift für Physik (52), 555 (1929), URL https://doi.org/10.1007/BF01339455. 12, 99, 103

[33] J. C. Slater and G. F. Koster, *Simplified LCAO method for the periodic potential problem*, Physical Review **94**(6), 1498 (1954), URL http://dx.doi.org/10.1103/PhysRev.94.1498. 12, 99, 103

[34] L. Ponet and S. Artyukhin, *First-principles theory of giant Rashba-like spin splitting in bulk GeTe*, Physical Review B **98**(17), 174102 (2018), URL http://dx.doi.org/10.1103/PhysRevB.98.174102. 12

[35] K. M. Rabe and J. D. Joannopoulos, *Theory of the structural phase transition of GeTe*, Physical Review B **36**(12), 6631 (1987), URL http://dx.doi.org/10.1103/PhysRevB.36.6631. 17

[36] T. Nonaka, G. Ohbayashi, Y. Toriumi, Y. Mori, and H. Hashimoto, *Crystal structure of GeTe and Ge2Sb2Te5 meta-stable phase*, Thin Solid Films **370**(1-2), 258 (2000), URL https://linkinghub.elsevier.com/retrieve/pii/S0040609099010901. 17

[37] P. Giannozzi, S. Baroni, N. Bonini, M. Calandra, R. Car, C. Cavazzoni, D. Ceresoli, G. L. Chiarotti, M. Cococcioni, I. Dabo, A. Dal Corso, S. de Gironcoli, S. Fabris, G. Fratesi, R. Gebauer, U. Gerstmann, C. Gougoussis, A. Kokalj, M. Lazzeri, L. Martin-Samos, N. Marzari, F. Mauri, R. Mazzarello, S. Paolini, A. Pasquarello, L. Paulatto, C. Sbraccia, S. Scandolo, G. Sclauzero, A. P. Seitsonen, A. Smogunov, P. Umari, and R. M. Wentzcovitch, *QUANTUM ESPRESSO: a modular and open-source software project for quantum simulations of materials.*, Journal of physics. Condensed matter : an Institute of Physics journal **21**(39), 395502 (2009), URL http://dx.doi.org/10.1088/0953-8984/21/39/395502. 19, 112

[38] D. R. Hamann, *Optimized norm-conserving Vanderbilt pseudopotentials*, Physical Review B - Condensed Matter and Materials Physics **88**(8), 1 (2013), URL http://dx.doi.org/10.1103/PhysRevB.88.085117. 19

[39] J. P. Perdew, J. A. Chevary, S. H. Vosko, K. A. Jackson, M. R. Pederson, D. J. Singh, and C. Fiolhais, *Atoms, molecules, solids, and surfaces: Applications of the generalized gradient approximation for exchange and correlation*, Physical Review B **48**(7), 4978 (1993), URL https://link.aps.org/doi/10.1103/PhysRevB.48.4978.2. 19, 99

[40] J. P. Perdew, K. Burke, and M. Ernzerhof, *Generalized gradient approximation made simple*, Physical Review Letters **77**(18), 3865 (1996), URL http://dx.doi.org/10.1103/PhysRevLett.77.3865. 19

[41] J. D. Pack and H. J. Monkhorst, *"special points for Brillouin-zone integrations"- a reply*, Physical Review B **16**(4), 1748 (1977), URL http://dx.doi.org/10.1103/PhysRevB.16.1748. 19

[42] A. A. Mostofi, J. R. Yates, G. Pizzi, Y. S. Lee, I. Souza, D. Vanderbilt, and N. Marzari, *An updated version of wannier90: A tool for obtaining maximally-localised Wannier functions*, Computer Physics Communications **185**(8), 2309 (2014), URL http://dx.doi.org/10.1016/j.cpc.2014.05.003. 19, 108, 112

[43] R. D. King-Smith and D. Vanderbilt, *Theory of polarization of crystalline solids*, Physical Review B **47**(3), 1651 (1993). 21

[44] D. Vanderbilt and R. D. King-Smith, *Electric polarization as a bulk quantity and its relation to surface charge*, Physical Review B **48**(7), 4442 (1993).

[45] R. Resta, *Quantum-mechanical position operator in extended systems*, Physical Review Letters **80**(9), 1800 (1998), 9709306.

[46] N. A. Spaldin, *A beginners guide to the modern theory of polarization*, Journal of Solid State Chemistry **195**, 2 (2012), 1202.1831.

[47] D. Vanderbilt, *Berry Phases in Electronic Structure Theory: Electric Polarization, Orbital Magnetization and Topological Insulators* (Cambridge University Press, 2018), URL http://dx.doi.org/10.1017/9781316662205. 21

[48] T. Thonhauser, D. Ceresoli, D. Vanderbilt, and R. Resta, *Orbital magnetization in periodic insulators*, Physical Review Letters **95**(13), 1 (2005), URL http://dx.doi.org/10.1103/PhysRevLett.95.137205.

[49] D. Ceresoli, T. Thonhauser, D. Vanderbilt, and R. Resta, *Orbital magnetization in crystalline solids: Multi-band insulators, Chern insulators, and metals*, Physical Review B - Condensed Matter and Materials Physics **74**(2), 1 (2006), URL http://dx.doi.org/10.1103/PhysRevB.74.024408.

[50] T. Thonhauser, *THEORY OF ORBITAL MAGNETIZATION IN SOLIDS*, International Journal of Modern Physics B **25**(11), 1429 (2011), URL http://dx.doi.org/10.1142/S0217979211058912. 21

[51] J. Krempaský, M. Fanciulli, L. Nicolaï, J. Minár, H. Volfová, O. Caha, V. V. Volobuev, J. Sánchez-Barriga, M. Gmitra, K. Yaji, K. Kuroda, S. Shin, F. Komori, G. Springholz, and J. H. Dil, *Fully spin-polarized bulk states in ferroelectric GeTe*, Physical Review Research **2**(1), 1 (2020). 26

[52] M. N. Baibich, J. M. Broto, A. Fert, F. N. Van Dau, F. Petroff, P. Eitenne, G. Creuzet, A. Friederich, and J. Chazelas, *Giant magnetoresistance of (001)Fe/(001)Cr magnetic superlattices*, Physical Review Letters **61**(21), 2472 (1988), URL http://dx.doi.org/10.1103/PhysRevLett.61.2472. 31

[53] G. Binasch, P. Grünberg, F. Saurenbach, and W. Zinn, *Enhanced magnetoresistance in layered magnetic structures with antiferromagnetic interlayer exchange*, Physical Review B **39**(7), 4828 (1989), URL http://dx.doi.org/10.1103/PhysRevB.39.4828.

[54] E. Y. Tsymbal and D. G. Pettifor, *Perspectives of giant magnetoresistance*, Solid State Physics - Advances in Research and Applications **56**(C), 113 (2001), URL http://dx.doi.org/10.1016/S0081-1947(01)80019-9.

[55] C. Chappert, A. Fert, and F. N. Van Dau, *The emergence of spin electronics in data storage*, Nature Materials **6**(11), 813 (2007), URL http://dx.doi.org/10.1038/nmat2024. 31

[56] N. A. Spaldin and R. Ramesh, *Advances in magnetoelectric multiferroics*, Nature Materials **18**(3), 203 (2019), URL https://doi.org/10.1038/s41563-018-0275-2. 32

[57] D. Khomskii, *Classifying multiferroics: Mechanisms and effects*, Physics **2**, 20 (2009), URL https://dx.doi.org/10.1103/Physics.2.20. 32, 33, 34, 35

[58] M. Fiebig, *Revival of the magnetoelectric effect*, Journal of Physics D: Applied Physics **38**(8), R123 (2005), URL http://dx.doi.org/10.1088/0022-3727/38/8/r01.

[59] M. Fiebig, T. Lottermoser, D. Meier, and M. Trassin, *The evolution of multiferroics*, Nature Reviews Materials **1**(8), 16046 (2016), URL https://doi.org/10.1038/natrevmats.2016.46.

[60] S.-W. Cheong and M. Mostovoy, *Multiferroics: a magnetic twist for ferroelectricity*, Nature Materials **6**(1), 13 (2007), URL https://doi.org/10.1038/nmat1804. 32

[61] N. A. Hill, *Why Are There so Few Magnetic Ferroelectrics?*, The Journal of Physical Chemistry B **104**(29), 6694 (2000), URL https://pubs.acs.org/doi/10.1021/jp000114x. 33

[62] J. T. Heron, J. L. Bosse, Q. He, Y. Gao, M. Trassin, L. Ye, J. D. Clarkson, C. Wang, J. Liu, S. Salahuddin, D. C. Ralph, D. G. Schlom, J. Íñiguez, B. D. Huey, and R. Ramesh, *Deterministic switching of ferromagnetism at room temperature using an electric field*, Nature **516**(7531), 370 (2014), URL https://doi.org/10.1038/nature14004. 33

[63] Y. S. Oh, S. Artyukhin, J. J. Yang, V. Zapf, J. W. Kim, D. Vanderbilt, and S. W. Cheong, *Non-hysteretic colossal magnetoelectricity in a collinear antiferromagnet*, Nature Communications **5**, 1 (2014), URL http://dx.doi.org/10.1038/ncomms4201. 34

[64] P. Radaelli, L. Chapon, A. Daoud-Aladine, C. Vecchini, P. Brown, T. Chatterji, S. Park, and S. Cheong, *Electric field switching of antiferromagnetic domains in ymn_2o_5: A probe of the multiferroic mechanism*, Phys. Rev. Lett. **101**, 067205 (2008), URL http://dx.doi.org/10.1103/PhysRevLett.101.067205. 34, 60

[65] N. Lee, C. Vecchini, Y. Choi, L. Chapon, A. Bombardi, P. Radaelli, and S.-W. Cheong, *Giant tunability of ferroelectric polarization in* $gdmn_2\mathbf{o}_5$, Phys. Rev. Lett. **110**, 137203 (2013), URL https://dx.doi.org/10.1103/PhysRevLett.110.137203. 34, 37, 38, 40

[66] L. Chapon, G. Blake, M. Gutmann, S. Park, N. Hur, P. Radaelli, and S.-W. Cheong, *Structural anomalies and multiferroic behavior in magnetically frustrated $tbmn_2o_5$*, Phys. Rev. Lett. **93**, 177402 (2004), URL http://dx.doi.org/10.1103/PhysRevLett.93.177402. 34

[67] L. Chapon, P. Radaelli, G. Blake, S. Park, and S. Cheong, *Ferroelectricity induced by acentric spin-density waves in ymn_2o_5*, Phys. Rev. Lett. **96**, 097601 (2006), URL http://dx.doi.org/10.1103/PhysRevLett.96.097601.

[68] G. Blake, L. Chapon, P. Radaelli, S. Park, N. Hur, S.-W. Cheong, and J. Rodríguez-Carvajal, *Spin structure and frustration in multiferroic rmn_2o_5 (r = tb, ho, dy)*, Phys. Rev. B **71**, 214402 (2005), URL http://dx.doi.org/10.1103/PhysRevB.71.214402.

[69] P. Radaelli, C. Vecchini, L. C. und P.J. Brown, S. Park, and S.-W. Cheong, *Incommensurate magnetic structure of ymn_2o_5: A stringent test of the multiferroic mechanism*, Phys. Rev. B **79**, 020404 (R) (2009).

[70] P. Radaelli and L. Chapon, *A neutron diffraction study of rmn_2o_5 multiferroics*, J. Phys. Cond. Mat. **20**, 434213 (2008), URL http://dx.doi.org/10.1088/0953-8984/20/43/434213.

[71] S. H. Zheng, J. J. Gong, Y. Q. Li, C. F. Li, Y. S. Tang, J. H. Zhang, L. Lin, Z. B. Yan, X. P. Jiang, S. W. Cheong, and J. M. Liu, *Abnormal dependence of multiferroicity on high-temperature electro-poling in $GdMn_2O_5$*, J. Appl. Phys. **126**(17) (2019), URL http://dx.doi.org/10.1063/1.5120971. 34

[72] J. A. Alonso, M. T. Casais, M. J. Martinez-Lope, J. L. Martínez, and M. T. Fernández-Díaz, *A structural study from neutron diffraction data and magnetic properties of RMn2O5 (R = La, rare earth)*, Journal of Physics Condensed Matter **9**(40), 8515 (1997), URL http://dx.doi.org/10.1088/0953-8984/9/40/017. 34

[73] C. Vecchini, A. Bombardi, L. C. Chapon, N. Lee, P. G. Radaelli, and S.-W. Cheong, *Magnetic phase diagram and ordered ground state of $gdmn_2o_5$ multiferroic studied by x-ray magnetic scattering*, Journal of Physics: Conference Series **519**, 012004 (2014), URL http://dx.doi.org/10.1088/1742-6596/519/1/012004. 34

[74] C. Vecchini, L. Chapon, P. Brown, T. Chatterji, S. Park, S.-W. Cheong, and P. Radaelli, *Commensurate magnetic structures of rmn_2o_5 (r = y, ho, bi) determined by single-crystal neutron diffraction*, Phys. Rev. B **77**, 134434 (2008). 34

[75] W. P. Mason and B. T. Matthias, *Theoretical model for explaining the ferroelectric effect in barium titanate*, Physical Review **74**(11), 1622 (1948), URL http://dx.doi.org/10.1103/PhysRev.74.1622. 35, 84

[76] A. Von Hippel, *Ferroelectricity, domain structure, and phase transitions of barium titanate*, Reviews of Modern Physics **22**(3), 221 (1950), URL http://dx.doi.org/10.1103/RevModPhys.22.221. 35, 84

[77] Y. J. Choi, H. T. Yi, S. Lee, Q. Huang, V. Kiryukhin, and S. W. Cheong, *Ferroelectricity in an ising chain magnet*, Phys. Rev. Lett. **100**(4), 6 (2008), URL http://dx.doi.org/10.1103/PhysRevLett.100.047601. 35

[78] E. A. Harris, *Related content EPR of Mn pairs in MgO and CaO*, Journal of Physics C: Solid State Physics (5), 338 (1972), URL https://doi.org/10.1088/0022-3719/5/3/014. 35

[79] G. Giovannetti and J. Van Den Brink, *Electronic correlations decimate the ferroelectric polarization of multiferroic HoMn2O5*, Physical Review Letters **100**(22), 2 (2008), URL https://dx.doi.org/10.1103/PhysRevLett.100.227603. 37

[80] R. A. de Souza, U. Staub, V. Scagnoli, M. Garganourakis, Y. Bodenthin, S.-W. Huang, M. García-Fernández, S. Ji, S.-H. Lee, S. Park, and S.-W. Cheong, *Magnetic structure and electric field effects in multiferroic ymn_2o_5*, Phys. Rev. B **84**, 104416 (2011), URL http://link.aps.org/doi/10.1103/PhysRevB.84.104416. 40

[81] M. J. Rice and E. J. Mele, *Elementary excitations of a linearly conjugated diatomic polymer*, Phys. Rev. Lett. **49**, 1455 (1982), URL http://dx.doi.org/10.1103/PhysRevLett.49.1455. 46, 50

[82] D. J. Thouless, M. Kohmoto, M. P. Nightingale, and M. Den Nijs, *Quantized hall conductance in a two-Dimensional periodic potential*, Physical Review Letters **49**(6), 405 (1982), URL http://dx.doi.org/10.1103/PhysRevLett.49.405.

[83] D. J. Thouless, *Quantization of particle transport*, Phys. Rev. B **27**, 6083 (1983), URL http://dx.doi.org/10.1103/PhysRevB.27.6083.

[84] S. Nakajima, T. Tomita, S. Taie, T. Ichinose, H. Ozawa, L. Wang, M. Troyer, and Y. Takahashi, *Topological thouless pumping of ultracold fermions*, Nature Physics **12**(4), 296 (2016), URL https://doi.org/10.1038/nphys3622. 50

[85] M. Atala, M. Aidelsburger, J. T. Barreiro, D. Abanin, T. Kitagawa, E. Demler, and I. Bloch, *Direct measurement of the zak phase in topological bloch bands*, Nature Physics **9**(12), 795 (2013), URL https://doi.org/10.1038/nphys2790. 46, 50

[86] Y. S. Oh, S. Artyukhin, J. J. Yang, V. Zapf, J. W. Kim, D. Vanderbilt, and S.-W. Cheong, *Non-hysteretic colossal magnetoelectricity in a collinear antiferromagnet*, Nature Communications **5**(1), 3201 (2014), URL https://doi.org/10.1038/ncomms4201. 60

[87] B. Monserrat and D. Vanderbilt, *Phonon-assisted spin splitting in centrosymmetric crystals* (4), 1 (2017), URL https://arxiv.org/abs/1711.06274. 61

[88] N. I. Kulikov and V. V. Tugushev, *Spin-density waves and itinerant antiferromagnetism in metals* **954** (1984), URL https://doi.org/10.1070/PU1984v027n12ABEH004088. 61

[89] E. Fawcett, *Spin-density-wave antiferromagnetism in chromium*, Reviews of Modern Physics **60**(1), 209 (1988), URL http://dx.doi.org/10.1103/RevModPhys.60.209. 61

[90] A. Singer, M. J. Marsh, S. H. Dietze, V. Uhlíř, Y. Li, D. A. Walko, E. M. Dufresne, G. Srajer, M. P. Cosgriff, P. G. Evans, E. E. Fullerton, and O. G. Shpyrko, *Condensation of collective charge ordering in chromium*, Physical Review B - Condensed Matter and Materials Physics **91**(11), 1 (2015), URL http://dx.doi.org/10.1103/PhysRevB.91.115134. 62, 63

[91] E. Torrontegui, S. Ibáñez, S. Martínez-Garaot, M. Modugno, A. del Campo, D. Guéry-Odelin, A. Ruschhaupt, X. Chen, and J. G. Muga, *Shortcuts to Adiabaticity*, Advances in Atomic, Molecular and Optical Physics **62**(September), 117 (2013), URL http://dx.doi.org/10.1016/B978-0-12-408090-4.00002-5. 62

[92] S. Deffner, C. Jarzynski, and A. del Campo, *Classical and quantum shortcuts to adiabaticity for scale-invariant driving*, Physical Review X **4**(2), 1 (2014), URL http://dx.doi.org/10.1103/PhysRevX.4.021013.

[93] B. B. Zhou, A. Baksic, H. Ribeiro, C. G. Yale, F. J. Heremans, P. C. Jerger, A. Auer, G. Burkard, A. A. Clerk, and D. D. Awschalom, *Accelerated quantum control using superadiabatic dynamics in a solid-state lambda system*, Nature Physics **13**(4), 330 (2017), URL http://dx.doi.org/10.1038/nphys3967. 62

[94] Y.-A. Soh and R. K. Kummamuru, *Spintronics in antiferromagnets*, Philosophical Transactions of the Royal Society A: Mathematical, Physical and Engineering Sciences **369**(1951), 3646 (2011), URL https://royalsocietypublishing.org/doi/10.1098/rsta.2011.0186. 62

[95] A. Singer, S. K. Patel, V. Uhlíř, R. Kukreja, A. Ulvestad, E. M. Dufresne, A. R. Sandy, E. E. Fullerton, and O. G. Shpyrko, *Phase coexistence and pinning of charge density waves by interfaces in chromium*, Physical Review B **94**(17), 1 (2016), URL https://link.aps.org/doi/10.1103/PhysRevB.94.174110. 62

[96] A. Singer, S. K. K. Patel, R. Kukreja, V. Uhlíř, J. Wingert, S. Festersen, D. Zhu, J. M. Glownia, H. Lemke, S. Nelson, M. Kozina, K. Rossnagel, M. Bauer, B. M. Murphy, O. M. Magnussen, E. E. Fullerton, and O. G. Shpyrko, *Photoinduced Enhancement of the Charge Density Wave Amplitude*, Physical Review Letters **117**(5) (2015), URL http://dx.doi.org/10.1103/PhysRevLett.117.056401. 62, 66, 72

[97] O. Gorobtsov, L. Ponet, and et al., *Femtosecond control of phonon dynamics near a magnetic order critical point*, Nature Communications, under review . 63, 64

[98] H. J. Zeiger, J. Vidal, T. K. Cheng, E. P. Ippen, G. Dresselhaus, and M. S. Dresselhaus, *Theory for displacive excitation of coherent phonons*, Physical Review B **45**(2), 768 (1992), URL http://dx.doi.org/10.1103/PhysRevB.45.768. 66

[99] C. W. Nicholson, C. Monney, R. Carley, B. Frietsch, J. Bowlan, M. Weinelt, and M. Wolf, *Ultrafast Spin Density Wave Transition in Chromium Governed by Thermalized Electron Gas*, Phys. Rev. Lett. **117**(13), 1 (2016), URL http://dx.doi.org/10.1103/PhysRevLett.117.136801. 66, 69

[100] D. I. Khomskii, *Basic Aspects of The Quantum Theory of Solids* (Cambridge University Press, Cambridge, 2010), URL http://dx.doi.org/10.1017/CBO9780511780271. 67

[101] C. Rackauckas and Q. Nie, *Differentialequations.jl–a performant and feature-rich ecosystem for solving differential equations in julia*, Journal of Open Research Software **5**(1) (2017), URL http://doi.org/10.5334/jors.151. 68

[102] J. L. Hostetler, A. N. Smith, D. M. Czajkowsky, and P. M. Norris, *Measurement of the electron-phonon coupling factor dependence on film thickness and grain size in Au, Cr, and Al*, Applied Optics **38**(16), 3614 (1999), URL http://dx.doi.org/10.1364/ao.38.003614. 69

[103] P. K. Mogensen and A. N. Riseth, *Optim: A mathematical optimization package for Julia*, Journal of Open Source Software **3**(24), 615 (2018), URL https://doi.org/10.21105/joss.00615. 69, 111

[104] J. A. Nelder and R. Mead, *A Simplex Method for Function Minimization*, The Computer Journal **7**(4), 308 (1965), URL http://dx.doi.org/10.1093/comjnl/7.4.308. 69

[105] S. M. Griffin, M. Lilienblum, K. Delaney, Y. Kumagai, M. Fiebig, and N. A. Spaldin, *From multiferroics to cosmology: Scaling behaviour and beyond in the hexagonal manganites* **1**, 1 (2012), 1204.3785, URL http://dx.doi.org/10.1103/PhysRevX.2.041022. 78

[106] S. Shen, J. Chen, J. Jian, F. Luo, J. Mei, and J. Cheng, *The effect of cooling rate on structural and electrical properties of multiferroic BLF-PT ceramics*, J. Am. Ceram. Soc. **101**(12), 5497 (2018), URL http://dx.doi.org/10.1111/jace.15804.

[107] G. F. Nataf, M. Guennou, J. M. Gregg, D. Meier, J. Hlinka, E. K. Salje, and J. Kreisel, *Domain-wall engineering and topological defects in ferroelectric and ferroelastic materials*, Nat. Rev. Phys. **2**(11), 634 (2020), URL http://dx.doi.org/10.1038/s42254-020-0235-z. 78

[108] W. Schranz, H. Kabelka, A. Sarras, and M. Burock, *Giant domain wall response of highly twinned ferroelastic materials*, Appl. Phys. Lett. **101**(14), 1 (2012), 1601.03590. 78

[109] W. J. Merz, *Domain formation and domain wall motions in ferroelectric BaTiO3 single crystals*, Phys. Rev. **95**(3), 690 (1954), URL https://doi.org/10.1103/PhysRev.95.690. 78

[110] P. Gao, J. Britson, J. R. Jokisaari, C. T. Nelson, S. H. Baek, Y. Wang, C. B. Eom, L. Q. Chen, and X. Pan, *Atomic-scale mechanisms of ferroelastic domain-wall-mediated ferroelectric switching*, Nat. Commun. **4**(2791), 1 (2013), URL http://dx.doi.org/10.1038/ncomms3791. 78

[111] H. Kliem and R. Tadros-Morgane, *Extrinsic versus intrinsic ferroelectric switching: Experimental investigations using ultra-thin PVDF Langmuir-Blodgett films*, Journal of Physics D: Applied Physics **38**(12), 1860 (2005), URL https://dx.doi.org/10.1088/0022-3727/38/12/002. 78

[112] A. K. Tagantsev, L. E. Cross, and J. Fousek, *Domains in Ferroic Crystals and Thin Films* (Springer New York, New York, NY, 2010), URL https://doi.org/10.1007/978-1-4419-1417-0. 78

[113] J. F. Scott, E. K. H. Salje, and M. A. Carpenter, *Domain wall damping and elastic softening in SrTiO3: Evidence for polar twin walls*, Phys. Rev. Lett. **109**, 187601 (2012), URL https://doi.org/10.1103/PhysRevLett.109.187601. 78, 80

[114] R. Inoue, S. Ishikawa, R. Imura, Y. Kitanaka, T. Oguchi, Y. Noguchi, and M. Miyayama, *Giant photovoltaic effect of ferroelectric domain walls in perovskite single crystals*, Scientific Reports **5**, 1 (2015), URL http://dx.doi.org/10.1038/srep14741. 78

[115] S. Körbel, J. Hlinka, and S. Sanvito, *Electron trapping by neutral pristine ferroelectric domain walls in $BiFeO_3$*, Physical Review B **98**(10), 100104 (2018), URL https://link.aps.org/doi/10.1103/PhysRevB.98.100104.

[116] S. Körbel and S. Sanvito, *Photovoltage from ferroelectric domain walls in BiFeO3*, Phys. Rev. B **102**(8), 1 (2020), URL https://dx.doi.org/10.1103/PhysRevB.102.081304.

[117] H. Huyan, L. Li, C. Addiego, W. Gao, and X. Pan, *Structures and electronic properties of domain walls in BiFeO3 thin films*, National Science Review **6**(4), 669 (2019), URL http://dx.doi.org/10.1093/nsr/nwz101. 78

[118] J. Seidel, L. W. Martin, Q. He, Q. Zhan, Y.-H. Chu, A. Rother, M. E. Hawkridge, P. Maksymovych, P. Yu, M. Gajek, N. Balke, S. V. Kalinin, S. Gemming, F. Wang, G. Catalan, J. F. Scott, N. A. Spaldin, J. Orenstein, and R. Ramesh, *Conduction at domain walls in oxide multiferroics*, Nat. Mater. **8**, 229 (2009), URL https://doi.org/10.1038/nmat2373. 78

[119] F. Li, L. Jin, Z. Xu, and S. Zhang, *Electrostrictive effect in ferroelectrics: An alternative approach to improve piezoelectricity*, Applied Physics Reviews **1**(1) (2014), URL https://dx.doi.org/10.1063/1.4861260. 79

[120] P. Marton, I. Rychetsky, and J. Hlinka, *Domain walls of ferroelectric BaTiO3 within the ginzburg-landau-devonshire phenomenological model*, Phys. Rev. B **81**(14), 144125 (2010). 79, 84, 85, 86, 87, 93

[121] W. Cao and L. E. Cross, *Theory of tetragonal twin structures in ferroelectric perovskites with a first-order phase transition*, Physical Review B **44**(1), 5 (1991), URL http://dx.doi.org/10.1103/PhysRevB.44.5. 87

[122] H.-L. Hu and L.-Q. Chen, *Ferroelectric Domain Formation*, Journal of the American Ceramic Society **81**, 492 (1998), URL http://dx.doi.org/10.1111/j.1151-2916.1998.tb02367.x. 79

[123] G. A. Schneider and L. M. Eng, *Stress-induced movement of ferroelastic domain walls in BaTiO3 using AFM* **480**, 1 (2001), URL papers://2973f1d5-d696-469c-80fa-0e7ffe9241d4/Paper/p1874. 79

[124] H. Lu, C.-W. Bark, D. E. de los Ojos, J. A. Universitat, C.-B. Eom, G. Catalan, A. Gruverman, and Th, *Mechanical Writing of Ferroelectric Polarization*, Alexei Gruverman Publications (56) (2012), URL http://dx.doi.org/10.1126/science.1218693. 80

[125] A. Abdollahi, C. Peco, D. Millán, M. Arroyo, G. Catalan, and I. Arias, *Fracture toughening and toughness asymmetry induced by flexoelectricity*, Phys. Rev. B - Condens. Matter Mater. Phys. **92**(9), 25 (2015), URL http://dx.doi.org/10.1103/PhysRevB.92.094101.

[126] K. Cordero-Edwards, N. Domingo, A. Abdollahi, J. Sort, and G. Catalan, *Ferroelectrics as Smart Mechanical Materials*, Adv. Mater. **29**(37), 1 (2017), URL http://dx.doi.org/10.1002/adma.201702210.

[127] K. Cordero-Edwards, H. Kianirad, C. Canalias, J. Sort, and G. Catalan, *Flexoelectric Fracture-Ratchet Effect in Ferroelectrics*, Phys. Rev. Lett. **122**(13), 135502 (2019), URL http://dx.doi.org/10.1103/PhysRevLett.122.135502. 80

[128] W. T. Lee, E. K. Salje, and U. Bismayer, *Domain wall diffusion and domain wall softening*, J. Phys. Condens. Matter **15**(8), 1353 (2003), URL http://dx.doi.org/10.1088/0953-8984/15/8/318. 80

[129] V. A. Zhirnov, *A Contribution To the Theory of Domain Walls in Ferroelectrics*, Soviet physics JETP **35**(5), 822 (1959). 80, 83, 85

[130] P. Ferraro, S. Grilli, and P. De Natale, eds., *Ferroelectric Crystals for Photonic Applications*, vol. 91 of *Springer Series in Materials Science* (Springer Berlin Heidelberg, Berlin, Heidelberg, 2014), URL http://link.springer.com/10.1007/978-3-642-41086-4. 80

[131] C. Stefani, L. Ponet, K. Shapovalov, P. Chen, E. Langenberg, D. G. Schlom, S. Artyukhin, M. Stengel, N. Domingo, and G. Catalan, *Mechanical Softness of Ferroelectric 180° Domain Walls*, Physical Review X **10**(4), 041001 (2020), URL http://dx.doi.org/10.1103/PhysRevX.10.041001. 80, 83, 89, 90

[132] C. Harnagea, A. Pignolet, M. Alexe, and D. Hesse, *Piezoresponse scanning force microscopy: What quantitative information can we really get out of piezoresponse measurements on ferroelectric thin films*, Integrated Ferroelectrics **38**(1-4), 23 (2001), URL http://dx.doi.org/10.1080/10584580108016914. 80

[133] U. Rabe, S. Amelio, E. Kester, V. Scherer, S. Hirsekorn, and W. Arnold, *Quantitative determination of contact stiffness using atomic force acoustic microscopy*, Ultrasonics **38**(1-8), 430 (2000), URL http://dx.doi.org/10.1016/S0041-624X(99)00207-3. 81

[134] L. Landau and E. M. E. M. Lifshitz, *Vol 7 - Theory of Elasticity* (1960). 83

[135] P. Ghosez, X. Gonze, and J. P. Michenaud, *First principle calculations of dielectric and effective charge tensors in barium titanate*, Ferroelectrics **153**(1), 91 (1994), URL http://dx.doi.org/10.1080/00150199408016548. 84

[136] J. B. MacChesney, P. K. Gallagher, and F. V. DiMarcello, *Stabilized Barium Titanate Ceramics for Capacitor Dielectrics*, Journal of the American Ceramic Society **46**(9), 411 (1963), URL https://doi.org/10.1111/j.1151-2916.1963.tb19771.x. 84

[137] R. F. B. D. Schofield, *An Investigation of Some Barium Titanate Compositions for Transducer Applications*, Canadian Journal of Physics **35**(1953), 594 (1957), URL https://doi.org/10.1139/p57-067. 84

[138] S. Ramakanth, S. Hamad, S. Venugopal Rao, and K. C. James Raju, *Magnetic and nonlinear optical properties of BaTiO3 nanoparticles*, AIP Advances **5**(5) (2015), URL http://dx.doi.org/10.1063/1.4921480. 84

[139] P. Ghosez, X. Gonze, and J. P. Michenaud, *A microscopic study of barium titanate*, Ferroelectrics **164**(1), 113 (1995), URL http://dx.doi.org/10.1080/00150199508221833. 84

[140] T. Tsuji, S. Saito, K. Fukuda, K. Yamanaka, H. Ogiso, J. Akedo, and Y. Kawakami, *Significant stiffness reduction at ferroelectric domain boundary evaluated by ultrasonic atomic force microscopy*, Applied Physics Letters **87**(7), 2003 (2005), URL http://dx.doi.org/10.1063/1.2012537. 84, 88, 89

[141] P. Chen, L. Ponet, K. Lai, R. Cingolani, and S. Artyukhin, *Domain wall-localized phonons in BiFeO3: spectrum and selection rules*, npj Computational Materials **6**(1) (2020), URL http://dx.doi.org/10.1038/s41524-020-0304-y. 84, 90, 98

[142] L.N.Bulaevskii, *Theory of Non-Uniform Anti Ferromagnetic Spin Chains*, Soviet Physics Jetp **17**(3), 684 (1963), URL http://www.jetp.ac.ru/cgi-bin/dn/e_017_03_0684.pdf. 85

[143] B. Meyer and D. Vanderbilt, *Ab initio study of ferroelectric domain walls in .(formula presented)*, Physical Review B - Condensed Matter and Materials Physics **65**(10), 1 (2002), URL http://dx.doi.org/10.1103/PhysRevB.65.104111. 85, 93

[144] P. Marton, *Discretisation originated Peierls–Nabarro barriers in simulations of ferroelectrics*, Phase Transitions **91**(9-10), 959 (2018), URL http://dx.doi.org/10.1080/01411594.2018.1515434. 85, 93, 94

[145] W. Voigt, *Lehrbuch der kristallphysik* (B. G. Teubner, Leipzig, Berlin, 1910). 86

[146] Y. Xiao, V. B. Shenoy, and K. Bhattacharya, *Depletion layers and domain walls in semiconducting ferroelectric thin films*, Physical Review Letters **95**(24), 1 (2005), URL http://dx.doi.org/10.1103/PhysRevLett.95.247603. 88

[147] P. Marton, *Modelling of Domain Structures* (July) (2007). 92

[148] R. Peierls, *The size of a dislocation*, Proc. Phys. Soc. **52**(1), 34 (1940), URL http://dx.doi.org/10.1088/0959-5309/52/1/305. 93

[149] F. R. Nabarro, *Dislocations in a simple cubic lattice*, Proc. Phys. Soc. **59**(2), 256 (1947), URL http://dx.doi.org/10.1088/0959-5309/59/2/309. 93

[150] J. Padilla, W. Zhong, and D. Vanderbilt, *First-principles investigation of 180° domain walls in BaT*, Physical Review B - Condensed Matter and Materials Physics **53**(10), R5969 (1996), URL http://dx.doi.org/10.1103/PhysRevB.53.R5969. 94

[151] A. Damascelli, *Probing the electronic structure of complex systems by ARPES*, Physica Scripta T **T109**, 61 (2004), URL http://dx.doi.org/10.1238/Physica.Topical.109a00061. 99

[152] P. Hohenberg and W. Kohn, *Inhomogeneous Electron Gas*, Physical Review **136**(3B), B864 (1964), URL http://dx.doi.org/10.1103/PhysRev.136.B864. 99

[153] W. Kohn and L. J. Sham, *Self-Consistent Equations Including Exchange and Correlation Effects*, Physical Review **140**(4A), A1133 (1965), URL http://dx.doi.org/10.1103/PhysRev.140.A1133. 99, 100

[154] D. R. Hamann, M. Schlüter, and C. Chiang, *Norm-Conserving Pseudopotentials*, Physical Review Letters **43**(20), 1494 (1979), URL https://link.aps.org/doi/10.1103/PhysRevLett.43.1494. 99, 101

[155] S. Louie, S. Froyen, and L. Cohen, *Nonlinear ionic Pseudopotentials*, Physical Review B **26**(4), 1738 (1982), URL http://link.aps.org/doi/10.1103/PhysRevB.26.1738{%}0Apapers3://publication/doi/10.1103/PhysRevB.26.1738.

[156] D. Vanderbilt, *Soft self-consistent pseudopotentials in a generalized eigenvalue formalism*, Physical Review B **41**(11), 7892 (1990), URL https://link.aps.org/doi/10.1103/PhysRevB.41.7892.

[157] D. Joubert, *From ultrasoft pseudopotentials to the projector augmented-wave method*, Physical Review B - Condensed Matter and Materials Physics **59**(3), 1758 (1999). 101

[158] J. P. Perdew, *Accurate Density Functional for the Energy: Real-Space Cutoff of the Gradient Expansion for the Exchange Hole*, Physical Review Letters **55**(16), 1665 (1985), URL https://link.aps.org/doi/10.1103/PhysRevLett.55.1665.

[159] J. P. Perdew and W. Yue, *Accurate and simple density functional for the electronic exchange energy: Generalized gradient approximation*, Physical Review B **33**(12), 8800 (1986), URL https://link.aps.org/doi/10.1103/PhysRevB.33.8800. 99

[160] R. M. Martin, *Electronic Structure* (Cambridge University Press, 2004), URL http://dx.doi.org/10.1017/CBO9780511805769. 99

[161] N. W. Ashcroft, N. D. Mermin, and S. Rodriguez, *Solid State Physics*, American Journal of Physics **46**(1), 116 (1978), URL http://aapt.scitation.org/doi/10.1119/1.11117. 101, 103

[162] G. H. Wannier, *The structure of electronic excitation levels in insulating crystals*, Physical Review **52**(3), 191 (1937), URL http://dx.doi.org/10.1103/PhysRev.52.191. 103

[163] N. Marzari, I. Souza, and D. Vanderbilt, *An Introduction to Maximally-Localized Wannier Functions*, Highlight the Month PsiK Newsletter **57**(3), 129 (2003), URL http://dx.doi.org/10.1103/PhysRevB.65.035109. 103

[164] N. Marzari, A. A. Mostofi, J. R. Yates, I. Souza, and D. Vanderbilt, *Maximally localized Wannier functions: Theory and applications*, Reviews of Modern Physics **84**(4), 1419 (2012), URL http://dx.doi.org/10.1103/RevModPhys.84.1419. 103, 104, 106, 108

[165] J. Kunes, *Wannier Functions and Construction of Model Hamiltonians* . 106

[166] E. I. Blount, *Formalisms of Band Theory*, Solid State Phys. - Adv. Res. Appl. **13**(C), 305 (1962), URL http://dx.doi.org/10.1016/S0081-1947(08)60459-2. 106

[167] S. B. Biner, *Programming Phase-Field Modeling*, URL https://doi.org/10.1007/978-3-319-41196-5. 109, 110

[168] Zureks, *Example of 2d mesh* (2007), [Online; accessed 20-January-2021], URL https://commons.wikimedia.org/wiki/File:Example_of_2D_mesh.png. 110

[169] M. Hestenes and E. Stiefel, *Methods of conjugate gradients for solving linear systems*, J. Res. Natl. Bur. Stand. (1934). **49**(6), 409 (1952), URL http://dx.doi.org/10.6028/jres.049.044. 111

[170] W. W. Hager and H. Zhang, *Guaranteed Descent and an Efficient Line Search*, SIAM J. Optim. **16**(1), 170 (2005), URL https://doi.org/10.1137/030601880. 111

[171] J. Revels, M. Lubin, and T. Papamarkou, *Forward-mode automatic differentiation in Julia*, arXiv:1607.07892 [cs.MS] (2016), URL https://arxiv.org/abs/1607.07892. 111

[172] P. H. Hoffmann, *A Hitchhiker's Guide to Automatic Differentiation*, Numerical Algorithms **72**(3), 775 (2016), URL http://dx.doi.org/10.1007/s11075-015-0067-6. 111